

Luminescence Thermometry

Fundamentals and Applications

ISBN: 978-94-6380-064-8

Printed by: ProefschriftMaken || www.proefschriftmaken.nl

Luminescence Thermometry

Fundamentals and Applications

Luminescentithermometrie

Basisprincipes en Applicaties
(met een samenvatting in het Nederlands)

Proefschrift

ter verkrijging van de graad van doctor aan de Universiteit Utrecht op gezag van de rector magnificus, prof. dr. H. R. B. M. Kummeling, ingevolge het besluit van het college voor promoties in het openbaar te verdedigen

op woensdag 19 december 2018

des middags te 4.15 uur

door

Robin Gabriël Geitenbeek

geboren op 3 augustus 1988 te Gouda

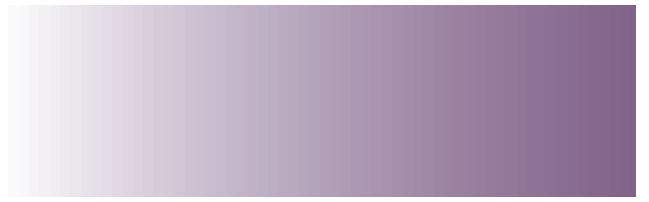
Promotoren:

Prof. dr. A. Meijerink
Prof. dr. ir. B. M. Weckhuysen
Prof. dr. A. van Blaaderen

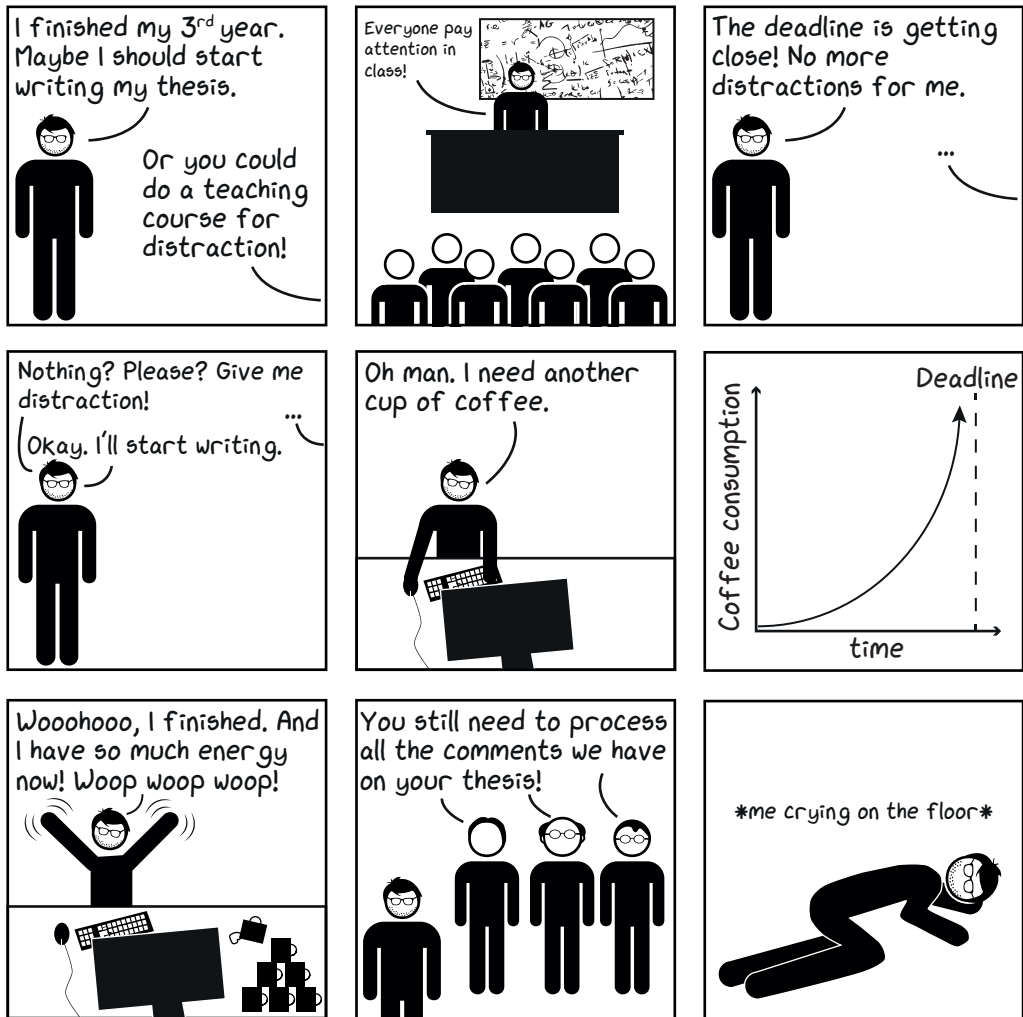
Dit proefschrift maakt deel uit van het onderzoeksprogramma 'Future methodologies in catalysis and solar fuels production' van het Netherlands Center for Multiscale Catalytic Energy Conversion (MCEC), een Gravitation Programma dat wordt gefinancierd door de Nederlandse Organisatie voor Wetenschappelijk Onderzoek (NWO).

Table of Contents

Chapter 1	Introduction	6
Chapter 2	Investigation and Modeling on Non-Boltzmann Luminescence in $\text{NaYF}_4:\text{Eu}^{3+}$: Implications for Luminescence Thermometry.	22
Chapter 3	$\text{NaYF}_4:\text{Er}^{3+}, \text{Yb}^{3+}/\text{SiO}_2$ Core/Shell Upconverting Nanocrystals for Luminescence Thermometry up to 900 K.	46
Chapter 4	In Situ Luminescence Thermometry To Locally Measure Temperature Gradients During Catalytic Reactions.	68
Chapter 5	Luminescence Thermometry to Monitor Temperature in a Microelectromechanical System for Scanning Transmission X-ray Microscopy.	82
Chapter 6	Luminescence Thermometry in Microfluidic Systems.	100
Chapter 7	Extrudate Sensors for Probing Metal-Support Interfacial Catalytic Reactions Using Operando SHINERS and Luminescence Thermometry	118
Chapter 8	Chemically and Thermally Stable Lanthanide-doped Y_2O_3 Nanoparticles for Remote Temperature Sensing in Catalytic Environments.	138
Chapter 9	Summary, Conclusions and Perspectives.	156
	Nederlandse samenvatting	164
	Dankwoord/Acknowledgements	180
	List of publications and conference contributions	186
	About the author	189



Chapter 1 – Introduction



Robin Geitenbeek



Alfons van Blaaderen



Bert Weckhuysen



Andries Meijerink

Classic thermometers

Measuring temperatures using thermometers is a routine operation in our modern society. If people are asked to visualize a thermometer, most people will think of the thermometers shown in Figure 1.1. Thermometers are useful devices, which are widely used in meteorology, health care and scientific research. A thermodynamic definition of the temperature involves the average kinetic energy of the atoms or molecules of a system, but there are very few cases where this property is directly measured, instead one resorts to the measurement of effects that can be directly related to the temperature such as the expansion of a liquid (Figure 1.1a), electric resistance (Figure 1.1b), blackbody radiation (Figure 1.1c) or the crystal phase transitions in liquid crystals (Figure 1.1d).

Commonly used thermometers are based on the expansion of liquids and exploit the high coefficient of thermal expansion of alcohol, pentane, xylene or mercury.⁵ Due to safety reasons, mercury is no longer used for thermometers in most countries. The temperature range of non-mercury-based thermometers is usually limited (<400 K). In the case of a resistance thermometer, the correlation between electric resistance and temperature is exploited (Figure 1.1b).⁶ In resistance thermometers platinum, nickel or copper are used to ensure a linear resistance-temperature relation with a high repeatability over a wide temperature range. Although the temperature range and accuracy has increased significantly by transitioning from liquid expansion to electric resistance measurements, the spatial resolution of the techniques is still limited to the mm-range and up.

Nanothermometry

Scientific knowledge is constantly expanding and the possibilities to create well defined structures on the nanoscale are well-established.⁷⁻⁹ However, the possibilities to measure physical parameters, especially temperature, on these length scales are still being developed. The current techniques to monitor temperature on the nanoscale are mainly based on the same principles as classical thermometers which are then downscaled to nanometer sizes.



Figure 1.1 – Classic thermometers. The most common thermometers based on the thermally induced expansion of a liquid¹ (a), changes in the electric resistance² (b), blackbody radiation³ (c) or crystal phase transitions in liquid crystals⁴ (d).

For example, Sadat and co-workers¹⁰ have been able to modify a resistance thermometer to monitor temperatures at sub- μm resolution by attaching a point contact thermocouple to an atomic force microscope (AFM) tip. By combining the thermometer with a high-resolution scanning probe technique, they were able to map temperatures on a metallic film with a temperature accuracy of ca. 10 mK and a spatial resolution of <100 nm. A second method monitors the expansion of a liquid at the nanoscale, as demonstrated by Yihua and co-workers.¹¹ In their work, they report on carbon nanotubes of 150 nm \times 12 μm , which are partially filled with gallium. Upon heating the sample, the gallium expands in the carbon nanotube. After proper calibration using an electron microscope to correlate the temperature to the increase of the gallium volume, they were able to monitor the temperature with a 5–10 % accuracy.

Although these works show that the classical thermometer concepts can be downscaled to the nanoregime, the systems do have many disadvantages. Due to the nature of atomic force microscopy, the technique of Sadat and co-workers is limited to surfaces. Furthermore, a contact between the AFM tip and the probed sample is required. This contact can also disturb the measurement by introducing an additional thermal dissipation pathway. The carbon nanotubes filled with gallium of Yihua and co-workers offers a non-contact technique and therefore does not influence the temperature measurement. However, due to the oxidation of the gallium inside the carbon nanotubes, the thermometers can only be used once and the measurements have a high temperature uncertainty. Finally, both techniques require expensive characterization tools (AFM and electron microscopy) and are hard to use for in situ temperature measurements.

The ideal nanothermometer should revolve around a non-invasive technique in order not to disturb the measurements, have a high thermal stability in order to measure temperature in a broad range in an accurate and reproducible manner and finally should function in a cheap and practical manner.

Luminescence thermometry

A technique that fulfils all the requirements for an ideal nanothermometer is luminescence thermometry.^{12,13} Luminescence thermometry is a technique in which a temperature-dependent luminescence phenomenon (such as peak position^{14,15}, peak intensity^{16–18} or lifetime^{19–21}) is probed to monitor temperature. In this PhD thesis we will focus on bandshape luminescence thermometry, in which the intensity ratio between two emission peaks is monitored with regard to temperature. Specifically, materials doped with trivalent lanthanide ions are used due to their unique luminescence properties.

Lanthanide ions have partially filled 4f-orbitals which are shielded by the more outlying 5s and 5p-orbitals and the electrons in these 4f-orbitals do not participate in chemical bonding. The emission spectra feature sharp emission lines which do not change (much) in different environments.²¹

The energy level of an electron configuration is determined by the kinetic energy of the

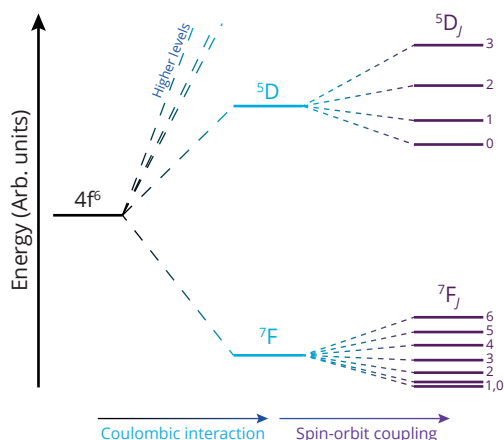


Figure 1.2 – Energy level splitting of the $4f^6$ -electron configuration in Eu^{3+} . Starting from the $4f^6$ electron configuration the splitting occurs via coulombic repulsion of the electrons (blue) and the coupling of the spin and orbital magnetic moments (purple).

electrons and the interaction between the 4f-electrons and the nucleus and core electrons. In addition, Coulombic repulsion between the different f-electrons and spin-orbit coupling²³ (and crystal field splitting), as shown in Figure 1.2, result in a rich landscape of energy levels for the trivalent lanthanide ions.^{24–26} Transitions between these energy levels can be induced by the absorption or emission of photons.²⁷ In Figure 1.3, the complete energy level diagram (up to 40000 cm^{-1}) for all lanthanides is presented. Because of the shielding of the 4f-electrons, the energy level diagram is insensitive to the chemical nature of the host and the energy levels are fixed, giving rise to characteristic luminescence for each type of lanthanide ion.

In some of the lanthanides, energy levels are present which are very close to each other. The energy difference between these states is small enough that thermal energy is sufficient to induce fast relaxation between the levels. These thermally coupled levels show a temperature dependence in their population distributions. The potential for this temperature-dependent luminescence for application in thermometry has been investigated in the literature for Gd^{3+} , Er^{3+} , Dy^{3+} , Eu^{3+} , Nd^{3+} and Pr^{3+} .^{28–33} The energy levels which are thermally coupled are shown in Figure 1.3 with a purple, green, cyan, red, deep red and blue window, respectively.

Traditionally the work horse of luminescence thermometry has been Er^{3+} .^{31,32,34–38} Here, the $^4\text{S}_{3/2}$ and $^2\text{H}_{11/2}$ state are separated by ca. 700 cm^{-1} , or several kT at 300 K (Figure 1.3). Due to the small energy difference, thermal energy is sufficient to establish Boltzmann

$$\frac{N_2}{N_1} = \frac{g_2}{g_1} e^{-\Delta E/kT} \quad (1.1)$$

equilibrium³⁹ between the $^4\text{S}_{3/2}$ and $^2\text{H}_{11/2}$ states at room temperature and higher,

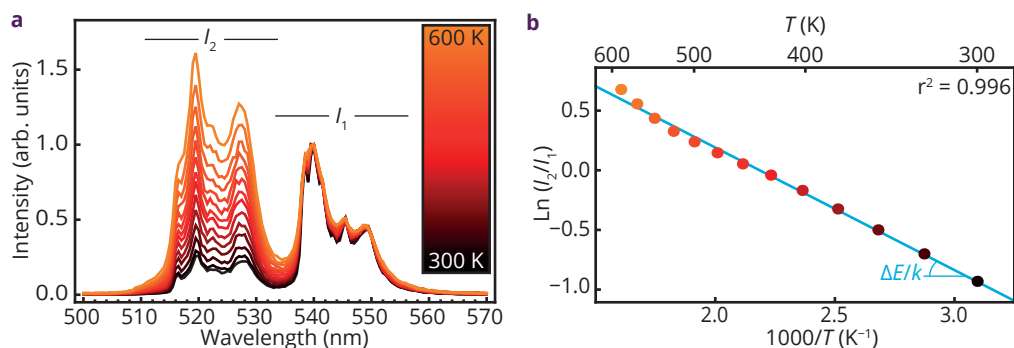


Figure 1.4 – Temperature-dependent luminescence. Temperature-dependent luminescence from the ${}^4S_{3/2}-{}^4I_{15/2}$ (I_1) and ${}^2H_{11/2}-{}^4I_{15/2}$ (I_2) transitions of $\text{NaYF}_4:\text{Er}^{3+},\text{Yb}^{3+}$ (a). The linear correlation between the natural logarithm of the fluorescence intensity ratio (FIR) and reciprocal temperature, $1000/T$ (b).

Here, N_i and g_i are the population and degeneracy of state i , respectively, ΔE is the energy difference between the two thermally coupled excited states, k is the Boltzmann constant

$$\frac{I_2}{I_1} = C e^{-\Delta E/kT}. \quad (1.2)$$

and T is the temperature. Since the emission intensity from an excited state is correlated to the population in that state, we can rewrite equation 1.1 to

Here, I_i is the emission intensity from state i and C is a constant to correlate population and emission intensity ratios. The linear correlation between $\text{Ln}(I_2/I_1)$ and $1/T$ can be exploited to get a calibration line for temperature sensing, as shown in Figure 1.4.

This calibration line can now be used to monitor temperature by converting the spectral output to $\text{Ln}(I_2/I_1)$ and finally to temperature. Note that from the steepness of the linear fit, ΔE can be calculated, which closely matches the ΔE observed in the emission spectra.

The thermal energy/temperature required to reach Boltzmann equilibrium is correlated to the energy difference, ΔE . If the ΔE becomes too large or the T too low, the radiative and non-radiative processes occur on similar timescales and the temperature dependence of the luminescence becomes more complex and does no longer follow equation (1.2).

The temperature dependence of the Er^{3+} luminescence (showing Boltzmann behavior already at room temperature) has generated a lot of scientific interest for luminescence thermometry in biological applications,^{40–42} which roughly work in the range of 300–350 K. By combining the luminescence thermometry with bio-imaging techniques it is possible to monitor temperatures in living organisms. By measuring local temperature variations, tumors can be localized, which are accompanied by an increased temperature due to rapid cell growth.⁴³

Temperature sensor performance

To reliably and reproducibly monitor temperatures, the temperature sensors should be

chemically and thermally stable. Besides the durability, the accuracy and sensitivity are

$$s_a = \frac{d(I_2/I_1)}{dT}. \quad (1.3)$$

important parameters that define the potential of a temperature sensor. An intuitive and useful parameter to define thermometer performance is the absolute thermal sensitivity,⁴⁴

Here, the absolute sensitivity, s_a is defined as the change in the fluorescence intensity ratio (FIR), $d(I_2/I_1)$, per change in temperature, dT . Although this parameter gives a good sense of how sensitive the luminescence thermometer can measure temperature it is not possible

$$s_r = \frac{1}{\text{FIR}} \frac{d\text{FIR}}{dT}. \quad (1.4)$$

to compare the results of different thermometry systems (e.g. mechanical or electrical thermometers). To compare the performance of different thermometers the relative sensitivity is commonly used,

The relative sensitivity,⁴⁵ s_r , is used as a figure of merit to compare different temperature sensors, independent of the nature of the sensor. Although the relative sensitivity is a good measure for the potential of a system, the final temperature resolution or temperature

$$\delta T = \frac{1}{s_r} (N/S)_{\text{FIR}}. \quad (1.5)$$

uncertainty is also defined by the measurement setup. In the case of low signal, a poor signal-to-noise ratio can result in large fluctuation in the spectral read-out and subsequently a low temperature resolution. The temperature uncertainty⁴⁶ is therefore a more useful performance parameter,

Here, the uncertainty in temperature, δT is determined both by the relative sensitivity and the setup by taking into account the noise-to-signal ratio, $(N/S)_{\text{FIR}}$.

Although the temperature uncertainty is a good measure, which takes into account both the potential of the temperature probes and the limitation of the experimental setup, it is still possible that other factors contribute to a lower temperature accuracy, such as systematic errors. To ensure the durability of the temperature probes, it is important to perform cycling experiments in which the sample is heated and cooled consecutively for several times, while monitoring the luminescence output. An example of this is shown in Figure 1.5 where Er^{3+} -doped NaYF_4 was heated from 300–900 K with intervals of 150 K for five times. Figure 1.5a shows the consistency of the luminescence output at specific temperatures and this is further illustrated when the natural logarithm of the FIR is plotted for the complete 5 cycles as shown in Figure 1.5b.

These results show the consistency of the experiments and the absence of hysteresis.

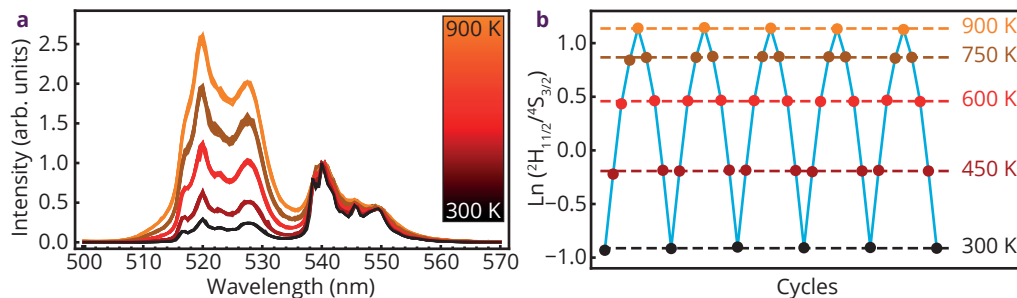


Figure 1.5 - Temperature cycling experiments. Temperature-dependent luminescence from the ${}^4S_{3/2}-{}^4I_{15/2}$ and ${}^2H_{1/2}-{}^4I_{15/2}$ transitions of $\text{NaYF}_4:\text{Er}^{3+},\text{Yb}^{3+}$ at specific temperatures upon heating and subsequent cooling (a). The natural logarithm of the fluorescence intensity ratio (FIR) at 300–900 K, for five consecutive heating cycles (b).

Additionally, it can give statistics on the measurement accuracy by calculating the standard deviation (SD) for intensity ratios measured at the same temperature in different cycles. For the different temperatures, the accuracy of the measurements can be determined by calculating the SD and taking the 95 % confidence interval from the mean value $\pm 2 \cdot \text{SD}$.

The role of temperature in catalysis

$$k = Ae^{-E_a/RT}. \quad (1.6)$$

In chemical reactors, temperature plays a crucial role, both with regard to the chemical kinetics as well as safety^{47,48} related to the thermal energy present in the reactor. In the ideal case of a homogeneously distributed temperature and concentration of chemical species, the reaction rate is determined by the Arrhenius equation,^{49,50}

Here, k is the reaction rate constant, A is the pre-exponential factor determined by the chemical reaction, E_a is the activation energy for the chemical reaction, R is the gas constant, and T is the temperature. From this equation it is evident that the temperature has a large effect on the rate at which chemical conversion occurs. When using the Arrhenius equation to describe reaction kinetics, a perfectly homogeneous temperature and concentration are assumed, which is not necessarily the case. In the case of an actual chemical reactor, stagnant flows can result in a residence time distribution⁵¹ and inhomogeneous temperature and reactant distribution as shown in Figure 1.6.

Due to non-uniform heat and mass transfer, temperatures in different regions of the reactor will differ.^{52,53} Both the temperature and residence time distribution can influence the composition of the product of the reaction. It is therefore important to understand chemical reactors and monitor the temperature distributions on the reactor scale. Typical techniques to monitor these temperatures use multiple thermocouples or infrared thermography. However, in order to monitor heat flow in these reactors, it is required to monitor temperature at many different points in the reactor, which is not possible with the surface sensing IR thermography⁵⁴ or would require a large number of thermocouples.

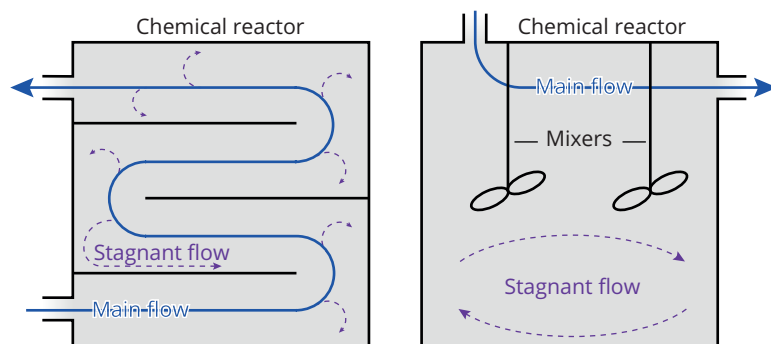


Figure 1.6 – Stagnant flow in reactors. A schematic representation of different reactor designs, resulting in stagnant flow and heterogeneous distributions of mass and heat.

Also at orders of magnitude smaller length scales it is important to realize that temperature distributions are not necessarily uniform. In the case of exothermic or endothermic reactions, the temperature can be significantly different at the reaction site (T_1 in Figure 1.7a) compared to the bulk volume of a reactor (T_2 in Figure 1.7a). Especially in the case of porous systems where both macro- and microkinetics occur, both temperature and concentration gradients can be generated on small length scales as shown in Figure 1.7b. To better understand catalytic processes, it is paramount to monitor temperature on relevant length scales which can range from nm in the case of chemical kinetics to m for stagnant flows and heat transfer effects in chemical reactors.

Luminescence thermometry is an ideal candidate for temperature sensing inside catalytic reactors due to the non-invasiveness of the technique and the accurate temperature read-outs. In this work we discuss several ideas to increase the temperature range of luminescent probes to monitor temperature profiles in chemical reactors for relevant temperature ranges (up to 900 K) and the applicability of the temperature probes in a chemical reactor is shown.

By combining luminescence thermometry with (confocal) microscopy the spatial resolution can be increased significantly. Using super-resolution microscopes it is possible to monitor luminescence from a spot size of ca 50 nm.⁵⁵ We have used this combination of luminescence thermometry with microscopy to obtain temperature maps in both microfluidic devices and model reactors on the (sub-) μm length scales.

Outline of this PhD thesis

To increase our understanding of chemical processes, it is important to monitor important parameters, such as temperature, at relevant length scales. In this PhD thesis, we aim to monitor temperature at the (sub-) μm regime during catalytically relevant conditions. To do this we have investigated a remote temperature sensing technique, bandshape luminescence thermometry in combination with light microscopy for application in catalytically relevant temperature regimes.

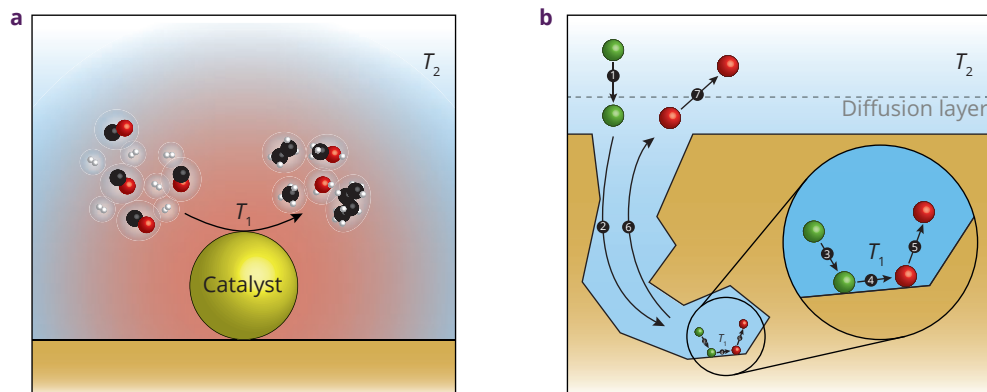


Figure 1.7 - Schematic of temperature heterogeneities in heterogeneous catalysis. A schematic representation of an exothermic reaction at the surface of a catalyst NP (a) and of the macro (1–7) and micro (3–5) kinetics in the pore of a catalyst particle (b).

A part of this PhD thesis focuses on the fundamentals of luminescence thermometry. Here, different lanthanide dopants, the source of the temperature-dependent luminescence, and several host materials have been evaluated to investigate the different temperature ranges and sensitivities in which these materials work. Furthermore, a more general description of the temperature-dependent emission for these lanthanide ions is given on the basis of thorough investigations of the excited state dynamics. Especially processes and conditions to realize Boltzmann equilibrium are discussed and evaluated.

The second part of this PhD thesis focuses on the application of luminescence thermometry. To showcase the potential of luminescence thermometry, several chemical reactions have been investigated and the temperature has been mapped in other systems in which the spatial resolution of ordinary thermometers no longer suffices.

Analysis and calibration of the temperature dependence for bandshape luminescence thermometry is commonly based on Boltzmann equilibrium of the coupled levels. In **Chapter 2** we investigate the validity of this assumption by analyzing and modeling the emission by Eu^{3+} in NaYF_4 from the $^5\text{D}_1$ level relative to the emission from $^5\text{D}_0$. The results show that for low Eu^{3+} concentrations temperature-dependent multiphonon relaxation accurately accounts for both the intensity ratio of the emissions and the dynamics of the emission decay. The analysis also reveals that Boltzmann equilibrium is not realized in the temperature regime investigated (300–900 K). Furthermore, upon increasing the Eu^{3+} concentration, cross-relaxation between neighboring Eu^{3+} ions enhances $^5\text{D}_1$ – $^5\text{D}_0$ relaxation rates, thereby extending the temperature range in which emission intensity ratios are usable for reliable and accurate temperature sensing (500–900 K). The insights obtained are important to recognize, understand, and control deviations from Boltzmann behavior in luminescence (nano)thermometry, and thus crucial for the development and understanding of reliable temperature sensors.

To monitor temperature in a wide range for catalytic application we extend the temperature

range for nanothermometry beyond 900 K in **Chapter 3** using silica coated NaYF₄ nanoparticles doped with the lanthanide ions Yb³⁺ and Er³⁺. Monodisperse ca. 20 nm NaYF₄:Er³⁺,Yb³⁺ nanocrystals were coated with a ca. 10 nm silica shell. Upon excitation with infrared radiation, bright green upconversion (UC) emission is observed. From the intensity ratio between ²H_{11/2} and ⁴S_{3/2} UC emission lines at 520 nm and 550 nm, respectively, the temperature can be determined up to at least 900 K with an accuracy of 1 to 5 K for silica coated NPs. For bare NaYF₄:Er³⁺,Yb³⁺ NPs the particles degrade above 600 K. Repeated thermal cycling experiments demonstrate the high durability and reproducibility of the silica coated nanocrystals as temperature probes without any loss of performance ensuring the applicability in harsh catalytic reactions.

This applicability for temperature sensing in a chemical reactor is further investigated in **Chapter 4**. Here, bandshape luminescence thermometry during in situ temperature measurements is reported by preparing three catalytically relevant systems, which show temperature-dependent luminescence. One of these systems was further investigated as a showcase for application. Microcrystalline NaYF₄ doped with Er³⁺ and Yb³⁺ was mixed with a commercial zeolite H-ZSM-5 to investigate the Methanol-to-Hydrocarbons (MTH) reaction, while monitoring the reaction products with on-line gas chromatography. Due to the exothermic nature of the MTH reaction, a front of increased temperature migrating down the fixed reactor bed was visualized, showing the potential for various applications of luminescence thermometry for in situ measurements in catalytic systems.

In **Chapter 5** temperature mapping was performed to understand temperatures inside a microreactor, which was used to perform catalytic characterization. Due to the inhomogeneous heating inside the reactor, high temperature discrepancies (> 100 K) have been observed, which can explain the surprising results found for the catalyst performance.

In **Chapter 6** we investigated the temperature distribution inside microfluidic channels in a 'lab-on-a-chip'. Due to the small channel sizes (100 μm), mass and heat transport and heat dissipation become more important processes and stirring is no longer required. However, measuring the temperature inside the microchannels properly is challenging. Here, we have shown that luminescence thermometry can properly address this problem from the μm to cm scale.

In **Chapter 7** we combine the NaYF₄ probe functionality to measure temperature with additional diagnostics, namely Raman spectroscopy. By combining these two diagnostic tools it becomes possible to probe temperature and chemical species at the catalyst surface, increasing our understanding of fundamental catalytic processes.

In **Chapter 8** we report temperature-dependent luminescence of Yb³⁺/Er³⁺-, Dy³⁺- and Eu³⁺-doped Y₂O₃ nanoparticles (NPs). The high chemical and thermal stability of Y₂O₃ makes these nanoprobables ideal for sensing in catalytic environments and form a more robust alternative for NaYF₄ which is used throughout this thesis. A systematic study of the three types of luminescent NPs reveals that the temperature-dependent luminescence of Yb³⁺/Er³⁺, Dy³⁺ and Eu³⁺ serves different temperature ranges: lower *T* regime (300–800

K, accuracy <5 K) for Yb³⁺/Er³⁺, intermediate *T* for Dy³⁺ (400–900+ K, accuracy <15 K) and high *T* for Eu³⁺ (550–900+ K, accuracy <12 K). We have deposited these lanthanide-doped Y₂O₃ NPs on α-Al₂O₃, a non-porous catalyst support material. The NPs are strongly adsorbed on the surface and no sintering was observed upon heating to 900 K for 12 h. The superior thermal and chemical stability of the Y₂O₃/α-Al₂O₃ host (compared to NaYF₄@SiO₂) in combination with different luminescent lanthanide dopants results in a robust system that can be tailored to monitor temperatures in different regimes with the highest possible sensitivity.

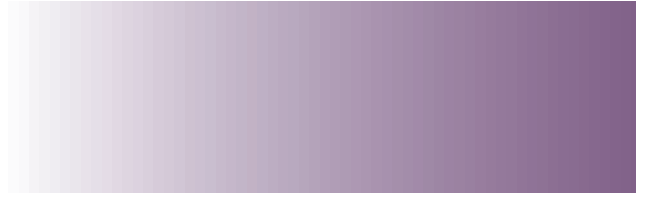
In **Chapter 9** the main findings and conclusions of this PhD thesis are summarized and an outlook for further research is presented.

References

1. AcuRite 8.5" Thermometer with Humidity <https://www.acurite.com/8-5-thermometer-with-hygrometer-00339.html>.
2. Medisana TM 700 Koortsthermometer <https://www.medisana.nl/nl/Gezondheidscontrole/Thermometer/TM-700-Koortsthermometer.html>.
3. Braun ThermoScan® 5 – IRT6020 <https://www.brauntherms.com/nl/producten/thermoscan-5-oor-thermometer-irt6020/>.
4. Fun & Feest Party Gadgets <https://www.bol.com/nl/p/stemmingsring/9200000021206887/>
5. Ride, D. L. *CRC Handbook of Chemistry and Physics*; CRC Press, Ed.; Boca Raton, **2005**.
6. Giancoli, D. C. *Physics: Principles with Applications*, 4th ed.; Hall, P., Ed.; **1995**.
7. Duan, H.; Wang, D. & Li, Y. Green Chemistry for Nanoparticle Synthesis. *Chem. Soc. Rev.* **2015**, *44*, 5778–5792.
8. Zhao, P.; Li, N. & Astruc, D. State of the Art in Gold Nanoparticle Synthesis. *Coord. Chem. Rev.* **2013**, *257*, 638–665.
9. Zhao, C.-X.; He, L.; Qiao, S. Z. & Middelberg, A. P. J. Nanoparticle Synthesis in Microreactors. *Chem. Eng. Sci.* **2011**, *66*, 1463–1479.
10. Sadat, S.; Tan, A.; Chua, Y. J. & Reddy, P. Nanoscale Thermometry Using Point Contact Thermocouples. *Nano Lett.* **2010**, *10*, 2613–2617.
11. Gao, Y.; Bando, Y.; Liu, Z.; Golberg, D. & Nakanishi, H. Temperature Measurement Using a Gallium-Filled Carbon Nanotube Nanothermometer. *Appl. Phys. Lett.* **2003**, *83*, 2913–2915.
12. Jaque, D. & Vetrone, F. Luminescence Nanothermometry. *Nanoscale* **2012**, *4*, 4301–4326.
13. Brites, C. D. S.; Lima, P. P.; Silva, N. J. O.; Millán, A.; Amaral, V. S.; Palacio, F. & Carlos, L. D. Thermometry at the nanoscale. *Nanoscale* **2012**, *4*, 4799–4829.
14. Li, S.; Zhang, K.; Yang, J.-M.; Lin, L. & Yang, H. Single Quantum Dots as Local Temperature Markers. *Nano Lett.* **2007**, *7*, 3102–3105.
15. Maestro, L. M.; Jacinto, C.; Silva, U. R.; Vetrone, F.; Capobianco, J. A.; Jaque, D. & Solé J. G. CdTe Quantum Dots as Nanothermometers: Towards Highly Sensitive Thermal Imaging. *Small* **2011**, *7*, 1774–1778.
16. Walker, G. W.; Sundar, V. C.; Rudzinski, C. M.; Wun, A. W.; Bawendi, M. G. & Nocera, D. G. Quantum-Dot Optical Temperature Probes. *Appl. Phys. Lett.* **2003**, *83*, 3555–3557.

17. Löw, P.; Kim, B.; Takama, N. & Bergaud, C. High-Spatial-Resolution Surface-Temperature Mapping Using Fluorescent Thermometry. *Small* **2008**, *4*, 908–914.
18. Yap, S. V.; Ranson, R. M.; Cranton, W. M.; Koutsogeorgis, D. C. & Hix, G. B. Temperature Dependent Characteristics of $\text{La}_2\text{O}_2\text{S}:\text{Ln}$ [Ln=Eu,Tb] with Various Ln Concentrations over 5–60 °C. *J. Lumin.* **2009**, *129*, 416–422.
19. Benninger, R. K. P.; Koç, Y.; Hofmann, O.; Requejo-Isidro, J.; Neil, M. A. A.; French, P. M. W. & deMello, A. J. Quantitative 3D Mapping of Fluidic Temperatures within Microchannel Networks Using Fluorescence Lifetime Imaging. *Anal. Chem.* **2006**, *78*, 2272–2278.
20. Haro-González, P.; Martínez-Maestro, L.; Martín, I. R.; García-Solé, J. & Jaque, D. High-Sensitivity Fluorescence Lifetime Thermal Sensing Based on CdTe Quantum Dots. *Small* **2012**, *8*, 2652–2658.
21. Yu, J.; Sun, L.; Peng, H. & Stich, M. I. J. Luminescent Terbium and Europium Probes for Lifetime Based Sensing of Temperature between 0 and 70 °C. *J. Mater. Chem.* **2010**, *20*, 6975.
22. Van Vleck, J. H. The Puzzle of Rare-Earth Spectra in Solids. *J. Phys. Chem.* **1937**, *41*, 67–80.
23. Walsh, B. M. *Judd-Ofelt Theory: Principles and Practices In Advances in Spectroscopy for Lasers and Sensing*, Springer Netherlands: Dordrecht, **2006**; pp 403–433.
24. Dieke, G. *Spectra and Energy Levels of Rare Earth Ions in Crystals*; Interscience, Ed.; New York, **1968**.
25. Carnall, W. T.; Crosswhite, H. & Crosswhite, H. M. *Energy Level Structure and Transition Probabilities of the Trivalent Lanthanides in LaF₃*, Argonne National Laboratory, Argonne, **1977**.
26. Peijzel, P. S.; Meijerink, A.; Wegh, R. T.; Reid, M. F. & Burdick, G. W. A Complete 4fⁿ energy Level Diagram for All Trivalent Lanthanide Ions. *J. Solid State Chem.* **2005**, *178*, 448–453.
27. Tanner, P. A. Some Misconceptions Concerning the Electronic Spectra of Tri-Positive Europium and Cerium. *Chem. Soc. Rev.* **2013**, *42*, 5090.
28. Heyes, A.; Seefeldt, S. & Feist, J. P. Two-Colour Phosphor Thermometry for Surface Temperature Measurement. *Opt. Laser Technol.* **2006**, *38*, 257–265.
29. Tripathi, G.; Rai, V. K. & Rai, S. B. Optical Properties of Sm³⁺:CaO-Li₂O-B₂O₃-BaO Glass and Codoped Sm³⁺:Eu³⁺. *Appl. Phys. B* **2006**, *84*, 459–464.
30. Rai, V. K.; Rai, D. K. & Rai, S. B. Pr³⁺ Doped Lithium Tellurite Glass as a Temperature Sensor. *Sensors Actuators A Phys.* **2006**, *128*, 14–17.
31. Xu, X.; Wang, Z.; Lei, P.; Yu, Y.; Yao, S.; Song, S.; Liu, X.; Su, Y.; Dong, L.; Feng, J. & Zhang, H. $\alpha\text{-NaYb(Mn)F}_4\text{:Er}^{3+}/\text{Im}^{3+}$ @NaYF₄ UCNPs as “Band-Shape” Luminescent Nanothermometers over a Wide Temperature Range. *ACS Appl. Mater. Interfaces* **2015**, *7*, 20813–20819.
32. Haro-González, P.; Martín, I. R.; Martín, L. L.; León-Luis, S. F.; Pérez-Rodríguez, C. & Lavín, V. Characterization of Er³⁺ and Nd³⁺ Doped Strontium Barium Niobate Glass Ceramic as Temperature Sensors. *Opt. Mater.* **2011**, *33*, 742–745.
33. Bizzak, D. J. & Chyu, M. K. Rare-earth Phosphor Laser-induced Fluorescence Thermal Imaging System. *Rev. Sci. Instrum.* **1994**, *65*, 102–107.
34. Quintanilla, M.; Cantelar, E.; Cussó, F.; Villegas, M. & Caballero, A. C. Temperature Sensing with Up-Converting Submicron-Sized LiNbO₃:Er³⁺/Yb³⁺ Particles. *Appl. Phys. Express* **2011**, *4*, 022601.
35. Cao, B. S.; He, Y. Y.; Feng, Z. Q.; Li, Y. S. & Dong, B. Optical Temperature Sensing Behavior of Enhanced Green Upconversion Emissions from Er-Mo:Yb₂Ti₂O₇ Nanophosphor. *Sensors Actuators B Chem.* **2011**, *159*, 8–11.

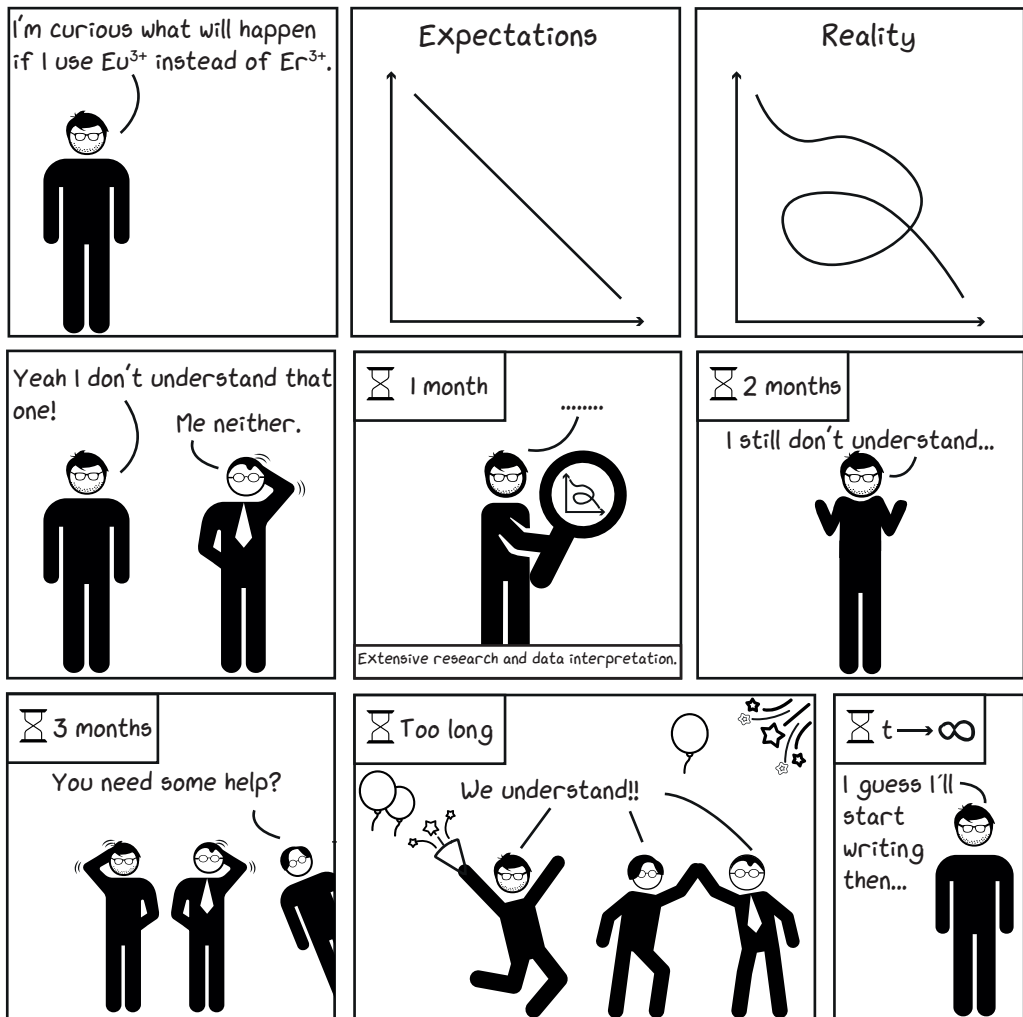
36. Singh, S. K.; Kumar, K. & Rai, S. B. Er³⁺/Yb³⁺ Codoped Gd₂O₃ Nano-Phosphor for Optical Thermometry. *Sensors Actuators A Phys.* **2009**, *149*, 16–20.
37. Alencar, M. A. R. C.; Maciel, G. S., de Araújo, C. B. & Patra, A. Er³⁺-Doped BaTiO₃ Nanocrystals for Thermometry: Influence of Nanoenvironment on the Sensitivity of a Fluorescence Based Temperature Sensor. *Appl. Phys. Lett.* **2004**, *84*, 4753–4755.
38. Li, T.; Guo, C.; Zhou, S.; Duan, C. & Yin, M. Highly Sensitive Optical Thermometry of Yb³⁺-Er³⁺ Codoped AgLa(MoO₄)₂ Green Upconversion Phosphor. *J. Am. Ceram. Soc.* **2015**, *98*, 2812–2816.
39. Svelto, O. *Principles of Lasers*, 5th ed.; Springer US: New York, **2010**.
40. Vetrone, F.; Naccache, R.; Zamarrón, A.; Juarranz de la Fuente, A.; Sanz-Rodríguez, F.; Martínez Maestro, L.; Martín Rodríguez, E.; Jaque, D.; García Solé, J. & Capobianco, J. A. Temperature Sensing Using Fluorescent Nanothermometers. *ACS Nano* **2010**, *4*, 3254–3258.
41. Liu, S.; Chen, G.; Ohulchanskyy, T. Y.; Swihart, M. T. & Prasad, P. N. Facile Synthesis and Potential Bioimaging Applications of Hybrid Upconverting and Plasmonic NaGdF₄:Yb³⁺,Er³⁺/Silica/Gold Nanoparticles. *Theranostics* **2013**, *3*, 275–281.
42. Dai, Y.; Kang, X.; Yang, D.; Li, X.; Zhang, X.; Li, C.; Hou, Z.; Cheng, Z.; Ma, P. & Lin, J. Platinum (IV) Pro-Drug Conjugated NaYF₄:Yb³⁺/Er³⁺ Nanoparticles for Targeted Drug Delivery and Up-Conversion Cell Imaging. *Adv. Healthc. Mater.* **2013**, *2*, 562–567.
43. Lee, J. & Kotov, N. A. Thermometer Design at the Nanoscale. *Nano Today* **2007**, *2*, 48–51.
44. dos Santos, P. V.; de Araujo, M. T.; Gouveia-Neto, A. S.; Medeiros Neto, J. A. & Sombra, A. S. B. Optical Temperature Sensing Using Upconversion Fluorescence Emission in Er³⁺/Yb³⁺-Codoped Chalcogenide Glass. *Appl. Phys. Lett.* **1998**, *73*, 578–580.
45. Wade, S. A.; Collins, S. F. & Baxter, G. W. Fluorescence Intensity Ratio Technique for Optical Fiber Point Temperature Sensing. *J. Appl. Phys.* **2003**, *94*, 4743–4756.
46. Baker, S. N.; McCleskey, T. M. & Baker, G. A. *An Ionic Liquid-Based Optical Thermometer*. **2005**, 171–181.
47. Goossens, E.; Donker, R. & van den Brink, F. Reactor Runaway in Pyrolysis Gasoline Hydrogenation. *Stud. Surf. Sci. Catal.* **1997**, *106*, 245–254.
48. Kao, C.-S. & Hu, K.-H. Acrylic Reactor Runaway and Explosion Accident Analysis. *J. Loss Prev. Process Ind.* **2002**, *15*, 213–222.
49. Arrhenius, S. *Zeitschrift für Phys. Chemie* **1889**, *4*, 226–248.
50. Logan, S. R. The Origin and Status of the Arrhenius Equation. *J. Chem. Educ.* **1982**, *59*, 279–281.
51. Wolf, D. & Resnick, W. Residence Time Distribution in Real Systems. *Ind. Eng. Chem. Fundam.* **1963**, *2*, 287–293.
52. Kim, S. D. & Kang, Y. Heat and Mass Transfer in Three-Phase Fluidized-Bed Reactors—an Overview. *Chem. Eng. Sci.* **1997**, *52*, 3639–3660.
53. Askri, F. Prediction of Transient Heat and Mass Transfer in a Closed Metal–hydrogen Reactor. *Int. J. Hydrogen Energy* **2004**, *29*, 195–208.
54. Bagavathiappan, S.; Lahiri, B. B.; Saravanan, T.; Philip, J. & Jayakumar, T. Infrared Thermography for Condition Monitoring—A Review. *Infrared Phys. Technol.* **2013**, *60*, 35–55.
55. Huang, B.; Bates, M. & Zhuang, X. Super-Resolution Fluorescence Microscopy. *Annu. Rev. Biochem.* **2009**, *78*, 993–1016.



Based on

- Geitenbeek, R. G.; de Wijn, H. W. & Meijerink, A. Investigation and Modeling on Non-Boltzmann Luminescence in $\text{NaYF}_4:\text{Eu}^{3+}$: Implications for Luminescence Thermometry. *Phys. Rev. Appl.* **2018**, *In Press*

Chapter 2 – Investigation and Modeling on Non-Boltzmann Luminescence in $\text{NaYF}_4:\text{Eu}^{3+}$: Implications for Luminescence Thermometry



Robin Geitenbeek



Harold de Wijn



Andries Meijerink

Abstract

Luminescence (nano)thermometry is an important technique for remote temperature sensing. The recent development of lanthanide-doped nanoparticles with temperature-dependent emission has expanded the field of applications, especially for ratiometric methods relying on the temperature variation of relative emission intensities from thermally coupled energy levels. Analysis and calibration of the temperature dependence is based on a Boltzmann equilibrium for the coupled levels. To investigate the validity of this assumption, here we analyze and model thermal equilibration for Eu^{3+} ${}^5\text{D}_1/{}^5\text{D}_0$ emission in NaYF_4 . The results show that for low Eu^{3+} concentrations temperature-dependent multi-phonon relaxation can accurately explain both the intensity ratio and emission decay dynamics. The analysis also reveals that a Boltzmann equilibrium is not realized in the temperature regime investigated (300–900 K). By increasing the Eu^{3+} concentration, cross-relaxation between neighboring Eu^{3+} ions enhances ${}^5\text{D}_1\text{--}{}^5\text{D}_0$ relaxation rates and extends the temperature range in which emission intensity ratios can be used for temperature sensing (500–900+ K). The results obtained are important to recognize, understand and control deviations from Boltzmann behavior in luminescence (nano)thermometry. By varying the dopant concentration, the range for accurate temperature sensing can be adjusted. These insights are crucial in the development and understanding of reliable temperature sensors.

Introduction

Luminescence thermometry^{1,2} is a powerful tool for remote temperature sensing. Potential applications range from bio-imaging³⁻⁵ at lower temperatures (<350 K) to nano-electronics^{6,7} and chemical reactors⁸⁻¹¹ at elevated temperatures (up to 1500 K). In recent years nanothermometry using luminescent nanoparticles has become an active field of research as this technique offers excellent spatial and temporal resolution for remote temperature sensing with high accuracy. Especially methods based on monitoring the intensity ratio between two or more emission peaks to determine the temperature are widely used.¹² The ratio is not affected by fluctuations of the overall intensity, e.g. by changes in alignment, light absorption and scattering or the concentration of luminescent species. The fluorescence intensity ratio (FIR) changes with temperature as it is determined by thermal population of two thermally coupled excited states separated by an energy difference ΔE . If ΔE is of the order of several kT , emission can be observed from both levels. The intensity of the emission is proportional to the population and as the temperature is raised the relative intensity of emission from the higher energy level will increase.

In the analysis of the intensity ratio it is commonly assumed that the population of the two states follows a Boltzmann distribution.¹³ The temperature regime in which the ratiometric thermometry has the highest accuracy is related to ΔE . The higher the temperature regime of interest, the larger ΔE should be. Depending on the application, temperature range and sensitivity that are required, luminescent probes with different values for ΔE must be selected. A necessary condition for reaching Boltzmann equilibrium, however, is that equilibration of two thermally coupled states is fast in comparison with other processes affecting their population, notably optical feeding and decay channels to the ground state. For larger ΔE , relaxation between thermally coupled levels becomes slower, so that deviations from Boltzmann equilibrium tend to occur. In the common analysis of the temperature dependence of the intensity ratio it is not always recognized that the population does not follow Boltzmann equilibrium and deviations from calibration curves are sometimes misinterpreted.¹⁴⁻¹⁶

In this chapter, we analyze deviations from Boltzmann equilibrium for lanthanide-based temperature sensors which are among the most widely used ratiometric temperature probes. Our prototypical example will be $\text{NaYF}_4:\text{Eu}^{3+}$. Deviations from Boltzmann equilibrium affect the temperature range that can be probed. We furthermore show how the temperature range can be extended by inducing additional relaxation paths, namely by cross-relaxation interaction between lanthanide (Ln) ions at higher Ln-doping concentrations. Insight in the validity of the Boltzmann equilibrium is crucial in the application of ratiometric luminescence (nano)thermometry.

In a broader sense, lanthanide (Ln) dopants in inorganic host materials are ideal for ratiometric (or bandshape) thermometry. The partly filled inner 4f shell of lanthanide ions gives rise to a large number of closely spaced energy levels.¹⁷ Efficient sharp line emissions can be observed in various spectral regions (IR, visible and UV) for different Ln³⁺ ions.

Many of the energy levels from which emission is observed have additional levels at higher energies which are exploited for luminescence thermometry. The sharp line emission from different closely spaced levels can be easily observed and separated which allows for a highly accurate determination of intensity ratios. Advantages of Ln-doped inorganic host materials over other optical probes (e.g. quantum dots¹⁸ or organic complexes¹⁹) are the high quenching temperature of emission,^{20,21} thermal stability of the material and the insensitivity of the optical properties to variations in the environment (such as pH, embedding medium/solvent, pressure etc.). For bio-imaging and other applications in the temperature range 300–600 K, Er³⁺ is a popular probe.^{22–24} The ⁴S_{3/2} and ²H_{11/2} levels of Er³⁺ are separated by ca. 700 cm⁻¹ and efficient green emission is observed from these levels. At temperatures above 600 K deviations from the Boltzmann equilibrium for the ⁴S_{3/2} and ²H_{11/2} level were observed,¹³ probably as a result of thermal population of even higher levels²⁵ (e.g. ⁴F_{7/2} for Er³⁺). Dy³⁺ and Eu³⁺ with larger energy gaps (1100 cm⁻¹ for the ⁴F_{9/2}–⁴I_{15/2} gap for Dy³⁺ and 1800 cm⁻¹ for the ⁵D₀–⁵D₁ gap for Eu³⁺) are promising candidates for ratiometric thermometry at higher temperatures.^{26,27} Presently there is however a lack of understanding on how deviations from Boltzmann equilibrium and cross-relaxation processes affect the thermal response of Ln-based ratiometric temperature sensors.

Here, we consider in detail the temperature-dependent Eu³⁺ emission in microcrystalline NaYF₄ and investigate the temperature range in which a Boltzmann equilibrium is established. Emission from the thermally coupled ⁵D₀ and ⁵D₁ states is measured and analyzed for a low-dopant concentration (0.4 % Eu³⁺) by using models for the temperature dependence of multi-phonon relaxation (MPR) processes. Both steady state and time-resolved measurements are reported and explained quantitatively using the same set of parameters. At higher dopant concentrations (>1 % Eu³⁺) cross-relaxation processes start to contribute to ⁵D₁–⁵D₀ equilibration and the temperature-dependent luminescence can be explained by including an extra term to account for cross-relaxation. The present study provides fundamental insight in thermal equilibration processes in the promising class of Ln-doped temperature sensors. The present work is focused on NaYF₄:Eu³⁺ but the model and conclusions are valid for other Ln-based (nano)thermometers. A better insight in the non-Boltzmann behavior and the use of dopant concentration to extend the effective temperature range are important in the application of luminescence thermometry for remote temperature sensing.

Results and Discussion

Structural Characterization. For the temperature-dependent luminescence studies, microcrystalline NaYF₄ doped with Eu³⁺ has been synthesized. Three different samples were prepared in which different amounts of Eu³⁺ were incorporated. The synthesis products were analyzed using scanning electron microscopy (SEM), powder X-ray diffraction (XRD) and inductively coupled plasma optical emission spectroscopy (ICP-OES). The as-synthesized particles were micrometer sized and mainly hexagonal NaYF₄ as shown in Figure 2.1a. The samples contained NaF impurities, as shown with XRD in Figure 2.1b. However, these impurities were successfully removed by washing the sample

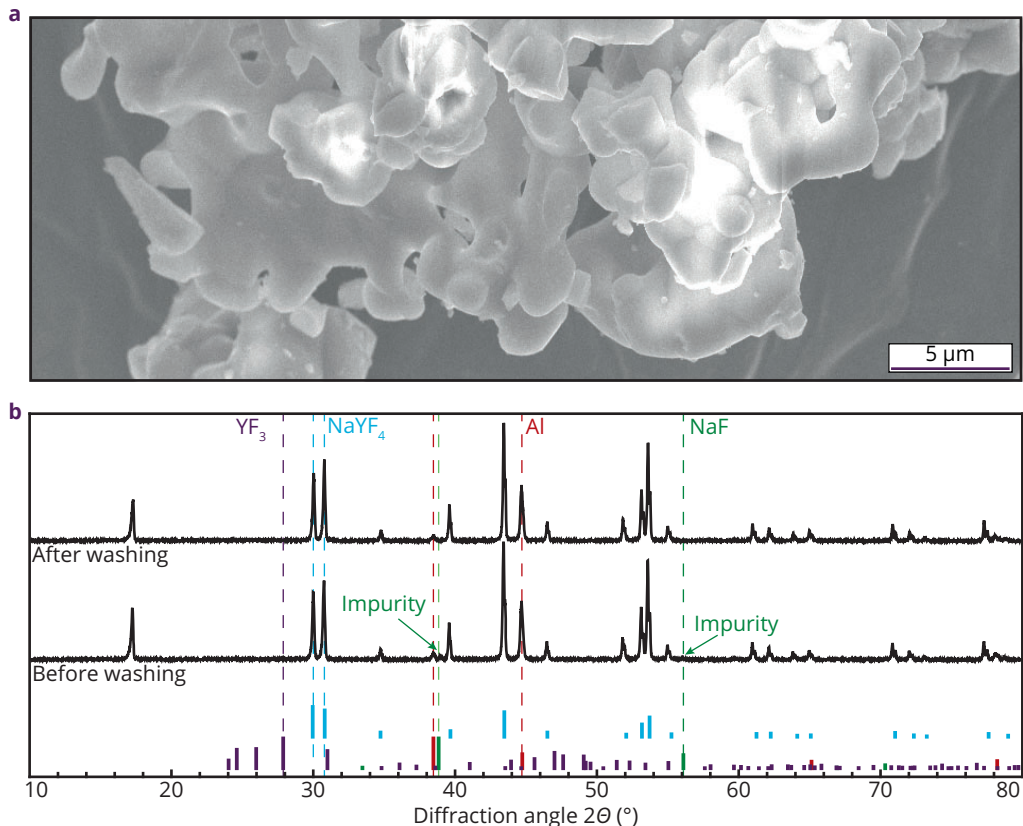


Figure 2.1 – Structural characterization. SEM micrograph of the prepared $\text{NaYF}_4:\text{Eu}^{3+}$ (a) and Cu K α X-ray diffractograms of $\text{NaYF}_4:\text{Eu}^{3+}$ before washing with H_2O to remove excess NaF and after washing with H_2O (b). The reference diffractograms include NaYF_4 (JCPDS00-064-0156, cyan), YF_3 (JCPDS04-007-0883, purple), NaF (JCPDS00-036-1455, green) and aluminum from the sample holder (JCPDS00-004-0787, red). The dashed lines represent angles where the major diffraction peaks of the references are expected.

with H_2O . The Eu^{3+} dopant concentrations, determined with ICP-OES, are 0.4 %, 5.5 % and 8.4 % for the three different samples. The low dopant sample (0.4 % Eu^{3+}) is used for the main part of the work while the two higher concentration samples are used to investigate the role of cross-relaxation.

Eu^{3+} emission in NaYF_4 . To assess to what extent Boltzmann equilibration is established, the temperature dependence of the ${}^5\text{D}_1/{}^5\text{D}_0$ (Figure 2.2a) Eu^{3+} luminescence in NaYF_4 for a low-dopant concentration (0.4 % Eu^{3+}) was studied to characterize the temperature-dependent emission for Eu^{3+} ions that are isolated from one another. Emission spectra were recorded at different temperatures between 300–900 K (from black to orange) with intervals of 25 K as shown in Figure 2.2b. Following excitation in the ${}^5\text{L}_6$ state at 395 nm, the system relaxes to the ${}^5\text{D}_1$ and ${}^5\text{D}_0$ states whose characteristic luminescence can be observed around 530 nm (${}^5\text{D}_1\text{--}{}^7\text{F}_1$) and 615 nm (${}^5\text{D}_0\text{--}{}^7\text{F}_2$).

In the case the ${}^5\text{D}_1$ and ${}^5\text{D}_0$ states are strongly coupled through fast equilibration, their

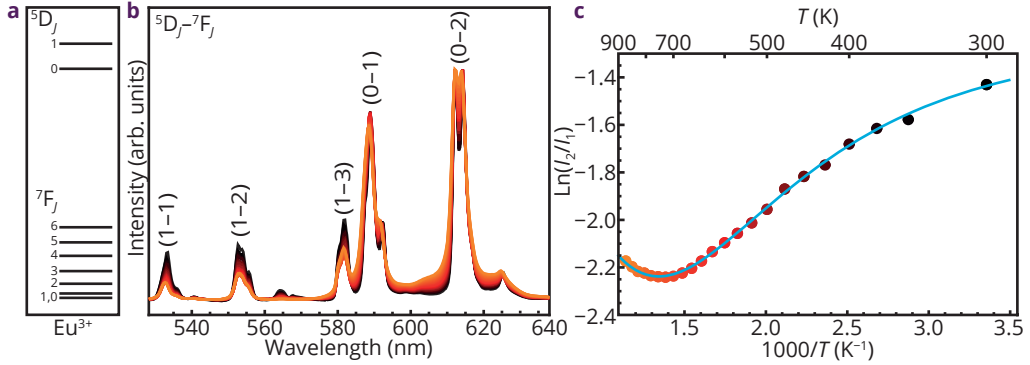


Figure 2.2 – Luminescence characterization. Emission spectra of $\text{NaYF}_4:\text{Eu}^{3+}$ (0.4 %) upon excitation at 395 nm taken at different temperatures ranging from 300 K (black) to 900 K (orange) with ${}^5\text{D}_j \rightarrow {}^7\text{F}_j$ transitions (a) labelled by the j numbers between brackets (b). The ratio between the integrated emission peaks originating from the ${}^5\text{D}_0$ and ${}^5\text{D}_1$ peaks were plotted vs. $1000/T$ (c). The cyan line is a fit as discussed later in this chapter.

populations N_2 and N_1 follow Boltzmann statistics,

$$\frac{N_2}{N_1} = \frac{g_2}{g_1} e^{-\Delta E/kT}, \quad (2.1)$$

in which g_1 and g_2 are the level multiplicities. Towards higher temperatures the ratio N_2/N_1 then would increase and so would the luminescence intensity of the ${}^5\text{D}_1 \rightarrow {}^7\text{F}_j$ ($J = 0-6$) transitions relative to the ${}^5\text{D}_0 \rightarrow {}^7\text{F}_j$ transitions. Instead, we initially observe the opposite, a decrease of the relative ${}^5\text{D}_1$ emission intensity, indicating that the conditions for Boltzmann equilibrium are not met.

To make this more quantitative, luminescence intensities were calculated by integrating the total luminescence intensity between 548–586 nm (I_2 , mainly ${}^5\text{D}_1$ emission) and 586–640 nm (I_1 , mainly ${}^5\text{D}_0$ emission). The ratio of I_2/I_1 was plotted logarithmically versus the reciprocal temperature $1/T$ in Figure 2.2c. Emission intensity scales linearly with the population of an emitting state. This results in an expected (Boltzmann) temperature dependence of the luminescence intensity ratio as shown in equation 2.2,

$$\frac{I_2}{I_1} = \frac{A_2 h \nu_2 N_2}{A_1 h \nu_1 N_1} = C e^{-\Delta E/kT}. \quad (2.2)$$

Here, A_i is the spontaneous emission rate and ν_i the frequency of the transition from state i to the ground state. The temperature-independent constant C accounts for differences in emission rates of luminescence transitions, the restrictions in the integration boundaries in the spectrum (cf. Figure 2.2c) and any residual optical dispersion. The constant C is around 0.5, as determined from fits to theory presented below. By plotting the logarithm of the luminescence intensity ratio vs. reciprocal temperature, a linear downward trend should be observed. Clearly, for $\text{NaYF}_4:\text{Eu}^{3+}$ 0.4 % this is not observed. Only above ca. 700 K ($1000/T < 1.4$) the expected trend is apparent showing that the luminescence intensity ratio of ${}^5\text{D}_1/{}^5\text{D}_0$ emission fails to satisfy Boltzmann statistics below 700 K.

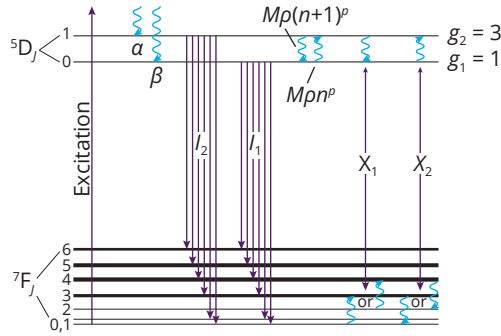


Figure 2.3 – Excited state dynamics upon excitation in ${}^5\text{L}_6$ energy level at 395 nm. The processes that determine excited state populations are excitation, direct relaxation to ${}^5\text{D}_1$ and ${}^5\text{D}_0$ levels with a degeneracy of g_2 and g_1 , (α and β , respectively), ${}^5\text{D}_1\text{-}{}^7\text{F}_j$ and ${}^5\text{D}_0\text{-}{}^7\text{F}_j$ emission (l_2 and l_1 , respectively), multi-phonon relaxation from the ${}^5\text{D}_1$ to the ${}^5\text{D}_0$ level ($Mp g_2 n^p$) and from the ${}^5\text{D}_0$ to the ${}^5\text{D}_1$ level ($Mp g_1 (1+n)^p$) and finally cross-relaxation from the ${}^5\text{D}_1$ to the ${}^5\text{D}_0$ level (X_1) and from the ${}^5\text{D}_0$ to the ${}^5\text{D}_1$ level (X_2).

Model. To understand and model the observed temperature-dependent luminescence, the populations N_1 of the ${}^5\text{D}_0$ and N_2 of the ${}^5\text{D}_1$ state are evaluated as they evolve in time at a given temperature. The populations are governed by feeding upon optical pumping into an even higher state, subsequent relaxation (α and β) to the ${}^5\text{D}_1$ and ${}^5\text{D}_0$ state, the radiative decay rates from these states to the ${}^7\text{F}$ multiplet (τ_2 and τ_1), phonon-induced relaxation processes connecting the ${}^5\text{D}_1$ and ${}^5\text{D}_0$ excited states and, at higher concentrations of Eu^{3+} , cross-relaxation (X_1 and X_2). The various processes are depicted in Figure 2.3. Bridging the energy gap ΔE between $4f^6$ states of an isolated Eu^{3+} ion generally has to occur via phonon emission and phonon absorption, known as multiphonon relaxation (MPR). The number of phonons that is needed to bridge the gap is p and is determined by dividing the energy gap ΔE by the maximum energy of vibrations (phonons) in the lattice.²⁸ MPR can be viewed as resonant energy transfer to a resonant overtone vibration in the host lattice or a combination of different phonons to bridge the gap between the ${}^5\text{D}_1$ and ${}^5\text{D}_0$ state. Multiphonon relaxation has been studied in the past in pioneering work by Riseberg and Moos²⁹ and Layne, Lowdermilk and Weber.³⁰ The energy gap ΔE between the ${}^5\text{D}_1$ and ${}^5\text{D}_0$ state is ca. 1800 cm^{-1} as calculated from the ${}^5\text{D}_1\text{-}{}^7\text{F}_1$ and ${}^5\text{D}_0\text{-}{}^7\text{F}_1$ emission peak positions from Figure 2.2. Since the maximum phonon energy in fluorides is ca. 500 cm^{-1} , it is expected that around four phonons are involved in MPR between the ${}^5\text{D}_1$ and ${}^5\text{D}_0$ excited state. Cross-relaxation involves partial energy transfer between neighboring ions. For Eu^{3+} , this can occur due to the similar energy difference between the ${}^5\text{D}_1$ and ${}^5\text{D}_0$ excited states and the ${}^7\text{F}_0$ and ${}^7\text{F}_3$ ground states. A Eu^{3+} ion can relax from the ${}^5\text{D}_1$ to the ${}^5\text{D}_0$ excited state by transferring the excess energy to a second Eu^{3+} which is excited from the ${}^7\text{F}_0$ to the ${}^7\text{F}_3$ level or vice versa. At elevated temperatures, as higher energy ${}^7\text{F}$ levels are thermally populated, additional cross-relaxation processes may contribute as well.

To evaluate the excited state populations, differential equations for the populations of the ${}^5\text{D}_0$ and ${}^5\text{D}_1$ states (N_1 and N_2) are considered:

$$\frac{dN_1}{dt} = \beta N^* - \frac{N_1}{\tau_1} + M\rho[(1+n)^p g_1 N_2 - n^p g_2 N_1] + X_1 N_2 - X_2 N_1, \quad (2.3)$$

$$\frac{dN_2}{dt} = \alpha N^* - \frac{N_2}{\tau_2} - M\rho[(1+n)^p g_1 N_2 - n^p g_2 N_1] - X_1 N_2 + X_2 N_1. \quad (2.4)$$

Here, the first term describes the ratio of feeding N^* into the ${}^5\text{L}_6$ level and the subsequent relaxation to the ${}^5\text{D}_1$ and ${}^5\text{D}_0$ states (α and β , respectively). Here, we assume that all excited ions relax to the ${}^5\text{D}_1$ or ${}^5\text{D}_0$ level, so that $\alpha + \beta = 1$. The second term accounts for the radiative relaxation, which depends on the population of the state and the radiative lifetime (τ_i). The third and fourth terms in equations 2.3 and 2.4 are of prime importance to the present analysis as they account for the multi-phonon-induced relaxation connecting the two emitting states. The final two terms become important at higher dopant concentrations and represent cross-relaxation processes, which depend on the population of the states involved and the effective rate of cross-relaxation (X_i) between neighboring Eu^{3+} ions. The multi-phonon relaxation rate from the ${}^5\text{D}_1$ to the ${}^5\text{D}_0$ level and vice versa (third and fourth term)³¹ scale with $M\rho$, the product of the net interaction matrix element of the two level system with the density of phonon states resonant with the two level system and g_i the degeneracy of state i . The MPR rates depend exponentially on p , the number of phonons needed to bridge the energy gap ΔE . Important for the present analysis is the temperature dependence of the multi-phonon relaxation processes. Phonon emission scales with $(n+1)^p$ and phonon absorption with n^p ,³² where n is the Bose-Einstein phonon occupation number, which is defined as³³

$$n = \frac{1}{\exp(\Delta E/pkT) - 1}. \quad (2.5)$$

The model presented can be applied to quantitatively model the observed temperature dependence of the emission intensity ratio under continuous excitation (as shown in Figure 2.2c). Note that in equations 2.3 and 2.4 degeneracy g_1 of ${}^5\text{D}_0$ comes in combined with N_2 , because the system, when residing in a particular sublevel of ${}^5\text{D}_1$ may, in accordance with MPR, relax to each of the g_1 sublevels of ${}^5\text{D}_0$, and similarly g_2 of ${}^5\text{D}_1$ goes combined with N_1 . Inclusion of g_1 and g_2 in equations 2.3 and 2.4 combined with equation 2.5 ensures conformity with Boltzmann statistics, in case of dominant thermal relaxation. In addition, the time dependence of the luminescence intensity for emission from both the ${}^5\text{D}_0$ and ${}^5\text{D}_1$ state can be modelled as a function of temperature and provide information on the temperature dependence of the relaxation rates between the ${}^5\text{D}_0$ and ${}^5\text{D}_1$ level. Below we analyze both the temperature-dependent excited state dynamics and intensity ratio based on equations 2.3 and 2.4. First, results for the low Eu^{3+} concentration (0.4 %) are considered to contain information on the parameters for isolated Eu^{3+} ions and next the role of additional relaxation processes by cross-relaxation processes at higher Eu^{3+} concentrations are discussed.

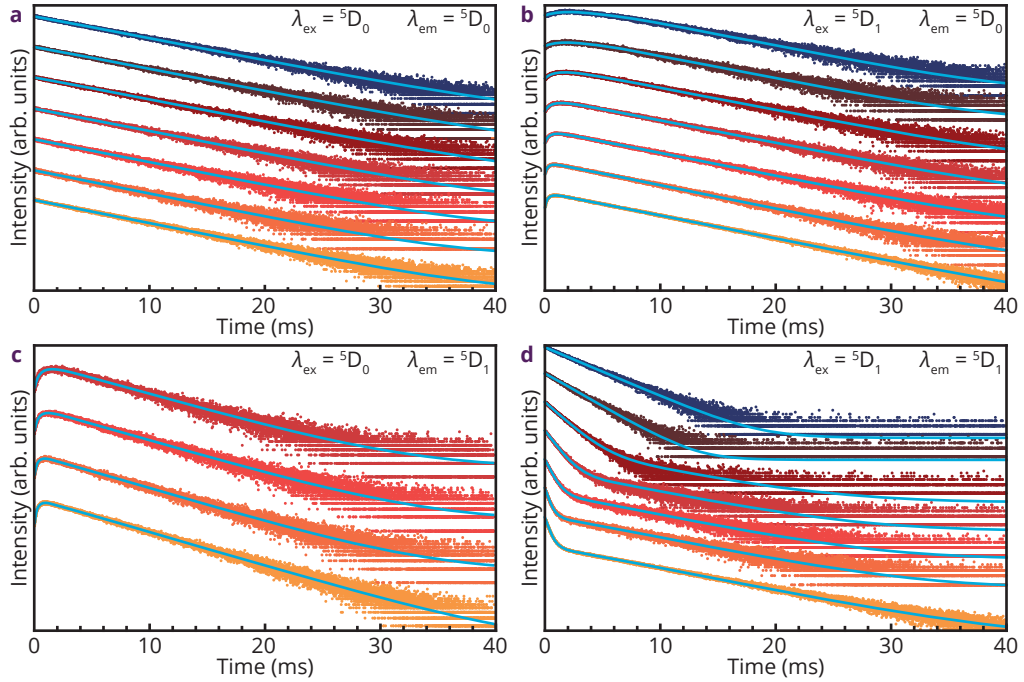


Figure 2.4 – Time-resolved spectroscopy measurements. Luminescence decay measurements in $\text{NaYF}_4:\text{Eu}^{3+}$ (0.4 %) at temperatures ranging from 300 K (dark blue) to 900 K (orange) while exciting in the $^5\text{D}_0$ and $^5\text{D}_1$ state and monitoring the $^5\text{D}_0$ level (a and b, respectively) and while exciting in the $^5\text{D}_0$ and $^5\text{D}_1$ level and monitoring the $^5\text{D}_1$ level (c and d, respectively). Biexponential fits are shown in cyan.

Excited state dynamics. Since the population in an excited state is proportional to the luminescence intensity from that state (equation 2.2), it is possible to validate equations 2.3 and 2.4 using luminescence decay measurements. In Figure 2.4 the luminescence decay is presented for the $^5\text{D}_0$ state upon excitation in $^5\text{D}_0$ (panel a) and $^5\text{D}_1$ (panel b) as well as for $^5\text{D}_1$ emission upon excitation in the $^5\text{D}_0$ (panel c) and $^5\text{D}_1$ (panel d). The panels show decay curves for a series of temperatures starting at 300 K, followed by 373 K to 873 K in 100 K steps (colors varying from dark blue to orange). An exception is panel c, because below 573 K the emission from $^5\text{D}_1$ is too weak for a measurable signal. The data was fitted with a bi-exponential fit for Figures 2.4a–d.

Upon excitation in the $^5\text{D}_0$ state, the $^5\text{D}_0$ emission intensity decays bi-exponentially for all temperatures with an initial fast decay time and a subsequent slow decay with a lifetime of ca. 6 ms (Figure 2.4a), comparable to radiative lifetimes for Eu^{3+} $^5\text{D}_0$ emission in NaYF_4 found in other works.^{27,34} Similar lifetimes were found upon excitation in the $^5\text{D}_1$ state in addition to an initial rise time, which become faster with increasing temperature. In the case of a significant contribution from cross-relaxation between a Eu^{3+} ion in the $^5\text{D}_0$ excited state and a neighboring ion in the $^7\text{F}_3$ ground state, multi-exponential decay is expected based on the random distribution of the ions in the lattice. However, this multi-exponential decay is not observed and therefore cross-relaxation (X_2) is negligible, as expected for

systems with such a low dopant concentration.³⁵

The ${}^5\text{D}_1$ emission for ${}^5\text{D}_0$ excitation, shown in Figure 2.4c, shows an initial rise and a subsequent decay in intensity. The long decay lifetime is comparable to the radiative lifetimes of the ${}^5\text{D}_0$ state. Again, the initial rise becomes faster with increasing temperature. Upon direct excitation in the ${}^5\text{D}_1$ level, as shown in Figure 2.4d, a fast, temperature-dependent decay is observed and a longer decay component is observed for temperatures higher than 473 K. The long component has a lifetime of ca. 6 ms and the fast component shows the same temperature dependency as the rise time in Figure 2.4b. Consequently, the short component is attributed to fast initial ${}^5\text{D}_1$ - ${}^5\text{D}_0$ decay. In the case of cross-relaxation between an ion in the ${}^5\text{D}_1$ excited state and an ion in the ${}^7\text{F}$ ground multiplet, this fast component is expected to be multi-exponential as a result of a variation in cross-relaxation rates for different local environments (variation in distances to neighboring Eu^{3+} ions). Since the fast component is of mono-exponential nature, cross-relaxation from the ${}^5\text{D}_1$ excited state (X_1) is not observed, as expected for systems with a low 0.4 % dopant concentration randomly distributed in the host lattice.

For a precise analysis of the decays in Figure 2.4, we apply the model developed in the previous section. The differential equations 2.3 and 2.4 can be solved analytically to obtain N_1 and N_2 vs. time. The resulting expression can be simplified because radiative lifetimes from the ${}^5\text{D}_0$ and the ${}^5\text{D}_1$ state are both ca. 6 ms and because of this coincidental similarity we can replace τ_1 and τ_2 in equations 2.3 and 2.4 with τ_R . Upon ignoring cross-relaxation ($X_1 = X_2 = 0$) the solution becomes

$$N_1 = C_1 \exp(-r_1 t) + \frac{g_1(1+n)^p}{g_2 n^p} C_2 \exp(-r_2 t), \quad (2.6)$$

$$N_2 = C_1 \exp(-r_1 t) + C_2 \exp(-r_2 t), \quad (2.7)$$

in which C_1 and C_2 are integration constants and the decay rates r_1 and r_2 are defined as

$$r_1 = \frac{1}{\tau_R} + \frac{1}{\tau_{NR}}, \quad (2.8)$$

$$r_2 = \frac{1}{\tau_R}, \quad (2.9)$$

with $1/\tau_{NR}$ defined as

$$\frac{1}{\tau_{NR}} = M\rho[g_1(1+n)^p + g_2 n^p]. \quad (2.10)$$

Fitting equations 2.6 and 2.7 to each set of decay curves in Figure 2.4 yields the decay rates r_1 and r_2 , which can be rewritten as τ_R and τ_{NR} using equations 2.8 and 2.9. The resulting values of τ_R and τ_{NR} are plotted vs. temperature in Figure 2.5 for the four different sets of temperature-dependent decay curves [${}^5\text{D}_0$ emission upon excitation in the ${}^5\text{D}_0$ and ${}^5\text{D}_1$ (black and purple) and ${}^5\text{D}_1$ emission upon excitation in the ${}^5\text{D}_1$ and ${}^5\text{D}_0$ (red and green)]

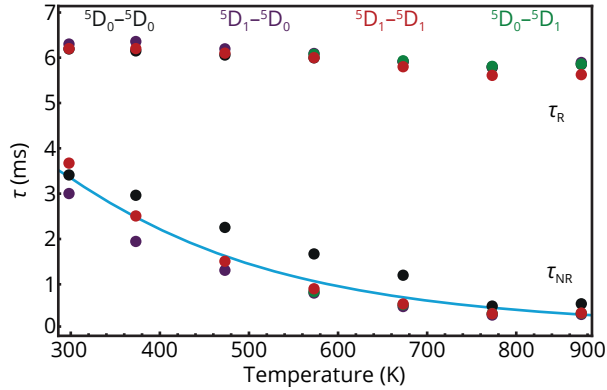


Figure 2.5 – Temperature-dependence of τ_R and τ_{NR} . Values of τ_R and τ_{NR} as function of temperature as obtained from the fits in Figure 2.4 and calculated using equations 2.8 and 2.9. The cyan fit through the τ_{NR} values is according to equation 2.10 and yielded $M\rho = 0.22 \pm 0.03 \text{ ms}^{-1}$ and $p = 3.7 \pm 0.2$.

and collected in Table 2.1–2.4.

The agreement between the temperature-dependent values for τ_R and τ_{NR} from the four different sets of decay curves is good. The radiative decay times are in first approximation temperature independent, but do show a small decrease with temperature (ca. 7 % decrease from 300–900 K), which is explained by a small increase of the radiative transition probability for vibrationally induced forced electric dipole transitions (increases with $2n+1$).^{36,37} The non-radiative decay time shows a much stronger decrease with temperature and closely follows the theoretically expected temperature dependence (equation 2.10, cyan curve). The parameters for the fit, $M\rho$ and p are $0.22 \pm 0.03 \text{ ms}^{-1}$ and 3.7 ± 0.2 , respectively. Since the maximum phonon energy in fluoride lattices is ca. 500 cm^{-1} and the energy gap

Table 2.1 – Fitted lifetimes Figure 2.4a. Fitted lifetimes (τ_1 and τ_2) of the decay measurements of the 5D_0 state upon excitation in the 5D_0 state the corresponding radiative (τ_R) and non-radiative lifetimes (τ_{NR}).

	300 K	373 K	473K	573K	673K	737K	873 K
$1/r_1$ (ms)	6.2	6.2	6.1	6.0	5.9	5.8	5.9
$1/r_2$ (ms)	2.2	2.0	1.6	1.3	1.0	0.5	0.5
τ_R (ms)	6.2	6.2	6.1	6.0	5.9	5.8	5.9
τ_{NR} (ms)	3.4	3.0	2.3	1.7	1.2	0.5	0.6

Table 2.2 – Fitted lifetimes Figure 2.4b. Fitted lifetimes (τ_1 and τ_2) of the decay measurements of the 5D_0 state upon excitation in the 5D_1 state the corresponding radiative (τ_R) and non-radiative lifetimes (τ_{NR}).

	300 K	373 K	473K	573K	673K	737K	873 K
$1/r_1$ (ms)	6.3	6.4	6.2	6.1	5.9	5.8	5.9
$1/r_2$ (ms)	2.0	1.5	1.1	0.7	0.5	0.3	0.3
τ_R (ms)	6.3	6.4	6.2	6.1	5.9	5.8	5.9
τ_{NR} (ms)	3.0	2.0	1.3	0.8	0.5	0.3	0.3

Table 2.3 – Fitted lifetimes Figure 2.4c. Fitted lifetimes (τ_1 and τ_2) of the decay measurements of the 5D_1 state upon excitation in the 5D_0 state the corresponding radiative (τ_R) and non-radiative lifetimes (τ_{NR}).

	300 K	373 K	473K	573K	673K	737K	873 K
$1/r_1$ (ms)	-	-	-	6.1	5.9	5.8	5.9
$1/r_2$ (ms)	-	-	-	0.7	0.5	0.3	0.3
τ_R (ms)	-	-	-	6.1	5.9	5.8	5.9
τ_{NR} (ms)	-	-	-	0.8	0.5	0.4	0.4

Table 2.4 – Fitted lifetimes Figure 2.4d. Fitted lifetimes (τ_1 and τ_2) of the decay measurements of the 5D_1 state upon excitation in the 5D_1 state the corresponding radiative (τ_R) and non-radiative lifetimes (τ_{NR}).

	300 K	373 K	473K	573K	673K	737K	873 K
$1/r_1$ (ms)	6.2	6.2	6.1	6.0	5.8	5.6	5.8
$1/r_2$ (ms)	2.3	1.8	1.2	0.8	0.5	0.3	0.3
τ_R (ms)	6.2	6.2	6.1	6.0	5.8	5.6	5.8
τ_{NR} (ms)	3.7	2.5	1.5	0.9	0.6	0.4	0.4

between the 5D_1 and 5D_0 excited states is ca. 1800 cm^{-1} , the number of phonons needed to bridge the energy gap, p , is in good agreement with the expected results. The good fit indicates that the theory for multi-phonon relaxation adequately describes the temperature dependence of the decay dynamics for Eu^{3+} emission in NaYF_4 . The fit parameters and equations 2.3 and 2.4 can now be used to obtain an expression for I_2/I_1 and to fit the results for the measured temperature dependence of the steady-state intensity ratio shown in Figure 2.2b.

Steady state measurements. Temperature-dependent luminescence as shown in Figure 2.2 has also been measured under continuous wave (CW) excitation in the 5L_6 level. Under CW excitation the system reaches a steady state and the population in the excited states N_1 and N_2 is constant in time ($dN_1/dt = 0$ and $dN_2/dt = 0$). Under these conditions, equations 2.3 and 2.4 can be solved, in the absence of cross-relaxation, resulting in

$$\frac{I_2}{I_1} = C \frac{\frac{\alpha}{\tau_R} + M\rho g_2 n^p}{\frac{\beta}{\tau_R} + M\rho g_1(1+n)^p}. \quad (2.11)$$

Equation 2.11 was fitted to the data in Figure 2.2c (cyan line). The fit is in good agreement with the obtained values for I_2/I_1 over the full range of temperatures with fitting parameters $C = 0.45 \pm 0.02$, $a = 0.77 \pm 0.08$, $\beta = 0.23 \pm 0.08$, $M\rho = 0.17 \pm 0.03\text{ ms}^{-1}$, and $p = 3.63 \pm 0.15$. The fitting parameter C correlates N_2/N_1 and I_2/I_1 , as I_2 and I_1 are intensities integrated over only a part of the total luminescence from the 5D_0 and 5D_1 in the emission spectra (Figure 2.2). The time τ_R , needed in these fits, was determined by averaging the long lifetime components of Figure 2.5 with the result of $6.0 \pm 0.1\text{ ms}$. The fractions a and β , which govern the feeding fraction of the 5D_1 and 5D_0 level, respectively, are consistent with expectations: relaxation from the 5L_6 excited state to the 5D_1 and 5D_0 states goes via multiple steps, resulting in a more efficient relaxation to the higher energy 5D_1 state compared to the 5D_0 state.

The value of $M\rho$, 0.17 ms^{-1} , closely matches the value of $M\rho$ determined from the excited-state dynamics, 0.22 ms^{-1} . The p values (number of phonons involved in the 5D_1 to 5D_0 MPR) obtained from the time-resolved and steady-state measurements, 3.7 and 3.63, are in good agreement and are consistent with the maximum phonon energy in fluorides (ca. 500 cm^{-1}) and the energy difference between the 5D_1 and 5D_0 states (ca. 1800 cm^{-1}).

In summary, the temperature dependence of both time-resolved and stationary state measurements have been consistently accounted for by the model presented in this chapter based on pure multi-phonon relaxation between 5D_1 and 5D_0 states. In addition, we have established that phonon bottlenecking of zone-boundary phonons³⁸ is absent by measuring luminescence decay at different excitation powers. In the case of phonon bottlenecking, a limited amount of available phonons influences the relaxation process resulting in slower equilibration between the 5D_1 and 5D_0 states. However, time-resolved luminescence measurements showed no difference while varying the excitation power, indicating that phonon bottlenecking is not present (data not shown here). The model was

also extended by incorporation of Raman relaxation processes but this did not improve the fits. The fact that the temperature-dependent properties for time-resolved and steady-state measurements can be explained using the same parameters indicates that the multi-phonon relaxation model accurately describes the relaxation processes between the ${}^5\text{D}_1$ and ${}^5\text{D}_0$ level.

Interestingly, the results show that even at the highest temperatures probed, a true Boltzmann equilibrium is not yet realized for the low-doped 0.4 % sample. This is evident from Figure 2.2 where only between 700 and 900 K the intensity ratio starts to increase towards a Boltzmann equilibrium. Between 300 K and 700 K the intensity ratio decreases while an increase of the ratio would be expected based on Boltzmann statistics predicting a higher ${}^5\text{D}_1$ population at higher temperatures. Conclusive evidence is obtained from the time-resolved data. These show that even at 900 K, bi-exponential decay curves are observed. For a true Boltzmann equilibrium where relaxation rates between two thermally coupled levels are much faster than radiative decay, a single exponential decay is expected that is identical for emission from both levels. Clearly, for Eu^{3+} this has not been realized at 900 K. In general, it is important to verify the validity of a Boltzmann equilibrium in luminescence thermometry when temperature-dependent data and calibration curves are based on Boltzmann statistics. In the past this has not always been the case,^{14–16} especially for ratiometric analysis relying on emission from states separated by a larger ΔE , as for example in Dy^{3+} and Eu^{3+} . Deviations from Boltzmann behavior sometimes go unnoticed or are not explained correctly.^{14–16} The present analysis shows that the temperature dependence of the emission intensity ratio outside the Boltzmann regime can be accurately modelled and be used to understand and predict deviations from Boltzmann behavior.

Cross-relaxation. To extend the temperature range for luminescence thermometry toward lower temperatures, it is desirable to make the equilibration among the coupled levels faster than MPR allows for levels separated by a large ΔE . A potential mechanism to induce relaxation is cross-relaxation (partial energy transfer between neighboring ions). This can be observed for Eu^{3+} at elevated doping levels. At higher concentrations of Eu^{3+} the distance between Eu^{3+} neighbors decreases and the effect of the cross-relaxation becomes important. For Eu^{3+} cross-relaxation can occur as the energy difference between the ${}^5\text{D}_0$ and ${}^5\text{D}_1$ excited states and the ${}^7\text{F}_0$ and ${}^7\text{F}_3$ ground states is similar. The ${}^5\text{D}_1$ – ${}^5\text{D}_0$ energy can be transferred to a neighboring Eu^{3+} in the ${}^7\text{F}_0$ ground state that is raised to the ${}^7\text{F}_3$ state. There is a small energy mismatch between the ${}^5\text{D}_0$ – ${}^5\text{D}_1$ and ${}^7\text{F}_0$ – ${}^7\text{F}_3$ gaps and the small energy mismatch can be overcome by emission or absorption of low energy phonons.

The cross-relaxation rates depend on the distribution of Eu^{3+} ions. As a result, every Eu^{3+} with a unique distribution of Eu^{3+} neighbors gives rise to a unique relaxation pathway. Subsequently, the average relaxation time of an ensemble of Eu^{3+} ions is governed by the distribution of configurations resulting in a multi-exponential decay during time-resolved luminescence as shown in Figures 2.6 and 2.7 for samples with Eu^{3+} concentrations of 5.5 % and 8.4 %, respectively. The time-resolved luminescence measurements cannot be fitted properly with a simple model with a fixed value for cross-relaxation rates X_1 and

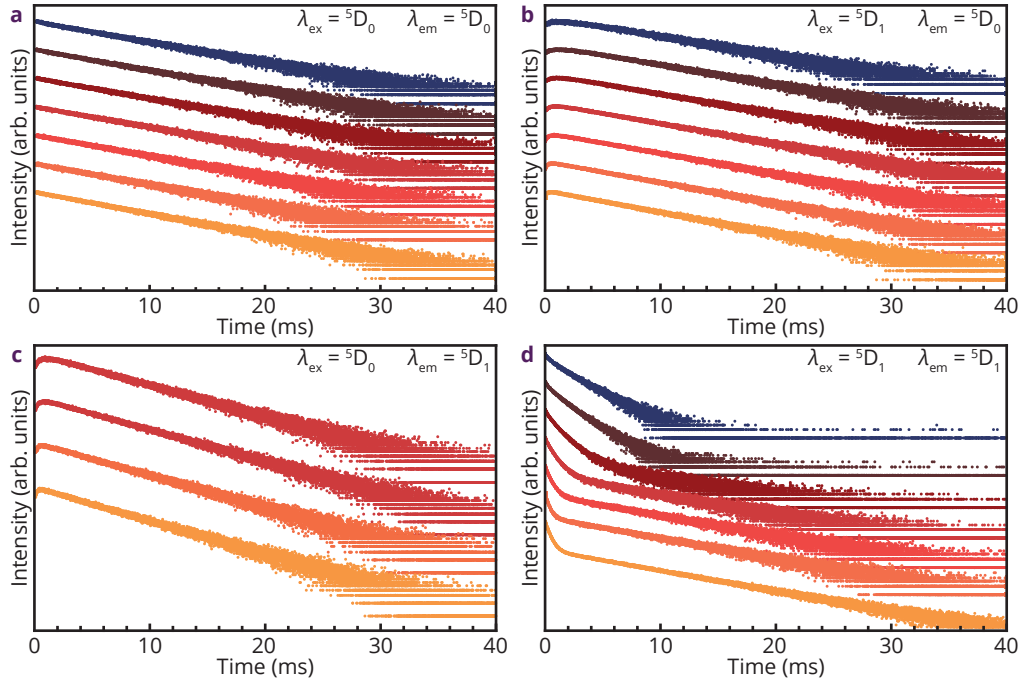


Figure 2.6 - Time-resolved spectroscopy measurements. Luminescence decay measurements in $\text{NaYF}_4:\text{Eu}^{3+}$ (5.5 %) at temperatures ranging from 300 K (dark blue) to 900 K (orange) while exciting in the $^5\text{D}_0$ and $^5\text{D}_1$ state and monitoring the $^5\text{D}_0$ level (a and b, respectively) and while exciting in the $^5\text{D}_0$ and $^5\text{D}_1$ level and monitoring the $^5\text{D}_1$ level (c and d, respectively).

X_2 because of different configurations of the Eu^{3+} ions in the lattice, and indeed a clear deviation from single exponential behavior was observed for the rise and initial decay part of the luminescence decay curves for the 5.5 % and 8.4 % Eu^{3+} -doped samples.

Stationary state measurements, on the other hand, have the virtue of integrating the decays over time. The temporal dependences of the various relaxation processes are thus integrated out. To explore the effect of the Eu^{3+} concentration on the temperature-dependent $^5\text{D}_1/{}^5\text{D}_0$ intensity ratio, the luminescence of two samples with a higher Eu^{3+} concentration, 5.5 % and 8.4 % has been measured as shown in Figure 2.8. The resulting temperature-dependent fluorescence intensity ratios (colored purple and red, respectively) are presented in Figure 2.9 in comparison with the results for 0.4 % (colored cyan) duplicated from Figure 2.2c.

We can rewrite equation 2.11 to include the temperature-dependent cross-relaxation processes, resulting in

$$\frac{I_2}{I_1} = C \frac{\frac{\alpha}{\tau_R} + M\rho g_2 n^p + X_2}{\frac{\beta}{\tau_R} + M\rho g_1 (1+n)^p + X_1}. \quad (2.12)$$

Here, X_1 and X_2 are the cross-relaxation terms for the $^5\text{D}_1 \rightarrow ^5\text{D}_0$ and $^5\text{D}_0 \rightarrow ^5\text{D}_1$ relaxations, respectively. The modelling is furthermore made to include the transition connecting the

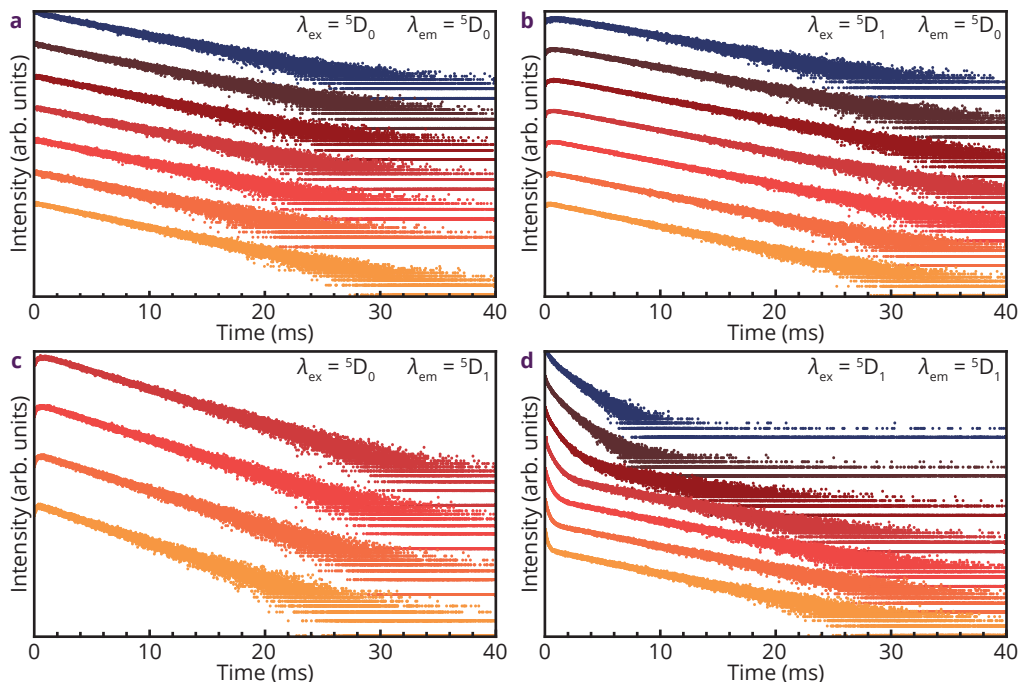


Figure 2.7 - Time-resolved spectroscopy measurements. Luminescence decay measurements in $\text{NaYF}_4:\text{Eu}^{3+}$ (8.4 %) at temperatures ranging from 300 K (dark blue) to 900 K (orange) while exciting in the $^5\text{D}_0$ and $^5\text{D}_1$ state and monitoring the $^5\text{D}_0$ level (a and b, respectively) and while exciting in the $^5\text{D}_0$ and $^5\text{D}_1$ level and monitoring the $^5\text{D}_1$ level (c and d, respectively).

$^7\text{F}_2$ and $^7\text{F}_4$ levels, which involves approximately the same energy (ca. 1800 cm^{-1}), and indeed contributes significantly at elevated temperatures. The thermal populations of the $^7\text{F}_2$ and $^7\text{F}_4$ are admittedly smaller, but the transition matrix elements connecting them are significantly larger, because $\Delta J = \pm 2$ as compared to $\Delta J = \pm 3$.

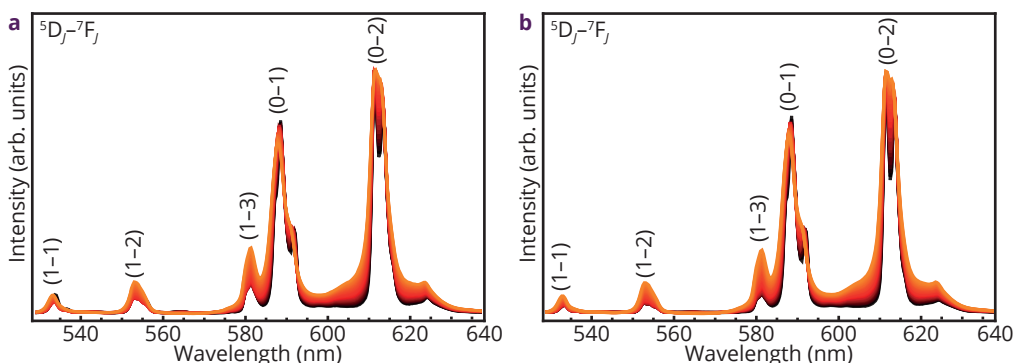


Figure 2.8 - Temperature-dependent luminescence. Emission spectra of $\text{NaYF}_4:\text{Eu}^{3+}$ (5.5 %) and $\text{NaYF}_4:\text{Eu}^{3+}$ (8.4 %) (a and b, respectively) upon excitation at 395 nm taken at different temperatures ranging from 300 K (black) to 900 K (orange).

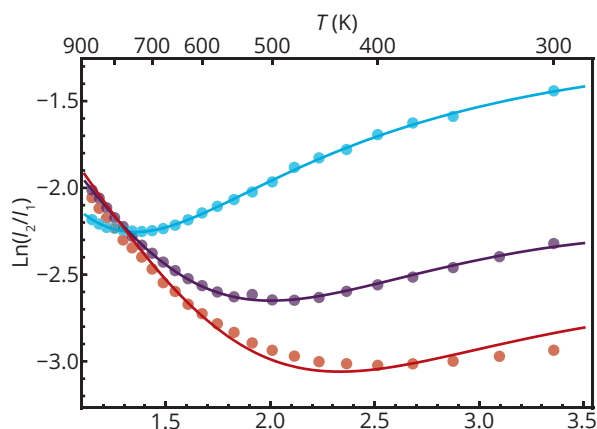


Figure 2.9 – Effect of Cross-relaxation. Log of the fluorescence intensity ratio plotted vs. $1000/T$ for the samples with Eu^{3+} concentrations of 0.4 % (cyan), 5.5 % (purple) and 8.4 % (red). The curves are fits of equation 2.11 to the 0.4 % data and of equations 2.12 with equations 2.13, 2.14 and 2.15 inserted to the 5.5 % and 8.4 % data.

To test the influence of Eu^{3+} concentration on the temperature-dependent ${}^5\text{D}_1/{}^5\text{D}_0$ intensity ratio, equation 2.12 was fitted to the temperature-dependent luminescence of two samples with a higher Eu^{3+} dopant concentration, 5.5 % and 8.4 % as shown in Figure 2.9. It is evident that the temperature dependence of the intensity ratio is strongly influenced by the Eu^{3+} concentration. For a higher concentration the ratio I_2/I_1 is much lower at room temperature as a result of faster ${}^5\text{D}_1 \rightarrow {}^5\text{D}_0$ relaxation and the temperature-dependent ${}^5\text{D}_1/{}^5\text{D}_0$ intensity ratio can be used to probe temperatures above ca. 500 K.

Modelling of the measured temperature dependence is complex and shows that also cross-relaxation processes starting from the higher energy ${}^7\text{F}_2$ level plays a role at elevated temperatures as the ${}^7\text{F}_2 \rightarrow {}^7\text{F}_4$ energy difference is also resonant with ΔE (${}^5\text{D}_1 \rightarrow {}^5\text{D}_0$) and has a significantly higher oscillator strength than the ${}^7\text{F}_0 \rightarrow {}^7\text{F}_3$ transition due to the favorable ΔJ value of 2. Based on Judd-Ofelt theory the transition probabilities for $\Delta J = 0, 2, 4$ or 6 (not $0 \rightarrow 0$) transitions are possible as forced electric dipole transition while the $\Delta J = 3$ (${}^7\text{F}_0 \rightarrow {}^7\text{F}_3$) transition is not.¹⁷ The reduced matrix elements $U^{(\lambda)}$ are all zero for the ${}^7\text{F}_0 \rightarrow {}^7\text{F}_3$ transition, while the matrix elements are large for the ${}^7\text{F}_2 \rightarrow {}^7\text{F}_4$ transition ($U^{(2)2} = 0.2226$, $U^{(4)2} = 0.0062$ and $U^{(6)2} = 0.0329$).¹⁷ Typically, forced electric dipole transitions ($\Delta J = 0, 2, 4$ or 6) are an order of magnitude stronger than other $J \rightarrow J$ transitions which makes cross-relaxation involving the ${}^7\text{F}_2 \rightarrow {}^7\text{F}_4$ transition favorable once these levels are thermally populated.

Cross-relaxation depends on the distribution of the Eu^{3+} ions over the lattice, notably the presence of nearest and next-nearest neighbors. A configuration of Eu^{3+} neighbors thus gives rise to a specific cross-relaxation rate that will vary for different Eu^{3+} ions. Faster cross-relaxation will occur for Eu^{3+} ions with one (or more) nearest Eu^{3+} neighbors. This will result in a multi-exponential decay. This is observed for samples with higher Eu^{3+} dopant levels of 5.5 % and 8.4 % as shown in Figures 2.6 and 2.7. However, if the total luminescence is monitored via steady-state measurements, the temporal dependence of the

various relaxation processes are averaged out and the intensity variations can be analyzed using an effective temperature-dependent cross-relaxation rate.

To model the cross-relaxation effects, we rewrite equation 2.12 to include

$$X_1 = g_1(X_{03}N'_0 + X_{24}N'_2), \quad (2.13)$$

and

$$X_2 = g_2(X_{03}N'_3 + X_{24}N'_4). \quad (2.14)$$

Here, X_{03} and X_{24} contain the relevant matrix elements for the transitions between the ${}^7\text{F}_0$ - ${}^7\text{F}_3$ and ${}^7\text{F}_2$ - ${}^7\text{F}_4$, respectively, and the populations of the ${}^7\text{F}_j$ states (having energy E_j) of the neighboring Eu^{3+} ions, N'_j is given by

$$N'_j = N^j(2J + 1) \frac{\exp(-E_j/kT)}{Z}, \quad (2.15)$$

in which N^j measures the density of adjacent Eu^{3+} contributing to cross-relaxation and Z is the state sum. Note that we assume here that the energy of the ${}^7\text{F}_j$ levels (E_j) is not affected by interactions with the neighboring Eu^{3+} ion in the ${}^5\text{D}_0$ or ${}^5\text{D}_1$ level. The phonon processes to compensate for the energy mismatch during cross-relaxation are also assumed to be much faster than cross-relaxation and are therefore omitted from equations 2.13 and 2.14.

To quantify the added effect of cross-relaxation in Figure 2.9, the data from the 5.5% (purple) and 8.4% (red) sample were fitted using equation 2.12 with equations 2.13 and 2.14. In the fitting procedure all obtained fitting parameters from the 0.4% sample (blue) were maintained, resulting in only 2 fitting parameters, X_{03} and X_{24} . The model with obtained values, ($X_{03} = 0.41 \pm 0.05 \text{ ms}^{-1}$ and $X_{24} = 4.0 \pm 0.4 \text{ ms}^{-1}$ for the 5.5% Eu^{3+} concentration and $X_{03} = 0.75 \pm 0.10 \text{ ms}^{-1}$ and $X_{24} = 9.7 \pm 1.4 \text{ ms}^{-1}$ for the 8.4% Eu^{3+} concentration) fits the data very well.

The ${}^7\text{F}_2$ - ${}^7\text{F}_4$ transition has a transition probability for cross-relaxation that is larger by an order of magnitude in comparison with the ${}^7\text{F}_0$ - ${}^7\text{F}_3$ transition. This is in line with the forced electric dipole character of the ${}^7\text{F}_2$ - ${}^7\text{F}_4$ transition. In fact, at elevated temperatures ${}^7\text{F}_2$ - ${}^7\text{F}_4$ is more effective, taking over from ${}^7\text{F}_0$ - ${}^7\text{F}_3$ above ca. 400 K as the dominant cross-relaxation process. We furthermore see that cross-relaxation rates increase roughly linearly with the Eu^{3+} concentration which is expected as the average number of Eu^{3+} neighbors increases linearly with Eu^{3+} concentration.

The analysis of the concentration dependence of the intensity ratio shows that the useful temperature range for luminescence thermometry can be controlled and extended through the dopant concentration. It also reveals that the dopant concentration is an important parameter in the evaluation of the performance of (nano)thermometers based on lanthanide-doped luminescent materials and the temperature regime in which Boltzmann equilibrium is reached.

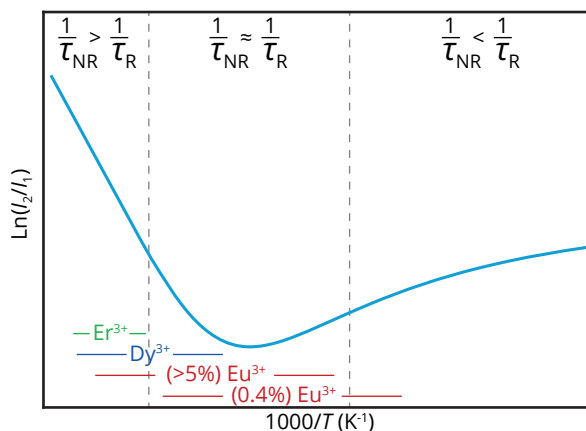


Figure 2.10 – Schematic representation of the proposed model. Fluorescence intensity ratio plotted vs. $1000/T$ for three lanthanide ions commonly used in luminescence thermometry. The energy gap ΔE between the thermally coupled levels increases from Er^{3+} to Dy^{3+} to Eu^{3+} . The drawn lines at the bottom indicate the temperature regimes that apply to these ions. In the case of $1/\tau_{\text{NR}} \ll 1/\tau_{\text{R}}$ the fluorescence intensity ratio will decrease with increasing temperature (right-hand side), in the case of $1/\tau_{\text{NR}} \approx 1/\tau_{\text{R}}$ there is a local minimum in the fluorescence intensity ratio (middle) and in the case of $1/\tau_{\text{NR}} \gg 1/\tau_{\text{R}}$ Boltzmann behavior determines an increase of the fluorescence intensity ratio with increasing T (left-hand side).

Implications of the present analysis are schematically depicted in Figure 2.10 for Eu^{3+} and two other lanthanide ions (Er^{3+} and Dy^{3+}) commonly used for luminescence thermometry. Three different temperature regimes can be discerned: non-radiative relaxation much faster than radiative decay (Boltzmann regime, left-hand side), non-radiative and radiative decay rates are similar (middle) and radiative decay faster than non-radiative decay (right-hand side). For the latter two regimes the temperature-dependence of the emission intensity ratio I_2/I_1 does not follow Boltzmann statistics. The relative intensity of the upper level I_2 can even decrease with increasing temperature, opposite to what is expected from Boltzmann statistics. The regime that is applicable strongly depends on the energy gap ΔE between the thermally coupled levels. The lines at the bottom mark for the three ions the valid regime (300–900 K), where the starting point at the right-hand side of the lines marks room temperature. The schematic shows that for Er^{3+} with the smallest ΔE (ca. 700 cm^{-1} for ${}^2\text{H}_{11/2}-{}^4\text{S}_{3/2}$) the Boltzmann behavior already starts below room temperature. For Dy^{3+} with a larger ΔE (ca. 1000 cm^{-1} for ${}^4\text{I}_{15/2}-{}^4\text{F}_{9/2}$) Boltzmann behavior is realized at temperatures higher than room temperature but well below 900 K. For Eu^{3+} with the largest ΔE (ca. 1800 cm^{-1} for ${}^5\text{D}_1-{}^5\text{D}_0$) Boltzmann equilibrium is not realized even at the highest temperatures investigated in this study (900 K). However, by introducing additional relaxation pathways e.g. through cross-relaxation at higher Eu^{3+} concentrations, the temperature regime for luminescence thermometry can be shifted towards lower temperatures. The present analysis shows that the validity of Boltzmann statistics needs to be considered in the application of luminescence thermometry based on both ΔE and the dopant concentration.

Conclusions

To investigate the validity of Boltzmann equilibrium in lanthanide-based luminescence thermometry, the temperature dependence of the ${}^5\text{D}_1$ and ${}^5\text{D}_0$ emission of Eu^{3+} in NaYF_4 has been investigated between 300 and 900 K. Both steady state and time-resolved luminescence spectroscopy experiments are reported for three different Eu^{3+} concentrations (0.4 %, 5.5 % and 8.4 %). For 0.4 % doping all decay curves for ${}^5\text{D}_1$ and ${}^5\text{D}_0$ emission (upon both ${}^5\text{D}_1$ and ${}^5\text{D}_0$ excitation) show a consistent behavior that can be explained by ${}^5\text{D}_1$ - ${}^5\text{D}_0$ and, at higher temperatures, ${}^5\text{D}_0$ - ${}^5\text{D}_1$ multi-phonon relaxation. Upon raising the temperature, relaxation rates increase as predicted by theoretical models for multi-phonon relaxation. The temperature dependence measured for the ${}^5\text{D}_1/{}^5\text{D}_0$ emission intensity ratio is in good quantitative agreement with the relaxation parameters determined from the temperature-dependent emission decay curves. The results reveal that even at the highest temperatures (up to 900 K), relaxation between the ${}^5\text{D}_0$ and ${}^5\text{D}_1$ level is not fast enough to establish Boltzmann equilibrium. This limits the temperature range in which $\text{NaYF}_4:\text{Eu}^{3+}$ can be used for ratiometric luminescence thermometry. To extend the temperature range, faster ${}^5\text{D}_1$ - ${}^5\text{D}_0$ relaxation can be realized by increasing the Eu^{3+} doping concentration to induce cross-relaxation between Eu^{3+} neighbors. Modelling of the temperature-dependent luminescence intensity ratio indicates that both ${}^5\text{D}_1$ - ${}^5\text{D}_0$ to ${}^7\text{F}_0$ - ${}^7\text{F}_3$ and ${}^5\text{D}_1$ - ${}^5\text{D}_0$ to ${}^7\text{F}_2$ - ${}^7\text{F}_4$ cross-relaxations contribute.

The present study gives insight in processes that determine equilibration between thermally coupled levels of lanthanide emitters used in ratiometric luminescence thermometry. Upon increasing the energy difference ΔE between levels, required for accurate sensing of high temperatures, relaxation rates decrease and deviations from Boltzmann equilibrium occur in the lower temperature regime. Models for the temperature dependence of multi-phonon relaxation rates can be used to quantitatively model the temperature dependence and give insight in the practical temperature range. The temperature range can be optimized by varying the lanthanide dopant concentration to enhance relaxation rates through cross-relaxation. In the development of lanthanide-based luminescent (nano)thermometers it is important to evaluate the validity of Boltzmann equilibration and understand deviations from Boltzmann behavior to extend and improve the accuracy of temperature calibration curves.

Experimental section

Synthesis of NaYF_4 . Microcrystalline NaYF_4 was prepared via a solid state synthesis.³⁴ In short, 15 mmol of NaF (>98 %, Sigma-Aldrich), 15 mmol of REF_3 (RE = Y, Eu, 99.99 %, Sigma-Aldrich) and 13.5 mmol of NH_4F (>98 %, Sigma-Aldrich) were mixed with a pestle and mortar and afterwards placed in an alumina crucible. The mixture was fired in the oven in an excess of NH_4F under a nitrogen atmosphere. The samples were heated to 300 °C for 3 h and afterwards heated to 550 °C for 8 h. The heating rate was 5 °C min^{-1} for both heating steps.

Setup. After synthesis, the samples were crushed with a pestle and mortar and the crystallinity was confirmed with X-ray diffraction measurements using a Philips PW1729 X-ray diffractometer. To remove the NaF impurities, samples were dispersed in H₂O and after dissolving the NaF the samples were centrifuged, decanted and dried to remove the H₂O. Luminescence measurements were performed using a 5 mW 405 ± 10 nm diode laser and an Ocean Optics QE Pro010451 CCD. Luminescence decay measurements were measured with an Ekspla NT 342B tunable laser, a Triax 550 single emission monochromator, a Hamamatsu R928 PMT and a EG&G Ortec Turbo-MCS multichannel scaler.

Acknowledgements

O. L. J. Gijzeman (Utrecht University) is gratefully acknowledged for the scientific discussions. This work was supported by the Netherlands Center for Multiscale Catalytic Energy Conversion (MCEC), an NWO Gravitation programme funded by the Ministry of Education, Culture and Science of the government of the Netherlands.

References

1. Jaque, D. & Vetrone, F. Luminescence nanothermometry. *Nanoscale* **2012**, *4*, 4301–4326.
2. Kusama, H.; Sovers, O. J.; Yoshioka, T. Line Shift Method for Phosphor Temperature Measurements. *Jpn. J. Appl. Phys.* **1976**, *15*, 2349–2358.
3. Vetrone, F.; Naccache, R.; Zamarrón, A.; Juarranz de la Fuente, A.; Sanz-Rodríguez, F.; Martínez Maestro, L.; Martín Rodríguez, E.; Jaque, D.; García Solé, J. & Capobianco, J. A. Temperature Sensing Using Fluorescent Nanothermometers. *ACS Nano* **2010**, *4*, 3254–3258.
4. Yang, J. M.; Yang, H. & Lin, L. Quantum dot nano thermometers reveal heterogeneous local thermogenesis in living cells. *ACS Nano* **2011**, *5*, 5067–5071.
5. Gota, C.; Okabe, K.; Funatsu, T.; Harada, Y. & Uchiyama, S. Hydrophilic fluorescent nanogel thermometer for intracellular thermometry. *J. Am. Chem. Soc.* **2009**, *131*, 2766–2767.
6. Aigouy, L.; Tessier, G.; Mortier, M. & Charlot, B. Scanning thermal imaging of microelectronic circuits with a fluorescent nanoprobe. *Appl. Phys. Lett.* **2005**, *87*, 1–3.
7. Bar-Cohen, A. & Wang, P. On-chip Hot Spot Remediation with Miniaturized Thermoelectric Coolers. *Microgravity Sci. Technol.* **2009**, *21*, 351–359.
8. Toebes, M. L.; Prinsloo, F. F.; Bitter, J. H.; van Dillen, A. J. & de Jong, K. P. Influence of oxygen-containing surface groups on the activity and selectivity of carbon nanofiber-supported ruthenium catalysts in the hydrogenation of cinnamaldehyde. *J. Catal.* **2003**, *214*, 78–87.
9. Grunwaldt, J. D.; Wagner, J. B. & Dunin-Borkowski, R. E. Imaging Catalysts at Work: A Hierarchical Approach from the Macro- to the Meso- and Nano-scale. *ChemCatChem* **2013**, *5*, 62–80.
10. Borodina, E.; Meirer, F.; Lezcano-González, I.; Mokhtar, M.; Asiri, A. M.; Al-Thabaiti, S. A.; Basahel, S. N.; Ruiz-Martinez, J. & Weckhuysen, B. M. Influence of the Reaction Temperature on the Nature of the Active and Deactivating Species during Methanol-to-Olefins Conversion over H-SSZ-13. *ACS Catal.* **2015**, *5*, 992–1003.
11. Geitenbeek, R. G.; Nieuwelink, A.-E.; Jacobs, T. S.; Salzmann, B. B. V.; Goetze, J.; Meijerink, A. & Weckhuysen, B. M. In Situ Luminescence Thermometry To Locally Measure Temperature Gradients during Catalytic Reactions. *ACS Catal.* **2018**, *8*, 2397–2401.

12. Brites, C. D. S.; Lima, P. P.; Silva, N. J. O.; Millán, A.; Amaral, V. S.; Palacio, F. & Carlos, L. D. Thermometry at the nanoscale. *Nanoscale* **2012**, *4*, 4799–4829.
13. Geitenbeek, R. G.; Prins, P. T.; Albrecht, W.; van Blaaderen, A.; Weckhuysen, B. M. & Meijerink, A. NaYF₄:Er³⁺,Yb³⁺/SiO₂ Core/Shell Upconverting Nanocrystals for Luminescence Thermometry up to 900 K. *J. Phys. Chem. C* **2017**, *121*, 3503–3510.
14. Čulubrk, S.; Lojpur, V.; Ahrenkiel, S. P.; Nedeljković, J. M. & Dramićanin, M. D. Non-contact thermometry with Dy³⁺ doped Gd₂Ti₂O₇ nano-powders. *J. Lumin.* **2016**, *170*, 395–400.
15. Cao, Z.; Zhou, S.; Jiang, G.; Chen, Y.; Duan, C. & Yin, M. Temperature dependent luminescence of Dy³⁺ doped BaYF₅ nanoparticles for optical thermometry. *Curr. Appl. Phys.* **2014**, *14*, 1067–1071.
16. Lojpur, V.; Čulubrk, S. & Dramićanin, M. D. Ratiometric luminescence thermometry with different combinations of emissions from Eu³⁺ doped Gd₂Ti₂O₇ nanoparticles. *J. Lumin.* **2016**, *169*, 534–538.
17. Carnall, W. T.; Crosswhite, H. & Crosswhite, H. M. *Energy Level Structure and Transition Probabilities of the Trivalent Lanthanides in LaF₃*, Argonne National Laboratory, Argonne, **1977**.
18. Zhao, Y.; Riemersma, C.; Pietra, F.; Koole, R.; de Mello Donegá, C. & Meijerink, A. High-temperature luminescence quenching of colloidal quantum dots. *ACS Nano* **2012**, *6*, 9058–9067.
19. Viveros-Andrade, A. G.; Colorado-Peralta, R.; Flores-Alamo, M.; Castillo-Blum, S. E.; Durán-Hernández, J. & Rivera, J. M. Solvothermal synthesis and spectroscopic characterization of three lanthanide complexes with high luminescent properties [H₂NMe₂]₃[Ln(III)(2,6-pyridinedicarboxylate)₃] (Ln = Sm, Eu, Tb): In the presence of 4,4'-Bipyridyl. *J. Mol. Struct.* **2017**, *1145*, 10–17.
20. Kissel, T.; Brübach, J.; Euler, M.; Froscher, M.; Litterscheid, C.; Albert, B. & Dreziler, A. Phosphor thermometry: On the synthesis and characterisation of Y₃Al₅O₁₂:Eu (YAG:Eu) and YAlO₃:Eu (YAP:Eu). *Mater. Chem. Phys.* **2013**, *140*, 435–440.
21. Allison, S. W. & Gillies, G. T. Remote thermometry with thermographic phosphors: Instrumentation and applications. *Rev. Sci. Instrum.* **1997**, *68*, 2615–2650.
22. Xu, X.; Wang, Z.; Lei, P.; Yu, Y.; Yao, S.; Song, S.; Liu, X.; Su, Y.; Dong, L.; Feng, J. & Zhang, H. α-NaYb(Mn)F₄:Er³⁺/Tm³⁺@NaYF₄ UCNPs as “Band-Shape” Luminescent Nanothermometers over a Wide Temperature Range. *ACS Appl. Mater. Interfaces* **2015**, *7*, 20813–20819.
23. Alencar, M. A. R. C.; Maciel, G. S.; de Araújo, C. B. & Patra, A. Er³⁺-doped BaTiO₃ nanocrystals for thermometry: Influence of nanoenvironment on the sensitivity of a fluorescence based temperature sensor. *Appl. Phys. Lett.* **2004**, *84*, 4753.
24. Haro-González, P.; Martín, I. R.; Martín, L. L.; León-Luis, S. F.; Pérez-Rodríguez, C. P. & Lavín, V. Characterization of Er³⁺ and Nd³⁺ doped Strontium Barium Niobate glass ceramic as temperature sensors. *Opt. Mater.* **2011**, *33*, 742–745.
25. Đaćanin Far, Lj.; Lukić-Petrović, S. R.; Đorđević, V.; Vuković, K.; Glais, E.; Viana, B. & Dramićanin, M. D. Luminescence temperature sensing in visible and NIR spectral range using Dy³⁺ and Nd³⁺ doped YNbO₄. *Sensors Actuators, A Phys.* **2018**, *270*, 89–96.
26. Cao, C.; Yang, H. K.; Chung, J. W.; Moon, B. K.; Choi, B. C.; Jeong, J. H. & Kim, K. H. Hydrothermal Synthesis and White Luminescence of Dy³⁺-Doped NaYF₄ Microcrystals. *J. Am. Ceram. Soc.* **2011**, *94*, 3405–3411.
27. Li, C.; Zhang, C.; Hou, Z.; Wang, L.; Quan, Z.; Lian, H. & Lin, J. β-NaYF₄ and β-NaYF₄:Eu³⁺ Microstructures: Morphology Control and Tunable Luminescence Properties. *J. Phys. Chem. C* **2009**, *113*, 2332–2339.
28. Blasse, G. & Grabmaier, B. *Luminescent Materials*, Springer, Berlin, **1994**.

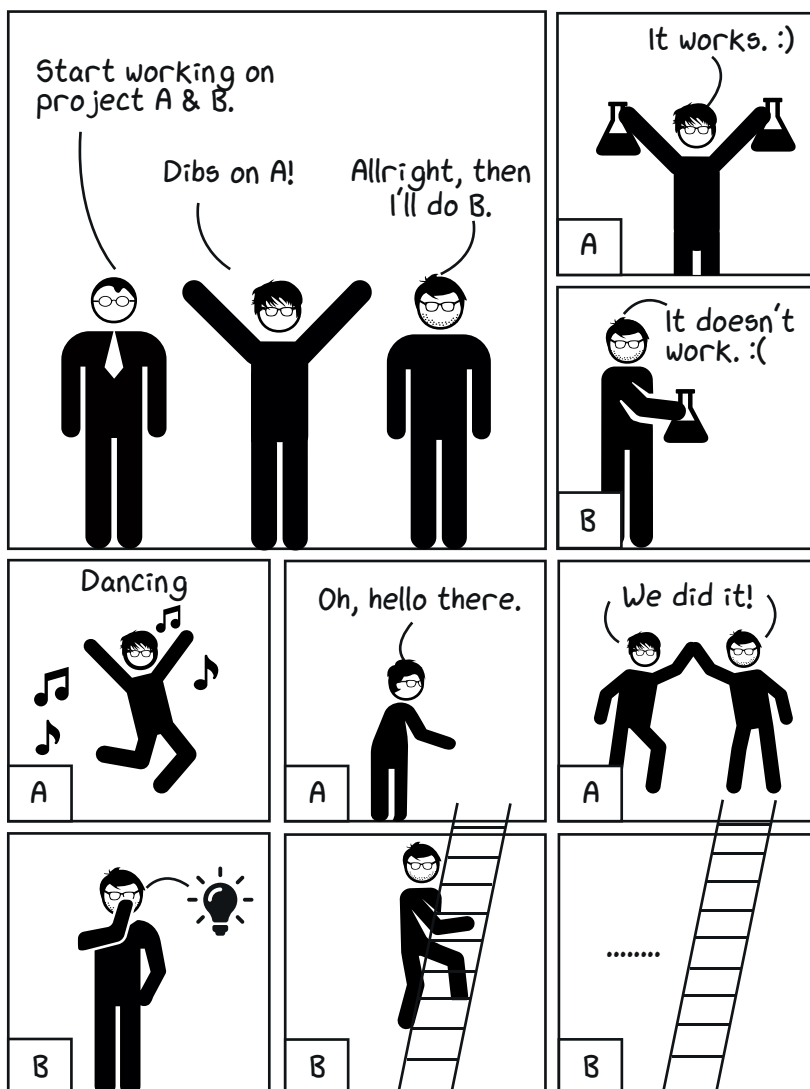
29. Riseberg, L. A. & Moos, H. W. Multiphonon Orbit-Lattice Relaxation of Excited States of Rare-Earth Ions in Crystals. *Phys. Rev.* **1968**, *174*, 429–437.
30. Layne, C. B.; Lowdermilk, W. H. & Weber, M. J. Multiphonon relaxation of rare-earth ions in oxide glasses. *Phys. Rev. B* **1977**, *16*, 10–20.
31. Henderson, B. & Imbusch, G. F. *Optical Spectroscopy of Inorganic Solids*, Oxford Science Publications, **2006**.
32. Orbach, R. Spin-lattice relaxation in rare-earth salts. *Proc. R. Soc. Lond. A*, **1961**, *264*, 458–484.
33. Egorov, S. A. & Skinner, J. L. On the theory of multiphonon relaxation rates in solids. *J. Chem. Phys.* **1995**, *103*, 1533–1543.
34. Ghosh, P. & Patra, A. Influence of Crystal Phase and Excitation Wavelength on Luminescence Properties of Eu³⁺-Doped Sodium Yttrium Fluoride Nanocrystals. *J. Phys. Chem. C* **2008**, *112*, 19283–19292.
35. Yu, D.-C.; Martín-Rodríguez, R.; Zhang, Q.-Y.; Meijerink, A. & Rabouw, F. T. Multi-photon quantum cutting in Gd₂O₂S:Ti³⁺ to enhance the photo-response of solar cells. *Light Sci. Appl.* **2015**, *4*, e344.
36. Grinberg, M. ²E→⁴A₂ fluorescence of Cr³⁺ in high and intermediate field garnets. *J. Lumin.* **1993**, *54*, 369–382.
37. Da Fonseca, R. J. M. & Abritta, T. Radiative and nonradiative processes in LiGa₃O₈:Mn⁴⁺. *Phys. B Condens. Matter* **1993**, *190*, 327–332.
38. de Wijn, H. W. Phonon physics in ruby studied by optical pumping and luminescence. *J. Lumin.* **2007**, *125*, 55–59.
39. Aarts, L.; van der Ende, B. M. & Meijerink, A. Downconversion for Solar Cells in NaYF₄:Er,Yb. *J. Appl. Phys.* **2009**, *106*, 023522.



Based on

- Geitenbeck, R. G.; Prins, P. T.; Albrecht, W.; van Blaaderen, A.; Weckhuysen, B. M. & Meijerink, A. NaYF₄:Er³⁺,Yb³⁺/SiO₂ Core/Shell Upconverting Nanocrystals for Luminescence Thermometry up to 900 K. *J. Phys Chem C* **2017**, *121*, 3503–3510.

Chapter 3 – $\text{NaYF}_4:\text{Er}^{3+}, \text{Yb}^{3+}/\text{SiO}_2$ Core/Shell Upconverting Nanocrystals for Luminescence Thermometry up to 900 K



Robin Geitenbeek



Tim Prins



Andries Meijerink

Abstract

The rapid development of nanomaterials with unique size-tunable properties forms the basis for a variety of new applications, including temperature sensing. Luminescent nanoparticles (NPs) have demonstrated potential as sensitive nanothermometers, especially in biological systems. Their small size offers the possibility of mapping temperature profiles with high spatial resolution. The temperature range is however limited which prevents the use in high temperature applications as e.g. nano-electronics, thermal barrier coatings and chemical reactors. In this work we extend the temperature range for nanothermometry beyond 900 K using silica coated NaYF_4 nanoparticles doped with the lanthanide ions Yb^{3+} and Er^{3+} . Monodisperse ca. 20 nm $\text{NaYF}_4:\text{Er}^{3+},\text{Yb}^{3+}$ nanocrystals were coated with a ca. 10 nm silica shell. Upon excitation with infrared radiation bright green upconversion (UC) emission is observed. From the intensity ratio between ${}^2\text{H}_{11/2}$ and ${}^4\text{S}_{3/2}$ UC emission lines at 520 nm and 550 nm, respectively, the temperature can be determined up to at least 900 K with an accuracy of 1 to 5 K for silica coated NPs. For bare $\text{NaYF}_4:\text{Er}^{3+},\text{Yb}^{3+}$ NPs the particles degrade above 600 K. Repeated thermal cycling experiments demonstrate the high durability and reproducibility of the silica coated nanocrystals as temperature probes without any loss of performance. The present results open avenues for the development of a new class of highly stable nanoprobcs by applying a silica coating around a wide variety of lanthanide-doped NPs.

Introduction

The broad range of potential applications for nanomaterials continues to stimulate research in the nanoregime where the size dependent physical and chemical properties are important in realizing technological breakthroughs.¹⁻⁸ One research area involves the development of detection techniques with sufficient spatial resolution enabled by the small size of nanomaterials. Temperature is an important parameter, but is not easy to measure with sufficient resolution, i.e. at the (sub)micrometer scale. In order to measure temperature accurately, several techniques have been developed. These techniques can be divided into three different categories: electrical,⁹ mechanical¹⁰ and optical techniques.^{11,12} Most electrical techniques combine the relation between temperature and resistance, voltage, conductivity or electrical capacity with Atomic Force Microscopy (AFM). Mechanical techniques revolve around an AFM tip composed of two metals and the temperature-dependent contact potential between these metals. Although a high resolution can be reached with these techniques, the techniques are limited to surfaces. Furthermore, the techniques require contact with the sample and can therefore initiate artificial heat fluxes.

Optical techniques rely on changes in the absorption or emission spectrum induced by temperature changes and do allow for remote temperature sensing. A promising method is luminescence thermometry.^{13,14} Luminescence thermometry exploits the temperature-dependence of the spectral position, bandwidth, intensity, polarization or lifetime of emission. However, most of these optical properties can also depend on other parameters, such as concentration of luminescent centers, spectral or intensity shifts induced by other factors besides temperature or fluctuations in the excitation power or spectral alignment. Fluorescence intensity ratio thermometry (FIRT) is a ratiometric measuring technique and consequently does not depend on variations in sample concentration, alignment or excitation power. This makes FIRT the ideal technique to measure temperature, since it does not require an internal standard.

FIRT is an active and expanding field of research. Most of the research presently focusses on *in vivo* thermometry for bioimaging.^{15,16} Research has for example shown that FIRT can be applied for cancer diagnosis.¹⁷ In cancer, rapid mitosis leads to increased cell temperatures. These increased cell temperatures can be monitored at an earlier stage than with conventional techniques for cancer diagnosis. The temperature probes should have a high accuracy in the physiological range. The range and the accuracy of the temperature measurements cannot be optimized simultaneously. Consequently, the highly sensitive temperature probes used for cancer diagnosis have a very limited measuring range (below 350 K).

Many applications – e.g. temperature sensing in nano-electronics,^{18,19} nanophotonics,^{20,21} thermal barrier coatings^{22,23} and chemical reactors^{24,25} – require a much broader temperature range compared to bioimaging. FIRT can be a promising technique in a wider temperature range. However, this requires the temperature probes to be robust and photostable up to elevated temperatures. Ln³⁺-doped materials are ideal candidates as temperature probes

due to their sharp emission lines (easy detection against a broad background), high thermal quenching temperatures of their emission and high photostability. The Ln^{3+} -doped materials can be organic clusters, metal/organic frameworks, glasses or (nano)crystals.^{26–29} The use of lanthanides in inorganic hosts is favored over organometallic materials, mostly because of the higher (thermal and photo) stability of the inorganic host and the lower energies of vibrations (phonons) in close proximity to the Ln^{3+} ion. It is well known that the main mechanism for quenching of the 4f–4f emission of Ln^{3+} is multi-phonon relaxation, a process in which energy is transferred from a Ln^{3+} excited state to vibrational excited states (heat) of the surrounding matrix. The relaxation rate depends exponentially on the number of phonons that needs to be excited. As a result, multi-phonon relaxation has a much lower probability in inorganic hosts which have low energy phonons (ca. 500 cm^{-1} for fluorides and oxides) compared to organic materials where large energy gaps can be bridged by a small number of high energy vibrations (e.g. 3000 cm^{-1} and 3500 cm^{-1} for C–H and O–H vibrations, respectively).³⁰

Based on these advantages, both doped glasses^{31,32} and doped crystalline materials^{33–35} have been investigated as functional materials for remote temperature sensing using FIRT. However, most of the works focus on bulk materials, with limited spatial resolution and no possibility to measure temperature in stable dispersions. Furthermore, research into both bulk and nanomaterials has led to temperature probes in a range up to 700 K.^{32,33,35} However, some applications require much higher temperatures, even up to 1500 K,³⁶ which cannot be measured with the currently available temperature probes. To measure temperature with sufficient spatial resolution and at elevated temperatures, new temperature (nano)probes need to be developed.

In this chapter, we report the application of $\text{NaY}_{0.8}\text{Yb}_{0.18}\text{Er}_{0.02}\text{F}_4$ nanocrystals (NCs) and $\text{NaY}_{0.8}\text{Yb}_{0.18}\text{Er}_{0.02}\text{F}_4/\text{SiO}_2$ core/shell ($\text{NaYF}_4@\text{SiO}_2$) nanocrystals as upconverting (UC) nanothermometers. The monodisperse core nanoparticles show temperature-dependent UC luminescence up to 600 K. The luminescence drops at higher temperatures due to oxidation of the ligands and coalescence of NCs. To overcome this problem, a silica coating has been grown around the core NCs, resulting in core/shell NCs. These $\text{NaYF}_4@\text{SiO}_2$ NCs show stable temperature-dependent UC luminescence up to 900 K. Repeated cycling between 300 K and 900 K shows that the durability of the $\text{NaYF}_4@\text{SiO}_2$ NCs is excellent. The accuracy of the measurements is also high, with standard deviations of 1 K and 5 K below and above 750 K, respectively. The present results show that NaYF_4 doped with Yb^{3+} and Er^{3+} can be used as a temperature probe up to 900 K after encapsulation in a protective silica shell. The broader temperature range, durability of the temperature probes and the non-invasiveness of FIRT makes this system ideal for measuring temperatures in a wide variety of systems and remote temperature sensing applications.

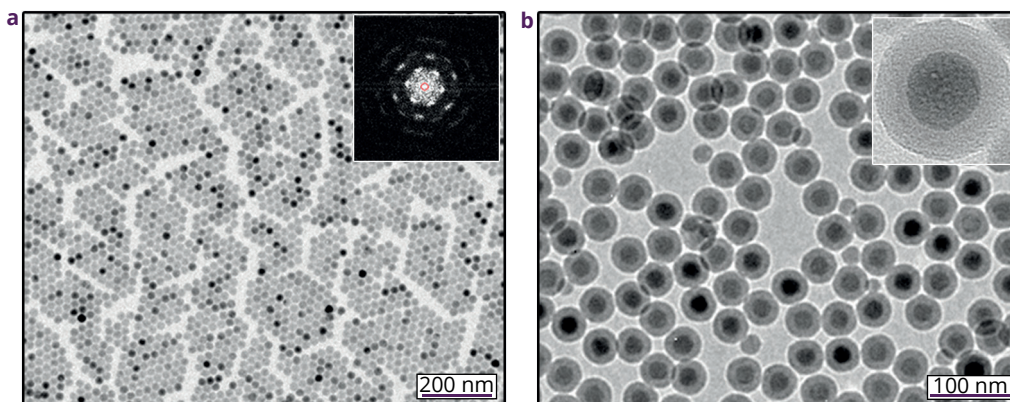


Figure 3.1 – TEM micrographs. TEM micrographs of the prepared NaYF₄ NCs (a) with an inset with a Fourier Transform showing hexagonal stacking and NaYF₄@SiO₂ NCs (b). The average diameter of the core NCs is 21.7 ± 1.1 nm and the silica shell is 10.0 ± 0.7 nm.

Results and Discussion

Structural Characterization. To determine the size, shape and crystallinity of both the NaYF₄ NCs and NaYF₄@SiO₂ NCs, we used different characterization methods such as transmission electron microscopy (TEM), energy dispersive X-ray spectroscopy (EDX) and powder X-ray diffraction (XRD) measurements. Figure 3.1 shows TEM images of the prepared NCs and Figure 3.2 shows the corresponding EDX spectra and XRD diffractograms.

Figure 3.1a shows that the synthesis yields monodisperse NCs of 21.7 ± 1.1 nm. The individual NCs are well separated due to the steric effects of the ligand layer, which suggests that the NCs can form a colloidal stable dispersion. These monodisperse NCs form hexagonally ordered domains, which is illustrated with the Fourier Transform in the inset. The overgrowth with silica yields monodisperse NaYF₄@SiO₂ NCs with an unaltered core and a uniform shell of 10.0 ± 0.7 nm, which are charge stabilized by surface silanol groups.

The elemental composition of the NCs was determined by EDX (Figures 3.2a and 3.2b). From the observed peaks, it can be concluded that Na, Y, F, Er and Yb are all present in the NaYF₄ NCs and NaYF₄@SiO₂ NCs. For the NaYF₄@SiO₂ NCs an additional peak for Si is observed and a strongly increased peak corresponding to O, as expected for silica overgrowth. The calculated stoichiometry for the NaYF₄ NCs, Na₁Y_{0.6}Er_{0.02}Yb_{0.08}F_{3.2}, is in fair agreement with the expected stoichiometry of Na₁Y_{0.8}Er_{0.02}Yb_{0.18}F₄.

Figures 3.2c and 3.2d show that the NCs have a hexagonal crystal structure (JCPDS No. 00-028-1192, cyan lines), as expected. Using the Scherrer equation,³⁷ a rough estimate of the core crystallite size can be calculated, which was ca. 18 nm and 17 nm for the NaYF₄ and NaYF₄@SiO₂ NCs, respectively. For the NaYF₄@SiO₂ NCs an extra broad band is present centered at a diffraction angle of ca. 28°, which is due to the amorphous silica.

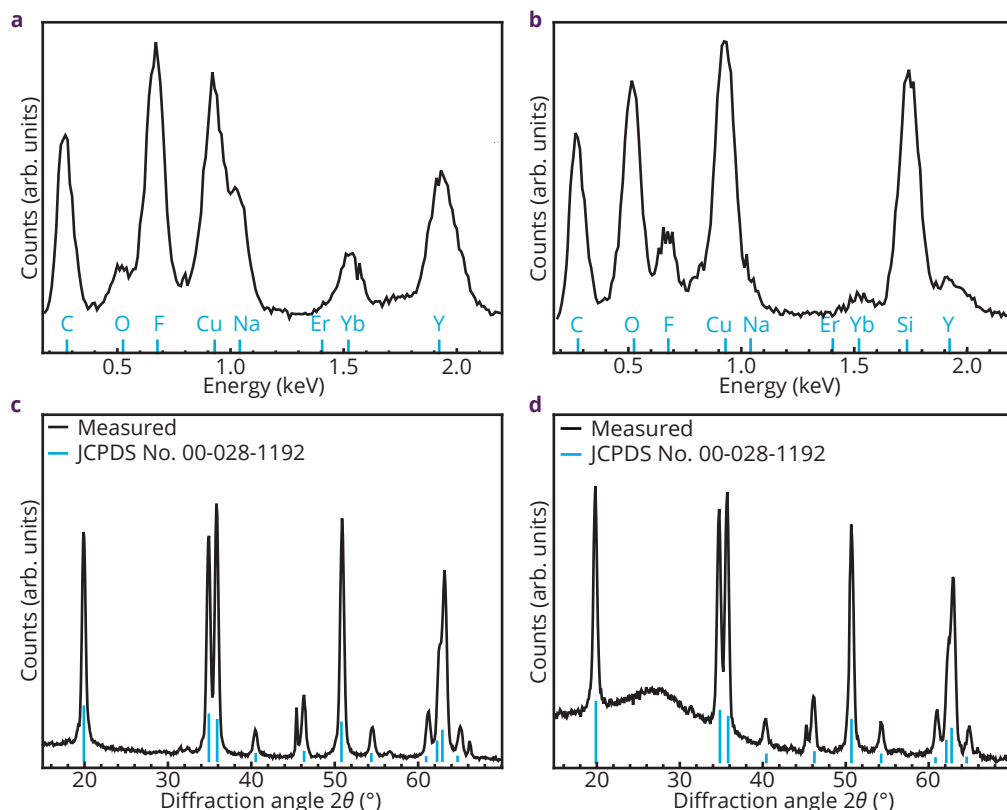


Figure 3.2 – EDX and XRD characterization of NaYF_4 NCs and $\text{NaYF}_4@\text{SiO}_2$ NCs. EDX spectra of NaYF_4 and $\text{NaYF}_4@\text{SiO}_2$ (a and b, respectively). Co K α XRD diffractograms of NaYF_4 NCs and $\text{NaYF}_4@\text{SiO}_2$ NCs (c and d, respectively). The cyan lines are reference values for hexagonal NaYF_4 (JCPDS No. 00-028-1192), the extra peaks are due to low impurity levels of NaF (JCPDS No. 00-036-1455).

By combining the data from TEM and EDX it was shown that NaYF_4 NCs doped with Er^{3+} and Yb^{3+} can be synthesized. The crystallite size from XRD and the NP size from TEM match very closely, indicating monocrystalline core NCs. Furthermore, silica overgrowth results in monodisperse $\text{NaYF}_4@\text{SiO}_2$ NCs in which the size, shape and crystal phase of the core NCs are unaltered.

Luminescence Properties. To investigate the luminescence properties of the NCs, room temperature emission and decay measurements were performed as shown in Figure 3.3. All measurements were performed using a continuous wave and a pulsed laser at 980 nm for the emission and decay measurements, respectively.

Figure 3.3a shows the upconversion (UC) emission spectrum upon excitation of Yb^{3+} at 980 nm. In the region between 500 nm and 700 nm three distinct peaks are observed, centered around 525 nm, 545 nm and 660 nm. These peaks correspond to the ${}^2\text{H}_{11/2}-{}^4\text{I}_{15/2}$, ${}^4\text{S}_{3/2}-{}^4\text{I}_{15/2}$ and ${}^4\text{F}_{9/2}-{}^4\text{I}_{15/2}$ transitions of Er^{3+} , respectively, as shown in Figure 3.3b.

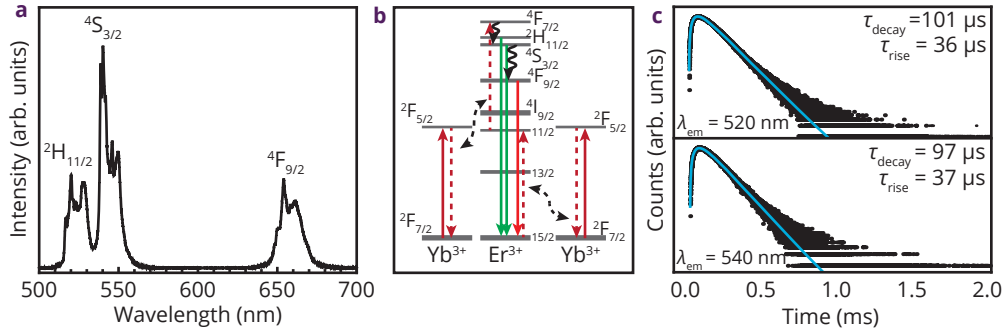


Figure 3.3 – Luminescence properties of NaYF₄ NCs. Emission spectrum of NaYF₄ NCs between 500 nm and 700 nm while exciting Yb³⁺ at 980 nm (a). The energy diagram of Er³⁺ and Yb³⁺, including the transitions involved in the upconversion process (b). The time-resolved luminescence measurements of emission from the ²H_{11/2} (520 nm) and ⁴S_{3/2} (545 nm) excited states upon excitation at 980 nm (c).

Figure 3.3c depicts the luminescence lifetime measurements of the ²H_{11/2} (top) and ⁴S_{3/2} (bottom) excited state. The experimental data is shown in black, while a bi-exponential fit is shown in cyan. In both cases, a rise and a subsequent decay in luminescence is observed. The rise times are ca. 35 μs and can be explained by the upconversion energy transfer from Yb³⁺ to Er³⁺. The decay time of ca. 100 μs is determined by both radiative decay to all lower levels and non-radiative relaxation to the ⁴F_{9/2} level of Er³⁺, in agreement with earlier reports.³⁸ The luminescence decay curves of the ²H_{11/2} (λ_{em} = 520 nm) and ⁴S_{3/2} (λ_{em} = 540 nm) excited state are nearly identical which is expected for excited states that are thermally coupled.

Fluorescence Intensity Ratio Nanothermometry. FIR nanothermometry with luminescent nanoparticles relies on measuring the intensity ratio of emission lines from thermally coupled excited states. The population ratio of two excited states is determined by a Boltzmann distribution, which includes a temperature-dependent factor,

$$\frac{N_2}{N_1} = \frac{g_2}{g_1} e^{-\Delta E/kT} \quad (3.1)$$

Here, ΔE is the energy difference between the two excited states, k is the Boltzmann constant and N_i is the population of state i. Emission intensities scale linearly with the population of an emitting state. This results in a temperature dependence of the luminescence intensity ratio,

$$\frac{I_2}{I_1} = \frac{A_2 h \nu_2 N_2}{A_1 h \nu_1 N_1} = C e^{-\Delta E/kT} \quad (3.2)$$

Here, I_i, g_i, A_i and ν_i are the (integrated) emission intensity, the degeneracy of the emitting level, the spontaneous emission rate and the frequency of the transition from state i to a lower lying state, respectively. For Er³⁺ in NaYF₄ NCs, the energy difference between the

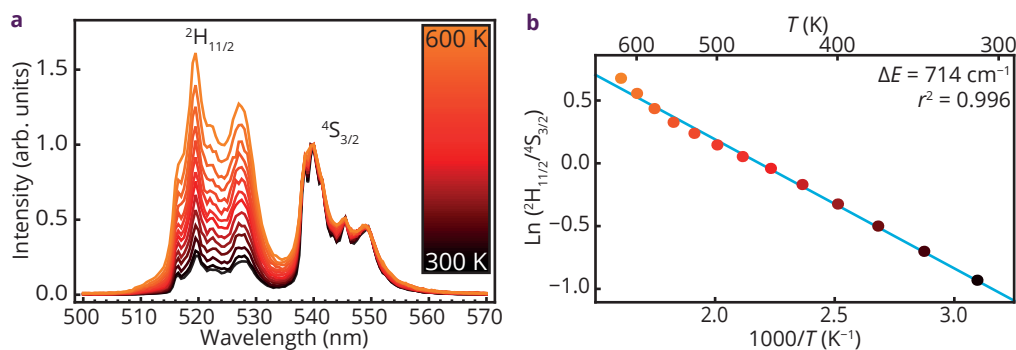


Figure 3.4 – Temperature-dependent luminescence properties of NaYF₄ NCs. Emission spectra of NaYF₄ NCs upon excitation at 980 nm for temperatures ranging from 300–600 K recorded with steps of 25 K (a). The linear relation between the natural logarithm of the integrated intensity ratio of the ²H_{11/2} and ⁴S_{3/2} peak vs. 1/T (b). The r-squared value for the fit, 0.996, is close to unity and the steepness of the fit corresponds to a ΔE of 714 cm⁻¹. Five spectra were measured at every temperature interval to estimate the error in the measurements; this error is within the dot size of the data points.

²H_{11/2} and ⁴S_{3/2} excited states is 711 cm⁻¹, as calculated from the spectrum in Figure 3.3a using the equation:

$$\bar{\lambda} = \frac{\sum \lambda_i I_i}{\sum I_i}. \quad (3.3)$$

To investigate the NCs as temperature probes, temperature-dependent luminescence measurements were performed on powders of NCs at temperatures ranging from 300–600 K with intervals of 25 K. Each temperature interval consisted of 1 minute of heating, followed by a dwell time of at least 15 minutes before measuring spectra to ensure that the sample temperature was the same as that recorded by the thermocouple in the heating stage. Furthermore, the thermocouple allows for monitoring and compensation of heating effects due to the laser heating.

Figure 3.4a shows spectra, recorded from 300 K (black) up to 600 K (orange). The spectra are normalized to the maximum intensity of the ⁴S_{3/2}–⁴I_{15/2} emission peak. Upon excitation at 980 nm, the characteristic luminescence peaks from the ²H_{11/2}–⁴I_{15/2} and the ⁴S_{3/2}–⁴I_{15/2} transitions can be observed at all temperatures. The energy difference between these peaks is calculated to be 710 cm⁻¹. The intensity ratio between these peaks changes with increasing temperature as expected for thermally coupled excited states.

To evaluate the temperature-dependent luminescence further, the natural logarithm of the integrated intensity ratio is plotted versus 1/T, as shown in Figure 3.4b. The data points can be fitted with a linear fit, as expected from equation 3.2. The quality of this fit is high, as shown by the r² value of 0.996. From the slope of the linear fit, the energy difference between the excited states, ΔE, is calculated to be 714 cm⁻¹ in these NCs. This calculated ΔE closely matches the experimental values of ΔE of 711 cm⁻¹ and 710 cm⁻¹ determined from Figure 3.3a and 3.4a, respectively.

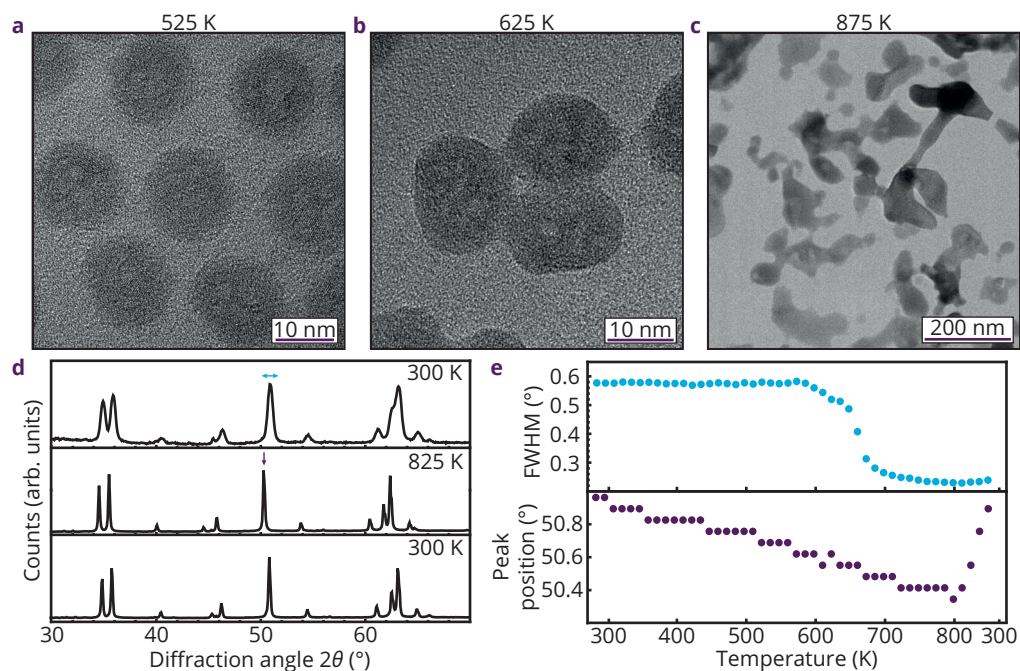


Figure 3.5 – In situ characterization of NaYF₄ NCs. In situ TEM micrographs of NaYF₄ NCs at 475 K, 625 K and 775 K (a, b and c respectively). In situ XRD diffractograms (d) of NaYF₄ NCs before heating, during heating and after heating to 825 K (top, middle and bottom, respectively) and the corresponding FWHM and peak position of the (201) diffraction peak at 51° vs. temperature (e).

Using the relation between temperature and luminescence intensity ratio of the ⁴S_{3/2} and the ²H_{11/2} peaks in Figure 3.4, it is evident that these NCs can be used as temperature probes from 300–600 K. At higher temperatures the overall luminescence intensity dropped and was too low to determine temperatures accurately. The intensity drop above 600 K is accompanied by a brown discoloration of the NC powders. The discoloration is most likely due to the oxidation of the organic ligands capping the NCs. Due to this decrease in luminescence intensity, the NCs cannot be used above 600 K for temperature sensing.

In situ structural characterization. In situ TEM and XRD measurements were performed in order to investigate the origin of the sudden drop in luminescence intensity above 600 K. TEM micrographs were taken in situ while heating the NCs, which were dropcasted on a special TEM heating chip, with intervals of 50 K up to 875 K. XRD measurements, taking ca. 12 min for one XRD pattern, were performed continuously, while heating the sample to 825 K in 9 h and afterward cooling down in 45 min.

Figure 3.5 shows the resulting TEM images of core NCs at 475 K, 625 K and 775 K (a–c, respectively). Figure 3.5d shows three diffractograms taken before heating, during heating and after heating (top, middle and bottom, respectively). The FWHM and peak position of the (201) diffraction peak at 51° were extracted from all diffractograms and plotted versus temperature as shown in Figure 3.5e (top and bottom, respectively).

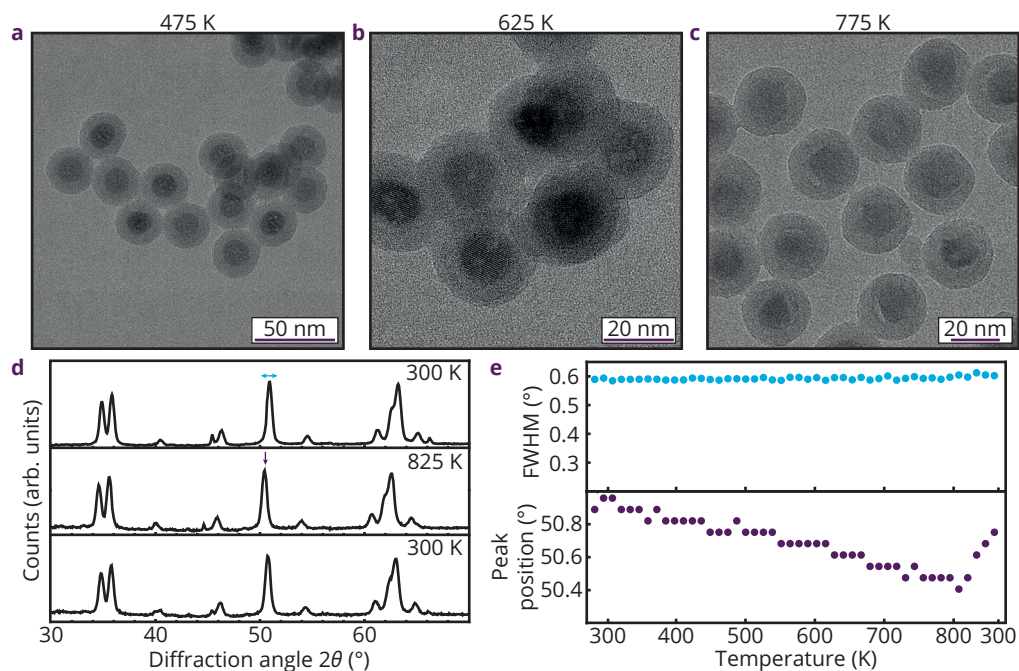


Figure 3.6 - In situ characterization of $\text{NaYF}_4@SiO_2$ NCs. In situ TEM micrographs of $\text{NaYF}_4@SiO_2$ NCs at 525 K, 625 K and 875 K (a, b and c, respectively). In situ XRD diffractograms (d) of $\text{NaYF}_4@SiO_2$ NCs before heating, during heating and after heating to 825 K (top, middle and bottom, respectively) and the corresponding FWHM and peak position of the diffraction peak at 51° vs. temperature (e).

Up to 575 K individual NCs can be observed in the TEM images. However, upon further heating, particles start to coalesce and subsequently melt together completely, forming large clusters of material. The temperature at which the coalescence starts, i.e. 625 K, matches the temperature at which the decrease in luminescence starts to occur. The XRD diffractograms show the characteristic peaks of hexagonal NaYF_4 shifting slightly upon heating due to thermal expansion of the crystal lattice. No phase transitions are observed, which is in accordance with investigations of Mathews and coworkers.³⁹ However, the diffraction peaks become irreversibly sharper around 625 K. The FWHM decreases from 0.6° to 0.2° , corresponding to an increase in crystallite size. To summarize, the results show that the NCs coalesce, starting at temperatures around 625 K.

The temperature at which the luminescence intensity decreases dramatically, corresponds to the temperature at which the NCs start to coalesce as confirmed with TEM and XRD. It is likely that the atomic alignment of the NCs during coalescence/sintering is imperfect, resulting in the introduction of defects in the crystals. These defects can act as quenching sites for luminescence and therefore explain the sudden decrease in luminescence intensity in addition to the ligand oxidation discussed above.

The same in situ measurements were performed on the $\text{NaYF}_4@SiO_2$ NCs as shown in Figure 3.6. In contrast to the NaYF_4 NCs, the $\text{NaYF}_4@SiO_2$ NCs remain well separated on

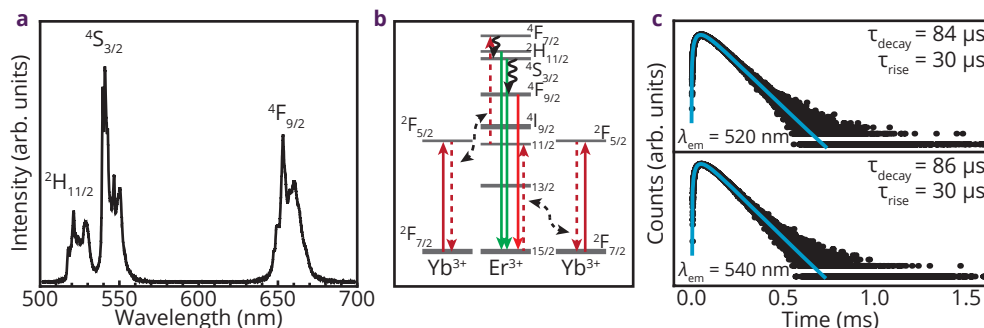


Figure 3.7 – Luminescence properties of NaYF₄@SiO₂ NCs. Emission spectrum of prepared NaYF₄@SiO₂ NCs between 500 nm and 700 nm while exciting Yb³⁺ at 980 nm (a) The energy diagram of Er³⁺ (b). The time-resolved luminescence measurements of the corresponding ²H_{11/2} and ⁴S_{3/2} excited states upon excitation at 980 nm (c).

the TEM images for all temperatures showing that no interparticle alloying or intraparticle coalescence occurs. The FWHM of the (201) diffraction peak at 51° is constant during the entire thermal cycle, suggesting that the crystallite size remains unaltered. The overgrowth with silica, resulting in the core/shell architecture, ensures that the NCs are thermally stable up to 875 K and show no luminescence quenching up to at least 900 K.

(Temperature-dependent) photoluminescence of NaYF₄@SiO₂ nanocrystals. To improve the temperature stability and thus extend the temperature range for nanothermometry, the NaYF₄ NCs were coated with a protective silica shell. The SiO₂ shell replaces the organic ligands and can prevent luminescence quenching due to oxidation of ligands and NCs coalescence. To investigate if the silica overgrowth has an effect on the luminescence properties of the NC cores, (time-resolved) room temperature luminescence measurements were performed similar to those shown in Figure 3.3. The results, included in Figure 3.7, reveal that the emission spectra are nearly identical except for a small increase in the relative intensity of the ⁴F_{9/2}–⁴I_{15/2} emission. Also the decay time of the ⁴S_{3/2} and ²H_{11/2} excited states are slightly shorter (85 μs after silica overgrowth vs. 100 μs before). The shortening of the lifetime suggests that non-radiative relaxation to lower lying ⁴F_{9/2} states has increased, which is consistent with the observed increase in relative intensity of the ⁴F_{9/2}–⁴I_{15/2} emission. The increase of non-radiative relaxation can be explained by the presence of hydroxyl groups in the silica shell.^{40,41} These hydroxyl groups are present because of incomplete condensation of neighboring silanol groups, Si–OH. These silanol groups condense to form typical Si–O–Si bonds in silica. The high energy O–H vibration (ca. 3500 cm⁻¹) gives rise to faster multiphonon relaxation.

Although the additional O–H vibrations gives rise to faster decay times as a result of multi-phonon relaxation, the energy levels of Er³⁺ remain unaltered due to the shielding of the f-orbitals. The unaltered energy levels dictate that the energy difference, ΔE, between the ²H_{11/2} and ⁴S_{3/2} state, and therefore the temperature-dependent luminescence, is not expected to change which is in agreement with the experimental results.

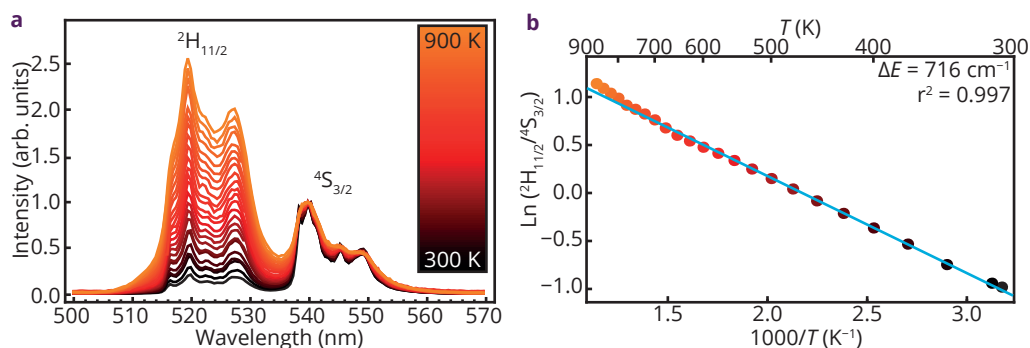


Figure 3.8 – Temperature-dependent luminescence properties of $\text{NaYF}_4@ \text{SiO}_2$ NCs. Emission spectra of $\text{NaYF}_4@ \text{SiO}_2$ NCs upon excitation at 980 nm taken at temperatures ranging from 300–900 K with steps of 25 K (a). The linear relation between natural logarithm of the integrated intensity ratio of the ${}^2\text{H}_{11/2}$ and ${}^4\text{S}_{3/2}$ peak is plotted vs. $1000/T$ (b). The r-squared value for the fit, 0.997, is close to unity and the steepness of the fit corresponds to a ΔE of 716 cm^{-1} . Five spectra were measured at every temperature interval to estimate the error in the measurements; this error is within the dot size of the data points.

In order to investigate the temperature-dependent luminescence properties of the silica coated NCs, emission spectra were measured at different temperatures under 980 nm excitation. Figure 3.8a shows the spectra taken from 300 K (black) up to 900 K (orange), normalized to the maximum intensity of the ${}^4\text{S}_{3/2}-{}^4\text{I}_{15/2}$ emission peak. The characteristic luminescence peaks from the ${}^2\text{H}_{11/2}-{}^4\text{I}_{15/2}$ and the ${}^4\text{S}_{3/2}-{}^4\text{I}_{15/2}$ transitions can be observed up to 900 K!

There is a small decrease in intensity but clearly the temperature stability of the emission is strongly improved in comparison to the NaYF_4 cores. At the temperature limit of our experimental set-up (900 K), the emission spectra are still well-resolved, suggesting that significantly higher temperatures can be probed. The emission intensity and signal-to-noise ratio hardly change between room temperature and 900 K. As can be observed in Figure 3.8a the signal-to-noise ratio remains high up to the highest temperatures. The temperature limit of 900 K is solely set by the limitations of our instrumentation.

To calibrate the silica coated NCs as a temperature probe, the natural logarithm of the integrated intensity ratio is plotted versus $1/T$ as shown in Figure 3.8b. The data points can be fitted with a linear fit, similar to Figure 3.4b.

The quality of the fit is high, as shown by the r-squared value of 0.997. From the slope of the linear fit, the energy difference between the excited states, ΔE , can be calculated to be 716 cm^{-1} and closely matches the experimental value of ΔE determined from the spectra and from the temperature-dependent emission spectra of the NaYF_4 core particles. The results show that the maximum temperature range of the core particles can be expanded up to at least 900 K by applying a protective silica shell. The linear fit shows good agreement with the data points over the full temperature range.

Thermal cycling experiment. In addition to having a high thermal stability and temperature accuracy, it is important that a temperature sensor can survive multiple thermal cycles

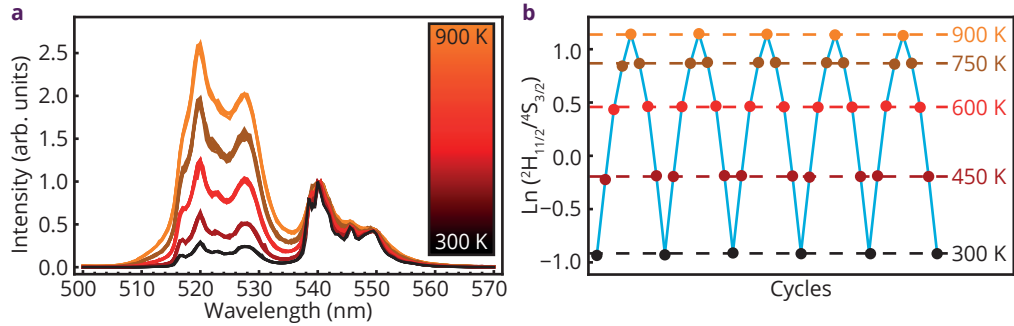


Figure 3.9 – Temperature cycling experiment of NaYF₄@SiO₂ NCs. Emission spectra of NaYF₄@SiO₂ upon excitation at 980 nm while cycling the temperature between 300 K, 450 K, 600 K, 750 K and 900 K for 5 times (a). The natural logarithm of the fluorescence intensity ratio plotted per cycle step (colored dots). The cyan line is for directing the eyes and the dashed lines are the means of the data points per temperature (b).

without change in properties. To investigate the durability of the NaYF₄@SiO₂ NCs, the temperature probes were cycled between 300 K and 900 K five times. During the heating up and cooling down in each cycle luminescence measurements were performed at 300 K, 450 K, 600 K, 750 K and 900 K.

Figure 3.9a shows the spectra taken at five different temperatures during the cycle experiment, normalized to the ⁴S_{3/2}–⁴I_{15/2} emission peak. The spectra at a specific temperature are very similar. At each temperature the intensity ratio of the two emission peaks was determined and plotted in Figure 3.9b. The data points follow identical trends during the five cycles (cyan line). The average fluorescence intensity ratios for each temperature were calculated from the data (dashed lines). The data points only have small deviations from the average. The thermal cycling experiment shows that the temperature probes are stable and durable up to 900 K.

The standard deviations in temperature are calculated to be 1.1 K, 1.8 K, 2.9 K, 5.2 K and 5.3 K for 300 K, 450 K, 600 K, 750 K and 900 K, respectively. These values are high compared to the very accurate temperature probes used for bio-imaging (< 0.5 K¹⁵). Temperature accuracies down to 0.2 or 0.3 K have been reported for the Yb/Er and Yb/Tm couple in the biologically interesting temperature window.^{46–49} The smaller standard deviations for temperature measurements in bio-imaging are expected based on the smaller temperature range. The probes used are optimized for this temperature range such that the change in intensity ratio with temperature is large.

In the case of FIRT, also the sensitivity S and relative sensitivity of a temperature probe are often used as a quality measure of the performance as a temperature sensor. S is defined as the change of the intensity ratio R with temperature,

$$S = \frac{dR}{dT}. \quad (3.4)$$

The relative sensitivity is defined as S/R (in % K⁻¹). For a large temperature range, the

change in the intensity ratio with temperature varies with temperature and thus the relative sensitivity will be different in different temperature regimes. For the $\text{NaYF}_4:\text{Er}^{3+},\text{Yb}^{3+}$ nanoparticles in the 300 to 900 K temperature range the sensitivity, calculated using equation 3.2 and 3.4 (with $C = 9.4$), shows that the relative sensitivity decreases from $1.02\% \text{ K}^{-1}$ at 300 K to $0.13\% \text{ K}^{-1}$ at 900 K. The $1.02\% \text{ K}^{-1}$ sensitivity is consistent with values typically found around 300 K for Er^{3+} (between 0.5 and $1.5\% \text{ K}^{-1}$).⁵⁰ The variation in relative sensitivity with temperature is inherent to using temperature probes in a wide range. The sensitivity of a temperature probe cannot be optimized for the full temperature window. Most applications which require a broader temperature sensing range do not require a sensitivity of 0.5 K. However, care should be taken that the error in the temperature measurement does not become too large. In our case a measurement error of ca. 5 K at 900 K is sufficient for most applications.

The present results demonstrate for the first time the use of ca. 50 nm NCs for high temperature nanothermometry using a silica coating to stabilize the NCs. Silica-stabilized NCs of other host materials (e.g. oxides) and also other Ln^{3+} dopants with a different ΔE between levels can be developed to realize other high temperature nanoprobe with potentially higher sensitivity in the high temperature range.⁵¹

Conclusions

We have reported $\text{NaYF}_4:\text{Er}^{3+},\text{Yb}^{3+}$ nanocrystals coated with a SiO_2 shell as stable nanoprobe for high temperature nanothermometry, up to 900 K. The temperature-dependent intensity ratio of emission from the ${}^2\text{H}_{11/2}$ level (520 nm) and the ${}^4\text{S}_{3/2}$ level (545 nm) follows a Boltzmann distribution. From the intensity ratio temperatures can be measured accurately (1 to 5 K accuracy) using remote sensing techniques. The temperature stability of the probes is confirmed by in situ TEM and XRD. The temperature-dependent luminescence remains unaltered in multiple cycling experiments between 300 K and 900 K. Based on these observations, the $\text{NaYF}_4:\text{Er}^{3+},\text{Yb}^{3+}$ nanoprobe provide a non-invasive temperature probe that is dispersible in liquids and has a broad range for temperature sensing. It can therefore be used for high resolution temperature sensing in a wide range of applications, including chemical reactors and nano-electronics. The reported method of strongly improving the thermal stability of nanoprobe by silica coating can be generally applied to enhance the performance of other nanoprobe.

Experimental Section

Chemicals. All chemicals were used without further purification. The following chemicals were purchased from Sigma-Aldrich: Cyclohexane (99.5 %, CH), oleic acid (90 %, OA), ethanol (>99.8 %, EtOH), methanol (>99.85 %, MeOH), sodium hydroxide (>97 %, NaOH), ammonium fluoride (>98 %, NH_4F), ammonium hydroxide (28 wt% in H_2O , ammonia) lanthanide acetate hydrates (99.9 %, $\text{Ln}(\text{Ac})_3$), tetraethyl orthosilicate (99.999 %, TEOS) and IGEPAL CO-520 ($(\text{C}_2\text{H}_4\text{O})_n \cdot \text{C}_{15}\text{H}_{24}\text{O}$ with $n \sim 5$, average Mn = 441 g mol^{-1} , NP-5). 1-octadecene (90 %, ODE) was purchased from Acros Organics.

Synthesis of NaYF₄ nanocrystals. The NaYF₄:Er³⁺,Yb³⁺ NCs are prepared via a coprecipitation method based on the work of Li and Zhang⁴⁷ with some adjustments based on the work of Wang and coworkers.⁴⁸ Furthermore, we have improved the protocol to obtain a higher fraction of ligands on the NP surface in order to increase the colloidal stability. This enhancement in colloidal stability is required for the shell growth with silica as explained below.

The synthesis of NaYF₄ NCs is performed in two steps—nucleation and growth. During the nucleation phase the reaction mixture is kept at room temperature to prevent the production of hazardous byproducts e.g. gaseous HF. These byproducts are formed at elevated temperatures due to the low decomposition temperature of the fluoride precursor, NH₄F. Once all the fluoride precursor has been used to prepare small nuclei of cubic NaYF₄, the temperature is increased and growth is initiated. The small nuclei are unstable at elevated temperatures and larger hexagonal NaYF₄ crystals are formed via Ostwald ripening-like growth,⁴⁹ resulting in the desired NCs.

The synthesis is performed in a Schlenk line to work under N₂ atmosphere and vacuum. During the reaction the reactants are stirred vigorously. First, 0.5 mmol of Ln(Ac)₃, with an Y:Yb:Er ratio of 80:18:2, is added to a mixture of 3 mL OA and 8.5 mL ODE. The resulting white, turbid dispersion is then degassed at 120 °C under vacuum for 90 min, to give a clear, slightly yellowish solution. Afterwards, the reaction mixture is flushed three times with vacuum and N₂ before cooling down to room temperature. This flushing is performed to remove any residual oxygen or water. Second, a mixture of NaOH and NH₄F in MeOH is prepared and added to the reaction mixture. These Na and F precursors are prepared by dissolving 1.25 mmol NaOH and 2 mmol NH₄F in 1.25 mL and 3.75 mL MeOH, respectively. The precursors are mixed just before the addition to the reaction mixture. This addition was done quickly to suppress the formation of unwanted NaF in the mixed precursor solution. The resulting white, turbid reaction mixture is subsequently stirred for ca. 16 h to form small (sub-10 nm) cubic NaYF₄ NCs.

Before the growth step is initiated, the excess MeOH is removed. This is done by heating the sample to 100 °C under vacuum for 30 min. Afterwards, the mixture is flushed with vacuum and N₂—as described above—before further heating the reaction mixture to 300 °C for 110 min, resulting in larger hexagonal NCs. Although the reaction mixture is flushed throughout the synthesis extensively, there are always trace amounts of oxygen left in the reaction mixture. Consequently, a small fraction of the organic materials present in the reaction mixture can be oxidized, resulting in a light brown discoloration of the clear solution. After cooling down to room temperature, the reaction mixture becomes slightly turbid.

After the synthesis, the reaction mixture is washed to remove excess reagents and solvents. This is done by adding 1 equivalent of EtOH, centrifuging with a relative centrifugal force (RCF) of 840 for 8 min and removing the supernatant. The resulting sediment is redispersed in 5 mL CH. This washing step is repeated two more times to obtain a dispersion of NCs

in 5 mL CH.

In the last step of the synthesis the ligand density is increased in order to enhance the colloidal stability of the NCs for the subsequent silica growth. This is done by adding 5 mL of OA and sonication for 15 min, resulting in a turbid dispersion. Afterwards 10 mL of EtOH is added and the dispersion is centrifuged at 840 rcf for 8 min. Finally, the sediment is redispersed in 5 mL CH to obtain a slightly yellowish dispersion.

Synthesis of NaYF₄@SiO₂ nanocrystals. A micro-emulsion method optimized in our group⁵⁰ is used to grow an inert SiO₂ layer around the NCs. In short, ca. 10 mg of NCs dispersed in CH is added to a mixture of 3 mmol NP-5 in 12 mL CH. Subsequently, 80 μ L of TEOS and 150 μ L of ammonia is added to the mixture, while stirring for at least 15 min between injections to ensure sample homogeneity. After the last addition, the sample is stirred for 1 min and kept for ca. 24 h to allow for the silica growth.

After the synthesis, excess precursors, apolar solvents and surfactants are removed. This is done by addition of 3 mL EtOH to break up the micelles and afterwards centrifuging at 15000 rcf. The supernatant is removed and the sediment is redispersed in 10 mL EtOH. The dispersion is centrifuged and the sediment is washed two more times with EtOH to obtain a slightly turbid dispersion of NaYF₄@SiO₂ NCs in EtOH.

Setups. Transmission electron microscopy (TEM) characterization was performed using a FEI Tecnai20F and a FEI Talos F200X (in combination with a heating holder from DENSSolutions) both operating at 200 kV for ex situ and in situ measurements, respectively. At least 100 NCs were used to determine the average diameter of the NCs in a sample and the standard deviation in the size distribution. Energy dispersive X-ray spectroscopy (EDX) measurements were performed using an ultrathin window EDAX-detector and subsequently analyzed using Tecnai Imaging and Analysis software.

Ex situ Powder X-ray diffraction (XRD) measurements were performed on a Bruker D2Phaser using Co K α radiation with a wavelength of 1.79 Å. In situ XRD measurements were performed on a Bruker-AXS D8 in combination with an X-ray reactor chamber of Anton Paar for temperature control using Co K α radiation with a wavelength of 1.79 Å.

Emission spectra and photoluminescence (PL) decay curves were recorded using an Edinburgh Instruments FLS920 spectrofluorometer equipped with a 450W xenon lamp and a Hamamatsu R928 photomultiplier tube. For upconversion emission spectra, a 980 nm 2W continuous wave laser was used for excitation in the ²F_{5/2} level of Yb³⁺. For PL decay measurements an optical parametric oscillator system, Opotek He 355 II, was used, with a pulse width of 10 ns, a repetition rate of 20 Hz and pulse energy of ca. 3 mJ. To control the temperature during luminescence measurements, a Linkam THMS600 Microscope Stage was used.

Acknowledgements

The authors acknowledge the assistance of J. Meeldijk and M. Versluijs-Helder, both from Utrecht University, with TEM and XRD measurements, respectively.

This work was supported by the Netherlands Center for Multiscale Catalytic Energy Conversion (MCEC), an NWO Gravitation programme funded by the Ministry of Education, Culture and Science of the government of the Netherlands. The authors acknowledge financial support from the European Research Council under the European Unions Seventh Framework Programme (FP-2007-2013)/ERC Advanced Grant Agreement 291667 HierarSACol.

References

- Kim, T.-H.; Cho, K.-S.; Lee, E. K.; Lee, S. J.; Chae, J.; Kim, J. W.; Kim, D. H.; Kwon, J.-Y.; Amaratunga, G.; Lee, S. Y.; Choi, B. L.; Kuk, Y.; Kim, J. M. & Kim, K. Full-Colour Quantum Dot Displays Fabricated by Transfer Printing. *Nat. Photonics* **2011**, *5*, 176–182.
- Jang, E.; Jun, S.; Jang, H.; Lim, J.; Kim, B. & Kim, Y. White-Light-Emitting Diodes with Quantum Dot Color Converters for Display Backlights. *Adv. Mater.* **2010**, *22*, 3076–3080.
- Lim, S. F.; Riehn, R.; Ryu, W. S.; Khanarian, N.; Tung, C.-K.; Tank, D. & Austin, R. H. In Vivo and Scanning Electron Microscopy Imaging of Upconverting Nanophosphors in *Caenorhabditis elegans*. *Nano Lett.* **2006**, *6*, 169–174.
- Zrazhevskiy, P.; Sena, M. & Gao, X. Designing Multifunctional Quantum Dots for Bioimaging, Detection, and Drug Delivery. *Chem. Soc. Rev.* **2010**, *39*, 4326–4354.
- van der Ende, B. M.; Aarts, L. & Meijerink, A. Lanthanide Ions as Spectral Converters for Solar Cells. *Phys. Chem. Chem. Phys.* **2009**, *11*, 11081–11095.
- Chuang, C.-H. M.; Brown, P. R.; Bulović, V. & Bawendi, M. G. Improved Performance and Stability in Quantum Dot Solar Cells through Band Alignment Engineering. *Nat. Mater.* **2014**, *13*, 796–801.
- Zhang, Y.; Tang, Z.-R.; Fu, X. & Xu, Y.-J. TiO₂-Graphene Nanocomposites for Gas-Phase Photocatalytic Degradation of Volatile Aromatic Pollutant: Is TiO₂-Graphene Truly Different from Other TiO₂-Carbon Composite Materials? *ACS Nano* **2010**, *4*, 7303–7314.
- Bezemer, G. L.; Bitter, J. H.; Kuipers, H. P. C. E.; Oosterbeek, H.; Holewijn, J. E.; Xu, X.; Kapteijn, F.; Van Dillen, A. J. & de Jong, K. P. Cobalt Particle Size Effects in the Fischer-Tropsch Reaction Studied with Carbon Nanofiber Supported Catalysts. *J. Am. Chem. Soc.* **2006**, *128*, 3956–3964.
- Mecklenburg, M.; Hubbard, W. A.; White, E. R.; Dhall, R.; Cronin, S. B.; Aloni, S. & Regan, B. C. Nanoscale Temperature Mapping in Operating Microelectronic Devices. *Science* **2015**, *347*, 629–633.
- Kim, K.; Chung, J.; Hwang, G.; Kwon, O. & Lee, J. S. Quantitative Measurement with Scanning Thermal Microscope by Preventing the Distortion due to the Heat Transfer through the Air. *ACS Nano* **2011**, *5*, 8700–8709.
- Smith, J. D.; Cappa, C. D.; Drisdell, W. S.; Cohen, R. C. & Saykally, R. J. Raman Thermometry Measurements of Free Evaporation from Liquid Water Droplets. *J. Am. Chem. Soc.* **2006**, *128*, 12892–12898.
- Quintanilla, M.; Cantelar, E.; Cussó, F.; Villegas, M. & Caballero, A. C. Temperature Sensing with Upconverting Submicron-Sized LiNbO₃:Er³⁺/Yb³⁺ Particles. *Appl. Phys. Express* **2011**, *4*, 022601.
- Brites, C. D. S.; Lima, P. P.; Silva, N. J. O.; Millán, A.; Amaral, V. S.; Palacio, F. & Carlos, L. D. Thermometry at the Nanoscale. *Nanoscale* **2012**, *4*, 4799–4829.

14. Jaque, D. & Vetrone, F. Luminescence Nanothermometry. *Nanoscale* **2012**, *4*, 4301–4326.
15. Gota, C.; Okabe, K.; Funatsu, T.; Harada, Y. & Uchiyama, S. Hydrophilic Fluorescent Nanogel Thermometer for Intracellular Thermometry. *J. Am. Chem. Soc.* **2009**, *131*, 2766–2767.
16. Yang, J. M.; Yang, H. & Lin, L. Quantum Dot Nano Thermometers Reveal Heterogeneous Local Thermogenesis in Living Cells. *ACS Nano* **2011**, *5*, 5067–5071.
17. Vetrone, F.; Naccache, R.; Zamarrón, A.; Juarranz de la Fuente, A.; Sanz-Rodríguez, F.; Martínez Maestro, L.; Martín Rodríguez, E.; Jaque, D.; García Solé, J. & Capobianco, J. A. Temperature Sensing Using Fluorescent Nanothermometers. *ACS Nano* **2010**, *4*, 3254–3258.
18. Bar-Cohen, A. & Wang, P. On-chip Hot Spot Remediation with Miniaturized Thermoelectric Coolers. *Microgravity Sci. Technol.* **2009**, *21*, 351–359.
19. Aigouy, L.; Tessier, G.; Mortier, M. & Charlot, B. Scanning Thermal Imaging of Microelectronic Circuits with a Fluorescent Nanoprobe. *Appl. Phys. Lett.* **2005**, *87*, 1–3.
20. Jundt, D. H. Temperature-Dependent Sellmeier Equation for the Index of Refraction, n_o , in Congruent Lithium Niobate. *Opt. Lett.* **1997**, *22*, 1553–1555.
21. Romero, J. J.; Arago, C.; Gonzalo, J. A.; Jaque, D. & Sole, J. G. Spectral and Thermal Properties of Quasiphase-Matching Second-Harmonic-Generation in $\text{Nd}^{3+}:\text{Sr}_{0.6}\text{Ba}_{0.4}(\text{NbO}_3)_2$ Multiself-Frequency-Converter Non-linear Crystals. *J. Appl. Phys.* **2003**, *93*, 3111–3113.
22. Feuerstein, A.; Knapp, J.; Taylor, T.; Ashary, A.; Bol-cavage, A. & Hitchman, N. Technical and Economical Aspects of Current Thermal Barrier Coating Systems for Gas Turbine Engines by Thermal Spray and EBPVD: A Review. *J. Therm. Spray Technol.* **2008**, *17*, 199–213.
23. Vaßen, R.; Jarligo, M. O.; Steinke, T.; Mack, D. E. & Stöver, D. Overview on Advanced Thermal Barrier Coatings. *Surf. Coat. Technol.* **2010**, *205*, 938–942.
24. Toebes, M.; Prinsloo, F. F.; Bitter, J. H.; van Dillen, A. J. & de Jong, K. P. Influence of Oxygen-Containing Surface Groups on the Activity and Selectivity of Carbon Nanofiber-Supported Ruthenium Catalysts in the Hydrogenation of Cinnamaldehyde. *J. Catal.* **2003**, *214*, 78–87.
25. Borodina, E.; Meirer, F.; Lezcano-Gonzalez, I.; Mokhtar, M.; Asiri, A. M.; Al-Thabaiti, S. A.; Basahel, S. N.; Ruiz-Martínez, J. & Weckhuysen, B. M. Influence of the Reaction Temperature on the Nature of the Active and Deactivating Species during Methanol-to-Olefins Conversion over H-SSZ-13. *ACS Catal.* **2015**, *5*, 992–1003.
26. Peng, H. S.; Huang, S. H. & Wolfbeis, O. S. Ratiometric Fluorescent Nanoparticles for Sensing Temperature. *J. Nanopart. Res.* **2010**, *12*, 2729–2733.
27. Cui, Y.; Xu, H.; Yue, Y.; Guo, Z.; Yu, J.; Chen, Z.; Gao, J.; Yang, Y.; Qian, G. & Chen, B. A Luminescent Mixed-Lanthanide Metal-Organic Framework Thermometer. *J. Am. Chem. Soc.* **2012**, *134*, 3979–3982.
28. Rai, V. K.; Rai, D. & Rai, S. Pr^{3+} Doped Lithium Tellurite Glass as a Temperature Sensor. *Sens. Actuators, A* **2006**, *128*, 14–17.
29. Pandey, A. & Rai, V. K. Optical Thermometry using FIR of Two Close Lying Levels of Different Ions in $\text{Y}_2\text{O}_3:\text{Ho}^{3+}-\text{Tm}^{3+}-\text{Yb}^{3+}$ phosphor. *Appl. Phys. B: Lasers Opt.* **2013**, *113*, 221–225.
30. Blasse, G. & Grabmaier, B. *Luminescent Materials*, Springer, Berlin, **1994**.
31. Tripathi, G.; Rai, V. K. & Rai, S. Optical Properties of $\text{Sm}^{3+}:\text{CaO}-\text{Li}_2\text{O}-\text{B}_2\text{O}_3-\text{BaO}$ Glass and Codoped $\text{Sm}^{3+}:\text{Eu}^{3+}$. *Appl. Phys. B: Lasers Opt.* **2006**, *84*, 459–464.

32. Haro-González, P.; Martín, I.; Martín, L.; León-Luis, S. F.; Pérez-Rodríguez, C. & Lavín, V. Characterization of Er³⁺ and Nd³⁺ Doped Strontium Barium Niobate Glass Ceramic as Temperature Sensors. *Opt. Mater.* **2011**, *33*, 742–745.
33. Singh, S. K.; Kumar, K. & Rai, S. Er³⁺/Yb³⁺ Codoped Gd₂O₃ Nano-Phosphor for Optical Thermometry. *Sens. Actuators, A* **2009**, *149*, 16–20.
34. Cao, B.; He, Y.; Feng, Z.; Li, Y. & Dong, B. Optical Temperature Sensing Behavior of Enhanced Green Upconversion Emissions from Er-Mo:Yb₂Ti₂O₇ Nanophosphor. *Sens. Actuators, B* **2011**, *159*, 8–11.
35. Li, D.; Wang, Y.; Zhang, X.; Yang, K.; Liu, L. & Song, Y. Optical Temperature Sensor Through Infrared Excited Blue Upconversion Emission in Tm³⁺/Yb³⁺ Codoped Y₂O₃. *Opt. Commun.* **2012**, *285*, 1925–1928.
36. Padture, N. P.; Gell, M. & Jordan, E. H. Thermal Barrier Coatings for Gas-Turbine Engine Applications. *Science* **2002**, *296*, 280–284.
37. Scherrer, P. Bestimmung der Größe und der Inneren Struktur von Kolloidteilchen mittels Röntgenstrahlen. *Nachr. Ges. Wiss. Goettingen* **1918**, *1918*, 98–100.
38. Suyver, J. F.; Grimm, J.; Van Veen, M. K.; Biner, D.; Krämer, K. W. & Güdel, H. U. Upconversion Spectroscopy and Properties of NaYF₄ Doped with Er³⁺, Tm³⁺ and/or Yb³⁺. *J. Lumin.* **2006**, *117*, 1–12.
39. Mathews, M.; Ambekar, B.; Tyagi, A. & Köhler, J. High Temperature X-ray Diffraction Studies on Sodium Yttrium Fluoride. *J. Alloys Compd.* **2004**, *377*, 162–166.
40. van Blaaderen, A. & Kentgens, A. Particle Morphology and Chemical Microstructure of Colloidal Silica Spheres Made from Alkoxysilanes. *J. Non-Cryst. Solids* **1992**, *149*, 161–178.
41. Zhang, L.; D’Acunzi, M.; Kappl, M.; Imhof, A.; van Blaaderen, A.; Butt, H.-J.; Graf, R. & Vollmer, D. Tuning the Mechanical Properties of Silica Microcapsules. *Phys. Chem. Chem. Phys.* **2010**, *12*, 15392–15398.
42. dos Santos, P. V.; de Araujo, M. T.; Gouveia-Neto, A. S.; Neto, J. A. M. & Sombra, S. B. Optical Thermometry Through Infrared Excited Upconversion Fluorescence Emission in Er³⁺ and Er³⁺-Yb³⁺-doped Chalcogenide Glasses. *J. Quantum Electron.* **1999**, *35*, 395–399
43. Li, C. R.; Dong, B.; Ming, C. G. & Lei, M. Application to Temperature Sensor Based on Green Upconversion of Er³⁺ Doped Silicate Glass. *Sensors* **2007**, *7*, 2652–2659.
44. Dong, N.-N.; Pedroni, M.; Piccinelli, F.; Conti, G.; Sbarbati, A.; Ramírez-Hernandez, J. E.; Maestro, L. M.; Iglesias-de la Cruz, M. C.; Sanz-Rodríguez, F.; Juarranz, A.; Chen, F.; Vetrone, F.; Capobianco, J. A.; Sole, J. G.; Bettinelli, M.; Jaque, D. & Speghini, A. NIR-to-NIR Two-Photon Excited CaF₂:Tm³⁺,Yb³⁺ Nanoparticles: Multifunctional Nanoprobes for Highly Penetrating Fluorescence Bio-Imaging. *ACS Nano* **2011**, *5*, 8665–8671
45. Li, C. R.; Dong, B.; Li, S. F. & Song, C. Er³⁺-Yb³⁺ Co-Doped Silicate Glass for Optical Temperature Sensor. *Chem. Phys. Lett.* **2007**, *443*, 426–429
46. Debasu, M. L.; Ananias, D.; Pastoriza-Santos, I.; Liz-Marzán, L. M.; Rocha J. & Carlos, L. D. All-In-One Optical Heater-Thermometer Nanoplatfrom Operative From 300 to 2000 K Based on Er³⁺ Emission and Blackbody Radiation. *Adv. Mater.*, **2013**, *25*, 4868–4874
47. Li, Z. & Zhang, Y. An Efficient and User-Friendly Method for the Synthesis of Hexagonal Phase NaYF₄:Er³⁺,Yb³⁺/Tm Nanocrystals with Controllable Shape and Upconversion Fluorescence. *Nanotechnology* **2008**, *19*, 345606.
48. Wang, F.; Deng, R. & Liu, X. Preparation of Core-Shell NaGdF₄ Nanoparticles Doped with Luminescent Lanthanide Ions to be Used as Upconversion-Based Probes. *Nat. Protoc.* **2014**, *9*, 1634–1644.

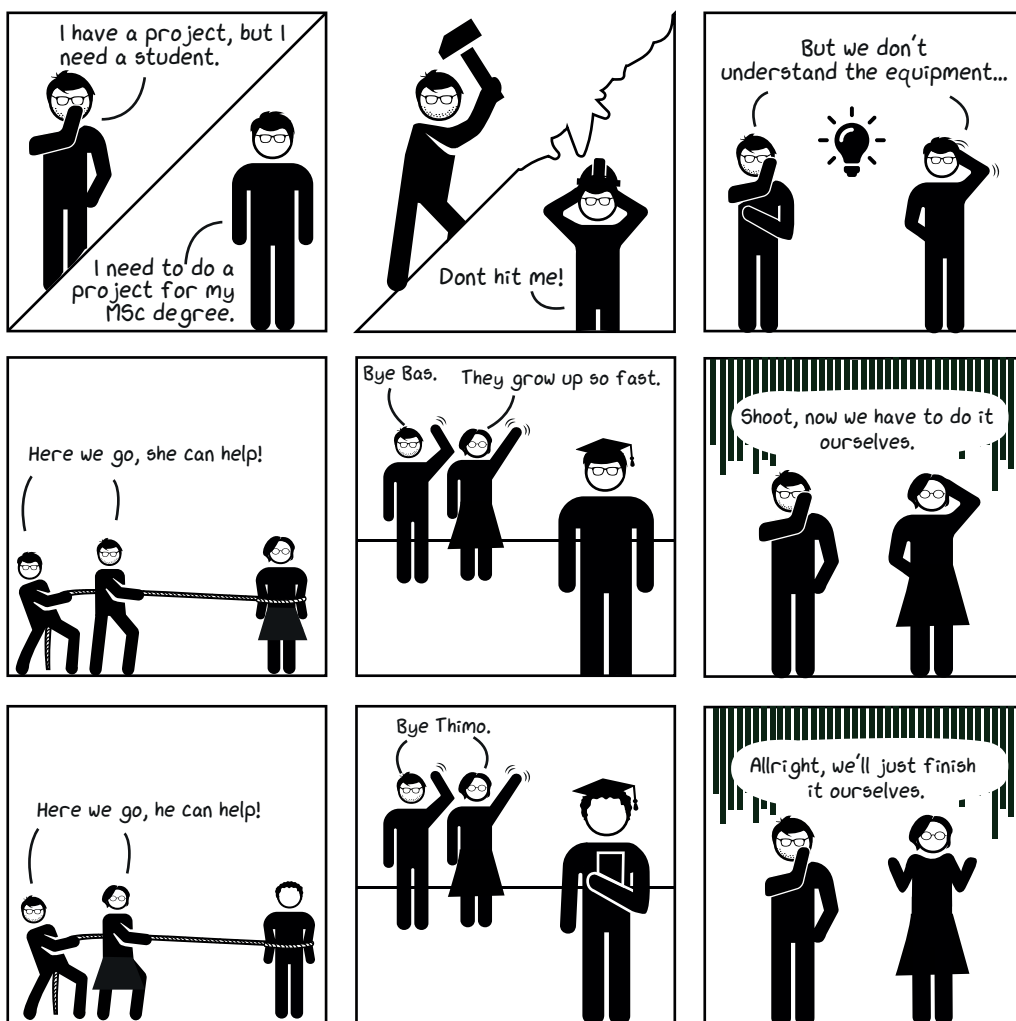
49. Rinkel, T.; Nordmann, J.; Raj, A. N. & Haase, M. Ostwald-Ripening and Particle Size Focussing of Sub-10 nm NaYF₄ Upconversion Nanocrystals. *Nanoscale* **2014**, *6*, 14523–14530.
50. Koole, R.; van Schooneveld, M. M.; Hilhorst, J.; de Mello Donegá, C.; 't Hart, D. C.; van Blaaderen, A.; Vanmaekelbergh, D. & Meijerink, A. On the Incorporation Mechanism of Hydrophobic Quantum Dots in Silica Spheres by a Reverse Microemulsion Method. *Chem. Mater.* **2008**, *20*, 2503–2512.
51. Dong, B.; Cao, B.; He, Y.; Liu, Z. & Feng, Z. Temperature Sensing and In Vivo Imaging by Molybdenum Sensitized Visible Upconversion Luminescence of Rare-Earth Oxides, *Adv. Mater.*, **2012**, *24*, 1987–1993



Based on

- Geitenbeck, R. G.; Nieuwelink, A.-E.; Jacobs, T. S.; Salzmann, B. B. V.; Goetze, J.; Meijerink, A. & Weckhuysen, B. M. In Situ Luminescence Thermometry To Locally Measure Temperature Gradients During Catalytic Reactions *ACS Catal.* **2018** *8*, 2397–2401.

Chapter 4 – In Situ Luminescence Thermometry To Locally Measure Temperature Gradients During Catalytic Reactions



Robin Geitenbeek



Anne-Eva Nieuwelink



Bas Salzmann



Thimo Jacobs

Abstract

Bandshape luminescence thermometry during in situ temperature measurements has been reported by preparing three catalytically relevant systems, which show temperature-dependent luminescence. One of these systems was further investigated as a showcase for application. Microcrystalline NaYF_4 doped with Er^{3+} and Yb^{3+} was mixed with a commercial zeolite H-ZSM-5 to investigate the Methanol-to-Hydrocarbons (MTH) reaction, while monitoring the reaction products with on-line gas chromatography. Due to the exothermic nature of the MTH reaction, a front of increased temperature migrating down the fixed reactor bed was visualized, showing the potential for various applications of luminescence thermometry for in situ measurements in catalytic systems.

Introduction

To optimize the activity, selectivity and stability of catalytic reactions, it is important to optimize parameters such as reaction temperature. However, interparticle heterogeneities and local gradients in the reactor due to exothermal or endothermal processes can result in lower or higher catalyst performances and even reactor runaways.¹ Although the local temperature profile is very important for catalytic performance in view of the Arrhenius equation, local temperature fluctuations are still difficult to analyze properly. To investigate the local temperature fluctuations, it is important to have a thermometry technique, which is non-invasive and has a high spatial and temporal resolution.

Bandshape luminescence thermometry^{2,3} is a promising method to locally measure temperatures non-invasively. This technique exploits two thermally coupled emitting states, which show temperature-dependent luminescence upon excitation due to a Boltzmann distribution of the emitting states. A great advantage of this technique is that it is based on the intensity ratio of emission from two states and is therefore independent of probe concentration or fluctuations in the excitation or light collection efficiency.

Bandshape luminescence thermometry has already been investigated thoroughly for bio-imaging application using lanthanide-doped organic complexes.⁴ By incorporating lanthanide ions, e.g. Er^{3+} , in inorganic (nano)crystals,⁵ the temperature range has been expanded^{6,7} resulting in a wider range of applications eligible for luminescence thermometry.^{8,9}

To understand the performance of a catalyst, it is important to investigate it under working conditions, resulting in an active field of catalyst research. In situ measurements are a powerful tool to expand our knowledge of catalytic systems. The simultaneous evaluation of the catalyst itself and the reaction products via for example gas chromatography (GC) can also give mechanistic insight in catalyst reactions and related deactivation pathways.

Previous in situ measurements to visualize a temperature gradient along a catalyst bed have been performed with either IR-thermography,^{10,11} NMR-thermometry¹² or using multiple thermocouples¹³ to monitor the temperature at different heights in a catalyst bed. For IR-thermography and NMR-thermometry, the resolution is limited typically to the mm range. Furthermore, the data interpretation for NMR-thermometry can be both cumbersome and dependent on the concentration of the probed species, while the interpretation of IR-thermography might become difficult if light absorbing species are present in the reactor. The use of thermocouples also yields a very limited spatial resolution and the non-invasiveness of the technique cannot be guaranteed. Hence, there is clear room for improved reactor and catalyst particle thermometry.

In this chapter, we demonstrate the potential for luminescence thermometry as an in situ measurement technique during catalytic processes. Therefore, three different systems have been prepared, all with different length scales to enable thermometry with varying spatial resolution. SEM micrographs of microcrystalline NaYF_4 of ca. 5–20 μm (a), 50 nm NaYF_4

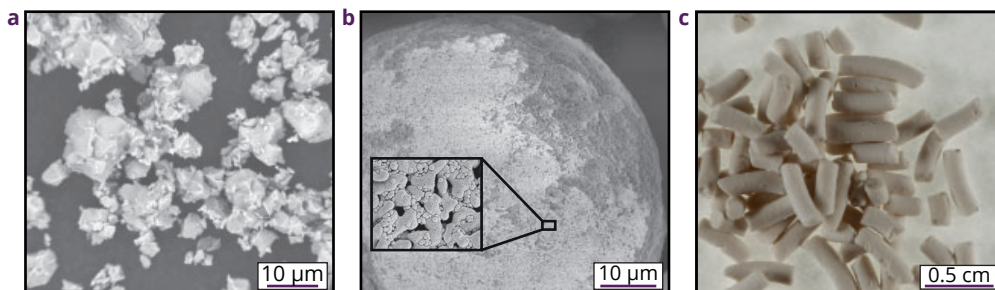


Figure 4.1 – Illustration of temperature probes. SEM micrographs of microcrystalline NaYF₄ (a), NaYF₄ nanoparticles (NPs) deposited on Al₂O₃ (b) and a photo of extrudates containing NaYF₄ NPs (c).

nanoparticles (NPs) deposited on a Al₂O₃ support (b) and finally a photograph of NaYF₄ NPs incorporated in extrudates (c) are shown in Figure 4.1. The NPs have a NaYF₄ core of ca. 20 nm and a SiO₂ shell to prevent sintering of particles and therefore increase the thermal stability. In all cases the NaYF₄ was doped with Er³⁺ and Yb³⁺, resulting in characteristic temperature-dependent luminescence.^{14,15}

Results and Discussion

Temperature-dependent luminescence. Luminescence studies showed temperature-dependent luminescence behavior for all three samples upon upconversion excitation¹⁴ at 980 nm, as shown in Figure 4.2. Here, the log of the intensity ratio of the two emitting states (⁴S_{3/2} and ²H_{11/2} excited state) is plotted vs. reciprocal temperature.

Figure 4.2 clearly shows that the ²H_{11/2}-⁴I_{15/2} emission intensity increases with respect to the ⁴S_{3/2}-⁴I_{15/2} emission upon increasing temperatures (black to orange). This temperature-dependent luminescence derives from the small energy difference between the ⁴S_{3/2} and ²H_{11/2} states, which was determined to be ca. 700 cm⁻¹ (several *kT*) from the spectra at 300 K. Due to the small energy difference between the ²H_{11/2} and the ⁴S_{3/2} state, thermal energy is sufficient to efficiently facilitate fast equilibration between the two excited states and therefore the two states are thermally coupled. Consequently, the populations of the two excited states is governed by a Boltzmann distribution,¹⁶

$$\frac{N_2}{N_1} = \frac{g_2}{g_1} e^{-\Delta E/kT}. \quad (4.1)$$

Here, N_2 and N_1 are the populations from state i , ΔE the energy difference between the two excited states, k the Boltzmann constant and T the temperature. Equation 4.1 shows that the ratio between N_2 and N_1 becomes higher with increasing temperature, which is in line with our observations in Figure 4.2. The emission intensity is proportional to the population and therefore we can rewrite equation 4.1, resulting in:

$$\text{Ln} \left(\frac{I_2}{I_1} \right) = \text{Ln}(C) - \frac{\Delta E}{kT}. \quad (4.2)$$

Here, the logarithm of the ratio of the emission intensities (I_2/I_1) scales linearly with

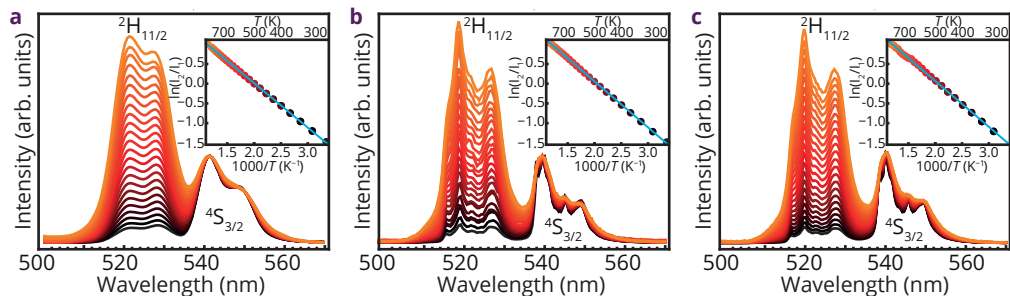


Figure 4.2 – Temperature-dependent emission spectra. Temperature-dependent luminescence spectra of NaYF₄ microcrystals (a), NaYF₄ NPs on Al₂O₃ (b) and NaYF₄ NPs in extrudates (c) upon excitation at 980 nm. The emission spectra are normalized on the ⁴S_{3/2}–⁴I_{15/2} emission peak (540–550 nm). The inset shows the linear correlation between the logarithm of the ratio of the two emission peaks vs. reciprocal temperature.

reciprocal temperature as shown in the inset of Figure 4.2. The linear behavior could be fitted (cyan lines) with linear fits and from the steepness of the curve the ΔE could be calculated. The calculated values of 700–750 cm⁻¹ correspond well with the value of ca. 700 cm⁻¹ obtained from the room temperature spectra.

Figure 4.2 shows that the temperature-dependent emission follows a clear trend. The linear fits are used to determine the reaction temperature from a spectral output with an accuracy of 1 to 5 K.

Methanol-to-Hydrocarbons reaction. To further investigate the applicability of the systems, the microcrystalline NaYF₄ was used as a showcase during the Methanol-to-Hydrocarbons (MTH) reaction by mixing it with a commercial, solid catalyst, zeolite H-ZSM-5, in a fixed bed reactor.

The NaYF₄:Er³⁺,Yb³⁺ in the reactor could be excited, using a fiber probe and temperature-dependent luminescence spectra were collected with the same fiber probe from different heights in the catalyst bed during the reaction. The reaction temperature was calculated from the luminescence output over the course of the reaction. It was shown that the local temperature during in situ measurements can be measured very accurately in a non-invasive manner.

The setup used during these experiments is shown in Figure 4.3. In MTH, after a short induction time, 100 % of the methanol is converted into a wide variety of hydrocarbons with dimethyl ether (DME) as intermediate product (according to the simplified reaction of the MTH process: 2 CH₃OH \rightleftharpoons CH₃OCH₃ + H₂O \rightarrow Light olefins + H₂O).

Under the current reaction conditions (discussed in Experimental Section), using H-ZSM-5 (Si/Al = 25) as catalyst, the main products of this reaction are propylene, ethylene and C₄ olefins as was measured with on-line GC as shown in Figure 4.4.

Extensive research has been done on the mechanism of this MTH process and the hydrocarbon pool mechanism is currently the most widely accepted reaction mechanism.^{17–19} The conversion of methanol into light olefins is exothermic, and the ΔH of the formation

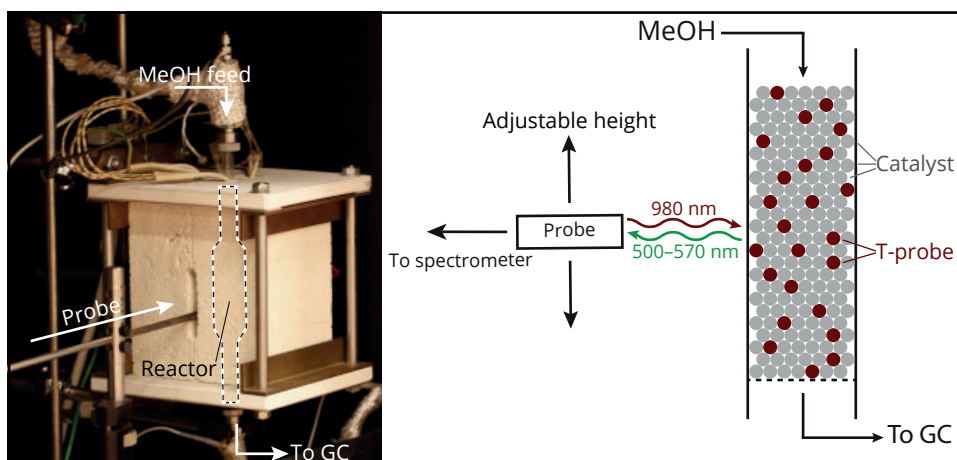


Figure 4.3 - In situ setup. Photograph of the setup used during in situ temperature measurements and a schematic representation of the fixed bed quartz reactor filled with catalyst and $\text{NaYF}_4:\text{Er}^{3+}, \text{Yb}^{3+}$. The MeOH is introduced from the top and all reaction products were analyzed with an on-line GC. An optical fiber probe was placed at three different heights of the reactor bed. In order to minimize the collection of specular reflection of the excitation laser, the reactor was axially rotated in such a way that the excitation laser hits the quartz window at an angle of ca. 120 degrees.

of typical reaction products, e.g., ethylene and propylene is -11 and -42 kJ mol^{-1} , respectively.²⁰ The methanol is introduced at the top of the reactor and fully converted in the top of the catalyst bed. Therefore, it is expected that the heat production is initially the highest at the top of the catalyst bed. Due to coke deposition, the catalyst deactivates over time,^{21–24} resulting in a longer path length of the methanol before it reaches active sites to do the conversion. In this way, only a small part of the bed moving down through the reactor is active towards methanol conversion. The combination of the exothermic nature of the reaction and the deactivation of the catalyst results in a heat front in the catalyst bed that shifts from top to bottom over time.

Temperature measurements. The three temperature profiles that were measured at the top, middle and bottom of the catalyst bed during the MTH reaction are shown in Figure 4.5. A trend-line is drawn through the data points to guide the eye. The temperature uncertainty²⁵ of the technique is very low at the start of the reaction (0.3 K) and increases over time due to reduced signal towards ca. 22 K between 110–140 min.

Note that before the reaction starts, the temperatures are different at the top, middle and bottom of the reactor. This is most likely due to the relatively cold (473 K) gasses, which are introduced to the fixed bed via the top. This phenomenon has also been observed by Yarulina and coworkers.¹³

At all three positions, we see a rapid increase of temperature upon starting the reaction. The temperature at the top spikes first, followed by a temperature maximum in the middle and afterwards a temperature maximum at the bottom of the reactor. At the conditions used, the reaction is operating at 100 % methanol conversion for 400 min, while the temperature

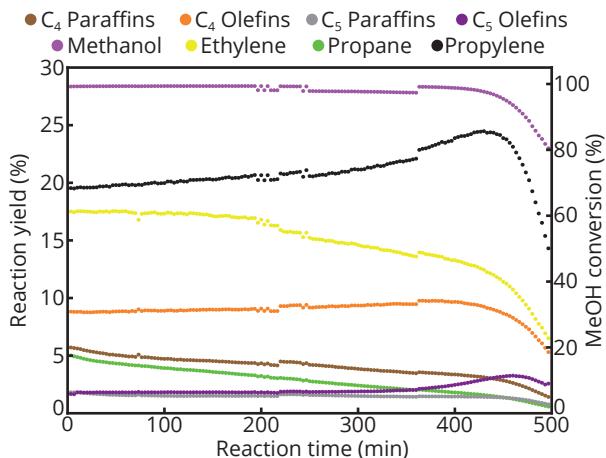


Figure 4.4 – Product analysis. Products obtained during the reaction as determined by on-line GC. The product yields are plotted on the left y-axis, while the MeOH conversion was plotted on the right y-axis. The higher carbon species ($\geq C_6$ olefins and paraffins, aromatics and coke) are no longer distinguishable with the GC and therefore not shown here.

at the bottom of the reactor is at its maximum around 30 min.

In the recent work of Yarulina et al.,¹³ the gradual deactivation of the catalyst bed is aligned with the temperature maxima at different heights in the reactor bed. When the regions in the reactor are nicely separated, the position, where methanol is converted, moves down after deactivation of the top of the reactor. A decrease in methanol conversion occurs when the deactivation front reaches the bottom of the catalyst bed. However, in comparison to the work of Yarulina et al., the results in Figure 4.5 were obtained with higher flow speeds and a relatively short reactor bed. Therefore, in this case, the active regions in the reactor bed are not separated and the temperature front is not aligned with the deactivation of the reactor. The three successive temperature maxima from top to bottom can be explained as a gradual activation of the catalyst bed. After this gradual activation, indicated by the three spikes in temperature that were shown in Figure 4.5, the temperature starts to decrease over the whole reactor. The temperature decrease is the largest for the bottom and middle of the reactor, while the top of the reactor stays warmer for a longer period. After 140 min of reaction, the temperature at all different points in the reactor is similar to the initial temperature before the reaction.

During the reaction, the temperature of the reactor is controlled by a thermocouple inside the oven. One explanation for the decrease after ca. 30 min is that the thermocouple feedback reduces the reactor heater power output after the fast temperature increase due to the exothermic reactions taking place. Since there is still more methanol converted at the top of the reactor than at the rest of the reactor, the top part cools down slower compared to the middle and bottom part as shown in Figure 4.6 (a–c).

From Figure 4.6 (d–f), it can be seen that during the reaction, the catalyst particles become darker due to coke deposition. This effect starts at the top of the reactor and after

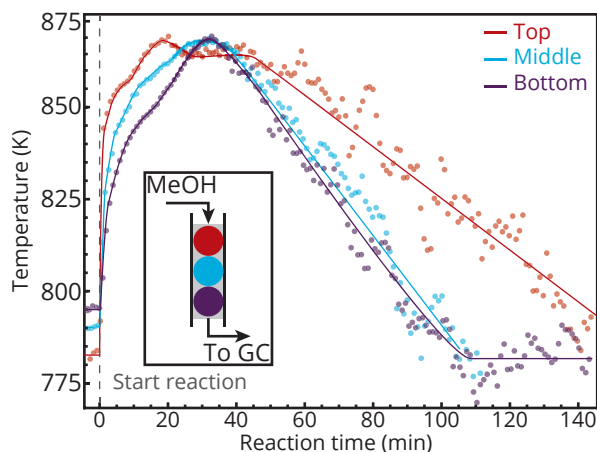


Figure 4.5 – Temperature measurements. Observed temperatures over time determined by luminescence thermometry at the top (red), middle (cyan) and bottom (purple) of a fixed bed reactor.

the reaction, the catalyst is completely coked. It is very interesting to see that the coke deposition only occurs at the zeolite particles; the temperature probes are not affected by the coke deposition and stay white, showing their inertness towards reactive gases. Despite the fact that the coke deposition on the catalyst particles absorbs the luminescence from the temperature probes, which severely reduces the luminescence intensity during experiments, it was still possible to measure sufficient luminescence output and calculate temperatures inside the reactor.

The measured temperature front which moves over the reactor is consistent with literature and the observations of the coke deposition during the reaction. This experiment shows the potential of luminescence thermometry to measure the temperature in catalytic reactions with a non-invasive probing technique.

Alternative temperature probe particles. Although the potential of luminescence thermometry has been demonstrated with these experiments, the microcrystalline temperature probes with a final size of 150–425 μm may have limited applicability in other experimental setups due to the size constraints. To ensure the applicability of luminescence thermometry in a broader range of catalytic systems, it is possible to prepare different temperature probe particles that can be embedded in or placed on different support materials, as shown in Figure 4.1.

Many different catalytic reactions exploit NP catalysts to increase the surface to volume ratio. In most cases, the catalyst NPs are supported on an inorganic material to increase their mechanical and thermal stability and to prevent activity loss of the catalyst due to sintering of the NPs. A widely-used support, Al_2O_3 is shown in the SEM image in Figure 4.1b. In order to measure the temperature at the surface of the support, it is possible to deposit $\text{NaYF}_4:\text{Er}^{3+}, \text{Yb}^{3+}@\text{SiO}_2$ core/shell NPs (zoom-in) and subsequently measure the temperature-dependent luminescence (inset) which is similar to the temperature-dependent

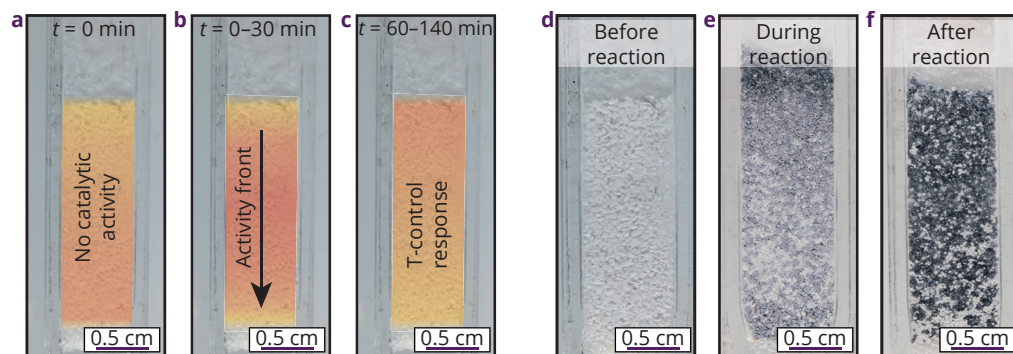


Figure 4.6 – Temperature and coke profiles. Temperature profiles of the reactor at $t = 0$ min (a), $t = 0-30$ min (b) and $t = 60-140$ min (c). Photographs of the reactor before (d), after 120 mins (e) and after 400 mins at the end of the reaction (f).

luminescence observed in Figure 4.1a. The NPs used in these extrudates were prepared as discussed in earlier work.¹⁵ To prevent sintering of the NPs at elevated temperatures, the particles are coated with a silica shell.²⁶ This ensures thermal stability up to at least 900 K.

For larger scale reactors, using bigger catalyst bodies, like extrudates, is more suitable to prevent a pressure drop in the reactor bed. Figure 4.1c shows a photograph of extrudates with $\text{NaYF}_4:\text{Er}^{3+}, \text{Yb}^{3+}@\text{SiO}_2$ core/shell NPs incorporated that can be added to a reactor system to locally measure the temperature in a larger reactor bed. These mm-sized extrudates show green upconversion luminescence upon excitation with a 980 nm laser source, which is temperature-dependent (inset) similar to the luminescence shown in Figures 4.1a and 4.1b.

By expanding the system from the microcrystalline $\text{NaYF}_4:\text{Er}^{3+}, \text{Yb}^{3+}$ in the showcase MTH reaction to NPs, which can be incorporated into supported systems or extrudates, the potential of luminescence thermometry has been greatly increased. By combining the luminescence thermometry with a confocal microscope with spectral output, the spatial resolution can be enhanced to the sub-micrometer regime enabling to investigate temperature heterogeneities at all different length scales.

Conclusions

In conclusion, using temperature-dependent luminescence of $\text{NaYF}_4:\text{Er}^{3+}, \text{Yb}^{3+}$ crystallites, the temperature was probed over the course of a catalytic reaction at different heights in a reactor bed. The obtained results show a clear potential for luminescence thermometry for non-invasive in situ temperature measurements. Using the luminescence output upon excitation of the temperature probes inside a working reactor, the temperatures were determined at three different heights. For the MTH process, it was shown that the introduction of the methanol leads to an increased temperature due to the exothermic nature of the MTH reaction and revealed differences in the time dependent temperature profiles at different heights in the reactor.

By decreasing the size of the temperature probes from micro- to nanoparticles, it is possible to incorporate the temperature probes in other catalyst particles, e.g. extrudates or other type of catalyst bodies and therefore increase the range of catalytic reactions that can be probed.

Until now, temperature heterogeneities at the sub-micrometer level are still poorly understood. By combining the temperature-dependent luminescence with e.g. confocal microscopy, it should be possible to make temperature maps with spatial resolutions in the sub-micrometer regime.

Experimental Section

Chemicals. All chemicals were used without further purification. The following chemicals were purchased from Sigma-Aldrich: Cyclohexane (99.5 %, CH), oleic acid (90 %, OA), ethanol (>99.8 %, EtOH), methanol (>99.85 %, MeOH), sodium fluoride (>98 %, NaF), sodium hydroxide (>97 %, NaOH), ammonium fluoride (>98 %, NH_4F), ammonium hydroxide (28 wt% in H_2O , ammonia) lanthanide acetate hydrates (99.9 %, $\text{Ln}(\text{Ac})_3$), tetraethyl orthosilicate (99.999 %, TEOS) and IGEPAL CO-520 ($(\text{C}_2\text{H}_4\text{O})_n \cdot \text{C}_{15}\text{H}_{24}\text{O}$ with $n \sim 5$, average $\text{Mn} = 441 \text{ g mol}^{-1}$, NP-5). 1-octadecene (90 %, ODE) was purchased from Acros Organics. Yttrium fluoride (>99.99 %, YF_3) was purchased from ChemPur. Ytterbium fluoride (>99.99 %, YbF_3) was purchased from Strem Chemicals. Erbium fluoride (>99.99 %, ErF_3) was purchased from Highways Internationals. Spherical $\alpha\text{-Al}_2\text{O}_3$ (99.9 % metals basis, average particle size 20–50 μm) was purchased from Alfa Aesar.

Preparation of microcrystalline NaYF_4 . Microcrystalline NaYF_4 doped with 19 % Yb^{3+} and 2 % Er^{3+} ($\text{NaYF}_4:\text{Er}^{3+}, \text{Yb}^{3+}$), was prepared via a solid state synthesis.²⁷ In short, 15 mmol of dried NaF, 15 mmol of REF_3 (RE = Y, Er, Yb) and 13.5 mmol of NH_4F were mixed with a pestle and mortar and afterwards placed in an alumina crucible. The mixture was fired in the oven in an excess of NH_4F under a nitrogen atmosphere. The samples were heated to 573 K for 3 h and afterwards heated to 823 K for 8 h. The heating rate was 5 K min^{-1} for both heating steps. The obtained powder was pressed into pellets, crushed and sieved. Afterwards, temperature-dependent luminescence studies have been performed as shown in Figure 4.2a. The sieve fraction of 150–425 μm was used during the experiments.

Preparation of $\text{NaYF}_4@\text{SiO}_2$ NPs. $\text{NaYF}_4@\text{SiO}_2$ nanoparticles (NPs) doped with 19 % Yb^{3+} and 2 % Er^{3+} of ca. 50 nm were prepared via an initial synthesis of NaYF_4 core particles (ca. 20 nm) and subsequent SiO_2 overgrowth as reported earlier.^{15,26,28,29}

Deposition of $\text{NaYF}_4@\text{SiO}_2$ NPs on $\alpha\text{-Al}_2\text{O}_3$ support. The $\text{NaYF}_4@\text{SiO}_2$ NPs were deposited on spherical $\alpha\text{-Al}_2\text{O}_3$ by adding a known concentration of the NPs in EtOH to ca. 300 mg $\alpha\text{-Al}_2\text{O}_3$ (sieve fraction >75 μm). This mixture was equilibrated for 1 min to allow for the NPs to adsorb on the alumina surface before filtering the $\text{NaYF}_4@\text{SiO}_2/\alpha\text{-Al}_2\text{O}_3$. The product obtained was washed with EtOH and dried overnight in static air at 333 K. Afterwards, temperature-dependent luminescence studies have been performed as shown in Figure 4.2b.

Preparation of NaYF₄/SiO₂ NPs in extrudates. The NaYF₄/SiO₂ NPs were prepared as described above and subsequently dried to obtain a powder. Afterwards, 3.2 g of powder was mixed with H₂O, 3.8 g silica (Davicat Si1302) and 0.2 g methylcellulose (4000 CP, Sigma Aldrich) in a Caleva Mixer Torque Rheometer. The obtained paste was then transferred to a single mini-screw extruder (Caleva) and extruded into 2 mm diameter cylindrical extrudates. The obtained extrudates were dried overnight at room temperature and subsequently calcined at 873 K. Afterwards, temperature-dependent luminescence studies have been performed as shown in Figure 4.2c.

Preparation of H-ZSM-5 catalyst. The catalyst for the Methanol-to-Hydrocarbons (MTH) reaction was a commercially available zeolite ZSM-5 from Zeolyst with a crystal size of 200–800 nm and Si/Al ratio of 25. In order to convert the zeolite into its H-form the zeolite powder was calcined at 823 K (5 K min⁻¹) for 10 h in air and afterwards pressed into pellets, crushed and sieved. The sieve fraction of 212–425 μm was used during the experiments.

In situ reactor setup. The MTH reaction was performed in a rectangular fixed bed quartz reactor (ID = 6 mm × 3 mm), filled with 165 mg catalyst and 165 mg temperature probes (T-probes). This leads to a volume ratio of ca. 5:1 catalyst/T-probes. Before the reaction, the reactor bed was activated at 823 K in 100 % O₂ for 1 h. The reaction was performed with a total weight hourly space velocity (WHSV) of 15 h⁻¹ in a He flow with 18 % MeOH saturation. This was obtained by flowing He through a MeOH saturator, kept at 303 K. All reaction products were analyzed using an on-line Interscience Compact GC equipped with an Rtx-wax and Rtx-1 column in series and an Rtx-1, Rt-TCEP and Al₂O₃/Na₂SO₄ in series, both connected to an FID. The total reactor bed was typically 21 mm high and an Avantes high-temperature optical fiber probe was placed at three different heights along the bed as shown in Figure 4.3. The probe contained 6 excitation fibers and 1 detection fiber with diameters of 400 μm. The probe was placed several mm from the reactor bed to ensure no overlap between the different measurement spots and a sufficient signal acquisition. A 980 nm continuous wave laser (0.5 W) was used to excite the sample via the probe before subsequent collection of the upconversion emission via the same probe. The collected light was led to an AvaSpec-2048L spectrometer via a short pass filter to filter out the excitation light source. The temperature calibration measurements were performed by the same spectrometry setup in combination with a Linkam THMS600 Microscope Stage. SEM images were made using a Phenom ProX.

Acknowledgements

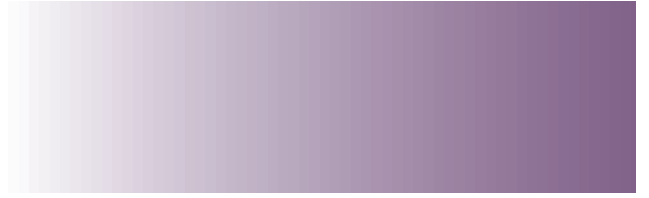
The authors acknowledge the assistance of Gareth Whiting (Utrecht University) during the preparation of the extrudates.

This work was supported by the Netherlands Center for Multiscale Catalytic Energy Conversion (MCEC), an NWO Gravitation programme funded by the Ministry of Education, Culture and Science of the government of the Netherlands.

References

1. Hwang, S. & Smith, R. Optimum Reactor Design in Methanation Processes with Nonuniform Catalysts *Chem. Eng. Commun.* **2009**, *196*, 616–642.
2. McLaurin, E. J.; Bradshaw, L. R. & Gamelin, D. R. Dual-Emitting Nanoscale Temperature Sensors *Chem. Mater.* **2013**, 1283–1292.
3. Jaque, D. & Vetrone, F. Luminescence Nanothermometry *Nanoscale* **2012**, *4*, 4301–4326.
4. Rao, X.; Song, T.; Gao, J.; Cui, Y.; Yang, Y.; Wu, C.; Chen, B. & Qian, G. A highly Sensitive Mixed Lanthanide Metal-Organic Framework Self-Calibrated Luminescent Thermometer *J. Am. Chem. Soc.* **2013**, *135*, 15559–15564.
5. Shen, J.; Sun, L. & Yan, C.-H. Luminescent Rare Earth Nanomaterials for Bioprobe Applications *Dalton Trans.* **2008**, *9226*, 5687–5697.
6. Li, D.; Wang, Y.; Zhang, X.; Yang, K.; Liu, L. & Song, Y. Optical Temperature Sensor through Infrared Excited Blue Upconversion Emission in $\text{Tm}^{3+}/\text{Yb}^{3+}$ Codoped Y_2O_3 *Opt. Commun.* **2012**, *285*, 1925–1928.
7. Heyes, A.; Seefeldt, S. & Feist, J. P. Two-Colour Phosphor Thermometry for Surface Temperature Measurement *Opt. Laser Technol.* **2006**, *38*, 257–265.
8. Vetrone, F.; Naccache, R.; Zamarrón, A.; Juarranz de la Fuente, A.; Sanz-Rodríguez, F.; Martínez Maestro, L.; Martín Rodríguez, E.; Jaque, D.; García Solé, J. & Capobianco, J. A. Temperature Sensing Using Fluorescent Nanothermometers. *ACS Nano* **2010**, *4*, 3254–3258.
9. Shinde, S. L. & Nanda, K. K. Wide-Range Temperature Sensing using Highly Sensitive Green-Luminescent ZnO and PMMA-ZnO Film as a Non-Contact Optical Probe *Angew. Chem. Int. Ed.* **2013**, *125*, 11535–11538.
10. Kimmerle, B.; Grunwaldt, J. D.; Baiker, A.; Glatzel, P.; Boye, P.; Stephan, S. & Schroer, C. G. Visualizing a Catalyst at Work during the Ignition of the Catalytic Partial Oxidation of Methane *J. Phys. Chem. C* **2009**, *113*, 3037–3040.
11. Simeone, M.; Saleme, L.; Allouis, C. & Volpicelli, G. Temperature Profile in a Reverse Flow Reactor for Catalytic Partial Oxidation of Methane by Fast IR Imaging *AIChE J.* **2008**, *54*, 2689–2698.
12. Koptuyg, I. V.; Khomichev, A. V.; Lysova, A. A. & Sagdeev, R. Z. Spatially Resolved NMR Thermometry of an Operating Fixed-Bed Catalytic Reactor *J. Am. Chem. Soc.*, **2008**, *130*, 10452–10453.
13. Yarulina, I.; Kapteijn, F. & Gascon, J. The Importance of Heat Effects in the Methanol to Hydrocarbons Reaction over ZSM-5: On the Role of Mesoporosity on Catalyst Performance *Catal. Sci. Technol.* **2016**, *6*, 5320–5325.
14. Menyuk, N.; Dwight, K. & Pierce, J. W. $\text{NaYF}_4:\text{Yb},\text{Er}$ - An Efficient Upconversion Phosphor *Appl. Phys. Lett.* **1972**, *21*, 159–161.
15. Geitenbeek, R. G.; Prins, P. T.; Albrecht, W.; van Blaaderen, A.; Weckhuysen, B. M. & Meijerink, A. $\text{NaYF}_4:\text{Er}^{3+},\text{Yb}^{3+}/\text{SiO}_2$ Core/Shell Upconverting Nanocrystals for Luminescence Thermometry up to 900 K *J. Phys. Chem. C* **2017**, *121*, 3503–3510.
16. Brites, C. D. S.; Lima, P. P.; Silva, N. J. O.; Millán, A.; Amaral, V. S.; Palacio, F. & Carlos, L. D. Thermometry at the Nanoscale *Nanoscale* **2012**, *4*, 4799–4829.
17. Olsbye, U.; Svelle, S.; Bjorgen, M.; Beato, P.; Janssens, T. V.W.; Joensen, F.; Bordiga, S. & Lillerud, K. P. Conversion of Methanol to Hydrocarbons: How Zeolite Cavity and Pore Size Controls Product Selectivity *Angew. Chem. Int. Ed.* **2012**, *51*, 5810–5831.

18. Ilias, S. & Bhan, A. Mechanism of the Catalytic Conversion of Methanol to Hydrocarbons *ACS Catal.* **2013**, *3*, 18–31.
19. Hemelsoet, K.; Van der Mynsbrugge, J.; De Wispelaere, K.; Waroquier, M. & Van Speybroeck, V. Unraveling the Reaction Mechanisms Governing Methanol-to-Olefins Catalysis by Theory and Experiment *ChemPhysChem* **2013**, *14*, 1526–1545.
20. Kumar, P.; Thybaut, J. W.; Svelle, S.; Olsbye, U. & Marin, G. B. Single-Event Microkinetics for Methanol to Olefins on H-ZSM-5 *Ind. Eng. Chem. Res.* **2013**, *52*, 1491–1507.
21. Mores, D.; Stavitski, E.; Kox, M. H. F.; Kornatowski, J.; Olsbye, U. & Weckhuysen, B. M. Space- and Time-Resolved in situ Spectroscopy on the Coke Formation in Molecular Sieves: Methanol-to-Olefin Conversion over H-ZSM-5 and H-SAPO-34 *Chem. Eur. J.* **2008**, *14*, 11320–11327.
22. Schulz, H. “Coking” of Zeolites during Methanol Conversion: Basic Reactions of the MTO-, MTP- and MTG Processes *Catal. Today* **2010**, *154*, 183–194.
23. Bleken, F. L.; Barbera, K.; Bonino, F.; Olsbye, U.; Lillerud, K. P.; Bordiga, S.; Beato, P.; Janssens, T. V. W. & Svelle, S. Catalyst Deactivation by Coke Formation in Microporous and Desilicated Zeolite H-ZSM-5 during the Conversion of Methanol to Hydrocarbons *J. Catal.* **2013**, *307*, 62–73.
24. Olsbye, U.; Svelle, S.; Lillerud, K. P.; Wei, Z. H.; Chen, Y. Y.; Li, J. F.; Wang, J. G. & Fan, W. B. The Formation and Degradation of Active Species during Methanol Conversion over Protonated Zeotype Catalysts *Chem. Soc. Rev.* **2015**, *44*, 7155–7176.
25. Wang, Z.; Ananias, D.; Carné-Sánchez, A.; Brites, C. D. S.; Imaz, I.; Maspocho, D.; Rocha, J. & Carlos, L.D. Lanthanide-Organic Framework Nanothermometers Prepared by Spray-Drying *Adv. Funct. Mater.* **2015**, *25*, 2824–2830.
26. Koole, R.; van Schooneveld, M. M.; Hilhorst, J.; de Mello Donegá, C.; ‘t Hart, D. C.; van Blaaderen, A.; Vanmaekelbergh, D. & Meijerink, A. On the Incorporation Mechanism of Hydrophobic Quantum Dots in Silica Spheres by a Reverse Microemulsion Method *Chem. Mater.* **2008**, *20*, 2503–2512.
27. Aarts, L.; van der Ende, B. M. & Meijerink, A. Downconversion for Solar Cells in NaYF₄:Er,Yb *J. Appl. Phys.* **2009**, *106*, 23522.
28. Li, Z. & Zhang, Y. An Efficient and User-Friendly Method for the Synthesis of Hexagonal-Phase NaYF₄:Yb,Er/Tm Nanocrystals with Controllable Shape and Upconversion Fluorescence *Nanotechnology* **2008**, *19*, 345606.
29. Wang, F., Deng, R. & Liu, X. Preparation of Core-Shell NaGdF₄ Nanoparticles Doped with Luminescent Lanthanide Ions to be used as Upconversion-Based Probes *Nat. Protoc.* **2014**, *9*, 1634–1644.



Based on

- Geitenbeek, R. G.; van Ravenhorst, I. K.; van der Eerden, A. M. J.; Meirer, F.; Meijerink, A. & Weckhuysen, B. M. State-of-the-Art Holder for the use of MEM Nano-Chips for STXM. *in preparation*

Chapter 5 – Luminescence Thermometry to Monitor Temperature in a Microelectromechanical System for Scanning Transmission X-ray Microscopy



Robin Geitenbeek



Ilse van Ravenhorst

Abstract

To comprehend the catalyst behavior under relevant working conditions, operando spectroscopy and microscopy measurements are required. Although multiple operando techniques are available, most probably only scanning transmission x-ray microscopy (STXM) is able to spatially resolve catalyst behavior with regards to organic compounds (coke deposition) and inorganic compounds (catalyst composition). In this chapter we introduce a homemade holder to perform in situ STXM measurements with a microelectromechanical system (MEMS) with a heating spiral of $300\ \mu\text{m} \times 300\ \mu\text{m}$. The temperature over the heating spiral has been successfully mapped up to $600\ \text{°C}$ with a spatial resolution of ca. $7\ \mu\text{m}$ and compared to the temperature read-out obtained from resistivity measurements in the heating spiral. In vacuum atmosphere, the temperatures obtained from luminescence thermometry matched well with the values obtained from the resistivity measurements and were fairly homogeneous over the whole area. Upon introduction of static air, the heat dissipation plays an important role and the maximum temperature reached in the reactor is $450\ \text{°C}$, compared to the set temperature of $600\ \text{°C}$ based on the electrical resistance feedback. In addition, the temperature homogeneity is gone, resulting in a temperature gradient of ca. $200\ \text{°C}$ in the reactor. A new design nanoreactor showed similar temperature maxima in air ($450\ \text{°C}$), but the temperature distribution was more homogeneous. The results show that large temperature differences over the distance of tens of μm s can occur and can be measured using luminescence thermometry in combination with confocal microscopy. Here, the temperature discrepancy is due to the heat dissipation but other effects could also occur, such as exo- or endothermic reactions.

Introduction

Catalyst deactivation is a large-scale problem in chemical manufacturing processes and is not always well understood.^{1–3} For instance, in the cobalt-catalyzed Fischer Tropsch synthesis, three main reasons for deactivation over time are conversion of the active phase of a catalyst,^{4–6} sintering or clustering of the catalyst nanoparticles,^{2,7,8} and coke deposition.^{2,9,10} This deposition of carbon-rich species either blocks the catalyst or pathways towards solid catalysts, resulting in a reduced activity or even complete deactivation of the catalyst. To prevent catalyst deactivation, it is paramount to understand the mechanisms that result in deactivation. Monitoring catalyst particles under working conditions, i.e. operando experiments,^{11–13} is therefore of tremendous importance.

Spectroscopic techniques, such as IR,^{14,15} Raman^{16,17} and UV-Vis spectroscopy^{18,19} focus mainly on the organic compounds surrounding the catalyst, such as adsorbates, products and coke. To get a better understanding of the whole catalytic system, the inorganic part should also be evaluated. X-ray spectroscopy focusses primarily on elements with higher atomic numbers and can therefore be a great asset to investigate the inorganic part of catalysts. Scanning transmission X-ray microscopy (STXM)²⁰ is of specific interest since both the organic part (i.e. carbon) and the inorganic part of the catalyst can be investigated with this technique. By combining STXM with on-line activity analysis (using gas chromatography or mass spectrometry) it is possible to perform in situ or operando measurements on single catalyst particles.^{21–23}

STXM combines microscopy with X-ray absorption spectroscopy, resulting in a microscopy technique that can monitor over a wide variety of chemical elements, including carbon. In STXM soft X-rays (<5 keV) are exploited to raster scan a region of interest to obtain a point-by-point image over a specific energy range. Each pixel then contains an X-ray absorption spectrum (XAS) or X-ray absorption near edge structure (XANES) of a specific element. In this way, spatial information on species can be obtained with a spatial resolution up to 10 nm.

Soft X-rays attenuate quickly in ambient atmosphere, therefore, experiments have to be performed in a vacuum chamber. In a typical STXM experiment, X-rays are focused using a Fresnel zone plate, in which the focal length, f , is determined by

$$f = \frac{2r_N \Delta r_N}{\lambda}. \quad (5.1)$$

Here, the r_N is the radius of the outermost Fresnel zone with a width of Δr_N and λ is the wavelength of the incoming X-rays. To maximize the selection of the first ordered light, an order sorting aperture is placed in between the zone plate and the sample, resulting in a limited space for operando measurements inside a miniature reactor (300–500 μm). In addition, the optical elements in the vacuum chamber are sensitive to temperature changes, resulting in defocusing of the incident X-rays. To heat samples during operando measurements without affecting the optical elements, conventional heating elements, such

as an oven or a heat gun, do not suffice.²⁴

Inspiration can be drawn from in situ transmission electron microscopy (TEM) in which microelectromechanical systems (MEMS) are currently being developed, which can withstand at least 1000 °C^{25,26} and further development has yielded MEMS which can flow gasses and withstand up to 14 bar of pressure.²⁷ Although these devices are applicable for operando studies using TEM, these kind of devices are not yet available for STXM.

In this chapter we introduce a microelectromechanical system (MEMS) nano-reactor with a miniaturized heating spiral (300 μm \times 300 μm) for STXM measurements. Due to the silicon nitride insulation of the heating spiral, the reactor will only be heated locally and heat transfer to the surroundings is minimized. Furthermore, gasses can be introduced into the reaction chamber to perform operando measurements, while continuously monitoring catalyst activity using on-line mass spectrometry and simultaneously performing STXM characterization of the solid catalyst material.

Although the temperature of the heating spiral can be monitored using the temperature-dependent resistance of the contacts, this read-out value contains no information about the homogeneity of the temperature on the heating spiral. Furthermore, the heating spirals are originally designed for TEM measurements and are thus calibrated to be used in vacuum. During operando measurements, the spiral is no longer under vacuum, therefore the temperature calibration might be wrong due to heat dissipation not present in vacuum systems.

To monitor both the temperature distribution and the effect of the surrounding atmosphere (e.g. vacuum or air) we have performed luminescence thermometry using microcrystalline $\text{NaYF}_4:\text{Er}^{3+}, \text{Yb}^{3+}$ deposited on the heating spiral to monitor the local temperature. Combining the temperature-dependent luminescence with confocal microscopy, temperature profiles were obtained for the heating spiral in different environments. Measurements in vacuum show great agreement between the set temperatures and the obtained temperatures using luminescence thermometry. In addition, the temperature distribution over the heating spiral is quite homogeneous. Only the outer part of the spiral is significantly cooler (400 °C vs. 600 °C in the center). Upon introducing static air in the nano-reactor, the temperature behavior is changed completely. Temperature discrepancies of 100–200 °C can easily be obtained between the set temperature and the temperature determined with luminescence thermometry. Furthermore, the homogeneity of the temperature is lost and a large gradient is observed from 450 °C in the center to 250 °C on the edges of the heating spiral.

The results show that temperature can be monitored up to at least 600 °C with a spatial resolution of ca. 10 μm . Clearly, the importance to monitor temperature under relevant reaction conditions is demonstrated, since these large temperature differences in the MEMS nano-reactor can have large effects on catalytic activity and selectivity, as well as on the related micro-spectroscopic data of single catalyst particles obtained during e.g. operando STXM measurements.

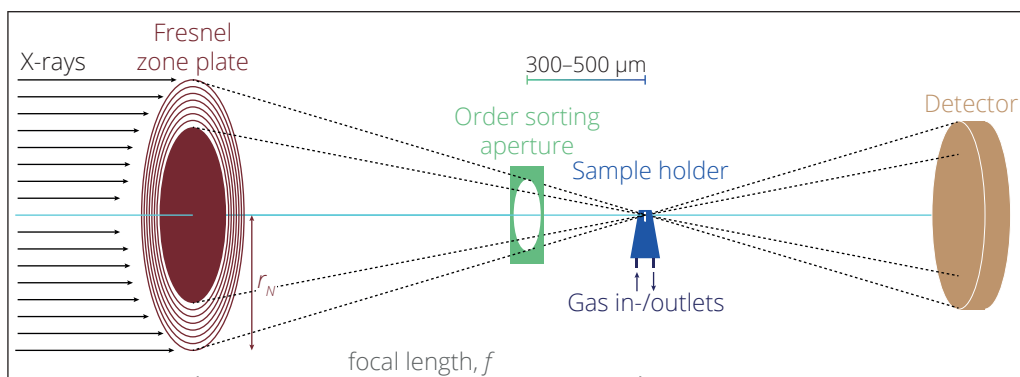


Figure 5.1 – Experimental setup for performing scanning transmission X-ray microscopy (STXM) measurements under in situ or operando conditions. The parallel x-ray beam is focused using a Fresnel zone plate and an order sorting aperture. The sample is placed at the focal length afterwards the transmitted x-rays are collected by the detector. The distance between the order sorting aperture and the focal point is only 300–500 μm in the case of the carbon K-edge.

Results and Discussion

STXM setup. In STXM, the absorption of specific X-rays is probed by monitoring the transmitted X-rays of a beam that passes through a sample as shown schematically in Figure 5.1. Using a Fresnel zone plate and an order sorting aperture, the X-ray beam can be focused to a 10 nm spot size, depending on the size of the zone plate, as shown in equation 5.1. The detector can monitor the intensity of the beam after passing through the sample and the absorption of the sample can be calculated upon comparison with the incident beam intensity. This focused beam can be used to raster scan the sample to produce a point-by-point image. By scanning multiple times with different energies, multiple elements and their oxidation states can be probed.

To monitor the carbon K-edge, at ca. 300 eV, with a resolution of ca. 50 nm, the distance between the sample and the order sorting aperture (OSA) should be 300–500 μm , resulting in a small working volume for operando micro-spectroscopy measurements.

In order to perform operando microspectroscopy measurements in this small volume a special STXM holder has been developed in our group. Recently, our group has used several generations of these STXM holders to perform successful experiments at synchrotrons.^{21–23,28–30} Figure 5.2 shows the most recent design of the holder. This holder consists of several parts to allow for in situ or operando spectroscopy measurements of solid catalysts with the nano-reactor. The MEMS reactor is held in place by a top plate. This pressing plate is connected with six screws onto the main part of the holder and provides the leak tight connection for gasses by pressing the in- and outlet of the reactor onto two O-rings (Figures 5.2a and 5.2b). The maximum flow rate of the mass flow controllers used to introduce gasses is 1 mL min^{-1} and the maximum pressure inside the MEMS reactor in these experiments is 5 bar. The orange part (Figure 5.2a) holds the four needles for the resistance temperature control in place which can be connected to the MEMS reactor

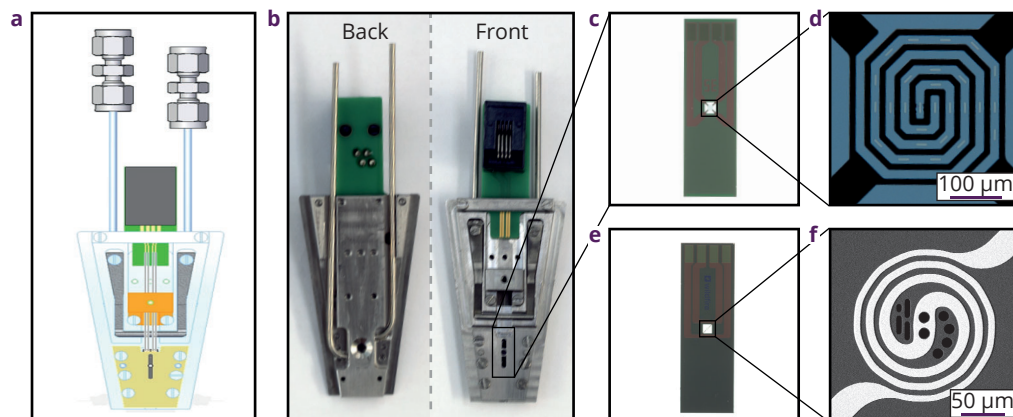


Figure 5.2 – Schematics and pictures of the STXM holder and two MEMS nano-reactors. Schematic representation (a) and photograph (b) of the STXM holder. The inlet and outlet at the top allow for gas flows. The original MEMS nano-reactor is shown on the zoom-in (c), with a further zoom-in of the heating spiral (d). The heating spiral in the transparent window in the middle can heat up to at least 600 °C. A newly designed MEMS reactor (e) with a zoom-in of the new heating spiral design (f).

(Figures 5.2c and 5.2e).

The temperature inside the MEMS nano-reactor can be controlled via a platinum heating spiral (Figures 5.2d and 5.2f). Using this spiral the temperature can be increased via Joule heating and simultaneously the temperature read-out can be done by monitoring the resistance and exploiting the near-linear response of resistivity with temperature. The spiral area is insulated with silicon nitride, ensuring that the heating is localized in the $300\ \mu\text{m} \times 300\ \mu\text{m}$ area with the transparent window for in situ measurements (Figure 5.2d). The new design for the heating spiral is smaller with a diameter of ca. $100\ \mu\text{m}$ (Figure 5.2f).

The manufacturer of the nano-reactors calibrates every batch, ensuring accuracy in the set temperatures. However, the design of the nano-reactors is mainly for TEM measurements, resulting in a calibration procedure based on a vacuum environment. For the in situ STXM measurements, gasses are introduced in the reactor, which can lead to temperature deviations. Furthermore, the temperature read-out is due to the resistance of the platinum wire, which gives a single value for temperature inside the MEMS reactor. This average value however is not sufficient to understand temperature heterogeneities, which can be present in the system.

In TEM, local temperature measurements using parallel beam electron diffraction have been performed to map the temperature in MEMS.^{31,32} In this method, small Au nanoparticles (NPs) are distributed over the surface and the temperature-dependent diffraction rings, due to the thermal expansion of the Au NPs, are investigated using selected area electron diffraction to determine the temperature. This method however is not applicable to the nano-reactor used in in situ STXM since the Au NP stability cannot be guaranteed and the measurements require a vacuum environment.

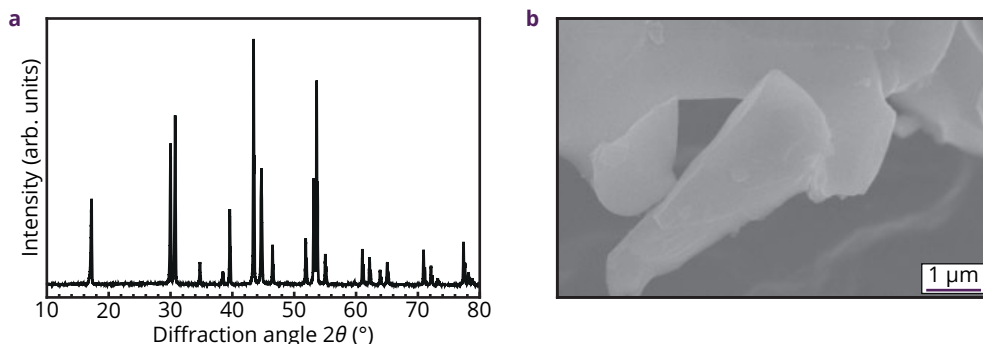


Figure 5.3 – Structural characterization of the temperature probes developed. Cu K α XRD diffractogram of the (a) and a SEM micrograph (b) of the synthesized NaYF₄ microcrystals. The peaks in the XRD diffractogram are a match to the reference lines of NaYF₄ (JCPDS No. 00-028-1192).

An alternative method, which relies on the temperature-dependent luminescence of lanthanide-doped nano-/microparticles does not have such restrictions. By monitoring the temperature-dependent luminescence of Er³⁺ temperature read-outs can be done both in vacuum and other atmospheres up to at least 600 °C.³³

NaYF₄:Er³⁺,Yb³⁺ Microcrystals. In order to investigate the temperature profile in the MEMS nano-reactor, luminescence thermometry measurements have been performed in combination with confocal microscopy. By monitoring the temperature-dependent luminescence of Er³⁺ ions in different spots on the heating spiral, the temperature distribution could be obtained.

The luminescence thermometry measurements in this work have been performed using microcrystalline NaYF₄ doped with Er³⁺ and Yb³⁺. To confirm the successful synthesis of the NaYF₄ host, X-ray diffraction (XRD) and scanning electron microscopy (SEM) measurements were performed as shown in Figure 5.3. The XRD diffractogram matches the hexagonal crystal structure of NaYF₄ (JCPDS No. 00-028-1192) and the SEM image shows the as prepared microparticles. ICP-OES measurements have been performed to obtain the dopant concentrations of the Er³⁺ and Yb³⁺, which were 2 and 19 %, respectively.

Temperature-dependent luminescence. To determine the temperature in the STXM holder, bandshape luminescence thermometry is exploited.^{34,35} Bandshape luminescence thermometry revolves around two closely spaced energy levels in thermal equilibrium.^{36–38} In this case, the lanthanide dopant Er³⁺ is used,^{39,40} in which the ²H_{11/2} and ⁴S_{3/2} excited states are separated by an energy difference of ca. 700 cm⁻¹ (several kT at room temperature) as shown in Figure 5.4a.

Upon excitation of the higher lying ⁴F_{7/2} energy level at 488 nm, the system quickly relaxes to the ²H_{11/2}/⁴S_{3/2} levels and characteristic temperature-dependent luminescence is observed between 510 and 560 nm, as shown in Figure 5.4b.

Due to small energy gap between the ⁴S_{3/2} and ²H_{11/2} levels, the equilibration is fast and the

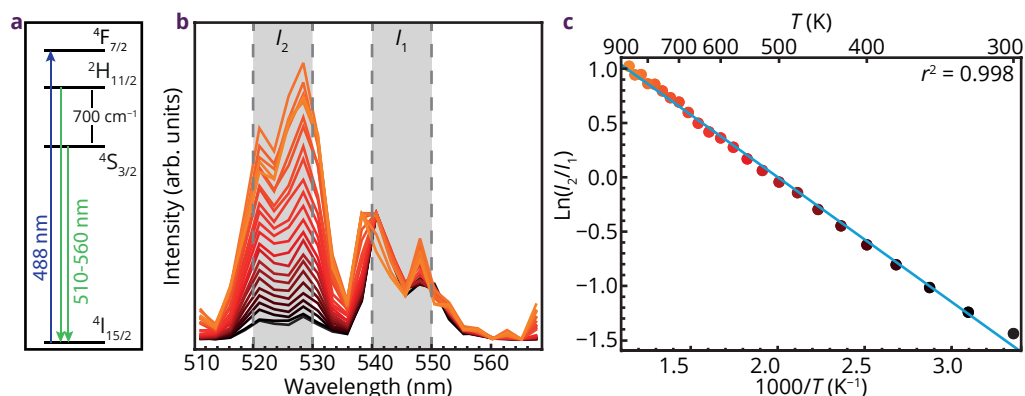


Figure 5.4 - Temperature-dependent luminescence of temperature probes. The energy levels (a) involved in the excitation and temperature-dependent luminescence of Er^{3+} (b). The Boltzmann behavior upon plotting the fluorescence intensity ratio on a log scale vs. reciprocal temperature (c).

luminescence intensity is determined by Boltzmann statistics, according to:

$$\frac{N_2}{N_1} = \frac{g_2}{g_1} e^{-\Delta E/kT} \quad (5.2)$$

Here, N_i is the population in state i , g_i is the degeneracy of state i , ΔE is the energy difference between the two energy levels, k is the Boltzmann constant and T is the absolute temperature. Since the emission intensity is correlated to the population of the emitting state, the luminescence intensity ratio can be rewritten as:

$$\frac{I_2}{I_1} = C e^{-\Delta E/kT} \quad (5.3)$$

Here, I_i is the emission intensity from state i and C is a temperature-independent constant. In

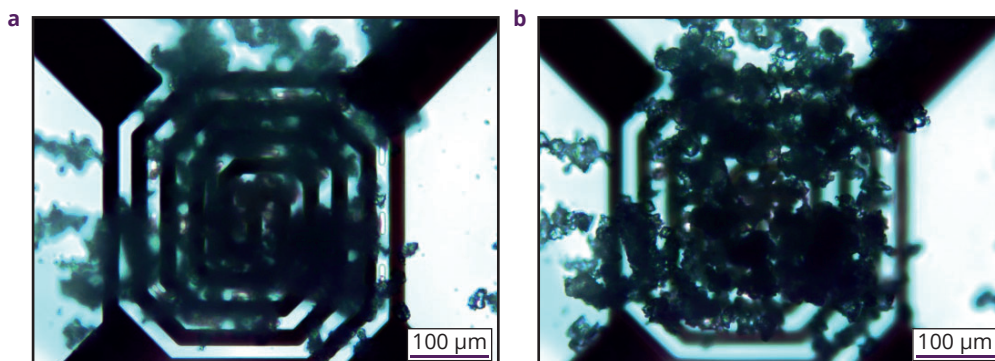


Figure 5.5 - Pictures of the NaYF_4 microcrystals dispersed on the heating spiral in the transparent window of the original MEMS nano-reactor. Optical microscopy images of the heating spiral with deposited NaYF_4 microcrystals with the spiral in focus (a) and the microcrystals in focus (b). The four contacts on the corners act as both heaters and integrated thermometers using electric resistance.

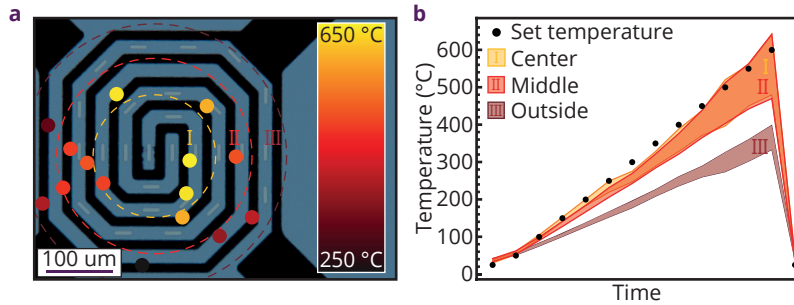


Figure 5.6 – Spatially resolved temperature measurements of the original MEMS nano-reactor in vacuum. Temperature measurements performed using a confocal microscope to monitor temperature at different spots of the heating spiral (a). The spiral is divided in three regions (I, II and III) and the average temperature of all the spots in a region is plotted vs. time while the set temperature (black dots) was varied (b).

the case of Boltzmann statistics, the correlation between the logarithm of the luminescence intensity ratio (I_2/I_1) should be linear with reciprocal temperature, which is shown in Figure 5.4c.

The correlation between the luminescence intensity ratio and reciprocal temperature could be fitted with a linear fit and show good agreement ($r^2 = 0.998$). This linear fit has been used in this work to evaluate luminescence output from measurements and calculate the corresponding temperatures.

Deposition of the NaYF₄ microcrystals. To monitor the temperature in the heating spiral, the NaYF₄ microcrystals were dropcasted on the spiral, as shown in Figure 5.5. Here, Figure 5.5a shows the spiral in focus, while Figure 5.5b shows the microcrystals in focus. The thickness of the NaYF₄ microcrystal layer is not uniform over the complete spiral. However, multiple measurements across varying thicknesses within one data set and between different data sets show that there is no correlation between the thickness of the layers of NaYF₄ used in this work and the temperature read-outs.

Temperature measurements in vacuum. After the successful deposition of the microcrystals, confocal microscopy is used to monitor the luminescence over the heating spiral at different temperatures. Using confocal microscopy, it is possible to obtain the spectral output in the range of 500–570 nm for every pixel in the microscopy image of Figure 5.6a. To obtain proper temperature read-outs, pixels are combined into regions of interest (ROIs), indicated by the colored circles of Figure 5.6a. Measurements were performed at room temperature and afterwards the temperature was increased from 50 °C to 600 °C with intervals of 50 °C (black points in Figure 5.6b). At every temperature, 6 luminescence measurements were performed for the full microscopy image and the temperature was determined per ROI. The colored dots in Figure 5.6a correspond with the temperature determined for that ROI at the temperature setpoint of 600 °C.

To get a better understanding of the temperature profile in the nano-reactor, the area of the spiral is divided in three areas (I, II and III). Here, area I is the area in the center of the

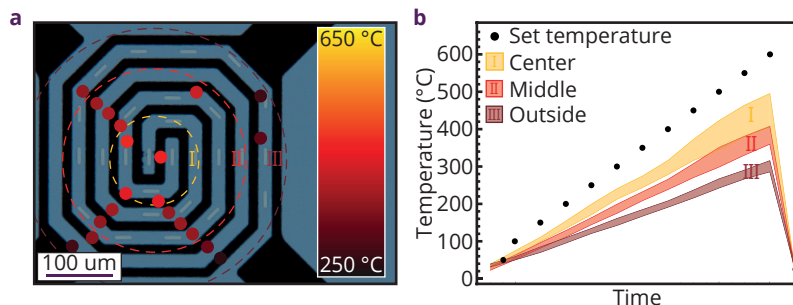


Figure 5.7 – Spatially resolved temperature measurements of the original MEMS nano-reactor in static air. Temperature measurements performed using a confocal microscope to monitor temperature at different spots of the heating spiral (a). The spiral is divided in three regions (I, II and III) and the average temperature of all the spots in a region is plotted vs. time while the set temperature (black dots) was varied (b).

spiral, area II is the area of the second ring around the center and area III is the outermost ring of the spiral. The different ROIs within an area are averaged and the standard deviation is determined. This was done for all temperatures and the data is shown in Figure 5.6b. Here, the temperatures within areas I (orange), II (red) and III (dark red) are plotted vs. time, while the set temperature is slowly increased from room temperature to 600 °C (black dots).

The results show that the temperature in areas I and II is identical, while area III is ca. 200 °C lower in temperature (at 600 °C). The temperatures in area I and II closely match the set temperatures, showing that the MEMS nano-reactor has an accurate temperature read-out via the resistance measurements. Furthermore, the temperature homogeneity is very good over the heating spiral. As expected, the outer turn of the spiral is colder, however, the heating is very localized on the spiral, resulting in a decrease of temperature of 200 °C already at the outermost parts of the spiral. In fact, luminescence measurements performed at ca. 50 μm from the heating spiral showed no changes with increased heating of the spiral (data not shown here), suggesting that the heating of the spiral is localized to within 50 μm of the heating spiral.

Temperature measurements in static air. Although the temperature measurements using luminescence thermometry are in good agreement with the temperature read-out using the resistance feedback, measurements in air are expected to differ due to heat dissipation. To monitor the effect of heat dissipation, the experiment performed above has been repeated under static air atmosphere, as shown in Figure 5.7.

Multiple ROIs have been measured to form a temperature distribution map as shown by the colored dots in Figure 5.7a. Similar to the vacuum experiments, the temperatures displayed with the colored dots in Figure 5.7a were obtained at a set temperature of 600 °C. Here, the luminescence measurements show a much lower temperature, with a maximum of ca. 450 °C. Upon dividing the spiral into three different areas (I, II and III), similar to the experiments in vacuum, it can be observed that the temperature homogeneity is no longer present. Figure 5.7b shows that a clear gradient is present within the heating spiral

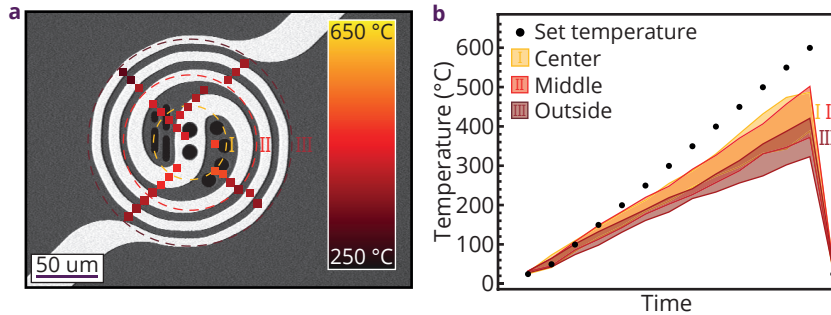


Figure 5.8 – Spatially resolved temperature measurements within latest generation of MEMS nano-reactor in static air. Temperature measurements performed using a confocal microscope to monitor temperature at different spots of the improved heating spiral (a). The spiral is divided in three regions (I, II and III) and the average temperature of all the spots in a region is plotted vs. time while the set temperature (black dots) was varied (b).

in which the inner part (area I) is hottest and the temperature gradually decreases towards the outside of the spiral (area II and III, respectively).

The results show that the atmosphere during measurements drastically influences the temperatures in the nano-reactor upon applying a specific voltage. Although the calibration is done properly for vacuum systems, heat dissipation in other atmospheres ensures that the temperature read-out via the resistance is no longer valid.

Temperature measurements in improved spiral design. In addition to the nano-reactor investigated in Figure 5.6 and 5.7, the latest generation MEMS nano-reactor of DENSSolutions⁴¹ (Figure 5.2e–f) has been investigated with regards to temperature heterogeneity. The improved heater design should result in no significant thermal expansion up to 700 °C in the monitored area and have a high temperature homogeneity. To test the improved properties of the new heater design, more temperature measurements have been performed using luminescence thermometry. Figure 5.8a shows the temperature read-outs at different spots along the new spiral design. Multiple ROIs have been measured to form a temperature distribution map as shown by the colored dots.

The measurements have been performed in static air atmosphere. Similar to the results of the original nano-reactor (Figure 5.7), the temperatures obtained are lower than the setpoint determined from resistance measurements. The obtained temperature of 450 °C at a setpoint of 600 °C is similar to the experiments on the old design spiral in air. Although the obtained temperatures are similar, clear differences in the distribution of the temperatures can be observed.

The temperature gradient is greatly repressed, as shown in Figure 5.8b. The heated area is divided in 3 areas (I, II and III) and the average temperature of the different ROIs within the areas are plotted while systematically increasing the temperature from room temperature to 600 °C. It can be observed in Figure 5.8b that the temperature differences between area I and II are negligible, showing that the temperature homogeneity is improved.

Furthermore, although area III is lower in temperature compared to area I and II, the temperature difference is much smaller compared to the old heating spiral (Figure 5.7b).

Luminescence thermometry measurements on the new design for the nano-reactor shows that, although the temperature decrease due to heat dissipation is still present, the distribution of temperature over the nano-reactor is more homogeneous. The experimental results of this chapter also demonstrate the potential and applicability of luminescence thermometry to monitor temperatures inside the MEMS nano-reactor introduced here. Additionally, the temperature can be mapped by combining the temperature-dependent luminescence of the $\text{NaYF}_4:\text{Er}^{3+}, \text{Yb}^{3+}$ microcrystals with confocal microscopy. ROIs of ca. $7 \mu\text{m}$ yielded sufficient spectral output to calculate temperatures up to $600 \text{ }^\circ\text{C}$.

The luminescence thermometry measurements performed in vacuum matched well with the temperature feedback of the MEMS nano-reactor, which is based on the temperature-dependent electrical resistance through the heating spiral. However, luminescence thermometry measurements performed under air resulted in significantly lower temperatures, $450 \text{ }^\circ\text{C}$ vs. $600 \text{ }^\circ\text{C}$ in vacuum. The results show that the MEMS nano-reactor, which is optimized for vacuum environment during TEM experiments, does not have accurate temperature read-outs in non-vacuum conditions. Additional experiments on the next-generation MEMS nano-reactor shows that the heat dissipation effect is similar but the temperature distribution over the nano-reactor is improved.

This work demonstrates that the localized temperature gradients can occur due to heat dissipation, which cannot be properly monitored using conventional thermometry techniques. For in situ or operando monitoring of chemical processes with STXM, localized temperature measurements are crucial to gain a full understanding of the processes that occur during X-ray measurements. This phenomenon is not limited to STXM but applies to any in situ measurement technique. This concept can be generalized further by considering for instance exothermic or endothermic reactions in catalysis in which local temperature gradients can occur.

To perform in situ or operando experiments properly, it is crucial that all relevant parameters, including temperature, are monitored on the relevant length scales. This work shows the clear potential for luminescence thermometry to monitor temperature with μm spatial resolution, allowing us to further develop our understanding of complex chemical reactions during in situ or operando measurements.

Conclusions

In this chapter we have introduced a new sample holder, containing a MEMS nano-reactor, for operando STXM measurements. A heating spiral can efficiently heat the nano-reactor and gas in-/outlets can introduce gasses, while at the same time monitoring reagents using on-line gas chromatography or mass spectrometry.

Although the STXM holder has been used in the past years during several synchrotrons measurements successfully, the temperature and the temperature distribution during in situ

measurements are difficult to monitor. The MEMS is adapted from an in situ TEM setup and therefore the temperature calibrations for the setup are performed in vacuum. The platinum heating spiral is used for Joule heating the nano-reactor and the linear response of electrical resistance with temperature is also exploited to monitor the temperature. Unfortunately, this method can only give an averaged value of the temperature within the reactor and insight in the temperature distribution is lacking. Using luminescence thermometry in combination with confocal microscopy, we have investigated the temperature and temperature distribution inside the MEMS in vacuum and static air. In vacuum the temperatures inside the MEMS measured with luminescence thermometry were homogeneously distributed over the heating spiral and matched the temperature read-out with electrical resistance up to at least 600 °C. In the case of air atmosphere, additional heat dissipation resulted in a temperature gradient from the center (450 °C) of the heating spiral to the outer turn (250 °C). A next generation reactor heater design has been evaluated afterwards in air and although the heating was more homogeneous, the maximum temperatures reached were similar to the temperatures reached in the previous experiments in static air, ca. 450 °C.

The results clearly show the potential of luminescence thermometry to map temperature with μm spatial resolution. Additionally, the results show that the local temperature fluctuations can result in significantly different temperatures compared to averaged temperature read-outs. The observed temperature discrepancy is due to the heat dissipation, however, other effects could also occur, such as exo- or endothermic reactions, in the case of operando STXM experiments. In order to investigate processes in which temperature is crucial, local temperature read-outs should be performed, and this work shows that luminescence thermometry has a great potential for this.

Experimental Section

Preparation of microcrystalline NaYF₄. Microcrystalline NaYF₄ doped with 19 % Yb³⁺ and 2 % Er³⁺ has been prepared using a solid state synthesis reported earlier by our group.⁴² In short, 15 mmol of dried NaF (Sigma-Aldrich, >98 %) , 15 mmol of RE₃ (RE = Y, Er, Yb, Sigma-Aldrich, 99.9 %) and 13.5 mmol of ammonium fluoride (Sigma-Aldrich, >98 %) were mixed with a pestle and mortar and afterwards placed in an alumina crucible. The mixture was heated in the oven in an excess of ammonium fluoride under a nitrogen atmosphere. The samples were heated to 573 K for 3 h and afterwards heated to 823 K for 8 h. The heating rate was 5 K min⁻¹ for both heating steps.

Setup. The STXM holder has been build inhouse and makes use of heating chips supplied by DENSSolutions and Else Kooi Lab. Temperature-mapping has been performed on a Nikon Eclipse 90i upright microscope. The microscope is equipped with a Nikon-Eclipse A1R scan head. Excitation was performed using a Melles Griot Argon ion 488 nm laser.

Acknowledgements

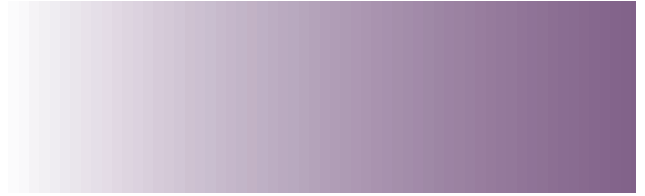
DENSSolutions is gratefully acknowledged for the fabrication of the nano-reactors and the valuable discussions. This work was supported by the Netherlands Center for Multiscale Catalytic Energy Conversion (MCEC), an NWO Gravitation programme funded by the Ministry of Education, Culture and Science of the government of the Netherlands as well as NWO and Shell Global Solutions International B.V. for a CHIPP research grant.

References

1. Tsakoumis, N. E.; Rønning, M.; Borg, Ø.; Rytter, E. & Holmen, A. Deactivation of Cobalt Based Fischer-Tropsch Catalysts: A Review. *Catal. Today* **2010**, *154*, 162–182.
2. Saib, A. M.; Moodley, D. J.; Ciobică, I. M.; Hauman, M. M.; Sigwebela, B. H.; Weststrate, C. J.; Niemantsverdriet, J. W. & van de Loosdrecht, J. Fundamental Understanding of Deactivation and Regeneration of Cobalt Fischer-Tropsch Synthesis Catalysts. *Catal. Today* **2010**, *154*, 271–282.
3. van Berge, P.; van de Loosdrecht, J.; Barradas, S. & van der Kraan, A. Oxidation of Cobalt Based Fischer-Tropsch Catalysts as a Deactivation Mechanism. *Catal. Today* **2000**, *58*, 321–334.
4. Zhou, W.; Chen, J. G.; Fang, K. G. & Sun, Y. H. The Deactivation of Co/SiO₂ catalyst for Fischer-Tropsch Synthesis at Different Ratios of H₂ to CO. *Fuel Process. Technol.* **2006**, *87*, 609–616.
5. Schanke, D.; Hilmen, A. M.; Bergene, E.; Kinnari, K.; Rytter, E.; Ådnanes, E. & Holmen, A. Reoxidation and Deactivation of Supported Cobalt Fischer-Tropsch Catalysts. *Energy & Fuels* **1996**, *10*, 867–872.
6. Kiss, G.; Kliewer, C. E.; DeMartin, G. J.; Culross, C. C. & Baumgartner, J. E. Hydrothermal Deactivation of Silica-Supported Cobalt Catalysts in Fischer-Tropsch Synthesis. *J. Catal.* **2003**, *217*, 127–140.
7. Bertole, C. J.; Mims, C. A. & Kiss, G. The Effect of Water on the Cobalt-Catalyzed Fischer-Tropsch Synthesis. *J. Catal.* **2002**, *210*, 84–96.
8. Claeys, M.; Dry, M. E.; Van Steen, E.; Van Berge, P. J.; Booyens, S.; Crous, R.; Van Helden, P.; Labuschagne, J.; Moodley, D. J. & Saib, A. M. Impact of Process Conditions on the Sintering Behavior of an Alumina-Supported Cobalt Fischer-Tropsch Catalyst Studied with an in Situ Magnetometer. *ACS Catal.* **2015**, *5*, 841–852.
9. Moodley, D. J.; van de Loosdrecht, J.; Saib, A. M.; Overett, M. J.; Datye, A. K. & Niemantsverdriet, J. W. Carbon Deposition as a Deactivation Mechanism of Cobalt-Based Fischer-Tropsch Synthesis Catalysts under Realistic Conditions. *Appl. Catal. A Gen.* **2009**, *354*, 102–110.
10. Lee, D.-K.; Lee, J.-H. & Ihm, S.-K. Effect of Carbon Deposits on Carbon Monoxide Hydrogenation over Alumina-Supported Cobalt Catalyst. *Appl. Catal.* **1988**, *36*, 199–207.
11. Cats, K. H.; Andrews, J. C.; Stéphan, O.; March, K.; Karunakaran, C.; Meirer, F.; de Groot, F. M. F. & Weckhuysen, B. M. Active Phase Distribution Changes within a Catalyst Particle during Fischer-Tropsch Synthesis as Revealed by Multi-Scale Microscopy. *Catal. Sci. Technol.* **2016**, *6*, 4438–4449.
12. Gonzalez-Jimenez, I. D.; Cats, K.; Davidian, T.; Ruitenbeek, M.; Meirer, F.; Liu, Y.; Nelson, J.; Andrews, J. C.; Pianetta, P.; de Groot, F. M. F. & Weckhuysen, B. M. Hard X-Ray Nanotomography of Catalytic Solids at Work. *Angew. Chem. Int. Ed.* **2012**, *51*, 11986–11990.
13. Cats, K. H.; Gonzalez-Jimenez, I. D.; Liu, Y.; Nelson, J.; van Campen, D.; Meirer, F.; van der Eerden, A. M. J.; de Groot, F. M. F.; Andrews, J. C. & Weckhuysen, B. M. X-Ray Nanoscopy of Cobalt Fischer-Tropsch Catalysts at Work. *Chem. Commun.* **2013**, *49*, 4622–4624.

14. Aldana, P. A. U.; Ocampo, F.; Kobl, K.; Louis, B.; Thibault-Starzyk, F.; Daturi, M.; Bazin, P.; Thomas, S. & Roger, A. C. Catalytic CO₂ Valorization into CH₄ on Ni-Based Ceria-Zirconia. Reaction Mechanism by Operando IR Spectroscopy. *Catal. Today* **2013**, *215*, 201–207.
15. Lesage, T.; Verrier, C.; Bazin, P.; Saussey, J. & Daturi, M. Studying the NO_x-Trap Mechanism over a Pt-Rh/Ba/Al₂O₃ Catalyst by Operando FT-IR Spectroscopy. *Phys. Chem. Chem. Phys.* **2003**, *5*, 4435–4440.
16. Hartman, T. & Weckhuysen, B. M. Thermally Stable TiO₂- and SiO₂-Shell-Isolated Au Nanoparticles for In Situ Plasmon-Enhanced Raman Spectroscopy of Hydrogenation Catalysts. *Chem. Eur. J.* **2018**, *24*, 3733–3741.
17. Cheng, S.; Yang, L.; Chen, D.; Ji, X.; Jiang, Z. jie; Ding, D. & Liu, M. Phase Evolution of an Alpha MnO₂-Based Electrode for Pseudo-Capacitors Probed by in Operando Raman Spectroscopy. *Nano Energy* **2014**, *9*, 161–167.
18. Goetze, J.; Meirer, F.; Yarulina, I.; Gascon, J.; Kapteijn, F.; Ruiz-Martínez, J. & Weckhuysen, B. M. Insights into the Activity and Deactivation of the Methanol-to-Olefins Process over Different Small-Pore Zeolites as Studied with Operando UV-Vis Spectroscopy. *ACS Catal.* **2017**, *7*, 4033–4046.
19. Groothaert, M. H.; Lievens, K.; Leeman, H.; Weckhuysen, B. M. & Schoonheydt, R. A. An Operando Optical Fiber UV-Vis Spectroscopic Study of the Catalytic Decomposition of NO and N₂O over Cu-ZSM-5. *J. Catal.* **2003**, *220*, 500–512.
20. Sakdinawat, A. & Attwood, D. Nanoscale X-Ray Imaging. *Nat. Photonics* **2010**, *4*, 840–848.
21. De Smit, E.; Swart, I.; Creemer, J. F.; Hoveling, G. H.; Gilles, M. K.; Tyliczszak, T.; Kooyman, P. J.; Zandbergen, H. W.; Morin, C. & Weckhuysen, B. M.; et al. Nanoscale Chemical Imaging of a Working Catalyst by Scanning Transmission X-Ray Microscopy. *Nature* **2008**, *456*, 222–225.
22. Al Samarai, M.; Meirer, F.; Karunakaran, C.; Wang, J.; Vogt, E. T. C.; Zandbergen, H. W.; Weber, T.; Weckhuysen, B. M. & De Groot, F. M. F. Unraveling the Redox Behavior of a CoMoS Hydrodesulfurization Catalyst: A Scanning Transmission X-Ray Microscopy Study in the Tender X-Ray Range. *J. Phys. Chem. C* **2015**, *119*, 2530–2536.
23. Ravenhorst, I. K.; Vogt, C.; Oosterbeek, H.; Bossers, K. W.; Moya-Cancino, J. G.; van Bavel, A. P.; van der Eerden, A. M. J.; Vine, D.; de Groot, F. M. F.; Meirer, F. & Weckhuysen, B. M. Capturing the Genesis of an Active Fischer-Tropsch Synthesis Catalyst with Operando X-ray Nano-Spectroscopy. *Angew. Chem. Int. Ed.* **2018**, *130*, 12133–12138.
24. Papavasiliou, J.; Avgouropoulos, G. & Ioannides, T. In Situ Combustion Synthesis of Structured Cu-Ce-O and Cu-Mn-O Catalysts for the Production and Purification of Hydrogen. *Appl. Catal. B Environ.* **2006**, *66*, 168–174.
25. Briand, D.; Krauss, A.; Van Der Schoot, B.; Weimar, U.; Barsan, N.; Göpel, W. & De Rooij, N. F. Design and Fabrication of High-Temperature Micro-Hotplates for Drop-Coated Gas Sensors. *Sensors Actuators, B Chem.* **2000**, *68*, 223–233.
26. Mele, L.; Konings, S.; Dona, P.; Evertz, F.; Mitterbauer, C.; Faber, P.; Schampers, R. & Jinschek, J. R. A MEMS-Based Heating Holder for the Direct Imaging of Simultaneous in-Situ Heating and Biasing Experiments in Scanning/Transmission Electron Microscopes. *Microsc. Res. Tech.* **2016**, *79*, 239–250.
27. Creemer, J. F.; Santagata, F.; Morana, B.; Mele, L.; Alan, T.; Iervolino, E.; Pandraud, G. & Sarro, P. M. An All-in-One Nanoreactor for High-Resolution Microscopy on Nanomaterials at High Pressures. *Proc. IEEE Int. Conf. Micro Electro Mech. Syst.* **2011**, 1103–1106.
28. de Groot, F. M. F., de Smit, E., van Schooneveld, M. M., Aramburo, L. R. & Weckhuysen, B. M. In-situ Scanning Transmission X-Ray Microscopy of Catalytic Solids and Related Nanomaterials. *ChemPhysChem* **2010**, *11*, 951–962.

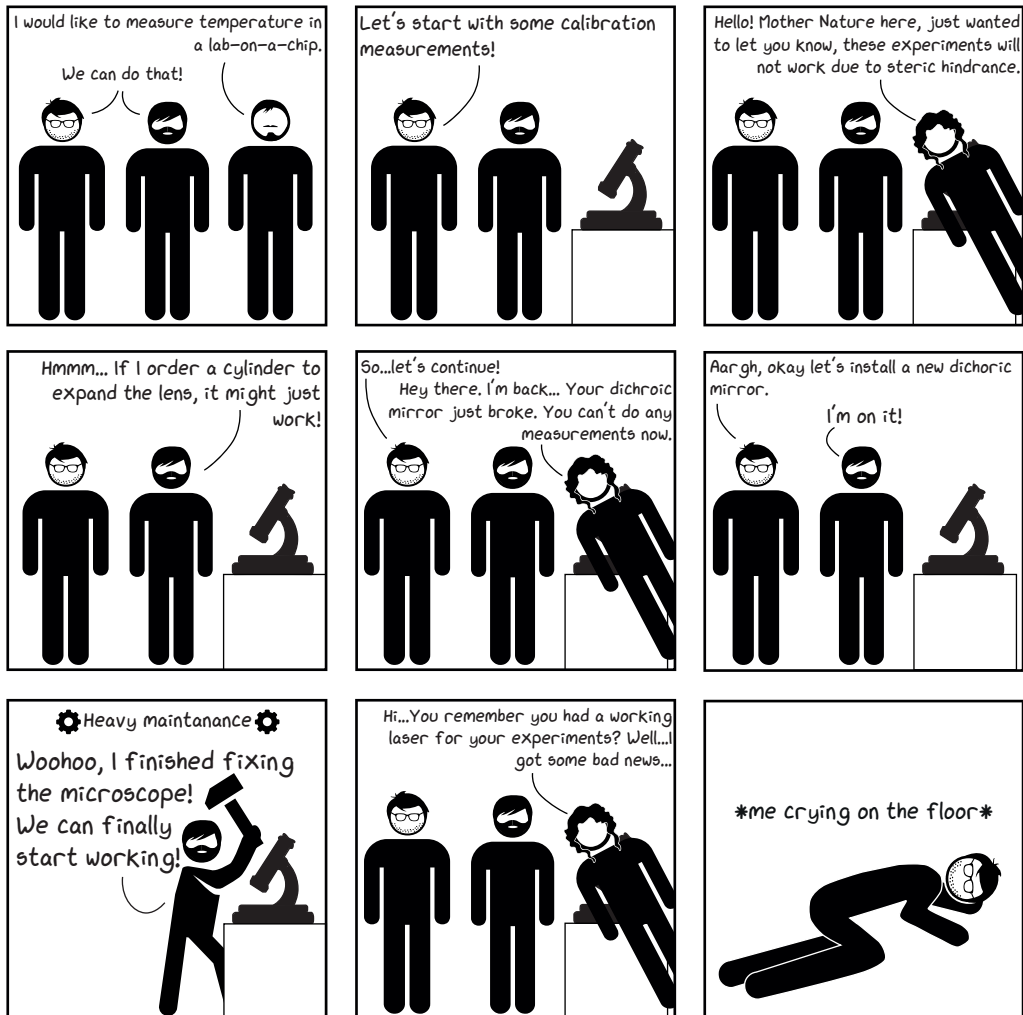
29. Aramburo, L. R., de Smit, E., Arstad, B., van Schooneveld, M. M., Sommer, L., Juhin, A., Yokosawa, T., Zandbergen, H. W., Olsbye, U., de Groot, F. M. F. & Weckhuysen, B. M. X-ray Imaging of Zeolite Particles at the Nanoscale: Influence of Steaming on the State of Aluminum and the Methanol-To-Olefin Reaction. *Angew. Chem. Int. Ed.* **2012**, *51*, 3616–3619.
30. Cicmil, D., Meeuwissen, J., Vantomme, A., Wang, J., van Ravenhorst, I. K., van der Bij, H. E., Muñoz-Murillo, A. & Weckhuysen, B. M. Polyethylene with Reverse Co-monomer Incorporation: From an Industrial Serendipitous Discovery to Fundamental Understanding. *Angew. Chem. Int. Ed.* **2015**, *54*, 13073–13079.
31. Niekel, F.; Kraschewski, S. M.; Müller, J.; Butz, B. & Spiecker, E. Local Temperature Measurement in TEM by Parallel Beam Electron Diffraction. *Ultramicroscopy* **2017**, *176*, 161–169.
32. Vendelbo, S. B.; Kooyman, P. J.; Creemer, J. F.; Morana, B.; Mele, L.; Dona, P.; Nelissen, B. J. & Helveg, S. Method for Local Temperature Measurement in a Nanoreactor for in Situ High-Resolution Electron Microscopy. *Ultramicroscopy* **2013**, *133*, 72–79.
33. Geitenbeek, R. G.; Prins, P. T.; Albrecht, W.; van Blaaderen, A.; Weckhuysen, B. M. & Meijerink, A. NaYF₄:Er³⁺,Yb³⁺/SiO₂ Core/Shell Upconverting Nanocrystals for Luminescence Thermometry up to 900 K. *J. Phys. Chem. C* **2017**, *121*, 3503–3510.
34. Jaque, D. & Vetrone, F. Luminescence Nanothermometry. *Nanoscale* **2012**, *4*, 4301–4326.
35. Brites, C. D. S.; Lima, P. P.; Silva, N. J. O.; Millán, A.; Amaral, V. S.; Palacio, F. & Carlos, L. D. Thermometry at the Nanoscale. *Nanoscale* **2012**, *4*, 4799–4829.
36. Pandey, A. & Rai, V. K. Optical Thermometry Using FIR of Two Close Lying Levels of Different Ions in Y₂O₃:Ho³⁺-Tm³⁺-Yb³⁺ Phosphor. *Appl. Phys. B Lasers Opt.* **2013**, *113*, 221–225.
37. Xu, X.; Wang, Z.; Lei, P.; Yu, Y.; Yao, S.; Song, S.; Liu, X.; Su, Y.; Dong, L. & Feng, J. α-NaYb(Mn)F₄:Er³⁺/Tm³⁺@NaYF₄ UCNPs as “Band-Shape” Luminescent Nanothermometers over a Wide Temperature Range. *ACS Appl. Mater. Interfaces* **2015**, *7*, 20813–20819.
38. Li, D.; Wang, Y.; Zhang, X.; Yang, K.; Liu, L. & Song, Y. Optical Temperature Sensor through Infrared Excited Blue Upconversion Emission in Tm³⁺/Yb³⁺ Codoped Y₂O₃. *Opt. Commun.* **2012**, *285*, 1925–1928.
39. Vetrone, F.; Naccache, R.; Zamarrón, A.; Juarranz de la Fuente, A.; Sanz-Rodríguez, F.; Martínez Maestro, L.; Martín Rodríguez, E.; Jaque, D.; García Solé, J. & Capobianco, J. A. Temperature Sensing Using Fluorescent Nanothermometers. *ACS Nano* **2010**, *4*, 3254–3258.
40. Li, T.; Guo, C.; Zhou, S.; Duan, C. & Yin, M. Highly Sensitive Optical Thermometry of Yb³⁺-Er³⁺ Codoped AgLa(MoO₄)₂ Green Upconversion Phosphor. *J. Am. Ceram. Soc.* **2015**, *98*, 2812–2816.
41. van Omme, J. T.; Zakhosheva, M.; Spruit, R. G.; Sholkina, M. & Pérez Garza, H. H. Advanced Microheater for in Situ Transmission Electron Microscopy; Enabling Unexplored Analytical Studies and Extreme Spatial Stability. *Ultramicroscopy* **2018**, *192*, 14–20.
42. Aarts, L.; van der Ende, B. M. & Meijerink, A. Downconversion for Solar Cells in NaYF₄:Er,Yb. *J. Appl. Phys.* **2009**, *106*, 023522.



Based on

- Vollenbroek, J. C.; Bomer, J. G.; van den Berg, A.; Odijk, M.; Nieuwelink, A.-E.; Weckhuysen, B. M.; Geitenbeek, R. G.; Meijerink, A. & Tiggelaar, R. M. Design and characterization of a microreactor for monodisperse catalytic droplet generation at both elevated temperatures and pressures. *NEMS*, **2017**, 746–751.
- Geitenbeek, R. G.; Vollenbroek, J. C.; Weijgertze, H. M. H.; Trégouët, C. B. M.; Nieuwelink, A.-E.; Kennedy, C.; Weckhuysen, B. M.; van Blaaderen, A.; Odijk, M.; van den Berg, A. & Meijerink, A. Luminescence Thermometry for In Situ Temperature Measurements in Microfluidic Devices. *Lab on a Chip*, *submitted*

Chapter 6 – Luminescence Thermometry in Microfluidic Systems



Robin Geitenbeek



Chris Kennedy



Corentin Trégouët



Mother Nature
(I don't like her)

Abstract

Microfluidics is a promising field of research with many applications, especially due to the more recent integrated functionalities such as temperature and pressure control or automatic sorting systems. Temperature control has resulted in broad applicability of microfluidics in e.g. polymerase chain reaction (PCR), temperature gradient focussing for electrophoresis and colloidal particle syntheses. Although many different methods for heating have been developed (e.g. microwave-assisted heating, Joule heating and exothermic reactions), it is still difficult to map the temperature within such a lab-on-a-chip. In this chapter, we introduce ratiometric bandshape luminescence thermometry in which the thermally coupled levels of Er^{3+} , Yb^{3+} -doped NaYF_4 nanoparticles are used as a promising method for temperature mapping in microfluidic systems. The results demonstrate in three different showcases, that temperatures can be monitored in a microfluidic channel accurately (0.5 °C) up to at least 120 °C with a spot size of ca. 1 mm using simple fiber optics. It is also shown that the spatial resolution can be enhanced further by combining bandshape luminescence thermometry with confocal microscopy, resulting in a spot size of ca. 9 μm . Continued experiments can further enhance the spatial resolution of the technique and also allow for 3D temperature profiling.

Introduction

Microfluidics is the science of systems that process small amounts of fluids (10^{-9} – 10^{-18} L). Originally, microfluidics became of interest rapidly due to the potential in analysis.^{1,2} The small quantities required, low costs, short analysis time and ability to carry out separation and detection with high resolution and sensitivity, make microfluidic devices ideal for portable analytics. Although applications in analytics was the driving force behind the expansion of the field, chemical synthesis relying on microfluidics has also gained a lot of attention recently.^{3–5} Performing reactions in flow can result in faster synthesis at smaller scales with the ability to detect ‘short-lived’ reaction intermediates and to monitor reaction kinetics over the course of the microfluidic device. As a result, both upscaling and high-throughput experiments can be performed by parallelization. A clear advantage of the parallelization is the safety and the absence of difficulties with volumetric upscaling as compared to batch syntheses.

In order to increase the applicability of microfluidic devices, different functionalities can be integrated. One of the most important functionalities in a microfluidic device is temperature control. By controlling the temperature distribution and the temperature range, applications such as polymerase chain reaction (PCR),^{6,7} temperature gradient focusing for electrophoresis^{8,9} and nanocrystal syntheses^{10,11} become possible.

Temperature control inside microfluidic devices can be obtained through multiple methods. External heating methods rely on producing heat outside the microchip and subsequently transferring the heat inside the microfluidic device. This was demonstrated using Peltier elements^{12,13} or externally heated fluids.¹⁴ Integrated heating techniques include exploiting endo- and exothermic processes,¹⁵ microwave heating^{16–19} and Joule heating.^{20–23} By fabrication of channels in close proximity of platinum microstructures, the channels can be heated efficiently by applying a voltage over the platinum microstructures.²⁴ An extra advantage of Joule heating is the ability to monitor temperature by exploiting the temperature-dependent resistance of the heating elements, made of for instance platinum,²⁵ nickel²⁶ or gold.²⁷ Since the resistance scales near-linearly with temperature, an accurate and relative fast read-out of temperature can be achieved. Although the spatial resolution of such a thermometer can be around 30 μm , monitoring temperature at multiple locations within a microfluidic device requires extensive electronics and can be limited due to spatial constraints.

To overcome this localization problem, non-invasive spectroscopic techniques have been developed to monitor temperature at multiple locations within microfluidic devices. The parameters observed in these spectroscopic techniques are for instance the luminescence intensity²⁸ or absorbance²⁹ of a dye molecule and the intensity ratio of the Stokes and anti-Stokes peaks in Raman spectroscopy.³⁰ Although the techniques work in principle, there are also several disadvantages. In the case of fluorescence or absorbance of dye molecules, the signal read-out is also heavily depending on the concentration of the dye. Small fluctuations in excitation power or probe concentration can result in inaccurate

temperature read-outs. In Raman spectroscopy, the ratio between Stokes and anti-Stokes peak are compared, resulting in a ratiometric technique which is no longer dependent on the probe concentration. However, Raman signals are typically very low and the local environment has a large influence on the Raman signal.

In this chapter we introduce bandshape luminescence thermometry^{31,32} as an alternative ratiometric spectroscopic technique to monitor temperature non-invasively. This type of luminescence thermometry exploits the changes in emission of two or more emission peaks with temperature.^{33,34} In this work, the lanthanide ion Er^{3+} incorporated in NaYF_4 nanoparticles (NPs) was used.^{35,36} In Er^{3+} , emission from 500–570 nm is due to the transitions from the excited state ${}^2\text{H}_{11/2}$ and ${}^4\text{S}_{3/2}$ to the ${}^4\text{I}_{15/2}$ ground state. The energy difference between the two excited states is ca. 700 cm^{-1} (or several kT), resulting in thermally coupled levels in which the populations are governed by Boltzmann statistics. This ratiometric temperature-dependent luminescence can be used to monitor temperatures in microfluidic devices.

Here, we showcase three different microfluidic devices to demonstrate the versatility of the luminescence thermometry. The first case shows a comparison between an integrated platinum resistance temperature detector (RTD) and the luminescence thermometry technique which showed good agreement (average offset around $0.34\text{ }^\circ\text{C}$) over a wide range of temperature up to at least $120\text{ }^\circ\text{C}$. The integrated RTD however was only able to monitor temperature at one specific spot while luminescence thermometry has the potential to monitor anywhere on the silicon/glass microreactor. The second showcase highlights the potential to monitor small temperature fluctuations due to the exothermic reaction of hydrochloric acid and ammonia. Here NPs coated with SiO_2 are dispersed in both liquids and upon mixing temperature increases of ca $15\text{ }^\circ\text{C}$ were observed in a polydimethylsiloxane (PDMS)/glass microfluidic device. The final showcase increasing the spatial resolution by combining the fluorescence measurements with confocal microscopy. Here, a glass/glass microreactor with a set temperature gradient was monitored. A temperature gradient of $60\text{--}40\text{ }^\circ\text{C}$ over $500\text{ }\mu\text{m}$ was monitored with a spatial resolution of $9\text{ }\mu\text{m}$, in initial experiments that did not yet fully explore 3D measurements and the highest resolution achievable.

These three examples show the great potential for bandshape luminescence thermometry to monitor temperatures within microfluidic devices. Using this non-invasive technique, temperatures up to at least $120\text{ }^\circ\text{C}$ can be monitored with high accuracy ($0.3\text{ }^\circ\text{C}$) and great spatial resolution in 3D (better than $9\text{ }\mu\text{m}$).

Results and Discussion

Temperature-dependent luminescence. To showcase the potential for luminescence thermometry in microfluidic devices, three different microfluidic devices were prepared and investigated. In all three setups, NaYF_4 NPs doped with Yb^{3+} and Er^{3+} , well known for remote temperature sensing,^{34–36} were used as temperature probes which are shown in Figure 6.1a–c. In the second example (Figure 6.1b), the NaYF_4 NPs were overgrown with a

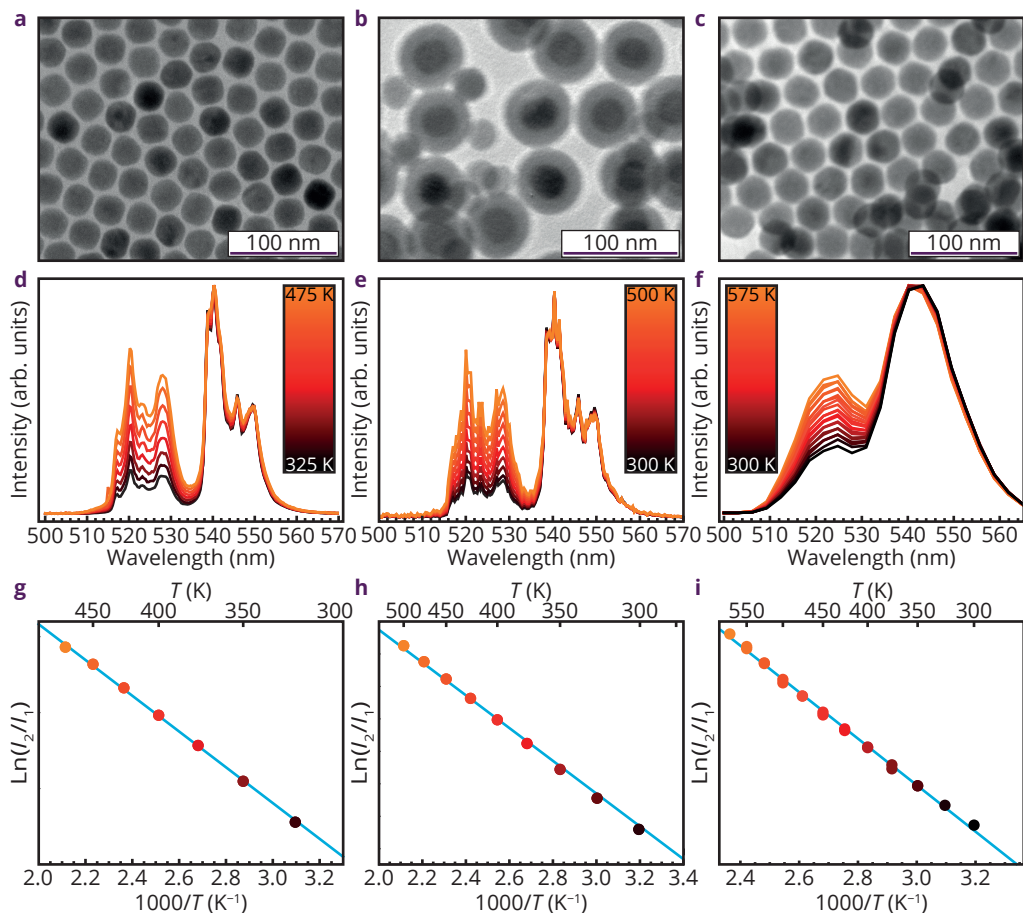


Figure 6.1 – Luminescence and structural characterization. TEM micrographs of NaYF₄ NPs (a,c) and NaYF₄@SiO₂ NPs (b) for the performed experiments. Temperature-dependent luminescence of Er³⁺-doped NaYF₄ NPs used for the different temperature sensing experiments in the different setups discussed in this chapter (d–f). The obtained calibration lines by plotting the logarithm of the fluorescence intensity ratio, Ln(I_2/I_1), vs. reciprocal temperature, $1/T$ (g–i).

protective layer of SiO₂ for chemical stability and dispersibility in polar solvents.³⁵

In all cases, the NPs showed typical temperature-dependent luminescence as shown in Figure 6.1d–f. At room temperature (black spectra) both emission peaks from the ²H_{11/2} (525 nm, I_2) and ⁴S_{3/2} (545 nm, I_1) excited state are observed. The small energy difference between the two excited states, ca. 700 cm⁻¹ (several kT at room temperature), guarantees quick relaxation between the two excited states and the population distribution is governed by Boltzmann statistics. Upon increasing temperature (black to orange) the additional thermal energy shifts the populations and the emission from the higher excited state (²H_{11/2}) becomes more pronounced.³³

Due to Boltzmann statistics, the correlation between the logarithm of the fluorescence

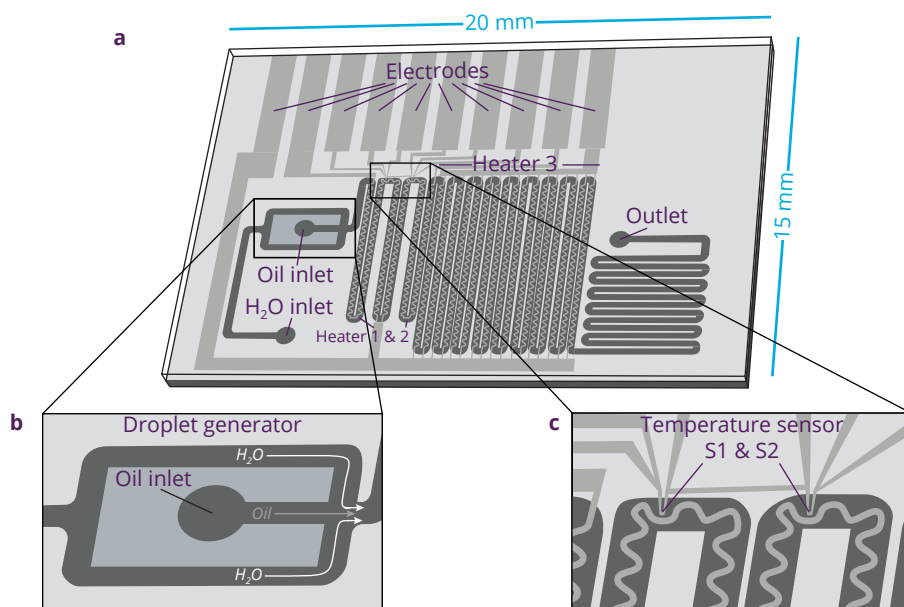


Figure 6.2 – Schematic overview of microfluidic device. Droplet flow microfluidic device for on chip heating and temperature sensing (a). Using the oil inlet and water inlet, droplets can be prepared (b) which can flow through the chip with channel dimensions of 150 μm . The droplets can be heated using the built-in platinum heaters and the temperature is controlled using two built-in platinum temperature sensors S1 and S2 (c).

intensity ratio $\ln(I_2/I_1)$ and reciprocal temperature is linear. The linear fits (cyan lines) for the three different temperature probes are shown in Figure 6.1g–i. The fits are of high quality ($r^2 = 0.999, 0.997$ and 0.998 , respectively) and are used throughout this chapter for temperature calculations from the obtained spectra during the experiments.

Luminescence thermometry on silicon/glass devices. The first experiment to showcase the potential of luminescence thermometry for temperature sensing in microfluidic devices is performed in the glass/silicon chip shown in Figure 6.2. Here, the microfluidic device contains several electrodes which are connected to integrated platinum heaters and two platinum temperature sensors (S1 and S2). The chip can either be used for continuous flow or droplet flow experiments because of the flow focusing geometry, using the two inlets.

In these experiments, the temperature was monitored using both the integrated platinum thermometers as well as the NaYF₄ NPs (Figure 6.1a) dispersed in 1-octadecene (ODE). First, the thermometers were compared by monitoring temperatures using both integrated thermometers S1 and S2 and the luminescence output at the same location. Figure 6.3a shows the obtained temperatures from both techniques by cycling the temperature between 70 and 120 °C. The red dots are the temperatures measured with the integrated thermometers while the cyan dots represent the temperatures calculated by exploiting the temperature-dependent luminescence from the NPs.

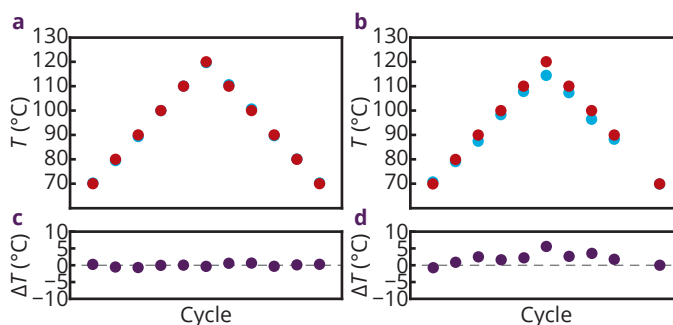


Figure 6.3 – Temperature measurements. Temperature measurements using the on-chip thermometers (red datapoints) and temperature-dependent luminescence from the NaYF₄ NPs (cyan dots). The temperatures were determined on the same spot as the platinum thermometer (a) and at the end of the chip (b). The temperature difference measured by the platinum thermometer and the NPs is plotted for the same spot (c) and the end of the chip (d).

The temperature outputs from both techniques match well as shown in Figure 6.3c. Here, the temperature difference between the two thermometry techniques is plotted. The maximum and mean discrepancies observed were 0.68 °C and 0.34 °C, respectively. These results show that the thermal resistance detectors are valid methods to monitor temperatures inside microfluidic channels even though the platinum sensors are located just outside the channels.

Figure 6.3b shows the datapoints obtained from both thermometers while monitoring the luminescence output at the end of the microfluidic device in the optical window. Note that only heater 1 and 2 were on during these experiments. The obtained temperatures from the integrated thermometers were cycled from 70–120 °C, similar to the previous experiment. However, since the luminescence output is monitored at a different spot in the chip, cooling down of the liquid passing through the device can result in lower temperatures monitored with luminescence thermometry. This can be observed in Figure 6.3d where larger temperature discrepancies between the two different temperature sensing techniques is shown. At 70 °C this effect is still minimal, however, at higher temperatures the temperature offset increases up to 5.6 °C at 130 °C. Although the temperature decrease was minimal due to the high thermal conductance of the silicon, the luminescence thermometry technique is sensitive enough to monitor these small temperature differences.

These experiments show very good agreement (errors less than 0.68 °C) between thermal resistance detector and the luminescence thermometry performance using dispersed NPs in the channels of a microfluidic device. Even though the platinum sensors are just outside the channels, the obtained temperatures from the resistance measurements are accurate. However, the fabrication of integrated platinum temperature sensors is difficult and requires several electrodes and space on the device. The luminescence thermometry technique shows a great potential for monitoring temperatures inside microfluidic devices by using a non-invasive spectroscopy technique, which can easily monitor temperatures at

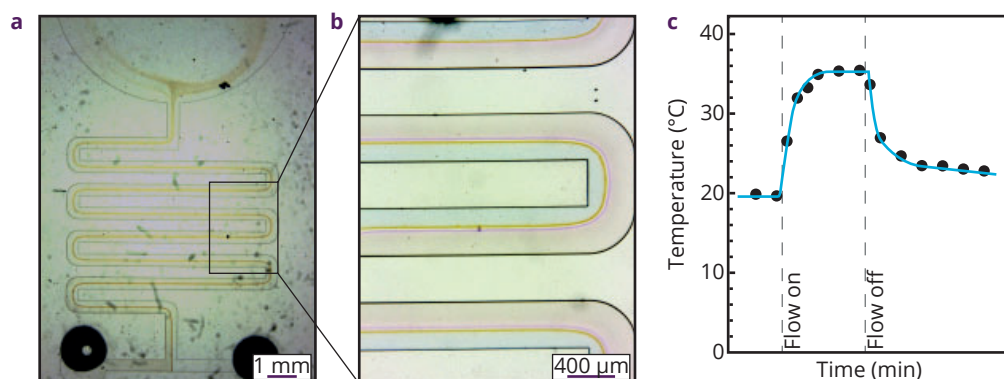


Figure 6.4 – PDMS microfluidic device. Optical microscopy image of a simple microfluidic device (a) with two inlets in which ammonia and hydrochloric acid are introduced in combination with a pH indicator thymol blue. The (lack of) mixing is visualized with the indicator having the red color at low pH, yellow color at intermediate pH and blue color at high pH (b). Temperature measurements which visualize the heating up due to mixing of the caustic soda and hydrochloric acid (c).

different locations at the chip.

Luminescence thermometry in PDMS/glass devices. The above experiments show the clear potential of the NaYF_4 NPs for temperature measurements in microfluidic devices. To further showcase the versatility of the luminescence thermometry for T-sensing in microfluidics, a second example is shown below.

Here, the potential of luminescence thermometry to monitor temperature changes during an exothermic chemical reaction is monitored. In these experiments, NaYF_4 NPs are encapsulated in a protective SiO_2 shell (Figure 6.1b) and afterwards transferred to a 5M NH_3 solution and a 4M HCl solution. These two solutions are then introduced to a simple PDMS/glass chip with a T-junction where the solutions meet and subsequently meander through the channels of the device as shown in Figure 6.4a and 6.4b. At the end of the meandering chip, the liquid is collected in a large chamber (top of Figure 6.4a) and an outlet expels the liquid afterwards.

The temperature-dependent luminescence of the NaYF_4 NPs, dispersed in both liquids, is monitored at the end of the meandering channels. Using the calibration line from Figure 6.1h, the spectral output was converted to temperature, as shown in Figure 6.4c.

Figure 6.4c shows that there is an increase of ca. 15 °C in temperature when the flow is turned on, indicating that the exothermicity of the reaction can be properly monitored. Upon turning the flow off, the temperature slowly decreases to room temperature.

Although the experiments show a clear increase in temperature due to the reaction of NH_3 and a HCl solution, the increase in temperature is relatively small. This is mostly like due to lack of mixing of the two liquids due to the laminar flow inside the microfluidic device.

To validate this, a pH indicator, thymol blue, was added to both liquids while flowing

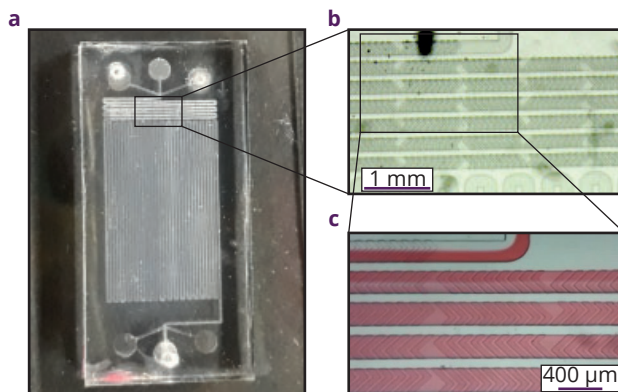


Figure 6.5 – PDMS microfluidic device with staggered herringbone mixer. Photograph of PDMS microfluidic device (a), a zoom-in on the staggered herringbone mixer at the start of the device (b) and the mixing using water and a red dye (c).

through the device. Thymol blue has a blue color in basic media ($\text{pH} = 8.0\text{--}9.6$), a red color in acidic media ($\text{pH} = 1.2\text{--}2.8$) and a yellow color at neutral pH. Images of the thymol blue flowing through the microfluidic device are shown in Figure 6.4a and 6.4b. It can be observed that the main volume of the liquid is still unmixed (red and blue) while some mixing occurs at the interface (yellow). Due to incomplete mixing, the exothermicity of the reaction is only limited to an increase of temperature of ca. $15\text{ }^{\circ}\text{C}$.

The mixing of the liquids can be enhanced using different on-chip techniques. One example is shown in Figure 6.5. Here, a staggered herring bone mixer is shown which can enhance mixing. This is illustrated by mixing water and a red dye solution as shown in Figure 6.5c. The fluids do not mix due to the laminar flow until the encounter with the staggered herringbone mixer and quickly after, a homogeneous red solution is obtained, indicating successful mixing.

Luminescence thermometry in glass/glass devices. The final showcase to present the potential of luminescence thermometry in microfluidics is shown below. Here, a microfluidic device is used in which a temperature gradient is introduced by integrated

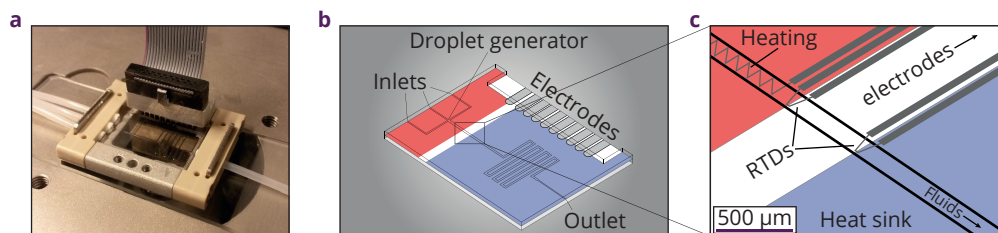


Figure 6.6 – Chip design. A photograph of the chip used during the luminescence thermometry experiments (a). A schematic overview of the chip, including the inlets and outlet, the droplet generator and the electrodes for integrated heating and temperature sensing (b). A zoom-in of the temperature gradient in the chip by exploiting a heat sink and platinum wires for heating and temperature sensing (c).

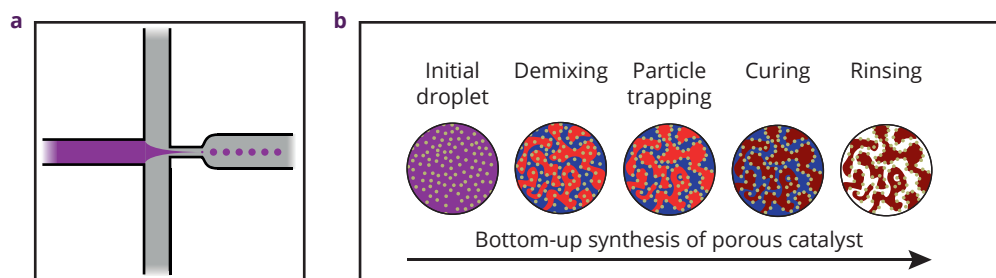


Figure 6.7 – Overview of microfluidics bottom-up synthesis of porous catalyst. Using flow focussing, droplets are created (a) with PEG and PPG (purple droplet) and TiO_2 NPs (brown dots). By cooling down rapidly the PEG and PPG are demixed (red and blue, respectively) and particles migrate to the surface. Subsequently UV curing hardens the PEG with a curing agent (dark red) and the PPG can be removed, resulting in porous catalyst particles (b).

platinum heaters and a cold sink as shown in Figure 6.6. The temperature gradient depends on the settings of the heater and usually results in a temperature decrease of ca. 10–20 °C over a distance of 500 μm .

The chip is designed to have a stable temperature gradient over a short distance in order to perform the bottom-up synthesis of porous catalyst particles as shown in Figure 6.7. Here, polyethylene glycol diacrylate (PEG-DA) and polypropylene glycol (PPG) are mixed with TiO_2 catalyst NPs. At higher temperatures, the droplets, dispersed in fluorinated oil, are a homogeneous mixture of PEG-DA, PPG and TiO_2 NPs. However, at lower temperatures, the PEG and PPG start to demix. In order to lower the surface tension, the TiO_2 NPs will adhere to the interface between the PEG and PPG. A curing agent present in the PEG can be activated using UV irradiation and the PEG hardens out. After retrieval from the microfluidic device, the PPG can be removed by rinsing the particles with ethanol, resulting in porous particles with TiO_2 NPs on the surface.

To control the demixing, particle trapping and curing, a stable temperature gradient is required, resulting in the design of the chip as shown in Figure 6.6. To monitor the temperature gradient, two platinum resistance thermometers are incorporated in the device separated by 500 μm . Although the measurements can be performed accurately as demonstrated in the first showcase of this work, two datapoints are insufficient to determine a temperature gradient properly.

In order to obtain a better understanding of the temperature distribution in the microfluidic channel, NaYF_4 NPs (Figure 6.1c) dispersed in cyclohexane were flushed through the microfluidic device. Information on the temperature distribution was obtained by monitoring the temperature-dependent luminescence using confocal microscopy while heating the channel by applying a potential of 25 V to the platinum heaters. In this fashion, it was possible to probe multiple spots of ca. 9 μm to reconstruct the temperature gradient in the channel, illustrated in Figure 6.8b.

Temperatures were calculated from the obtained spectra and a temperature distribution was

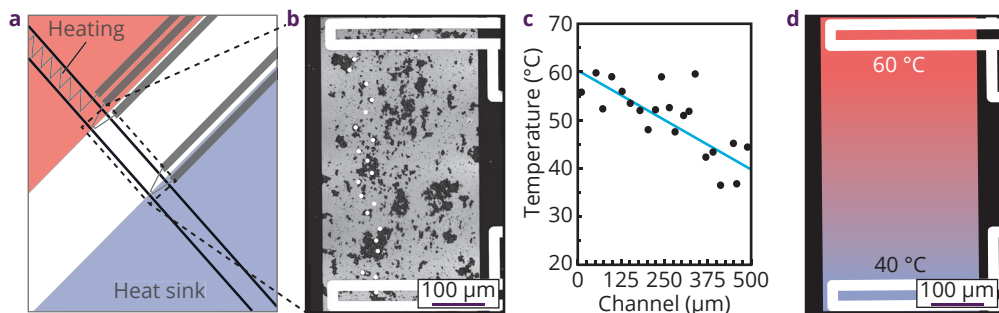


Figure 6.8 – Confocal microscopy measurements. A schematic representation of the channel area that is designed with the temperature gradient (a). A confocal microscopy image of the area between the two RTDs in white (b). Specific regions of interest (ROIs) are shown as white circles. The temperature gradient was visualized by plotting the obtained temperatures from the different ROIs vs. location in the channel (c). Finally, the temperature gradient in the channel has been illustrated (d).

found as shown in Figure 6.8c. Here, the obtained temperatures are plotted vs. the position in the microchannel. The temperatures obtained show a decrease from ca. 60 °C to 40 °C. This is further visualized in Figure 6.8d, where a temperature gradient is shown in which the red color represents 60 °C and the blue color represents 40 °C. Note that the results in Figure 6.8c are still preliminary. The temperature still fluctuates around the trend line with a mean difference of 3.6 °C between the datapoints and the linear fit. Even though the uncertainty in these measurements is still relatively high, the trend of the temperature gradient can be observed. Further experiments using confocal microscopy are in progress and are aimed at improving the accuracy of the experiments.

The three different showcases demonstrate the versatility and robustness of the luminescence thermometry technique for monitoring temperatures within microfluidic devices. By dispersing NPs in the fluids, non-invasive luminescence techniques can be exploited to monitor temperatures within silicon/glass, glass/glass or PDMS/glass microfluidic devices with high accuracy (ca. 0.5 °C) up to at least 120 °C.

The approach to use lanthanides in inorganic NPs has multiple advantages. In this work we show that the temperature probes can be used in both polar and apolar solvents by changing the surface of the NPs. The surface chemistry of NPs is well investigated^{37,38} and can be used for instance to attach the NPs to the inner channel wall of the microfluidic chip as fixed local temperature probes. The inorganic host is inert and the f-f transitions of the lanthanide dopants (responsible for the temperature-dependent luminescence) is not influenced by the environment which ensures non-invasive temperature sensing that can be universally applied without the need for calibration.

The use of 980 nm IR excitation induces upconversion, resulting in temperature-dependent luminescence in the visible region with minimal background fluorescence. Care has to be taken to verify that the IR excitation does not give rise to sample heating.

The showcases demonstrate that a large variety of microfluidic devices can be investigated

with different spatial resolutions. For simple cases in which the spatial resolution is limited to the different regions on the microfluidic device, fiber optics are sufficient to localize excitation and detection of light to the 0.5 mm regime, allowing to monitor the temperature in single channels. If higher spatial resolutions are required, confocal microscopy can be used to reach higher spatial resolutions, down to 9 μm in this work.

Conclusions

In summary, we have investigated the potential for luminescence thermometry in microfluidics. After preparing NaYF_4 and $\text{NaYF}_4@\text{SiO}_2$ core/shell NPs doped with Er^{3+} and Yb^{3+} , the temperature-dependent luminescence of the Er^{3+} ions has been exploited to determine temperatures by monitoring the spectral output. The as-synthesized NaYF_4 NPs were dispersed in apolar solvents. After growing a SiO_2 shell, the NPs could be transferred to polar media and many procedures also exist (e.g. coating with linear alkanes like octadecanol) to have these particles dispersed stably in apolar solvents as well.

To showcase the potential of bandshape luminescence thermometry, the temperature inside three different microfluidic devices was monitored. The microfluidic devices were made of silicon/glass, glass/glass or PDMS/glass. The results show good agreement between the luminescence output and the temperatures determined by integrated platinum RTDs with an average difference of 0.34 $^\circ\text{C}$ up to 120 $^\circ\text{C}$. The three different examples show that temperature can be monitored in systems with a constant temperature, a temperature gradient or even temperature profiles due to exothermic reactions.

In two examples, fiber optics have been used for the detection of the fluorescence signal, resulting in a spot size of ca. 1 mm. Although the spot size is quite large for microfluidics, the probe can be used to monitor temperatures at different parts of the microfluidic device easily. To increase the spatial resolution of local temperature measurements and in addition the extension to 3D measurements, the final showcase was performed using confocal microscopy. In this way, temperature measurements could be performed with a spatial resolution down to at least 9 μm .

The showcases highlighted in this chapter show that bandshape luminescence thermometry has clear potential for temperature measurements within microfluidic setups. Due to the ratiometric nature of the technique, the measurements are independent of probe concentration and the upconversion luminescence ensures minimal background fluorescence. Using a simple fiber probe system spot sizes of ca. 1 mm can be monitored with high accuracy (0.5 $^\circ\text{C}$) up to at least 120 $^\circ\text{C}$. The spatial resolution can be enhanced further and expanded to 3D by combining the fluorescence measurements with (confocal) microscopy.

Experimental Section

Chemicals. All chemicals were used without further purification. The following chemicals were purchased from Sigma-Aldrich: Cyclohexane (99.5 %, CH), oleic acid (90 %, OA), ethanol (>99.8 %, EtOH), methanol (>99.85 %, MeOH), sodium hydroxide (>97 %, NaOH).

NaOH), ammonium fluoride (>98 %, NH_4F), ammonium hydroxide (28 wt% in H_2O , ammonia), rare-earth acetate hydrates (99.9 %, $\text{RE}(\text{Ac})_3 \cdot x\text{H}_2\text{O}$), tetraethyl orthosilicate (99.999 %, TEOS), and IGEPAL CO-520 ($(\text{C}_2\text{H}_4\text{O})_n \cdot \text{C}_{15}\text{H}_{24}\text{O}$ with $n \sim 5$, average $\text{Mn} = 441 \text{ g mol}^{-1}$, NP-5). 1-octadecene (90 %, ODE) was purchased from Acros Organics.

Setup. Luminescence measurements using the fiber probe were performed using a MDL-III-980nm-500mW laser. Upon excitation light was collected via a fiber patch cord and a shortpass filter to the OceanOptics QEPro CCD detector. Confocal microscopy images were taken using a Leica SP8 microscope with a 40x/0.55 long working distance objective. The integrated Coherent Chameleon II Ti:Sapphire laser was tuned to 980 nm.

NP synthesis. $\text{NaYF}_4@\text{SiO}_2$ nanoparticles (NPs) doped with 18 % Yb^{3+} and 2 % Er^{3+} of ca. 50 nm were prepared via an initial synthesis of NaYF_4 core particles (ca. 25 nm) and subsequent SiO_2 overgrowth as reported earlier.^{35,39}

Silicon/glass chip. The microreactor is fabricated in the cleanroom of the MESA+ Nanolab at the University of Twente. The reactor consists of a silicon and MEMPAX (borosilicate glass) substrate anodically bonded together. Fluidic channels are etched into the silicon substrate by Deep Reactive Ion Etching (DRIE). A 200 nm SiO_2 layer is thermally grown onto walls of the channels by dry oxidation of the silicon substrate. Channels are 150 μm deep and vary from 150–300 μm in depth. Buffered HF is used to wet etch small trenches (200 nm) into the MEMPAX substrate into which a 10 nm tantalum adhesion layer and 190 nm platinum is sputtered. Subsequently, the Ta/Pt electrodes are covered with 1 μm of SiO_2 via plasma-enhanced chemical vapor deposition to insulate them from the channels.

PDMS/glass chip. For fabrication of the PDMS/glass chips a mold out of SU-8, a commonly used epoxy-based photoresist, is made in the MESA+ Nanolab at the University of Twente. Using photolithography, SU-8 structures of 100 μm high and 200 μm wide are fabricated on a silicon substrate. After development these structures are used as a softlithography mold for casting PDMS. A PDMS vs. curing agent mass ratio of 10:1 is used. The PDMS is then poured on the silicon/SU-8 mold after which it is cured in an oven for two hours at 60 °C. After curing, in- and outlets of 1 mm are punched in the PDMS chip, subsequently the PDMS is treated in an O_2 plasma oven for 2 minutes after which it is bonded to a glass substrate. Finally the PDMS/glass chip is heated to 60 °C for 30 minutes to ensure proper bonding.

Glass/glass chip. The chip consists of two wafers of borosilicate glass on top of each other. Semicircular channels are etched with HF in the top wafer: a protective layer of resin (1.7 μm of olin photoresist) is spin-coated and patterned on the wafer to expose only specific regions to the acid which can subsequently be used to draw the channels. On the top wafer, 100 nm of platinum is specifically deposited over a small recess and an adhesive layer of tantalum using lithography to design electrodes, connecting pads, and a heat sink which consists of large area of platinum in both sides of the channels to dissipate heat laterally. Finally 1 μm of silicon dioxide is grown on top of it via plasma-enhanced chemical vapor deposition (except on the connecting pads) to avoid chemical reaction in our solutions at

the contact of platinum. Holes are made in the top wafer by powder blasting to access the connecting pads and the two wafers are bonded together at high temperature and high pressure, and finally diced into several microfluidic chips. The channels cross the dicing lines to provide opening inlets and outlets.

References

1. Manz, A.; Harrison, D. J.; Verpoorte, E. M. J.; Fettinger, J. C.; Paulus, A.; Lüdi, H. & Widmer, H. M. Planar Chips Technology for Miniaturization and Integration of Separation Techniques into Monitoring Systems. Capillary Electrophoresis on a Chip. *J. Chromatogr. A* **1992**, *593*, 253–258.
2. Whitesides, G. M. The Origins and the Future of Microfluidics. *Nature* **2006**, *442*, 368–373.
3. Köhler, J. M.; Held, M.; Hübner, U. & Wagner, J. Formation of Au/Ag Nanoparticles in a Two Step Micro Flow-through Process. *Chem. Eng. Technol.* **2007**, *30*, 347–354.
4. Wang, H.; Nakamura, H.; Uehara, M.; Miyazaki, M. & Maeda, H. Preparation of Titania Particles Utilizing the Insoluble Phase Interface in a Microchannel Reactor. *Chem. Commun.* **2002**, *2*, 1462–1463.
5. Nightingale, A. M. & DeMello, J. C. Segmented Flow Reactors for Nanocrystal Synthesis. *Adv. Mater.* **2013**, *25*, 1813–1821.
6. Maltezos, G.; Johnston, M.; Taganov, K.; Srichantaratsamee, C.; Gorman, J.; Baltimore, D.; Chantratita, W. & Scherer, A. Exploring the Limits of Ultrafast Polymerase Chain Reaction Using Liquid for Thermal Heat Exchange: A Proof of Principle. *Appl. Phys. Lett.* **2010**, *97*, 264101.
7. Hua, Z.; Rouse, J. L.; Eckhardt, A. E.; Srinivasan, V.; Pamula, V. K.; Schell, W. A.; Benton, J. L.; Mitchell, T. G. & Pollack, M. G. Multiplexed Real-Time Polymerase Chain Reaction on a Digital Microfluidic Platform. *Anal. Chem.* **2010**, *82*, 2310–2316.
8. Matsui, T.; Franzke, J.; Manz, A. & Janasek, D. Temperature Gradient Focusing in a PDMS/Glass Hybrid Microfluidic Chip. *Electrophoresis* **2007**, *28*, 4606–4611.
9. Ross, D. & Locascio, L. E. Microfluidic Temperature Gradient Focusing. *Anal. Chem.* **2002**, *74*, 2556–2564.
10. Mirhosseini Moghaddam, M.; Baghbanzadeh, M.; Sadeghpour, A.; Glatter, O. & Kappe, C. O. Continuous-Flow Synthesis of CdSe Quantum Dots: A Size-Tunable and Scalable Approach. *Chem. - A Eur. J.* **2013**, *19*, 11629–11636.
11. Song, Y.; Hormes, J. & Kumar, C. S. S. R. Microfluidic Synthesis of Nanomaterials. *Small* **2008**, *4*, 698–711.
12. Khandurina, J.; McKnight, T. E.; Jacobson, S. C.; Waters, L. C.; Foote, R. S. & Ramsey, J. M. Integrated System for Rapid PCR-Based DNA Analysis in Microfluidic Devices. *Anal. Chem.* **2000**, *72*, 2995–3000.
13. Yang, J.; Liu, Y.; Rauch, C. B.; Stevens, R. L.; Liu, R. H.; Lenigk, R. & Grodzinski, P. High Sensitivity PCR Assay in Plastic Micro Reactors. *Lab Chip* **2002**, *2*, 179–187.
14. Mao, H.; Yang, T. & Cremer, P. S. A Microfluidic Device with a Linear Temperature Gradient for Parallel and Combinatorial Measurements. *J. Am. Chem. Soc.* **2002**, *124*, 4432–4435.
15. Guijt, R. M.; Dodge, A.; van Dedem, G. W. K.; de Rooij, N. F. & Verpoorte, E. Chemical and Physical Processes for Integrated Temperature Control in Microfluidic Devices. *Lab Chip* **2003**, *3*, 1.
16. Shah, J. J.; Geist, J. & Gaitan, M. Microwave-Induced Adjustable Nonlinear Temperature Gradients in Microfluidic Devices. *J. Micromechanics Microengineering* **2010**, *20*, 105025.
17. Bykov, Y. V.; Rybakov, K. I. & Semenov, V. E. High-Temperature Microwave Processing of Materials. *J. Phys. D. Appl. Phys.* **2001**, *34*, R55–R75.

18. Geist, J.; Shah, J. J.; Rao, M. V. & Gaitan, M. Microwave Power Absorption in Low-Reflectance, Complex, Lossy Transmission Lines. *J. Res. Natl. Inst. Stand. Technol.* **2007**, *112*, 177.
19. Kappe, C. O. & Dallinger, D. The Impact of Microwave Synthesis on Drug Discovery. *Nat. Rev. Drug Discov.* **2006**, *5*, 51–63.
20. Jiao, Z.; Huang, X.; Nguyen, N.-T. & Abgrall, P. Thermocapillary Actuation of Droplet in a Planar Microchannel. *Microfluid. Nanofluidics* **2008**, *5*, 205–214.
21. Jiao, Z. J.; Huang, X. Y. & Nguyen, N.-T. Manipulation of a Droplet in a Planar Channel by Periodic Thermocapillary Actuation. *J. Micromechanics Microengineering* **2008**, *18*, 045027.
22. Selva, B.; Marchalot, J. & Jullien, M.-C. An Optimized Resistor Pattern for Temperature Gradient Control in Microfluidics. *J. Micromechanics Microengineering* **2009**, *19*, 065002.
23. Vigolo, D.; Rusconi, R.; Piazza, R. & Stone, H. A. A Portable Device for Temperature Control along Microchannels. *Lab Chip* **2010**, *10*, 795.
24. Pattekar, A. V. & Kothare, M. V. A Microreactor for Hydrogen Production in Micro Fuel Cell Applications. *J. Microelectromechanical Syst.* **2004**, *13*, 7–18.
25. Lagally, E. T.; Emrich, C. A. & Mathies, R. A. Fully Integrated PCR-Capillary Electrophoresis Microsystem for DNA Analysis. *Lab Chip* **2001**, *1*, 102.
26. Arata, H. F.; Rondelez, Y.; Noji, H. & Fujita, H. Temperature Alternation by an On-Chip Microheater to Reveal Enzymatic Activity of β -Galactosidase at High Temperatures. *Anal. Chem.* **2005**, *77*, 4810–4814.
27. Burns, M. A. An Integrated Nanoliter DNA Analysis Device. *Science.* **1998**, *282*, 484–487.
28. Ross, D.; Gaitan, M. & Locascio, L. E. Temperature Measurement in Microfluidic Systems Using a Temperature-Dependent Fluorescent Dye. *Anal. Chem.* **2001**, *73*, 4117–4123.
29. Wätzig, H. The Measurement of Temperature inside Capillaries for Electrophoresis Using Thermochromic Solutions. *Chromatographia* **1992**, *33*, 445–448.
30. Liu, K. L.; Davis, K. L. & Morris, M. D. Raman Spectroscopic Measurement of Spatial and Temporal Temperature Gradients in Operating Electrophoresis Capillaries. *Anal. Chem.* **1994**, *66*, 3744–3750.
31. Jaque, D. & Vetrone, F. Luminescence Nanothermometry. *Nanoscale* **2012**, *4*, 4301–4326.
32. Brites, C. D. S.; Lima, P. P.; Silva, N. J. O.; Millán, A.; Amaral, V. S.; Palacio, F. & Carlos, L. D. Thermometry at the Nanoscale. *Nanoscale* **2012**, *4*, 4799–4829.
33. Li, T.; Guo, C.; Zhou, S.; Duan, C. & Yin, M. Highly Sensitive Optical Thermometry of Yb^{3+} - Er^{3+} Codoped $\text{AgLa}(\text{MoO}_4)_2$ Green Upconversion Phosphor. *J. Am. Ceram. Soc.* **2015**, *98*, 2812–2816.
34. Vetrone, F.; Naccache, R.; Zamarrón, A.; Juarranz de la Fuente, A.; Sanz-Rodríguez, F.; Martínez Maestro, L.; Martín Rodríguez, E.; Jaque, D.; García Solé, J. & Capobianco, J. A. Temperature Sensing Using Fluorescent Nanothermometers. *ACS Nano* **2010**, *4*, 3254–3258.
35. Geitenbeek, R. G.; Prins, P. T.; Albrecht, W.; Van Blaaderen, A.; Weckhuysen, B. M. & Meijerink, A. $\text{NaYF}_4:\text{Er}^{3+},\text{Yb}^{3+}/\text{SiO}_2$ Core/Shell Upconverting Nanocrystals for Luminescence Thermometry up to 900 K. *J. Phys. Chem. C* **2017**, *121*, 3503–3510.
36. Xu, X.; Wang, Z.; Lei, P.; Yu, Y.; Yao, S.; Song, S.; Liu, X.; Su, Y.; Dong, L.; Feng, J. & Zhang, H. α - $\text{NaYb}(\text{Mn})\text{F}_4:\text{Er}^{3+}/\text{Tm}^{3+}@\text{NaYF}_4$ UCNPs as “Band-Shape” Luminescent Nanothermometers over a Wide Temperature Range. *ACS Appl. Mater. Interfaces* **2015**, *7*, 20813–20819.
37. Albanese, A.; Tang, P. S. & Chan, W. C. W. The Effect of Nanoparticle Size, Shape, and Surface Chemistry on Biological Systems. *Annu. Rev. Biomed. Eng.* **2012**, *14*, 1–16.

38. Kango, S.; Kalia, S.; Celli, A.; Njuguna, J.; Habibi, Y. & Kumar, R. Surface modification of inorganic nanoparticles for development of organic–inorganic nanocomposites—A review. *Prog. Polym. Sci.* **2013**, *38*, 1232–1261.
39. Koole, R.; van Schooneveld, M. M.; Hilhorst, J.; de Mello Donegá, C.; 't Hart, D. C.; van Blaaderen, A.; Vanmaekelbergh, D. & Meijerink, A. On the Incorporation Mechanism of Hydrophobic Quantum Dots in Silica Spheres by a Reverse Microemulsion Method. *Chem. Mater.* **2008**, *20*, 2503–2512.



Based on

- Geitenbeek, R. G.; Hartman, T.; Whiting, G. & Weckhuysen, B. M. Extrudate Sensors for Probing Metal-Support Interfacial Catalytic Reactions Using Operando SHINERS and Luminescence Thermometry, *Nat. Catal.*, *submitted*

Abstract

The search for novel heterogeneous catalysts depends on our detailed knowledge of the active phase. Insights in the relationship between activity and structure, including the underlying reaction mechanism, contribute to the development of new or improved catalysts. In this work, we have developed a unique set of catalyst extrudate sensors that allowed for the simultaneous detection of local temperature and surface species. Core/shell nanoparticles consisting of $\text{Yb}^{3+}, \text{Er}^{3+}$ -codoped $\text{NaYF}_4@ \text{SiO}_2$, able to probe the temperature changes as a function of the applied reactions conditions, have been combined with supported $\text{Au}@ \text{SiO}_2$ core/shell nanoparticles, capable of enhancing the Raman signals of surface species. The principle of this sensing approach has been explored for the CO hydrogenation over Rh catalysts. The CO hydrogenation mechanism over Rh was studied using a combination of shell-isolated nanoparticle-enhanced Raman spectroscopy, on-line mass spectrometry and infrared spectroscopy. The combination of the different methods provides a unique approach towards the further understanding of the relevant parameters in operando spectroscopy measurements.

Introduction

The design of the ideal heterogeneous catalyst requires detailed knowledge of the interaction with its environment.¹ Since chemical reactions over solid catalysts are dictated by their surface properties, a variety of characterization techniques are required to probe the catalyst-reactant interface. In particular when the measurements are performed in situ or operando, the information obtained will contribute to a better understanding of operating catalysts.²⁻⁴

A new generation of spectroscopic techniques therefore focuses on higher sensitivity for improved spatial and temporal resolution. An example of a recent technique, is shell-isolated nanoparticle-enhanced Raman spectroscopy (SHINERS).^{5,6} The conduction electrons at the surface of the metal nanoparticles (NPs) resonate in a wide spectral region around the laser wavelength, resulting in a strong enhancement of the Raman signal.⁷ The isolating SiO₂ shell ensures a stable nanostructure for characterization of the structure of the catalyst, as well as adsorbed species up to 400 °C.⁸ The advantage of using Raman-based spectroscopic techniques in addition to for example infrared (IR) spectroscopy, is the ability to observe vibrations in the low wavenumber regime and characterize direct metal-adsorbate interactions. However, the yield of shell-isolated nanoparticles (SHINs) in a typical synthesis is usually not sufficient for practical operando experiments in heterogeneous catalysis. In situ experiments are therefore carried out separately from product analysis on similar bulk catalysts.⁹

Another recent invention involving NP sensors for heterogeneous catalysis, is bandshape luminescence thermometry.^{10,11} Bandshape luminescence thermometry, a technique with many applications ranging from catalysis¹² to bio-imaging,¹³ relies on temperature-dependent luminescence in which the ratio between two (or more) emission peaks changes with temperature.

Temperature, in addition to catalyst structure and composition, plays an important role for the activity and selectivity of catalytic reactions.¹⁴ To fully correlate catalytic processes to the conditions, it is important to monitor reaction temperature on the same length scale as XAS, IR or SHINERS, i.e. measuring the temperature of an individual catalyst particle. Temperature sensing on the catalyst particle level still proves to be difficult. A few temperature measurements have been performed during catalytic reactions,¹⁵ mainly using nuclear magnetic resonance (NMR),¹⁶ black body radiation^{17,18} or by the use of multiple thermocouples.¹⁹ Although using multiple thermocouples can give a general idea of temperature gradients in chemical reactors, monitoring temperatures on smaller length scales is still rather difficult. In addition, thermocouples can disturb a reactor bed and non-invasiveness cannot be guaranteed. IR-thermography is difficult to implement if light absorbing species are present, while the interpretation of NMR-thermometry is cumbersome and depends on the concentration of the probed species.¹⁶ In order to monitor temperature using a non-invasive method with sufficient spatial resolution, bandshape luminescence thermometry can be exploited.^{10,11}

We have therefore developed a set of extrudate sensors that can be practically implemented in a reactor bed for both luminescence thermometry and SHINERS, in addition to the already existing variety of characterization techniques. SHINs are assembled on the outside of a SiO₂ extrudate containing Yb³⁺,Er³⁺-codoped NaYF₄@SiO₂ core/shell nanoparticles which in this work are exploited for their temperature-dependent luminescence of the Er³⁺ dopant.^{20,21} Here, the ⁴S_{3/2} and ²H_{11/2} excited states are separated by an energy difference of ca. 700 cm⁻¹ (or several kT at room temperature)²² and the population of the energy levels is governed by Boltzmann statistics,²³ resulting in unique temperature-dependent luminescence.

As a showcase, CO hydrogenation has been performed in which syngas (a CO/H₂ mixture) is converted into hydrocarbons, such as methane, ethane and propane. Rh catalysts were impregnated over these extrudate sensors to monitor reaction temperature and SHINERS during the Rh-catalyzed CO hydrogenation reaction. Rh is an interesting metal for the study of CO hydrogenation because it can produce hydrocarbons, alcohols and other oxygenates, depending on the experimental conditions.²⁴ Its catalytic properties are often ascribed to the position of Rh in the periodic table. On the left side of Rh and above, elements such as Fe and Co dissociate CO to form hydrocarbons in Fischer-Tropsch synthesis. In contrast, on the right and below, Pd and Pt do not dissociate CO and produce methanol.

We show that SHINERS allow for accurate measurements of adsorbed species under reaction conditions, while the temperature sensors allow for local temperature read-outs within a single catalyst particle in a reactor bed. The products of CO hydrogenation (i.e. CH₄, C₃H₈, CO₂ and H₂O) were monitored with on-line MS, while increasing the temperature up to a setpoint of 350 °C and simultaneously monitoring temperature and surface species. The increase of catalytic activity at elevated temperatures is directly correlated with the SHINER and FT-IR spectra for the first time under operando conditions. The importance of the temperature measurements of the catalytic system itself was demonstrated by monitoring the catalyst temperature during CO hydrogenation, where a mismatch was observed between the set temperature and the actual temperature obtained with luminescence thermometry.

Moreover, upon changing the CO/H₂ ratio in the gas at a constant flow speed, temperature differences of up to 40 °C were observed. The main reason for the temperature mismatch was accredited to heat dissipation in the reactor by H₂. These results show that the local temperature can significantly differ from temperature read-outs of ‘bulk’ methods, emphasizing the need for local temperature measurements during operando experiments.

The results presented show the clear potential for luminescence thermometry in combination with other diagnostic tools, in this work SHINERS. These tools can be further complemented by the incorporation of e.g. UV-Vis spectroscopy. The potential to simultaneously monitor crucial parameters, such as temperature and surface species, under reaction conditions at the single catalyst particle level allows for new insights to be obtained for catalytic reaction mechanics, as showcased here for catalytic CO hydrogenation.

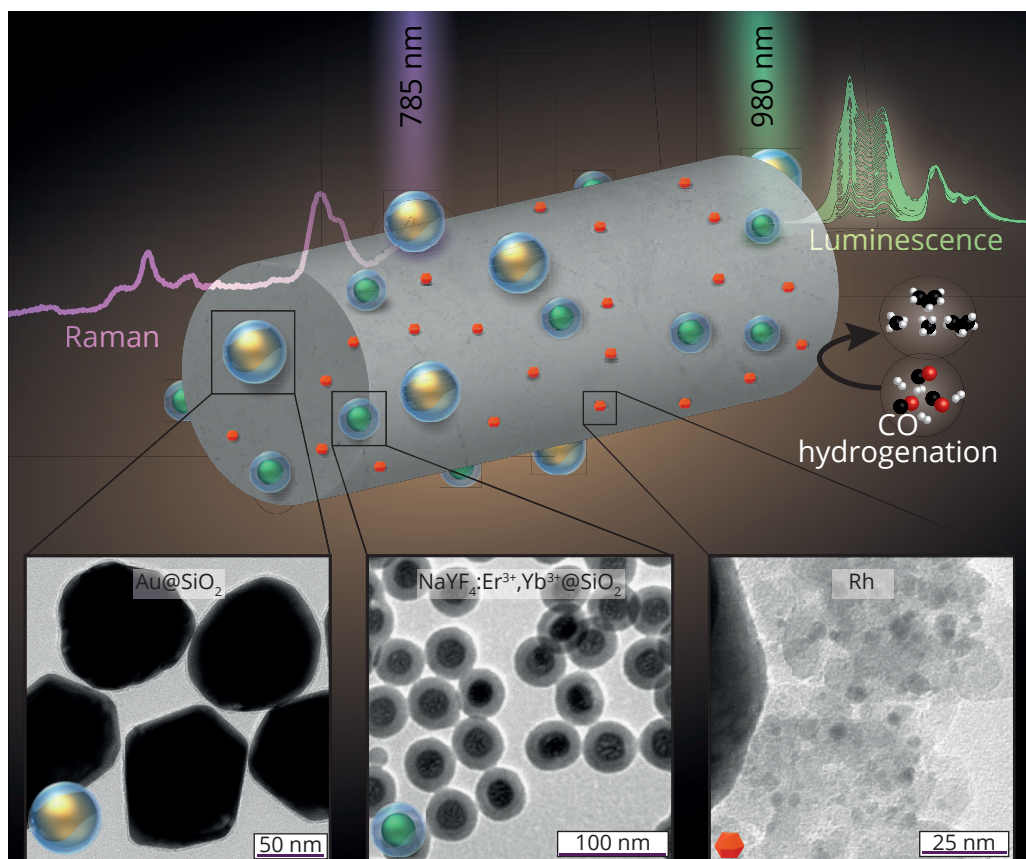


Figure 7.1 – Schematic illustration of an catalyst extrudate sensor for operando spectroscopy research. The grey SiO_2 -extrudate carrying Au@SiO_2 SHINs (gold spheres), Rh catalysts (red particles) and $\text{NaYF}_4@\text{SiO}_2$ temperature sensors (green spheres) to simultaneously measure temperature and SHINERS. TEM micrographs of the prepared Au@SiO_2 SHINs (left zoom-in), $\text{NaYF}_4@\text{SiO}_2$ temperature sensors (middle zoom-in), and Rh catalyst NPs (right zoom-in).

Results and Discussion

Sensor overview. To enable SHINERS measurements with simultaneous temperature measurements using luminescence thermometry, mm-sized catalyst extrudates containing $\text{NaYF}_4@\text{SiO}_2$ were prepared with ca. 1:1 weight ratio $\text{NaYF}_4@\text{SiO}_2$ and SiO_2 binder. Subsequently, Au@SiO_2 SHINs were deposited on the exterior surface of the extrudate followed by a wet-impregnation with RhCl_3 and subsequent oxidation and reduction to form 1 wt% Rh/ SiO_2 . The experimental details of the prepared system can be found in the Experimental Section as well as in previous work^{5,8,12,25}. Figure 7.1 shows a schematic representation of the prepared sensor system in which SHINERS (purple spectrum) and luminescence thermometry (green spectra) are combined.

Structural characterization. The Au@SiO_2 particles (Yellow spheres, $D = 88 \pm 7.8$ nm; $\text{SiO}_2 = 2.6 \pm 0.4$ nm) used for SHINERS are shown in the left inlay of Figure 7.1. The NaYF_4

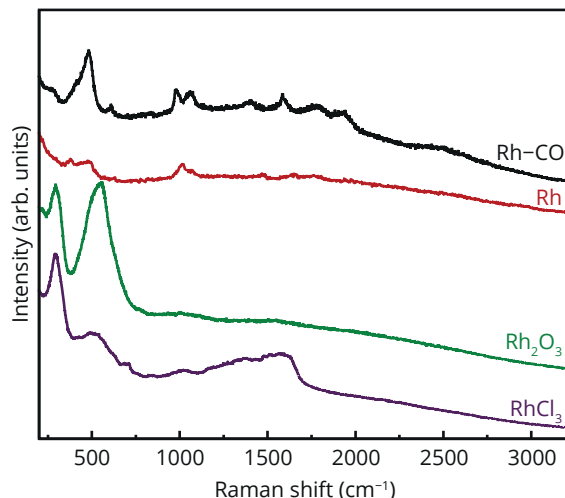


Figure 7.2 – SHINER spectra of the RhCl_3 -impregnated extrudates at different stages. RhCl_3 was observed directly after impregnation and drying. After calcination in $10 \text{ mL min}^{-1} \text{ O}_2$ and $40 \text{ mL min}^{-1} \text{ Rh}_2\text{O}_3$ was observed. Under $10 \text{ mL min}^{-1} \text{ H}_2$, all Rh–O vibrations were removed and CO was subsequently adsorbed.

cores (green spheres, $D = 25.4 \pm 1.4 \text{ nm}$) of the $\text{NaYF}_4@\text{SiO}_2$ NPs ($D = 45.9 \pm 1.7 \text{ nm}$) are doped with 18 % Yb^{3+} and 2 % Er^{3+} and are shown in the middle inlay of Figure 7.1. The Er^{3+} dopant is responsible for the temperature-dependent luminescence in the visible region ($\lambda_{\text{em}} = 500\text{--}570 \text{ nm}$), while the Yb^{3+} dopant allows for efficient upconversion excitation²⁶ in the infrared region ($\lambda_{\text{exc}} = 980 \text{ nm}$). The wet-impregnation of the Rh catalyst (red particles, right inlay of Figure 7.1) was monitored with SHINERS (Figure 7.2) and the deposition of the $\text{Au}@\text{SiO}_2$ SHINs and the presence of $\text{NaYF}_4@\text{SiO}_2$ were confirmed by SEM images of the extrudates (Figure 7.3). Rhodium NPs were not observed in the SEM images, most likely due to the small size of the rhodium NPs. In order to confirm the presence of all the elements present within the nanostructures, the catalyst extrudates were investigated using STEM-EDX and the results are shown in Figure 7.4. In the TEM images,

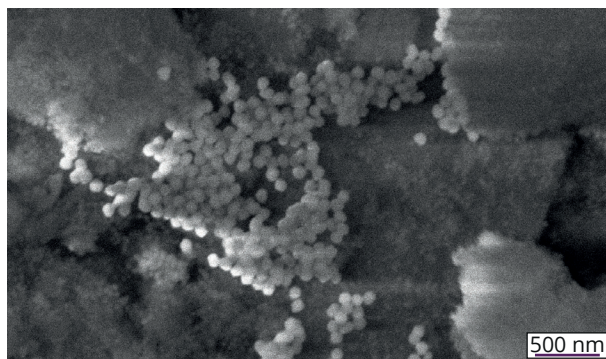


Figure 7.3 – SEM overview of extrudate surface. Scanning Electron Microscopy (SEM) image of $\text{Au}@\text{SiO}_2$ SHINs (bright spots of ca. 100 nm) aggregated with RhCl_3 deposited on SiO_2 -extrudates containing $\text{NaYF}_4@\text{SiO}_2$ NPs.

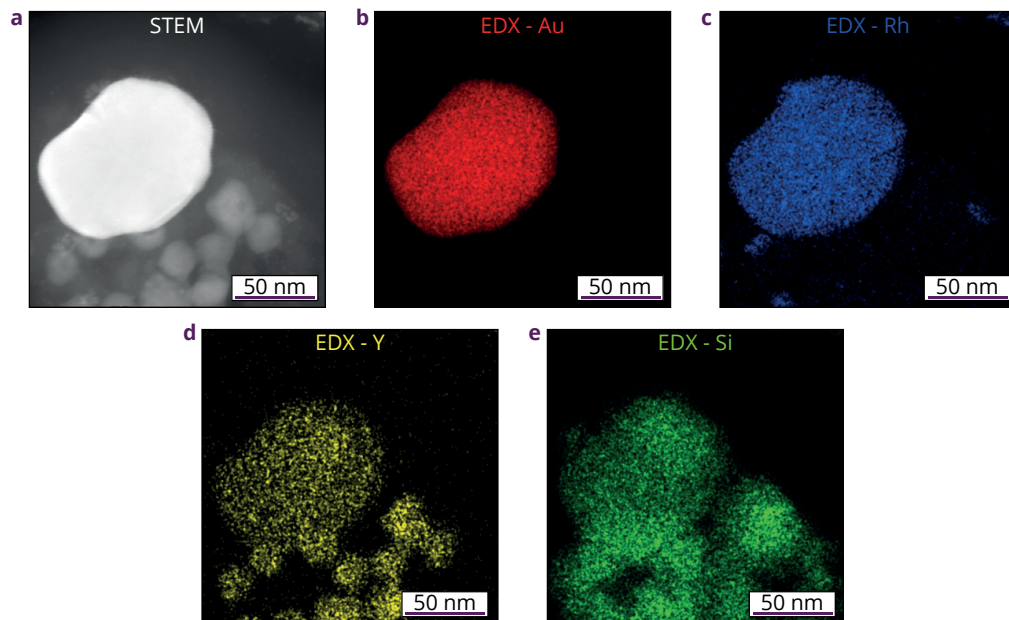


Figure 7.4 – Elemental analysis. Scanning Transmission Electron Microscopy (STEM)-Energy Dispersive X-ray (EDX) analysis measurements of the catalyst system with a STEM overview (a) and EDX maps of Au, Rh, Y and Si (b–e, respectively).

Au@SiO₂, NaYF₄@SiO₂, Rh and SiO₂ (from the extrudate) can be observed, indicating that all different parts of the system have been incorporated successfully. The prepared particles, shown in Figure 7.1, can now be used to monitor catalysis by performing SHINERS, luminescence thermometry as well as on-line mass spectrometry (MS). Using this operando spectroscopy approach, catalyst composition, temperature and catalytic activity can be monitored simultaneously and insight into the reaction mechanism can be obtained.

Temperature-dependent luminescence. To monitor the temperature using temperature-dependent luminescence, the unique energy levels of the Er³⁺ dopant ions in the NaYF₄ were exploited. The three relevant energy levels for this temperature-dependent luminescence are shown in Figure 7.5a. After excitation to a higher lying excited state, the system quickly relaxes to the ²H_{11/2} and ⁴S_{3/2} levels of Er³⁺. The energy difference between these excited states is ca. 700 cm⁻¹, or several *kT* at room temperature. Fast non-radiative relaxation between these thermally coupled states results in a population distribution between the excited states, governed by Boltzmann statistics. Figure 7.5b shows the temperature-dependent luminescence from transitions of the ²H_{11/2} and ⁴S_{3/2} excited state to the ⁴I_{15/2} ground state. Higher temperatures result in more thermal energy and a higher population of the high-energy excited state, ²H_{11/2}. By increasing the temperature with intervals of 25 K from 298 K/25 °C up to 873 K/600 °C (black to orange) it can be observed in Figure 7.5b that the ratio between the two emitting states changes drastically.

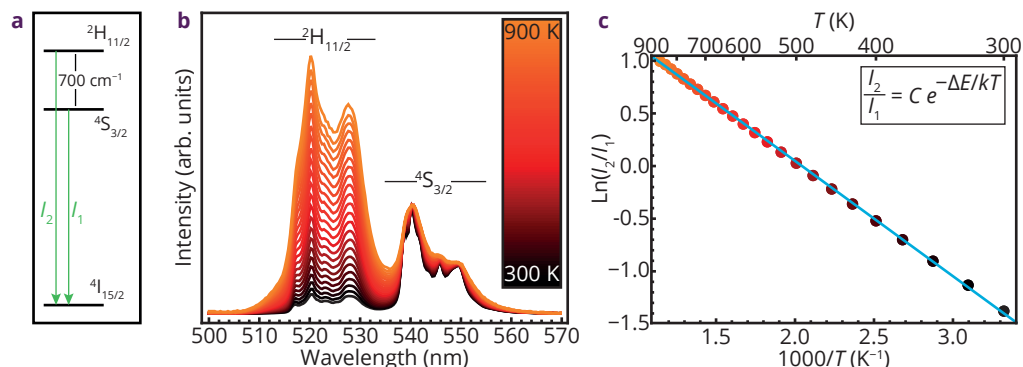


Figure 7.5 - Temperature-dependent luminescence of $\text{NaYF}_4:\text{Er}^{3+}, \text{Yb}^{3+}$. The energy levels ${}^2\text{H}_{11/2}$ and ${}^4\text{S}_{3/2}$ of Er^{3+} (a) are thermally coupled states, resulting in temperature-dependent luminescence which is governed by Boltzmann statistics (b). Due to the Boltzmann statistics, the logarithm of the luminescence intensity ratio plotted versus $1000/T$ yields a linear fit (c).

The Boltzmann behavior (inset Figure 7.5c), where ΔE is the energy difference between the excited states, C a temperature-independent constant, I_i is the emission intensity from state i , k is the Boltzmann constant and T is temperature, can be exploited to monitor temperatures accurately by plotting the logarithm of the luminescence intensity ratio (I_2/I_1) vs. reciprocal temperature ($1000/T$), as shown in Figure 7.5c.

The datapoints show a clear linear correlation between the logarithm of the luminescence intensity ratio and the reciprocal temperature with a linear fit (cyan line) that shows good agreement ($r^2 = 0.999$). The slope of the fit should correspond to $\Delta E/k$, it was found that the ΔE was in good agreement with the value observed in emission spectra (735 vs. 690 cm^{-1}). Furthermore, temperature-dependent luminescence characterization of the NaYF_4 cores, $\text{NaYF}_4@\text{SiO}_2$ core/shells and $\text{NaYF}_4@\text{SiO}_2$ incorporated extrudates all showed similar behavior (data not shown here). These measurements show that the temperature probes can be used to monitor temperature up to at least 900 K by exploiting the calibration curve shown in Figure 7.5c.

CO hydrogenation reaction. To investigate the effect of temperature on the CO adsorption and the related reaction steps in CO hydrogenation, luminescence thermometry, SHINERS and on-line MS measurements were performed simultaneously. Figure 7.6a shows the production of methane and propane, (CH_4 and C_3H_8), over time (black and green lines, respectively), while heating up the systems to different temperatures (gray boxes). Note that the mentioned temperatures were all measured by luminescence thermometry. The production of CH_4 , C_3H_8 , CO_2 and H_2O was determined by integrating the corresponding peaks ($m/z = 15, 38-42, 44$ and 18 , respectively) from the mass spectra (Figure 7.7). The C_2H_6 production could not be determined reliably, as the MS peaks overlapped with CO. Figure 7.6a shows that the increase in temperature from RT to $348 \text{ }^\circ\text{C}$ resulted in a higher catalytic activity as expected for the Rh-catalyzed CO hydrogenation.²⁷ Furthermore, a low conversion to CO_2 is observed starting at $171 \text{ }^\circ\text{C}$, remaining constant at $213 \text{ }^\circ\text{C}$ and

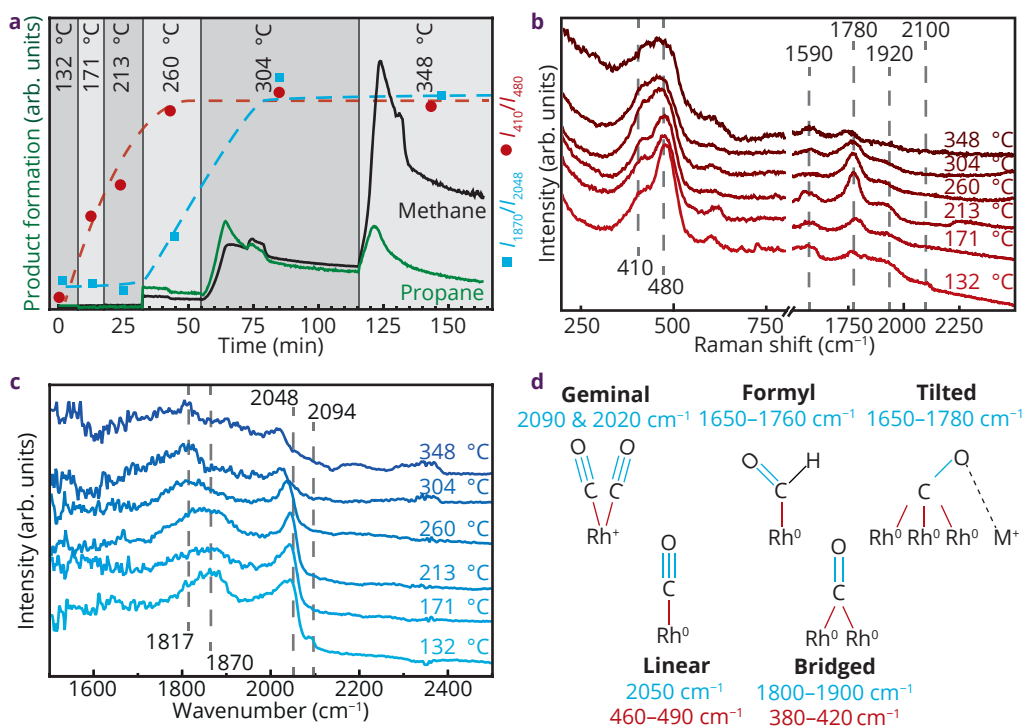


Figure 7.6– Combined operando MS, luminescence thermometry, SHINERS and in situ FT-IR spectroscopy. Methane/Propane production over time (green lines) while continuously monitoring temperature using luminescence thermometry (gray areas) and the ratio between the intensity of the SHINERS (orange dots + dashed line) and FT-IR signal (blue squares + dashed line) for bridged CO and linear CO (a). SHINER spectra obtained at different temperatures as determined by luminescence thermometry, specific Raman shifts for adsorbed CO are highlighted with dashed lines (b). FT-IR spectra obtained at different reaction temperatures, as determined by luminescence thermometry, specific wavenumbers for adsorbed CO are highlighted with dashed lines (c). Structures of adsorbed CO on Rh surfaces with typical vibration energies shown in blue and orange (d).³⁴

above. The H₂O production goes, as expected, hand in hand with hydrocarbon production (Figure 7.7). At the same time, SHINER spectra were obtained at all temperatures, and the increase in catalytic activity can be correlated to structural changes at the catalyst surface. The SHINER spectra in Figure 7.6b show a peak in the lower wavenumber regime at 480 cm⁻¹ with a shoulder at 410 cm⁻¹, which are assigned to the stretching vibrations of linearly (Rh–CO) and bridged (Rh₂–CO) adsorbed carbonyls, respectively.^{28,29} The activity of Rh in CO hydrogenation is sometimes associated with the ratio of bridged vs. linear carbonyls,³⁰ with the activity increasing for an increased amount of bridged carbonyls. Other work demonstrated that single site Rh and Rh^{x+} were the most important for CO insertion and blocking the bridged CO sites led to an improved selectivity towards longer oxygenates.^{31,32}

The ratio between the two peaks changes with temperature and is plotted in Figure 7.6a with red dots; the dashed line is added as a guide for the eye. With increasing temperature, the intensity of the $\nu(\text{Rh-CO})$ at 480 cm⁻¹ decreases, whereas the intensity of the

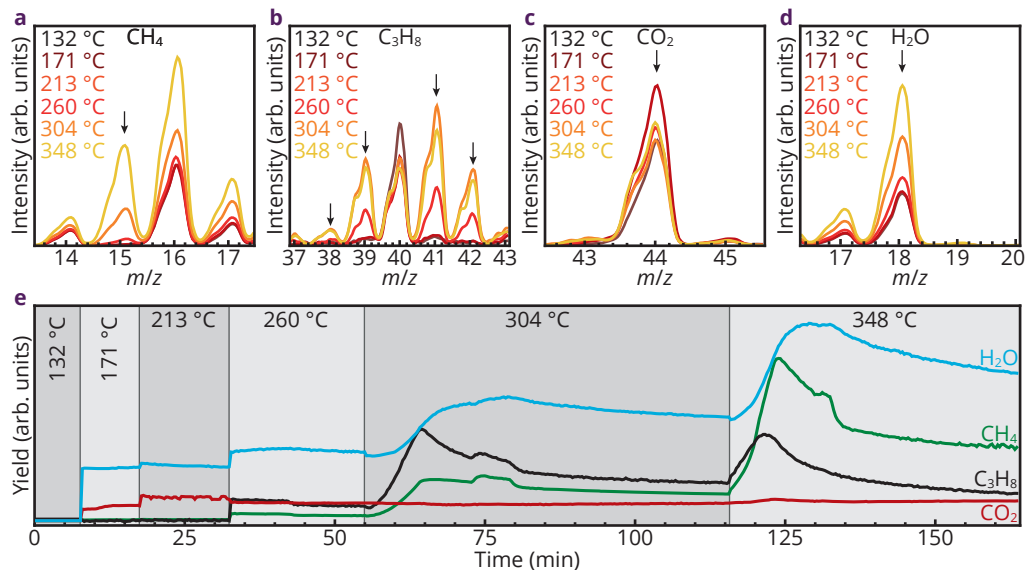


Figure 7.7 – Product formation. Mass spectrometry results determined at different temperature ranging from 132 °C (black) to 348 °C (orange). The production of CH₄ (a), C₃H₈ (b), CO₂ (c) and H₂O (d) were monitored and plotted over time, while increasing the temperature (e).

$\nu(\text{Rh}_2\text{-CO})$ at 410 cm^{-1} remains similar. At 260 °C, when the first reaction products are observed, the $\nu(\text{Rh}_2\text{-CO})/\nu(\text{Rh-CO})$ intensity ratio reaches the ratio of 0.8, and does not depend on temperature anymore. This observation is in line with previous works and is confirmed using IR microspectroscopy (Figure 7.6c); the signal intensity of the linear carbonyls decreases for active Rh catalysts, indicating that these species are reacting on the surface.^{30–32}

Furthermore, in the spectral region between 1500–2500 cm^{-1} , a set of bands is observed that are associated with the C–O stretching vibrations of adsorbed carbonyls and intermediates/reaction products. Formate species show a peak at 1590 cm^{-1} , broad features of bridged and linear CO are observed between 1800–2000 cm^{-1} and in addition an unknown feature at 1780 cm^{-1} is observed. The intensity of the unknown band increases to a maximum at 213 °C and subsequently decreases at higher temperatures. Two assignments are possible for the band at 1780 cm^{-1} : tilted carbonyls ($\text{Rh}_3\text{C-O-M}^+$)³³ or adsorbed formyl/aldehyde species³⁴ (Figure 7.6d). The presence of formyls indicates that the pathway to alkanes involves hydrogen-assisted CO dissociation, as shown in Figure 7.8a. Furthermore, the maximum conversion to propane during CO hydrogenation was found to coincide with the strongest intensity of the 1780 cm^{-1} band at 260 °C, indicating that the species associated with the 1780 cm^{-1} band potentially plays an important role in the CO insertion mechanism. Several adsorbates, intermediates and products that appear in the mechanism can be distinguished using SHINERS (red, Figure 7.8b) and MS (cyan, Figure 7.8c), and together can be used to form a better understanding of the involved pathway. No alcohols or oxygenates were observed in the products over the Rh/SiO₂ catalysts in this work,

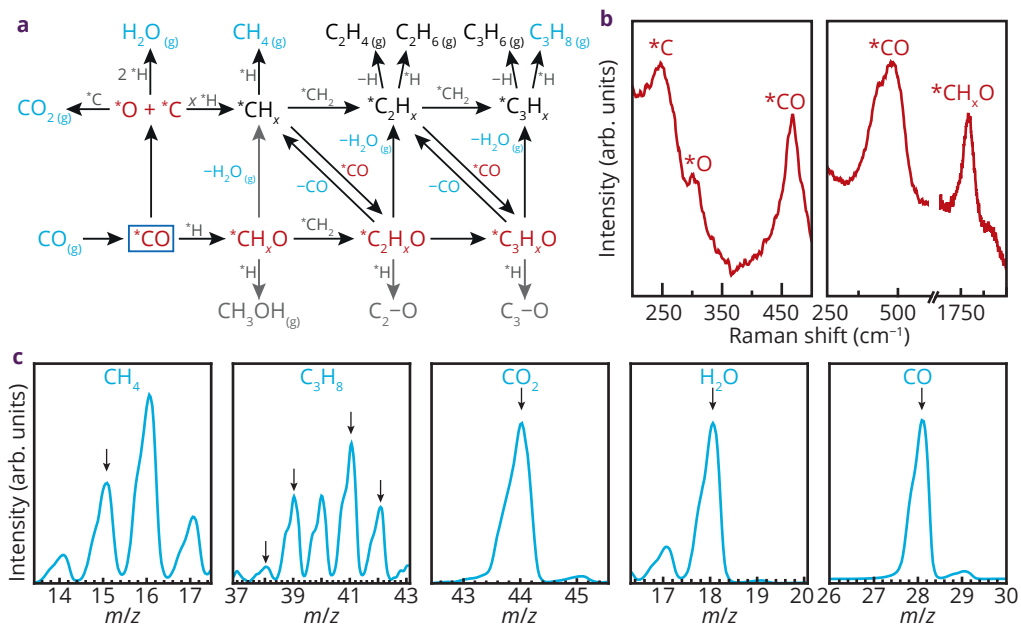


Figure 7.8 - CO hydrogenation mechanism over Rh. The CO hydrogenation mechanism with the compounds spectroscopically observed; highlighted in green for compounds that are observed with on-line MS, highlighted in orange for compounds that are observed with SHINERS and highlighted in blue squared compounds that are observed with additional FT-IR spectroscopy experiments (a). The SHINER spectra of the respective adsorbed species (b). The MS spectra of the specific regions where the products are detected (c).

indicating that the mechanism most likely follows the upper side of the mechanism with direct CO dissociation. However, the band at 1780 cm^{-1} could originate from formyl or aldehyde species, which would point towards a pathway that follows the lower side of the mechanism. Under CO hydrogenation conditions, water is removed so that light alkanes are finally produced.

In order to obtain a definite conclusion about the mechanism, the origin of the peak at 1780 cm^{-1} should be investigated. To distinguish between tilted carbonyl and formyl species, experiments with deuterium isotopes (D_2) were performed to validate the previous findings and assign the 1780 cm^{-1} band. As mentioned above, the peak at 1780 cm^{-1} can be assigned to either tilted carbonyl species ($\text{Rh}_3\text{C-O-M}^+$) or adsorbed formyls. If adsorbed formyls are present, the C–O stretching vibration is directly influenced by the connected hydrogen and the Raman shift will be influenced by replacing hydrogen with deuterium in the reaction and a redshift of $10\text{--}20\text{ cm}^{-1}$ is expected.^{35,36} In contrast, when the unknown band is related to a tilted carbonyl, no shift in the band position is expected. Therefore, H_2 , CO and D_2 were introduced in an alternating fashion at $250\text{ }^\circ\text{C}$ when the 1780 cm^{-1} was at its most intense (Figure 7.9).

The effect of H_2 on adsorbed carbonyls was directly observed with the increase of the peak

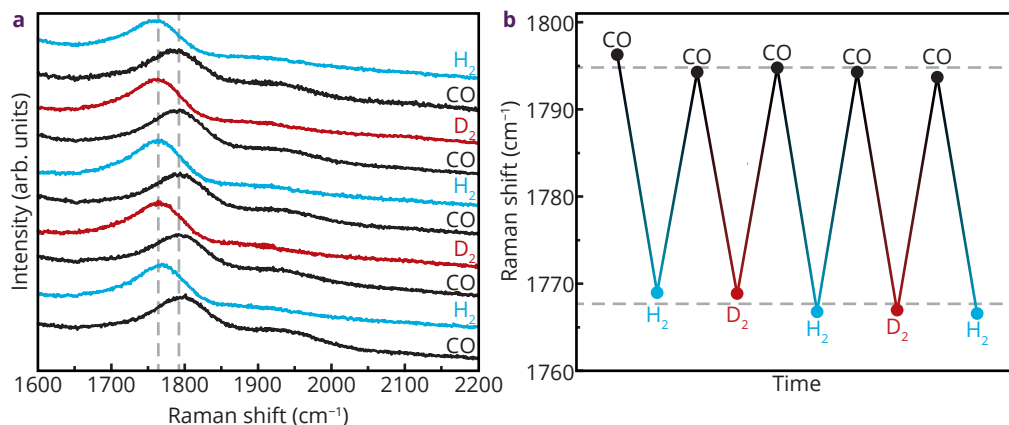


Figure 7.9 - H_2 and D_2 isotope studies. SHINERS spectra of CO hydrogenation at 250 °C over Rh/Au@SiO₂ with H_2 and D_2 (a). The SHINERS peak locations of the unknown band under the specified conditions (b).

intensity at 1795 cm^{-1} and a concurrent red shift to 1767 cm^{-1} . A subsequent introduction of CO returned the bands to their initial position. When D_2 was introduced, the unknown band increased in intensity again and shifted to the same position as for H_2 (red spectra compared to blue spectra in Figure 7.9a). These results indicate that the band at 1780 cm^{-1} is not a formyl or aldehyde species, but most probably a tilted carbonyl. A logical assignment of the tilted carbonyl is a CO species at the Rh/SiO₂ interface, also explaining why it can be observed with SHINERS, but is not seen with FT-IR (Figure 7.6). As oxygenates were not observed in the reaction products, the absence of formyls in SHINERS is also justified. Moreover, when H_2 and D_2 were introduced, the Raman intensity of the linear and bridged carbonyls were reduced in intensity. Therefore, linear carbonyls are most probably the most reactive species during the hydrogenation reaction, whereas tilted carbonyls are relatively inert.

Heat dissipation effects. An important observation with luminescence thermometry is that the set temperature and the local temperature differ significantly. The set temperatures of the reactor were 100–350 °C, with 50 °C intervals but the measured temperatures in Figure 7.6a could be 30 °C off. Temperature offsets can be introduced in a catalytic system due to heat dissipation, temperature heterogeneities in the heating or exo- and endothermic effects. To know the exact temperature of the catalyst bed under the applied conditions is essential, since the selectivity of CO hydrogenation is known to be dependent on the temperature (Figure 7.6a) as well as the H_2 :CO feed ratio. To push the selectivity towards the synthesis of longer hydrocarbons, one can decrease both the H_2 :CO ratio and reaction temperature.³⁷ These temperature heterogeneities can be induced by for instance the cooling effect of the gas feed during chemical reactions. However, the effect of the feed ratio on the actual temperature is often not investigated and the temperature is assumed to be constant. We have therefore performed an extra experiment to investigate the effect of the gas flow on the temperature at the catalyst particles. The temperature measurements were

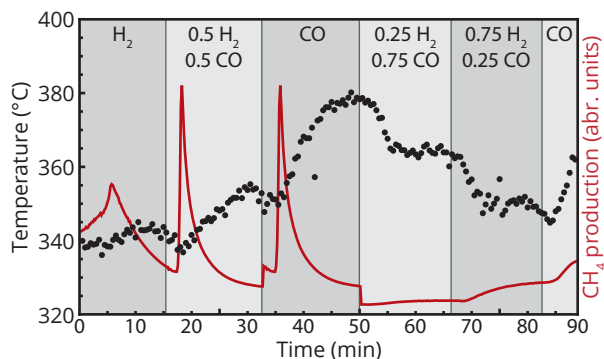


Figure 7.10 – Atmosphere-dependent temperatures. Temperatures obtained from continuous luminescence thermometry measurements (blue dots) while varying the composition of the constant gas flow from H_2 to CO (gray boxes). The production of CH_4 was monitored simultaneously with MS (red line).

performed continuously while varying the gas feed. The set temperature and total gas flow were kept constant at $350\text{ }^\circ\text{C}$ and 20 mL min^{-1} , respectively, while the gas composition was varied from pure H_2 to pure CO via several mixtures in between, as shown in Figure 7.10.

Figure 7.10 clearly shows that the composition of the gas flowing over the catalyst particle has a large effect on the local temperature. High H_2 partial pressures result in lower temperatures, while high CO partial pressures result in higher temperatures. The high thermal conductivity of H_2 ($186\text{ mW m}^{-1}\text{ K}^{-1}$ compared to $25\text{ mW m}^{-1}\text{ K}^{-1}$ for CO at 300 K)³⁸ can provide an efficient pathway for heat dissipation and therefore explain the results qualitatively. The large temperature difference observed, ca. $40\text{ }^\circ\text{C}$, clearly shows the necessity of monitoring temperature locally and the added functionality of the luminescence thermometry measurements.

The delays in temperature changes upon varying the gas composition can be explained by monitoring the production of CH_4 in parallel to the temperature measurements. Upon introduction of the CO in the system (0.5 H_2 , 0.5 CO , second gray box), the system is still H_2 rich and the introduction of CO results in a burst of CH_4 production. Afterwards, the excess H_2 has reacted and the ratio between the H_2 (high thermal conductivity) and CO (low thermal conductivity) gasses stabilizes, resulting in a decrease in catalytic activity and an increase in temperature.

Conclusions

Catalyst extrudate sensors were developed for use in applied catalysis that allow for the simultaneous operando monitoring of reaction temperature with luminescence thermometry and surface species with SHINERS. In this work, they were applied for the study of CO hydrogenation over a Rh catalyst. The extrudates consisted of SiO_2 and various nanoparticles, namely a Rh catalyst, Au@SiO_2 SHINs and $\text{NaYF}_4@\text{SiO}_2$ T-probes. With SHINERS, various surface species were observed under CO hydrogenation conditions up to $350\text{ }^\circ\text{C}$ that were used for researching the CO hydrogenation mechanism. Coupled

to the product analysis with on-line MS, a mechanistic pathway for CO hydrogenation was explored. In addition, using luminescence thermometry, the local temperature at the catalyst particle could be effectively determined, and demonstrated that the set temperature deviated of the actual temperature in the reactor. Experiments in which the gas feed was varied have shown that the main reason for this is heat dissipation, showing that the temperature can vary by 40 °C when the gas composition is changed from H₂ to CO at 350 °C. The results show that the crucial parameters for chemical reactions (i.e., adsorbed species and temperature) should be monitored under relevant conditions (operando) and at relevant length scales (at the catalyst particle). In order to compare results between different operando studies, it is paramount that the local temperature can be monitored to account for temperature deviations due to heat dissipation and/or exo- and endothermic reactions at the catalyst surface. Different types of catalyst extrudate sensors, as developed in this work, can be prepared for a wide variety of catalysts and support oxides and using an on-line activity measurements, the formation of reaction products can be coupled to the observed spectral features of surface reaction intermediates. In other words, this work opens up a new way of assessing catalyst reactivity within a reactor bed, thereby focusing on the local temperature as well as the surface intermediates locally formed within catalyst grains along the reactor bed.

Experimental Section

Materials. All chemicals were used without further purification. The following chemicals were purchased from Sigma-Aldrich: Cyclohexane (99.5 %, CH), oleic acid (90 %, OA), ethanol (>99.8 %, EtOH), methanol (>99.85 %, MeOH), sodium hydroxide (>97 %, NaOH), ammonium fluoride (>98 %, NH₄F), ammonium hydroxide (28 wt% in H₂O, ammonia), rare-earth acetate hydrates (99.9 %, RE(Ac)₃), tetraethyl orthosilicate (99.999 %, TEOS), IGEPAL CO-520 ((C₂H₄O)_n•C₁₅H₂₄O with n ~ 5, average Mn = 441 g mol⁻¹, NP-5) and methylcellulose (4000 CP), (3-aminopropyl)trimethoxysilane (APTMS, 97 %), sodium silicate solution (27 % SiO₂ in 14 % NaOH), Rhodamine 6G, RhCl₃ (98 %), hydroxylamine hydrochloride (>98 %). 1-octadecene (90 %, ODE) and trisodium citrate dihydrate (99 %) were purchased from Acros Organics. Demineralized water was purified with a Milli-Q system (18.2 MΩ) before use. The purity of the gases used in the experiments was 99.99% and was passed through a filter consisting of ZnO, Al₂O₃ and activated coal.

Setup. Raman spectroscopy measurements were performed on a Renishaw InVia Raman microscope, using 785 nm diode laser excitation through a 50x objective (0.5 NA). In situ experiments were all performed under 0.8 mW (i.e., 1.67·10⁵ W·cm⁻²), with an integration time of 10s. SHINER spectra of RhCl₃ and Rh₂O₃ were obtained with 1s integration time. FT-IR spectra were obtained on a Spotlight 400 FT-IR microscope (PerkinElmer) equipped with a MCT array (mercury cadmium telluride) detector. FT-IR measurements were taken with an aperture size of 100 × 100 μm and integrated over 256 scans, with 4 cm⁻¹ resolution. TEM images were recorded using a FEI Tecnai 12 Icor TEM operating at 120 kV. Samples were prepared by drop-casting a colloidal solution on a carbon-coated copper grid, which were left to dry in air. TEM images of the extrudate were obtained by

gently scraping the outer surface of the spent catalyst and dispersing it in 2-propanol after which a drop was dried on a carbon coated copper grid. Scanning Transmission Electron Microscopy-Energy Dispersive X-ray analysis (STEM-EDX) images were obtained on a FEI Talos F200X electron microscope operating at 200 kV. Upconversion luminescence spectra were obtained with an MDL-III-980nm-2W continuous wave laser, Ocean Optics VIS-NIR combined light source and detection probe, an Ocean optics QEPro CCD detector and Ocean Optics software. The temperature and atmosphere during the experiments was controlled using a CCR1000 stage (Linkam).

Preparation of temperature sensors. $\text{NaYF}_4@\text{SiO}_2$ nanoparticles (NPs) doped with 18 % Yb^{3+} and 2 % Er^{3+} of ca. 50 nm were prepared via an initial synthesis of NaYF_4 core particles (ca. 25 nm) and subsequent SiO_2 overgrowth as reported earlier.^{25,39–41}

Synthesis of catalyst extrudates. Extrudates containing $\text{NaYF}_4@\text{SiO}_2$ NPs were prepared by mixing 3.2 g of dried $\text{NaYF}_4@\text{SiO}_2$ NPs with 3.8 g silica (Davicat Si1302), 0.2 g methylcellulose and water in a Caleva Mixer Torque Rheometer. The obtained paste was then transferred to a single mini-screw extruder (Caleva) and extruded into 2 mm diameter cylindrical extrudates. The obtained extrudates were dried overnight at room temperature and afterwards calcined at 873 K in air.

Synthesis of $\text{Au}@\text{SiO}_2$. $\text{Au}@\text{SiO}_2$ NPs of ca. 90 nm were prepared via seeded growth of Au core particles (ca. 88 nm) and subsequent SiO_2 overgrowth as reported earlier.^{5,8} 30 mL H_2O and 300 μL of 1 % (w/v) HAuCl_4 were added to a 250 mL roundbottomflask and were rapidly brought to a boil in a preheated oil bath, under vigorous stirring. 0.9 mL of 1 % (w/v) trisodium citrate solution was added when the solution was boiling. The flask was removed from heat after 10 min, resulting in ruby red colloidal solution with Au seeds of ca. 16 nm. 1.4 mL of the seeds solution was then added to 112 mL mQ water and 2.0 mL 1 % (w/v) trisodium citrate was added. Au NPs were grown by adding dropwise 2.8 mL $\text{NH}_2\text{OH}\cdot\text{HCl}$ and 1 % (w/v) HAuCl_4 over 30 min. 15 mL of colloidal Au NPs solution was mixed with 0.4 mL aqueous APTMS (1.0 mM) solution and stirred for 20 min. Subsequently, 1.4 mL of a sodium silicate solution (diluted to 0.54 wt%, pH = 10.8) was added under vigorous stirring. The flask was placed in an aluminum heating mantle at 90 °C and stirred for 45 min. After synthesis, the particles were centrifuged and washed 3 times in mQ water and finally stored in 1 mL mQ water.

Deposition of $\text{Au}@\text{SiO}_2$ on extrudates. 0.25 mL of a colloidal solution $\text{Au}@\text{SiO}_2$ was concentrated to 25 μL and mixed with 50 μL aqueous RhCl_3 (0.01M). The colloidal solution immediately became unstable, resulting in a grey/purple mixture. This mixture was slowly added to a dried extrudate until the pores were filled (1 mL g^{-1}), leaving the aggregated SHINs on the outside of the extrudate.

Operando Spectroscopy Experiments. 1 wt% Rh/SiO_2 was prepared by a wet-impregnation method: the extrudates, containing $\text{Au}@\text{SiO}_2$ and $\text{NaYF}_4@\text{SiO}_2$ NPs were immersed in 0.1 M aqueous RhCl_3 for 24h. An extrudate (ca. 10 mg) was then loaded into a CCR1000 stage (Linkam) where gas atmosphere and temperature could be controlled. It was first

dried at 80 °C for 2 h, then at 120 °C for 2 h and subsequently at 300 °C (3 °C min⁻¹) for 1 h, all in 10 mL min⁻¹ O₂ and 40 mL min⁻¹ Ar. After calcination, the extrudates were reduced in 10 mL min⁻¹ H₂ at 250 °C (3 °C min⁻¹) for 30 min. These synthesis steps were followed with in situ SHINERS in Figure 7.2. They were then ready for CO hydrogenation experiments. CO hydrogenation was performed under 2.5 mL min⁻¹ CO and 5 mL min⁻¹ H₂.

Acknowledgements

Andries Meijerink (Utrecht University, UU) is gratefully acknowledged for his valuable input and discussions. Nynke Krans (UU) is thanked for her contributions to the TEM-EDX measurements. Iris ten Have (UU) is thanked for her contributions to the SEM measurements.

This work was supported by the Netherlands Center for Multiscale Catalytic Energy Conversion (MCEC), an NWO Gravitation programme funded by the Ministry of Education, Culture and Science of the government of the Netherlands. The Netherlands Organization for Scientific Research (NWO) and Shell Global Solutions in the framework of the Chemical Innovation Partnership Project (CHIPP) are thanked for financial support.

References

1. Ertl, G., *Reactions at Solid Surfaces*, John Wiley & Sons, Inc., Hoboken, **2009**.
2. Bañares, M. A. Operando Spectroscopy: The Knowledge Bridge to Assessing Structure-Performance Relationships in Catalyst Nanoparticles. *Adv. Mater.* **2011**, *23*, 5293–5301.
3. Buurmans, I. L. C. & Weckhuysen, B. M. Heterogeneities of Individual Catalyst Particles in Space and Time as Monitored by Spectroscopy. *Nat. Chem.* **2012**, *4*, 873–886.
4. Weckhuysen, B. M. Determining the active site in a catalytic process: Operando Spectroscopy is More than a Buzzword. *Phys. Chem. Chem. Phys.* **2003**, *5*, 4351–4360.
5. Li, J. F.; Huang, Y. F.; Ding, Y.; Yang, Z. L.; Li, S. B.; Zhou, X. S.; Fan, F. R.; Zhang, W.; Zhou, Z. Y.; Wu, D.-Y.; Ren, B.; Wang, Z. L. & Tian, Z.-Q. Shell-Isolated Nanoparticle-Enhanced Raman Spectroscopy. *Nature*, **2012**, *464*, 392–395.
6. Ding, S.-Y.; Yi, J.; Li, J.-F.; Ren, B.; Wu, D.-Y.; Panneerselvam, R. & Tian, Z.-Q. Nanostructure-Based Plasmon-Enhanced Raman Spectroscopy for Surface Analysis of Materials. *Nat. Rev. Mater.* **2016**, *1*, 16021.
7. Schlücker, S. Surface-Enhanced Raman Spectroscopy: Concepts and Chemical Applications. *Angew. Chem. Int. Ed.* **2014**, *53*, 4756–4795.
8. Hartman, T. & Weckhuysen, B. M. Thermally Stable TiO₂- and SiO₂-Shell-Isolated Au Nanoparticles for In Situ Plasmon-Enhanced Raman Spectroscopy of Hydrogenation Catalysts. *Chem. Eur. J.* **2018**, *24*, 3733–3741.
9. Zhang, H.; Wang, C.; Sun, H.-L.; Fu, G.; Chen, S.; Zhang, Y.-J.; Chen, B.-H.; Anema, J. R.; Yang, Z.-L.; Li, J.-F. & Tian, Z.-Q. In Situ Dynamic Tracking of Heterogeneous Nanocatalytic Processes by Shell-isolated Nanoparticle-Enhanced Raman Spectroscopy. *Nat. Commun.* **2017**, *8*, 15447.
10. Jaque, D. & Vetrone, F. Luminescence Nanothermometry. *Nanoscale* **2012**, *4*, 4301–4326.
11. Brites, C. D. S.; Lima, P. P.; Silva, N. J. O.; Millán, A.; Amaral, V. S.; Palacio, F. & Carlos, L. D. Thermometry at the Nanoscale. *Nanoscale* **2012**, *4*, 4799–4829.

12. Geitenbeek, R. G.; Nieuwelink, A.-E.; Jacobs, T. S.; Salzmann, B. B. V.; Goetze, J.; Meijerink, A. & Weckhuysen, B. M. W. In Situ Luminescence Thermometry To Locally Measure Temperature Gradients during Catalytic Reactions. *ACS Catal.* **2018**, *8*, 2397–2401.
13. Vetrone, F.; Naccache, R.; Zamarrón, A.; de la Fuente, A. J.; Sanz-Rodríguez, F.; Maestro, L. M.; Rodríguez, E. M.; Jaque, D.; Solé, J. G. & Capobianco, J. A. Temperature Sensing Using Fluorescent Nanothermometers. *ACS Nano* **2010**, *4*, 3254–3258.
14. Hwang, S. & Smith, R. Optimum Reactor Design in Methanation Processes with Nonuniform Catalysts. *Chem. Eng. Commun.* **2009**, *196*, 616–642.
15. Grunwaldt, J. D.; Wagner, J. B. & Dunin-Borkowski, R. E. Imaging Catalysts at Work: A Hierarchical Approach from the Macro- to the Meso- and Nano-Scale. *ChemCatChem* **2013**, *5*, 62–80.
16. Koptyug, I. V.; Khomichev, A. V.; Lysova, A. A. & Sagdeev, R. Z. Spatially Resolved NMR Thermometry of an Operating Fixed-Bed Catalytic Reactor. *J. Am. Chem. Soc.* **2008**, *130*, 10452–10453.
17. Kimmerle, B.; Grunwaldt, J.-D.; Baiker, A.; Glatzel, P.; Boye, P.; Stephan, S. & Schroer, C. G. Visualizing a Catalyst at Work during the Ignition of the Catalytic Partial Oxidation of Methane. *J. Phys. Chem. C* **2009**, *113*, 3037–3040.
18. Simeone, M.; Saleme, L.; Allouis, C. & Volpicelli, G. Temperature Profile in a Reverse Flow Reactor for Catalytic Partial Oxidation of Methane by Fast IR Imaging. *AIChE J.* **2008**, *54*, 2689–2698.
19. Yarulina, I.; Kapteijn, F. & Gascon, J. The Importance of Heat Effects in the Methanol to Hydrocarbons Reaction over ZSM-5: On the Role of Mesoporosity on Catalyst Performance. *Catal. Sci. Technol.* **2016**, *6*, 5320–5325.
20. Li, T.; Guo, C.; Zhou, S.; Duan, C. & Yin, M. Highly Sensitive Optical Thermometry of Yb³⁺-Er³⁺ Codoped AgLa(MoO₄)₂ Green Upconversion Phosphor. *J. Am. Ceram. Soc.* **2015**, *98*, 2812–2816.
21. Xu, X.; Wang, Z.; Lei, P.; Yu, Y.; Yao, S.; Song, S.; Liu, X.; Su, Y.; Dong, L. & Feng, J. α-NaYb(Mn)F₄:Er³⁺/Tm³⁺@NaYF₄ UCNPs as “Band-Shape” Luminescent Nanothermometers over a Wide Temperature Range. *ACS Appl. Mater. Interfaces* **2015**, *7*, 20813–20819.
22. Carnall, W. T.; Crosswhite, H. & Crosswhite, H. M. *Energy Level Structure and Transition Probabilities of the Trivalent Lanthanides in LaF₃*, Argonne National Laboratory, Argonne, **1977**.
23. Svelto, O. *Principles of Lasers*, Springer, New York, **2010**.
24. Spivey, J. J. & Egbebi, A. Heterogeneous Catalytic Synthesis of Ethanol from Biomass-Derived Syngas. *Chem. Soc. Rev.* **2007**, *36*, 1514.
25. Geitenbeek, R. G.; Prins, P. T.; Albrecht, W.; van Blaaderen, A.; Weckhuysen, B. M. & Meijerink, A. NaYF₄:Er³⁺,Yb³⁺/SiO₂ Core/Shell Upconverting Nanocrystals for Luminescence Thermometry up to 900 K. *J. Phys. Chem. C* **2017**, *121*, 3503–3510.
26. Auzel, F. Upconversion and Anti-Stokes Processes with f and d Ions in Solids. *Chem. Rev.* **2004**, *104*, 139–173.
27. Mazidi, S. K.; Sadeghi, M. T. & Marvast, M. A. Optimization of Fischer-Tropsch Process in a Fixed-Bed Reactor Using Non-Uniform Catalysts. *Chem. Eng. Technol.* **2013**, *36*, 62–72.
28. Williams, C. T.; Black, C. A.; Weaver, M. J. & Takoudis, C. G. Adsorption and Hydrogenation of Carbon Monoxide on Polycrystalline Rhodium at High Gas Pressures. *J. Phys. Chem. B* **1997**, *101*, 2874–2883.
29. Williams, C. T.; Chen, K.-Y.; Takoudis, C. G. & Weaver, M. J. Reduction Kinetics of Surface Rhodium Oxide by Hydrogen and Carbon Monoxide at Ambient Gas Pressures As Probed by Transient Surface-Enhanced Raman Spectroscopy. *J. Phys. Chem. B* **1998**, *102*, 4785–4794.

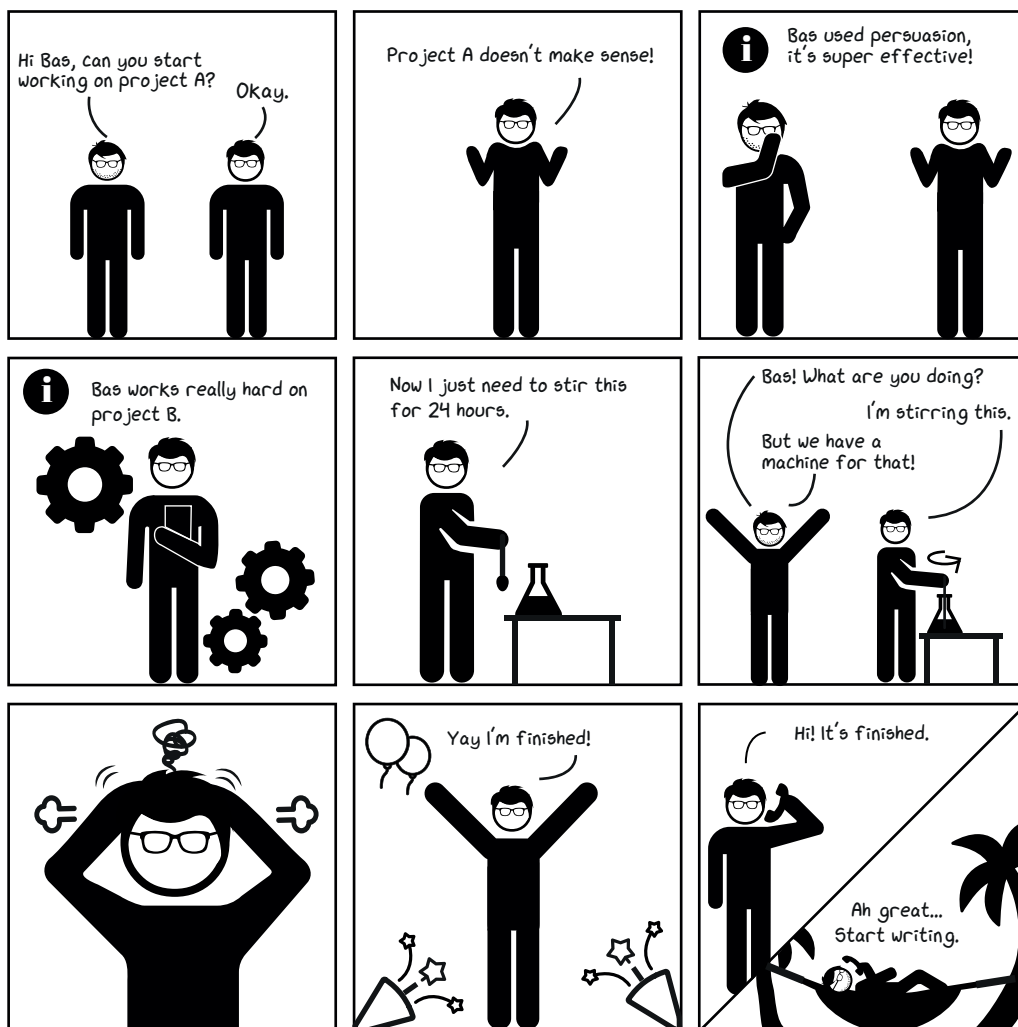
30. Arakawa, H.; Takakazu, F.; Masaru, I.; Kazuhiko, T.; Takehiko, M. & Yoshihiro, S. High Pressure In Situ FTIR Study of CO Hydrogenation over Rh/SiO₂ Catalyst. *Chem. Lett.* **1985**, *14*, 23–26.
31. Chuang, S. S. C. & Pien, S. I. Role of Silver Promoter in Carbon Monoxide Hydrogenation and Ethylene Hydroformylation over Rh/SiO₂ catalysts. *J. Catal.* **1992**, *138*, 536–546.
32. Chuang, S. S. C. & Pien, S. I. Infrared Study of the CO Insertion Reaction on Reduced, Oxidized, and Sulfided Rh/SiO₂ Catalysts. *J. Catal.* **1992**, *135*, 618–634.
33. Tóth, M.; Kiss, J.; Oszkó, A.; Pótári, G.; László, B. & Erdőhelyi, A. Hydrogenation of Carbon Dioxide on Rh, Au and Au–Rh Bimetallic Clusters Supported on Titanate Nanotubes, Nanowires and TiO₂. *Top. Catal.* **2012**, *55*, 747–756.
34. Chuang, S. S. C.; Stevens, R. W. & Khatri, R. Mechanism of C₂⁺ Oxygenate Synthesis on Rh Catalysts. *Top. Catal.* **2005**, *32*, 225–232.
35. Weng, S. X.; Anderson, A. & Torrie, B. H. Raman and Far-Infrared Spectra of Crystalline Formaldehyde, H₂CO and D₂CO. *J. Raman Spectrosc.* **1989**, *20*, 789–794.
36. Mitchel, W. J.; Xie, J.; Jachimowski, T. A. & Weinberg, W. H. Carbon Monoxide hydrogenation on the Ru(001) Surface at Low Temperature Using Gas-Phase Atomic Hydrogen: Spectroscopic Evidence for the Carbonyl Insertion Mechanism on a Transition Metal Surface. *J. Am. Chem. Soc.* **1995**, *117*, 2606–2617.
37. Castner, D. G.; Blackadar, R. L. & Samorjai, G. A. CO Hydrogenation over Clean and Oxidized Rhodium Foil and Single Crystal Catalysts. Correlations of Catalyst Activity, Selectivity, and Surface Composition. *J. Catal.* **1980**, *66*, 257–266.
38. Rumble, J. R. *CRC Handbook of Chemistry and Physics*, CRC Press, Boca Raton, **2017**.
39. Koole, R.; van Schooneveld, M. M.; Hilhorst, J.; de Mello Donegá, C.; 't Hart, D. C.; van Blaaderen, A.; Vanmaekelbergh, D. & Meijerink, A. On the Incorporation Mechanism of Hydrophobic Quantum Dots in Silica Spheres by a Reverse Microemulsion Method. *Chem. Mater.* **2008**, *20*, 2503–2512.
40. Li, Z. & Zhang, Y. An Efficient and User-Friendly Method for the Synthesis of Hexagonal-Phase NaYF₄:Yb,Er/Tm Nanocrystals with Controllable Shape and Upconversion Fluorescence. *Nanotechnology* **2008**, *19*, 345606.
41. Wang, F.; Deng, R. & Liu, X. Preparation of Core-Shell NaGdF₄ Nanoparticles Doped with Luminescent Lanthanide Ions to Be Used as Upconversion-Based Probes. *Nat. Protoc.* **2014**, *9*, 1634–1644.



Based on

- Geitenbeck, R. G.; Salzmann, B. B. V.; Nieuwelink, A.-E.; Meijerink, A. & Weckhuysen, B. M. Chemically and Thermally Stable Lanthanide-doped Y_2O_3 Nanoparticles for Remote Temperature sensing in Catalytic Environments. *Chem. Eng. Sci.* **2018**, *In Press*

Chapter 8 – Chemically and Thermally Stable Lanthanide-doped Y_2O_3 Nanoparticles for Remote Temperature Sensing in Catalytic Environments



Robin Geitenbeek



Bas Salzmann



Andries Meijerink

Abstract

Luminescent nanoparticles have great potential for remote temperature sensing. Mapping of high temperature profiles under harsh conditions that are common in chemical reactors requires new thermally and chemically stable (nano)probes. In this chapter, we report temperature-dependent luminescence of $\text{Yb}^{3+}/\text{Er}^{3+}$ -, Dy^{3+} - and Eu^{3+} -doped Y_2O_3 nanoparticles (NPs). We have deposited these lanthanide-doped Y_2O_3 NPs on $\alpha\text{-Al}_2\text{O}_3$, a non-porous catalyst support material. The NPs are strongly adsorbed on the surface and no sintering was observed upon heating to 900 K for 12 h. The high chemical and thermal stability of Y_2O_3 makes these nanoprob es ideal for sensing in catalytic environments. A systematic study of the three types of luminescent NPs reveals that the temperature-dependent luminescence of $\text{Yb}^{3+}/\text{Er}^{3+}$, Dy^{3+} and Eu^{3+} serves different temperature ranges: lower T regime (300–800 K, accuracy <5 K) for $\text{Yb}^{3+}/\text{Er}^{3+}$, intermediate T for Dy^{3+} (400–900+ K, accuracy <15 K) and high T for Eu^{3+} (550–900+ K, accuracy <12 K). The superior thermal and chemical stability of the $\text{Y}_2\text{O}_3/\alpha\text{-Al}_2\text{O}_3$ host in combination with different luminescent lanthanide dopants results in a robust system that can be tailored to monitor temperatures in different regimes with the highest possible sensitivity.

Introduction

Temperature control is crucial for the optimization of the activity and selectivity of catalytic reactions.^{1,2} The exponential temperature dependence for many chemical reactions that is evident from the Arrhenius equation makes it paramount to minimize local temperature variations. However, due to exothermal or endothermal processes, interparticle heterogeneities and stagnant flows, temperature fluctuations can occur in the nanoscopic and mesoscopic regime. It is important to accurately monitor these temperature fluctuations in order to improve catalyst performance. Until recently, temperatures were monitored in situ using multiple thermocouples,³ IR thermography^{4,5} or NMR thermometry.⁶ Although these techniques can be used to visualize temperature profiles, the spatial resolution is typically limited to the mm range and the non-invasiveness of the technique is not always guaranteed. Recently, in situ temperature monitoring using bandshape luminescence thermometry has been developed as a non-invasive technique for remote temperature sensing. The technique relies on changes in the luminescence intensity ratio of two emission peaks at different temperatures.⁷⁻⁹ Especially lanthanide (Ln) ions are promising for this technique. Ln ions have a rich energy level structure in the UV, visible and near-infrared spectral region. The energy levels arise from the many different configurations of electrons in the partially filled inner 4f shell. Efficient sharp line emission is observed from different energy levels. Emission lines originating from two thermally coupled energy levels separated by an energy difference ΔE can easily be separated because of the sharpness of the lines. This is a clear advantage over broad band emitters for bandshape thermometry.

Originally, nanothermometry probes were investigated for temperature sensing in biological environments, typically for temperatures up to 50 °C.^{10,11} The temperature range for luminescence thermometry could be extended by using more stable inorganic hosts.¹²⁻¹⁴ Recently, we explored coating luminescent Ln-doped nanoparticles (NPs) with an inert silica shell to increase the thermal stability and chemical inertness to enable remote temperature sensing in chemical reactors.¹⁵ We demonstrated the applicability for in situ temperature monitoring in a chemical reactor using microcrystalline particles doped with luminescent Ln ions.⁹ Our previously reported host system for Ln dopants, $NaYF_4$, can be oxidized and the hexagonal crystal structure is not stable above ca. 900 K.¹⁵ Furthermore, the Er^{3+} dopant, responsible for the characteristic temperature-dependent luminescence, no longer shows the expected temperature dependency above ca. 800 K because of thermal population of additional energy levels which become thermally accessible.

In this chapter, we investigate Y_2O_3 NPs of ca. 100 nm as an alternative, more robust host material for luminescence nanothermometry. Y_2O_3 is known for its superior thermal stability (melting point 2700 K) and chemical inertness. To extend the temperature range that can be monitored, different Ln dopants are incorporated, namely Yb^{3+}/Er^{3+} , Dy^{3+} and Eu^{3+} . All three dopants show characteristic temperature-dependent luminescence with an optimum performance in different temperature ranges: Er^{3+} shows characteristic temperature-dependent luminescence from 300–800 K, Dy^{3+} and Eu^{3+} from 400 K (Dy^{3+}) and 550 K (Eu^{3+}) to at least 900 K. Via deposition of the Y_2O_3 NPs on microcrystalline

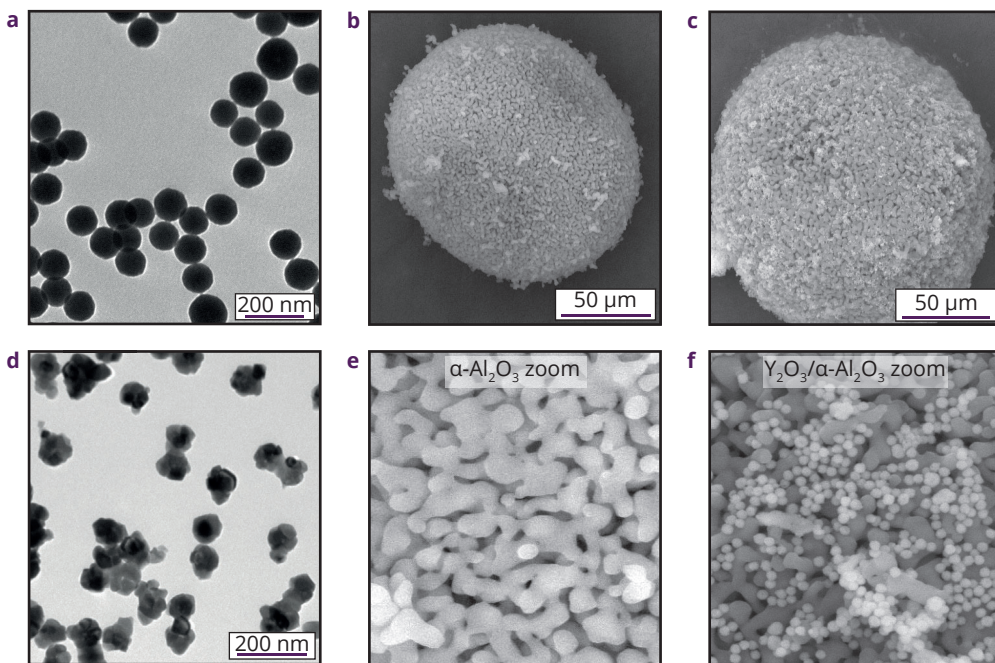


Figure 8.1 – Overview of Y_2O_3 and Al_2O_3 particles. TEM image of as-synthesized (a) and 1073 K calcined Y_2O_3 NPs (d), SEM image of $\alpha\text{-Al}_2\text{O}_3$ without and with 5 wt% Y_2O_3 NPs deposited (b and c, respectively). Zoom-ins of the structure of the microcrystalline Al_2O_3 support (e) shows more detail and the adsorbed Y_2O_3 NPs on the Al_2O_3 support can be observed (f).

$\alpha\text{-Al}_2\text{O}_3$, a non-porous, highly stable support, a material is created that can act as both catalyst and nanothermometer: active catalysts such as nickel and silver can be co-deposited on the alumina.^{16,17} We demonstrate that the $\text{Y}_2\text{O}_3/\alpha\text{-Al}_2\text{O}_3$ system is robust: prolonged washing with ethanol and heating of the dry sample to 873 K does not affect the distribution of NPs on the surface, indicating that no particle desorption or sintering occurs. This gives the Y_2O_3 NPs on $\alpha\text{-Al}_2\text{O}_3$ great potential for luminescence thermometry in catalytic reactors. In addition, combining luminescence thermometry with (confocal) fluorescence microscopy make the $\text{Y}_2\text{O}_3:\text{Ln}^{3+}$ NPs promising for high temperature imaging in applications where high spatial resolution is required, such as microfluidics,^{18,19} nano-electronics^{20,21} and nanophotonics.^{22,23}

Results and discussion

Preparation of $\text{Y}_2\text{O}_3/\alpha\text{-Al}_2\text{O}_3$ particles. Lanthanide-doped Y_2O_3 NPs were synthesized and subsequently deposited on a microcrystalline $\alpha\text{-Al}_2\text{O}_3$ support. Details on the NP synthesis and deposition are provided in the Experimental Section. To investigate the size, shape and crystallinity of the prepared lanthanide-doped NPs and $\text{Y}_2\text{O}_3/\alpha\text{-Al}_2\text{O}_3$ particles, we used a variety of characterization techniques such as transmission electron microscopy (TEM), scanning electron microscopy (SEM) and X-ray diffraction (XRD). Y_2O_3 NPs were

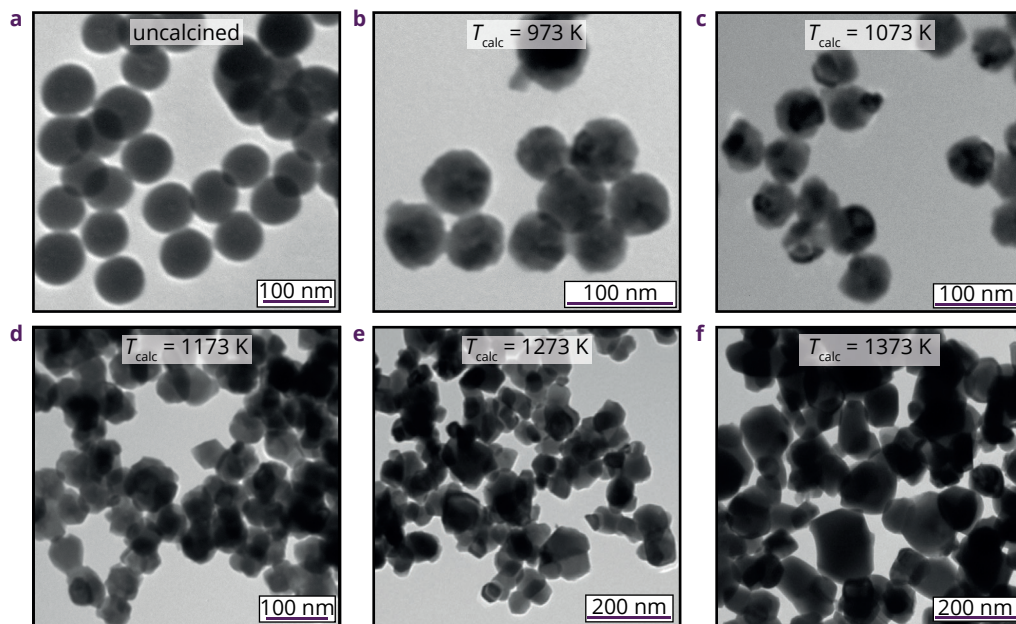


Figure 8.2 – Calcination experiments. TEM images of as-synthesized Y_2O_3 NPs (a) and upon subsequent calcination at 973, 1073, 1173, 1273 and 1373 K (b–f, respectively).

prepared by a homogeneous precipitation technique using different lanthanide precursor mixtures to incorporate the desired concentrations of Ln dopants. In Figure 8.1a a TEM image of the as-synthesized Y_2O_3 NPs is shown, revealing a particle size of 80 ± 9 nm. The NPs were calcined to remove chemically bound H_2O and CO_2 , improve the crystallinity and enhance the luminescence efficiency. After calcination at 1073 K the average crystallite size decreased to 71 ± 10 nm (Figure 8.1d). An overview of the changes in particle size and shape upon calcination at different temperatures is given in Figures 8.2b–f, showing TEM images of the Y_2O_3 NPs after calcination at temperatures between 973 K and 1373 K.

To investigate the influence of the calcination temperature on the morphology, crystallinity and size of the Y_2O_3 NPs, X-ray diffractograms were recorded following calcination of the as-synthesized NPs between 973 and 1373 K in steps of 100 K (Figure 8.3). The XRD patterns show that the as-prepared NPs have low crystallinity (no clear Y_2O_3 XRD peaks). After calcination at 973 K, diffraction peaks corresponding to the cubic Y_2O_3 crystal structure are observed. From the width of the diffraction peaks the crystallite size can be determined using the Debye-Scherrer equation.²⁴ The average crystallite size was determined to increase from 15 to 27 nm upon calcination at temperatures of 973 to 1373 K. These sizes are much smaller than the nanoparticle size (70–80 nm) which indicates that the NPs consist of many smaller nanocrystalline domains. This is typically observed for NPs synthesized using precipitation techniques.^{25,26} For calcination temperatures of 1173 K and higher the NPs show increasing clustering (Figure 8.2 d–f). Large agglomerates

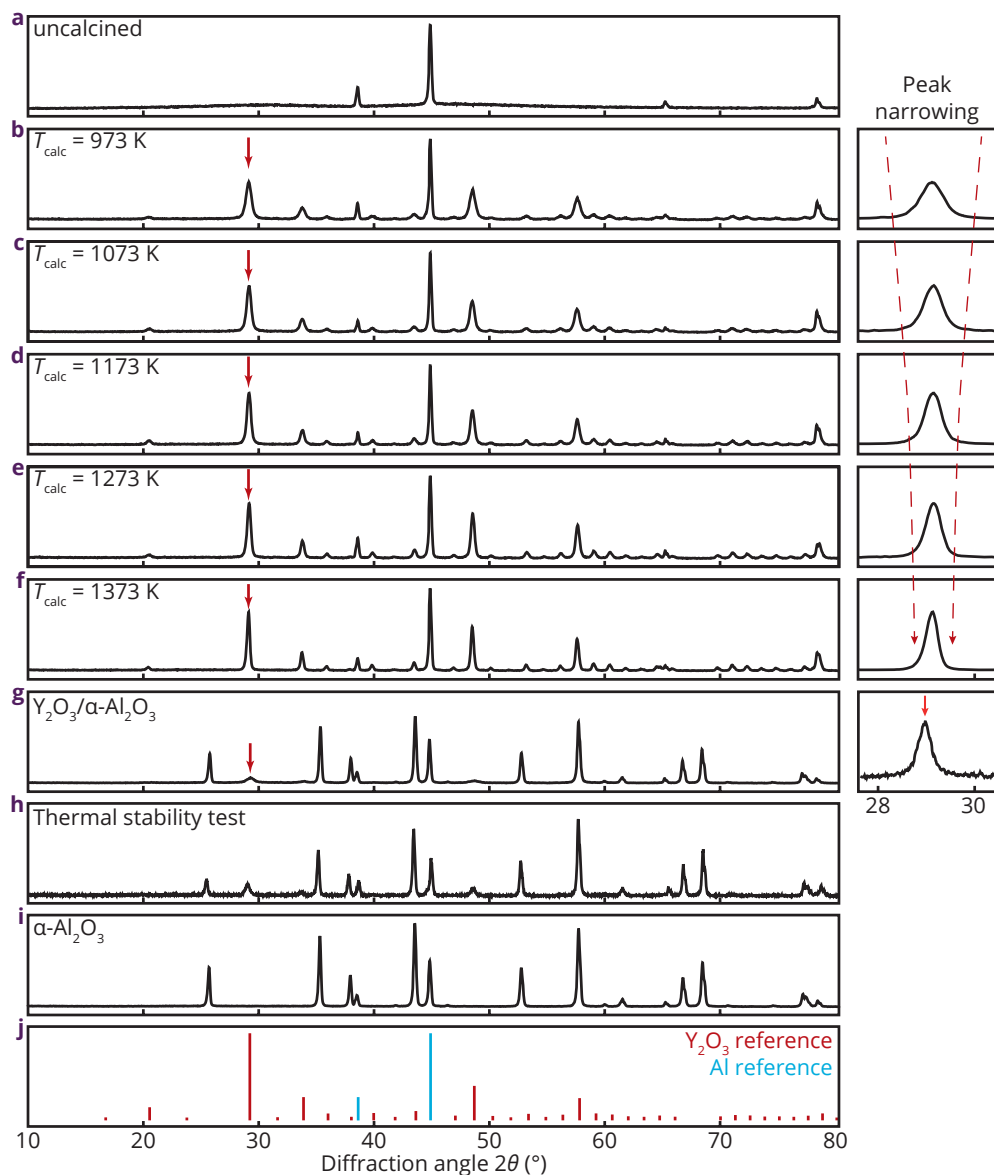


Figure 8.3 – XRD characterization. Cu K α XRD diffractograms of Y_2O_3 NPs before calcination (a) and after calcination at 973, 1073, 1173, 1273 and 1373 K (b–f respectively). XRD diffractograms of $\text{Y}_2\text{O}_3/\alpha\text{-Al}_2\text{O}_3$ particles (g), $\text{Y}_2\text{O}_3/\alpha\text{-Al}_2\text{O}_3$ particles after heating for 12 h to 873 K (h), $\alpha\text{-Al}_2\text{O}_3$ (i) and reference diffractograms (j). The extra frames to the right show magnifications of the diffraction peak located at $2\theta = 29^\circ$.

of clustered Y_2O_3 NPs are undesired for deposition on the surface of $\alpha\text{-Al}_2\text{O}_3$. Therefore 1073 K is considered as the optimal calcination temperature. This is the highest temperature for which individual NPs are maintained thus allowing for the highest degree of crystallinity, ca. 17 nm domains, for non-agglomerated NPs. Figure 8.1d shows the 1073 K calcined

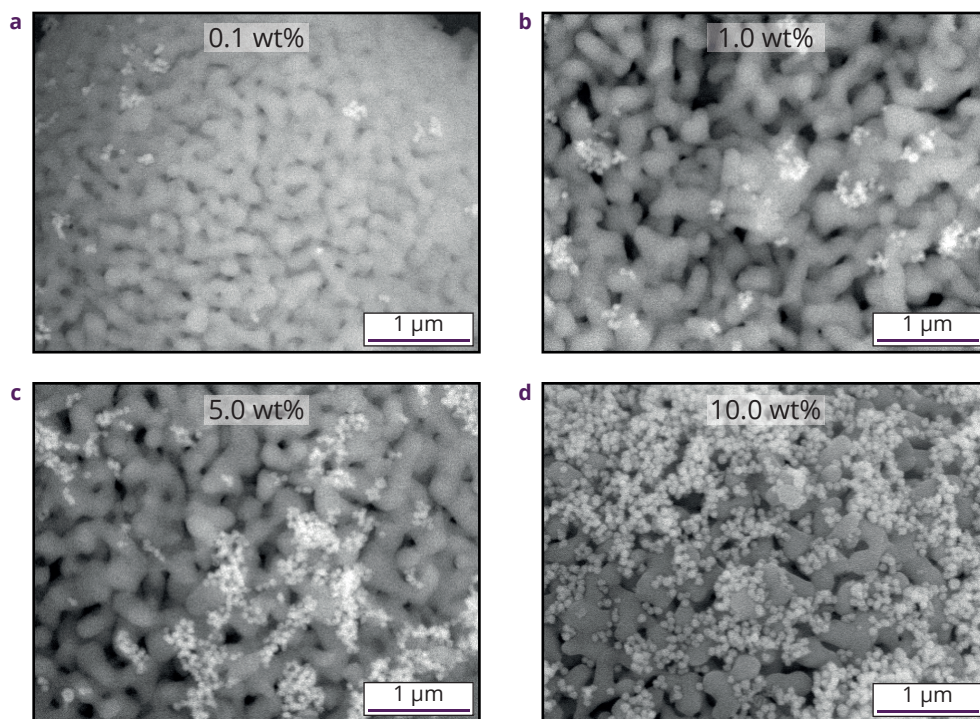


Figure 8.4 – Weight loadings. SEM images of 0.1, 1.0, 5.0 and 10.0 wt% Y_2O_3 NPs on $\alpha-Al_2O_3$ (a-d, respectively).

NPs with an average size of 70 nm.

The luminescent NPs were incorporated in a catalytically relevant matrix by deposition of the calcined Y_2O_3 NPs on a microcrystalline $\alpha-Al_2O_3$ support. This support material is ideal for our purposes since it is non-porous, thermally and chemically stable and can be made catalytically active by deposition of active metal NPs (e.g. Ni or Ag).^{16,17} Figures 8.1b and 8.1c show SEM images of $\alpha-Al_2O_3$ without and with deposited Y_2O_3 NPs. The Y_2O_3 NPs appear as lighter spots on the darker grey background of $\alpha-Al_2O_3$. The NPs are distributed over the surface of the Al_2O_3 microcrystalline structure both as individual particles and in larger agglomerates. XRD diffractograms confirm the presence of both $\alpha-Al_2O_3$ and Y_2O_3 (Figure 8.3g). Note that the high temperature calcination step of the NPs was done before deposition to prevent a reaction between $\alpha-Al_2O_3$ and (uncalcined) Y_2O_3 , resulting in the formation of yttrium-aluminate phases such as $Y_3Al_5O_{12}$ (YAG), $YAlO_3$ (YAP) or $Y_4Al_2O_9$ (YAM).

An important condition for monitoring the temperature during catalysis using the $Y_2O_3/\alpha-Al_2O_3$ particles, is to have a high luminescence signal from the lanthanide-doped Y_2O_3 NPs. At the same time, the fraction of $\alpha-Al_2O_3$ surface covered by Y_2O_3 should be limited to leave sufficient free space for the catalyst NPs. By screening the luminescence intensity of samples with different weight loadings between 0.1 and 10.0 wt% of Y_2O_3

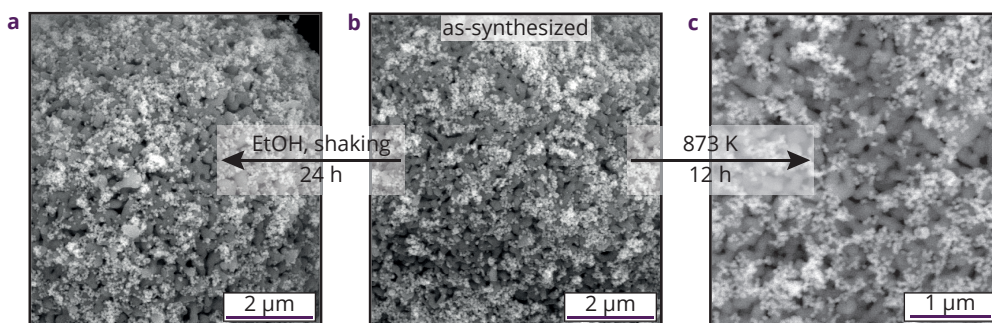


Figure 8.5 – Stability experiments. SEM image of Y_2O_3 NPs deposited on $\alpha\text{-Al}_2\text{O}_3$ (b), after shaking the sample for 24 h in EtOH (a) and heating the sample to 873 K for 12 h (c).

NPs, the optimal loading of these NP for the present experiments was determined to be ca. 5 wt%. SEM images for different weight loadings can be found in Figure 8.4. For the 5 wt% sample approximately 10 % of the surface is covered and the luminescence signal from the NPs was measured to be strong enough for remote luminescence measurements.

Stability of $\text{Y}_2\text{O}_3/\alpha\text{-Al}_2\text{O}_3$ particles. A key property of the nanoparticle temperature probes for application in catalytic environments is a high stability. Therefore, a several experiments were performed to examine the stability of the particles. First, the mechanical stability was assessed by shaking the particles in ethanol for 24 h on a roller shaker. SEM images (Figure 8.5) before and after shaking in ethanol show no significant difference. Furthermore, ICP-OES measurements of aliquots of the ethanol after filtering ($D_{\text{pore}} = 0.2 \mu\text{m}$) of the particles shows no presence of yttrium, indicating that the NPs did not desorb from the alumina surface or leached into the ethanol.

Secondly, the thermal stability of the particles was assessed by heating the particles to 873 K for 12 h. The surface of the particles was not altered and no significant sintering of NPs was observed by SEM, see Figure 8.5c. Moreover, as confirmed with XRD both the crystal phases of Y_2O_3 and $\alpha\text{-Al}_2\text{O}_3$ were preserved and the crystallite size of Y_2O_3 remained constant (Figure 8.3). These experiments show that the Y_2O_3 NPs are firmly attached to the $\alpha\text{-Al}_2\text{O}_3$ support material and are stable upon heating to 873 K for at least 12 h. This high intrinsic chemical and thermal robustness makes these particles of high interest for sensing in catalytic environments.

Temperature-dependent luminescence. The Y_2O_3 NPs were doped with different lanthanide ions. Ln^{3+} ions replace Y^{3+} ions in the host lattice and doping with different types of Ln^{3+} ions gives flexibility in the temperature range that can be probed and the spectral window for the luminescence measurements. ICP-OES was done to measure the Ln concentrations and shows that the three different samples were doped with 1 % Yb^{3+} and 1 % Er^{3+} , 0.9 % Dy^{3+} and 5 % Eu^{3+} , close to the nominal concentrations used in the NP synthesis. These $\text{Yb}^{3+}/\text{Er}^{3+}$, Dy^{3+} and Eu^{3+} dopants are responsible for a unique temperature-dependent luminescence. Figure 8.6 shows the temperature-dependent emission spectra

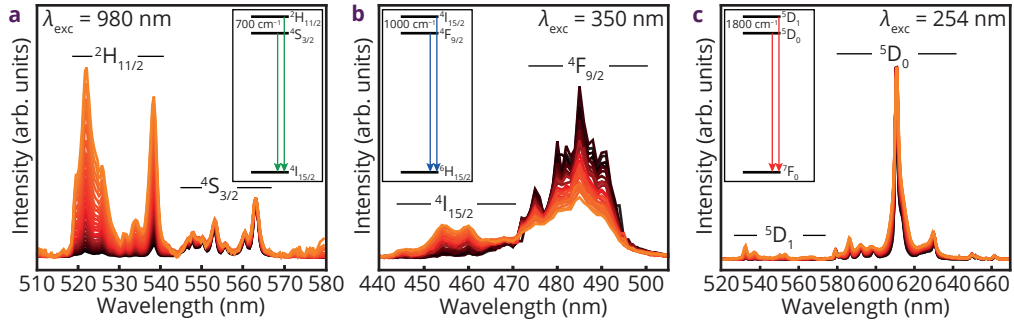


Figure 8.6 - Temperature-dependent luminescence. Luminescence spectra of $Y_2O_3:Er^{3+},Yb^{3+}$ (a), $Y_2O_3:Dy^{3+}$ (b) and $Y_2O_3:Eu^{3+}$ (c) at 300 K (black) up to 900 K (orange).

and energy level schemes of the three emitting Ln^{3+} ions. The transitions responsible for emission from the two thermally coupled energy levels that is used for temperature sensing are indicated. The energy gap between the two levels is ca. 700 cm^{-1} for Er^{3+} ($^4S_{3/2}-^2H_{11/2}$), ca. 1000 cm^{-1} for Dy^{3+} ($^4F_{9/2}-^4I_{15/2}$) and ca. 1800 cm^{-1} for Eu^{3+} ($^5D_0-^5D_1$). As a general rule, a larger energy gap shifts the optimal range for temperature sensing to higher temperatures.

The upconversion²⁷ luminescence spectra of 5 wt% loading Er^{3+} -doped $Y_2O_3/\alpha-Al_2O_3$ particles upon excitation of the Yb^{3+} codopant ($\lambda_{exc} = 980\text{ nm}$) at temperatures ranging from 300–900 K (black to orange) are shown in Figure 8.6a. The Yb/Er upconversion couple is well-known for temperature sensing and relies on 980 nm IR-excitation of Yb^{3+} which is followed by energy transfer from two Yb^{3+} ions to Er^{3+} which brings the Er^{3+} ion to the $^4S_{3/2}/^2H_{11/2}$ levels emitting in the green spectral region. The spectra show two sets of emission peaks between 510–545 nm and 545–570 nm from the $^2H_{11/2}-^4I_{15/2}$ and $^4S_{3/2}-^4I_{15/2}$ transitions, respectively. A clear trend in the emission spectra can be seen upon normalization on the highest $^4S_{3/2}$ emission peak at 564 nm. The temperature-dependent luminescence arises from thermal population of the higher energy $^2H_{11/2}$ state which is governed by Boltzmann statistics,

$$\frac{I_2}{I_1} = C e^{-\Delta E/kT} . \quad (8.1)$$

Here, I_i is the emission intensity from state i , C is a temperature-independent prefactor, ΔE is the energy difference between the two thermally coupled excited states, k is the Boltzmann constant and T is the temperature. Based on Boltzmann statistics, the correlation between the log of the fluorescence intensity ratio [$\text{Log}(I_2/I_1)$] is varying linearly with reciprocal temperature. This linear correlation can be exploited to determine temperatures from spectral outputs. Figure 8.7a shows the linear correlation for Er^{3+} in the temperature range marked in green. Note that above 800 K the linear correlation no longer holds (red area). This is most likely due to additional excited states that become thermally accessible. In this case the simple Boltzmann statistics for a two-level system no longer properly describes the temperature-dependent behavior.

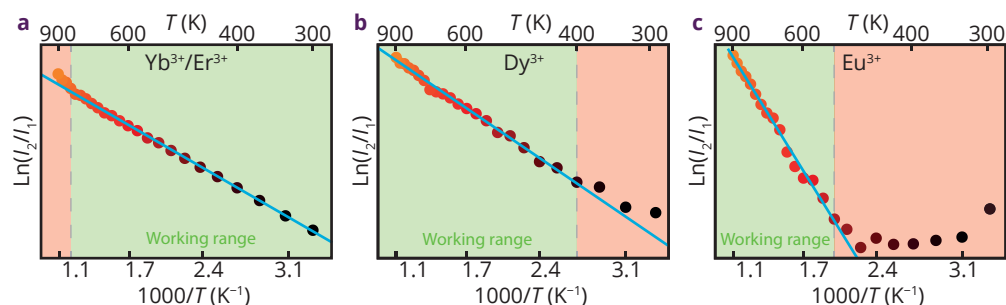


Figure 8.7 – Linear temperature regimes. Plots of $\text{Log}(I_2/I_1)$ vs. reciprocal temperature for Er^{3+} , Dy^{3+} and Eu^{3+} (a–c, respectively). The regime for a linear response is marked by a green area and corresponds to the T-range that can be probed.

In Figures 8.6b and 8.6c the temperature-dependent emission spectra of Dy^{3+} and Eu^{3+} are shown for UV excitation at 350 and 254 nm. For Dy^{3+} , the emission intensity from the lower energy ${}^4\text{F}_{9/2}$ level continuously decreases relative to the ${}^4\text{I}_{15/2}$ emission with temperature. The plot of $\text{Log}(I_2/I_1)$ vs. $1000/T$ (Figure 8.7b) is however not linear between 300 and 400 K, which indicates that the behavior does not follow Boltzmann statistics. For Boltzmann statistics it is crucial that non-radiative relaxation rates between thermally coupled levels is fast compared to rates of emission from individual levels. For larger energy gaps relaxation rates between levels are slowed down and only at elevated temperatures Boltzmann equilibrium is reached, explaining the deviation below 400 K for Dy^{3+} . Starting from 400 K the response is linear and the system can be used to monitor temperatures using the linear correlation. Note that the luminescence measurements were performed before deposition on $\alpha\text{-Al}_2\text{O}_3$ due to an overall lower luminescence signal because of the weak absorption strength of Dy^{3+} at the excitation wavelength. Optimizing the luminescence signal by using a strongly absorbing sensitizer that transfers the energy to Dy^{3+} can improve the performance.

Temperature-dependent emission spectra for Eu^{3+} -doped Y_2O_3 NPs on an $\alpha\text{-Al}_2\text{O}_3$ support are shown in Figure 8.6c. For Eu^{3+} the energy gap between the coupled ${}^5\text{D}_1$ and ${}^5\text{D}_0$ levels is 1800 cm^{-1} , which is significantly larger than for Er^{3+} and Dy^{3+} . Surprisingly, emission from the higher energy ${}^5\text{D}_1$ level initially decreases with increasing temperature (between 300 and 400 K). This is opposite to what is expected for Boltzmann behavior but can be explained by slow ${}^5\text{D}_1\text{-}{}^5\text{D}_0$ relaxation. Relaxation becomes faster at higher temperatures which explains the initial rise in relative ${}^5\text{D}_0$ intensity. In Figure 8.7c the $\text{Log}(I_2/I_1)$ vs. $1000/T$ for the ${}^5\text{D}_1/{}^5\text{D}_0$ emission of Eu^{3+} in Y_2O_3 is plotted and shows that above ca. 550 K a linear increase is observed. The temperature intervals for which the Dy^{3+} - and Eu^{3+} -doped systems have a linear response extend to at least 900 K, the maximum temperature we could probe with our current setup. It will be interesting to extend the temperature range to determine the upper limit for temperature sensing with Dy^{3+} - and Eu^{3+} -doped Y_2O_3 NPs.

The sensitivity of a temperature probe is determined by the relative change in signal with temperature, i.e. the steepness of the slopes of the fits in Figure 8.7. The steepness

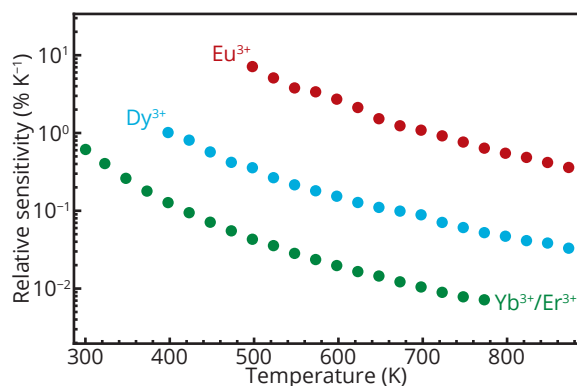


Figure 8.8 – Relative sensitivities. Relative sensitivity plotted vs. temperature for the Yb^{3+}/Er^{3+} (green), Dy^{3+} (cyan) and Eu^{3+} (red) doped Y_2O_3 NPs.

corresponds to $\Delta E/k$ and therefore the sensitivity for the Eu^{3+} -doped NPs is the highest followed by Dy^{3+} and Er^{3+} . The relative sensitivity²⁸ we determined for the Yb^{3+}/Er^{3+} , Dy^{3+} and Eu^{3+} -doped systems are plotted in Figure 8.8 and match values reported in the literature, see also Table 8.1.^{29–31} Using these different dopants, we have not only expanded the temperature range in which temperatures can be monitored but also are able to do this with high sensitivity. However, the accuracy of temperature measurements is also determined by the instrumentation and signal-to-noise ratio in the luminescence spectra. Furthermore, the reproducibility under varying measuring conditions and after multiple heating cycles is important to obtain an accurate and reliable temperature sensor.

To investigate the long-term reproducibility of the temperature sensors, we performed luminescence experiments in which the temperature was cycled from 300–900 K in four steps as shown in Figure 8.9. The emission spectra are very similar for equal temperatures in all three systems during multiple heating cycles. This indicates a stable system with good reproducibility. The differences between spectra taken at the same temperature during distinct cycles give statistics on the accuracy of the temperature probes. The standard deviation (SD) in the temperature measurements was very low for the Yb^{3+}/Er^{3+} -doped NPs, intermediate for the Dy^{3+} -doped sample and the highest for the Eu^{3+} -doped sample, as shown in Table 8.1. Note that the SD decreases with increasing temperature for the Eu^{3+} NPs due to the increase of signal for the lower intensity 5D_1 emission peak, resulting in a higher signal-to-noise ratio.

Ln-doped NPs have been shown to be promising temperature probes combining a stable

Table 1 – Performance parameters of the Yb^{3+}/Er^{3+} -, Dy^{3+} - and Eu^{3+} -doped systems.

Sample	T range (K)	Relative sensitivity (% K ⁻¹)	SD in T measurements (K)
Yb^{3+}/Er^{3+}	273–773	0.6 (at 273 K)–0.007 (at 773 K)	0.7 (at 273 K)–2.8 (at 773 K)
Dy^{3+}	373–873	1.0 (at 373 K)–0.03 (at 873 K)	8.0 (at 373 K)–14.4 (at 873 K)
Eu^{3+}	500–873	7.1 (at 500 K)–0.36 (at 873 K)	11.9 (at 500 K)–7.9 (at 873 K)

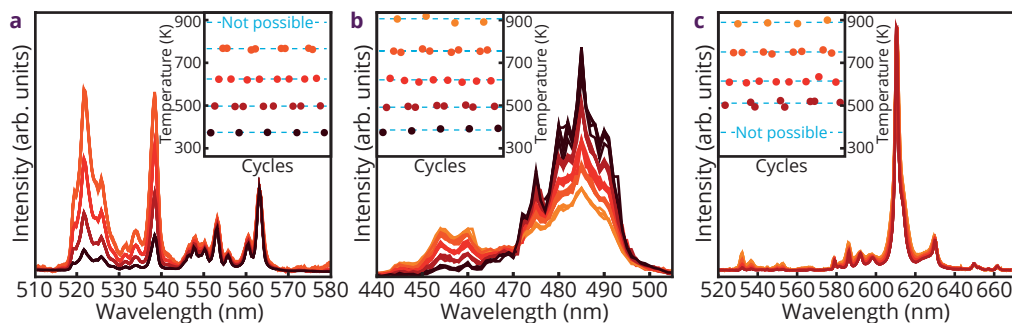


Figure 8.9 — Cycling experiments. Luminescence spectra of $\text{Y}_2\text{O}_3:\text{Yb}^{3+}/\text{Er}^{3+}$ (a), $\text{Y}_2\text{O}_3:\text{Dy}^{3+}$ (b) and $\text{Y}_2\text{O}_3:\text{Eu}^{3+}$ (c) taken while cycling between 300 K (black) up to 900 K (orange) in four steps. The insets show the calculated temperature based on the spectral output during the different steps in the cycles (if possible).

performance with a temperature accuracy of <15 K, which is superior to temperature resolutions found using IR thermometry^{4,5} and NMR.⁶ The temperature probes are applicable over a wide temperature range (300–900+ K) and in different spectral windows. The Y_2O_3 NP host offer great potential for further development of stable, reproducible and accurate probes for remote temperature sensing in catalytic environments and, because of their nanometer size, with high spatial resolution. The present results also demonstrate the versatility of Ln-dopants for remote luminescence temperature sensing.

Conclusions

We have successfully prepared and characterized Ln-doped Y_2O_3 nanoparticles for remote temperature sensing and deposited these on $\alpha\text{-Al}_2\text{O}_3$. Three different lanthanide combinations, $\text{Yb}^{3+}/\text{Er}^{3+}$, Dy^{3+} and Eu^{3+} were incorporated as luminescent temperature probes. The doped NPs deposited on an $\alpha\text{-Al}_2\text{O}_3$ support have high thermal and chemical stability, indicating that temperatures can be monitored under harsh catalytic reactor conditions in a non-invasive manner. The temperature-dependent luminescence of the lanthanide dopants shows that the different dopants cover a broad temperature range in an accurate and reproducible manner. The Er^{3+} emission can be used to monitor temperatures from 300 to 800 K with a high accuracy (<5 K). The Dy^{3+} and Eu^{3+} dopants are promising for temperature sensing in higher temperature regimes starting at 400 K (Dy^{3+}) and 550 K (Eu^{3+}) to at least 900 K with higher relative sensitivity than Er^{3+} . In all cases, the standard deviation of the temperature sensors is small (<15 K). The high chemical and thermal stability of the $\text{Y}_2\text{O}_3/\alpha\text{-Al}_2\text{O}_3$ system, combined with the accurate and reproducible non-invasive temperature sensing capabilities make this system ideal for remote mapping of temperature profiles in catalytic reactors. The Y_2O_3 NP host offers great versatility via incorporation of different luminescent lanthanides for remote temperature sensing in different optical windows, different temperature regimes and, because of the nanosize, with high spatial resolution. This is not only of interest in the field of catalysis but also in other areas where remote sensing of high temperatures is required, such as nano-electronics, microfluidics and nanophotonics.

Experimental Section

Chemicals. All chemicals were used without further purification. The chemicals $Y(NO_3)_3 \cdot 6H_2O$, $Eu(NO_3)_3 \cdot 6H_2O$, $Dy(NO_3)_3 \cdot 6H_2O$, $Er(NO_3)_3 \cdot 6H_2O$, and $Yb(NO_3)_3 \cdot 6H_2O$ with a purity of 99.99 % were purchased from Sigma-Aldrich. Urea (99.5 % purity) and ethanol (100 % purity, containing traces of H_2O) were purchased from Strem Chemicals.

Synthesis of Y_2O_3 NPs. The Y_2O_3 NPs were prepared via a homogenous precipitation technique based on the works of Sohn & Fukushima.^{31,32} In all experiments, 178.5 mL purified water and 240 μ mol urea are added to a round-bottom flask. While stirring vigorously, 0.72 mmol $RE(NO_3)_3$ ($RE = Y, Eu, Dy, Er$ and/or Yb) dissolved in 1.5 mL purified water is added to the solution. The solution is subsequently heated to 358 K while measuring the pH every 20 minutes. After a subsequent strong decline (from 6.8 to 5.5) and slow rise of the pH (to 6.4), the heating is stopped and the solution is allowed to cool down to room temperature. Afterwards, the solution is centrifuged and the precipitate is washed three times with water and finally dispersed in ethanol to prevent aggregation of the uncalcined NPs. The sample is dried overnight at 333 K and calcined in static air for 3 h using a ramp of 5 K/min.

Deposition of Y_2O_3 NPs on $\alpha-Al_2O_3$. Various masses of Y_2O_3 NPs and $\alpha-Al_2O_3$ are weighed to obtain loadings of 0.1, 1.0, 5.0, 10 and 20 wt% with a total mass of 300 mg. The Y_2O_3 NPs are subsequently sonicated in ethanol to yield a concentration 5 mg NPs/mL. The dispersions are transferred to the vials containing $\alpha-Al_2O_3$ and are carefully shaken for one minute. Afterwards, the $Y_2O_3/\alpha-Al_2O_3$ particles are dried overnight at 333 K.

Adsorption and mechanical stability of $Y_2O_3/\alpha-Al_2O_3$ particles. A sample with a weight loading of 5 wt% Y_2O_3 on $\alpha-Al_2O_3$ (total mass of 300 mg) is separated into six separate vials. 2 mL of ethanol is added to each flask and shaken for 1 min up to 24 h. In order to identify any desorbed Y_2O_3 NPs, the dispersions were left for 5 minutes to let the particles sediment. The elemental concentration of yttrium and aluminum in the supernatant is investigated with inductively coupled plasma optical emission spectroscopy (ICP-OES)

Experimental setup. XRD diffractograms were recorded on a PW 1729 Philips diffractometer utilizing Cu $K\alpha$ radiation between $2\theta = 10$ and 80° . TEM images were taken with a Tecnai 10 Philips microscope at 15 keV using a BSE detector. SEM images were made on a FEI XL30S FEG operating at 15 kV. Concentrations were measured with ICP-OES on a Perkin-Elmer Optima 8300 Optical Emission Spectrometer. Luminescence spectra of Dy^{3+} were recorded with an Edinburgh Instruments FL900 spectrophotometer equipped with a R928 PMT while the luminescence spectra of the Yb^{3+}/Er^{3+} - Eu^{3+} -doped samples were measured using an Ocean Optics QEPro CCD. Temperature control was obtained via a THMS600 heating stage of Linkam Scientific Instruments.

Acknowledgments

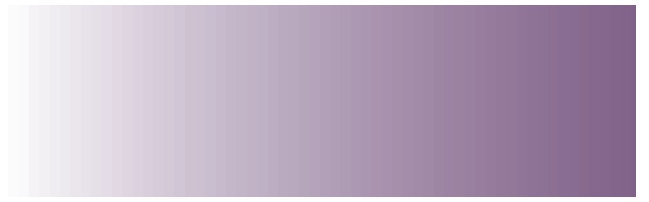
The authors acknowledge the assistance of Christa van Oversteeg during the ICP-OES measurements. This work was supported by the Netherlands Center for Multiscale Catalytic Energy Conversion (MCEC), an NWO Gravitation programme funded by the Ministry of Education, Culture and Science of the government of the Netherlands.

References

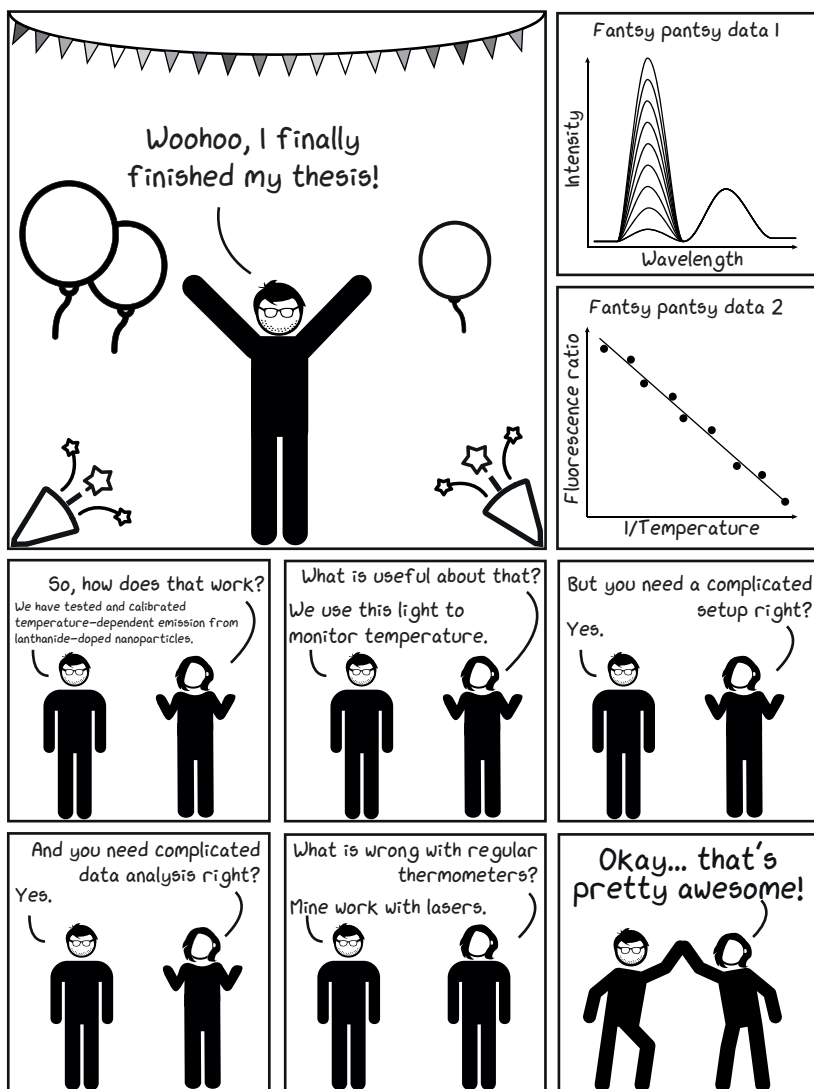
1. Hwang, S. & Smith, R. Optimum reactor design in methanation processes with nonuniform catalysts. *Chem. Eng. Commun.* **2009**, *196*, 616–642.
2. Mazidi, S. K.; Sadeghi, M. T. & Marvast, M. A. Optimization of Fischer-Tropsch Process in a Fixed-Bed Reactor Using Non-uniform Catalysts. *Chem. Eng. Technol.* **2013**, *36*, 62–72.
3. Yarulina, I.; Kapteijn, F. & Gascon, J. The importance of heat effects in the methanol to hydrocarbons reaction over ZSM-5: on the role of mesoporosity on catalyst performance. *Catal. Sci. Technol.* **2016**, *6*, 5320–5325.
4. Kimmerle, B.; Grunwaldt, J.-D.; Baiker, A.; Glatzel, P.; Boye, P.; Stephan, S. & Schroer, S.G. Visualizing a catalyst at work during the ignition of the catalytic partial oxidation of methane. *J. Phys. Chem. C* **2009**, *113*, 3037–3040.
5. Simeone, M.; Salemm, L.; Allouis, C. & Volpicelli, G. Temperature profile in a reverse flow reactor for catalytic partial oxidation of methane by fast IR imaging. *AIChE J.* **2008**, *54*, 2689–2698.
6. Koptuyug, I. V.; Khomichev, A. V.; Lysova, A. A. & Sagdeev, R. Z. Spatially Resolved NMR Thermometry of an Operating Fixed-Bed Catalytic Reactor. *J. Am. Chem. Soc.* **2008**, *130*, 10452–10453.
7. Geitenbeek, R. G.; Nieuwelink, A.-E.; Jacobs, T. S.; Salzmann, B. B. V.; Goetze, J.; Meijerink, A. & Weckhuysen, B. M. In Situ Luminescence Thermometry To Locally Measure Temperature Gradients during Catalytic Reactions. *ACS Catal.* **2018**, *8*, 2397–2401.
8. Jaque, D. & Vetrone, F. Luminescence nanothermometry. *Nanoscale* **2012**, *4*, 4301–4326.
9. Brites, C. D. S.; Lima, P. P.; Silva, N. J. O.; Millan, A.; Amaral, V. S.; Palacio, F. & Carlos, L. D. Thermometry at the nanoscale. *Nanoscale* **2012**, *4*, 4799–4829.
10. Vetrone, F.; Naccache, R.; Zammaron, A.; de la Fuente, A. J.; Sanz-Rodriguez, F.; Maestro, L. M.; Rodriguez, E. M.; Jaque, D.; Solé, J. G. & Capobianco, J. A. Temperature Sensing Using Fluorescent Nanothermometers. *ACS Nano* **2010**, *4*, 3254–3258.
11. Okabe, K.; Inada, N.; Gota, C.; Harada, Y.; Funatsu, T. & Uchiyama, S. Intracellular temperature mapping with a fluorescent polymeric thermometer and fluorescence lifetime imaging microscopy. *Nat. Commun.* **2012**, *3*, 705.
12. Haro-González, P.; Martín, I. R.; Martín, L. L.; León-Luis, S. F.; Pérez-Rodríguez, C. & Lavín, V. Characterization of Er³⁺ and Nd³⁺ doped Strontium Barium Niobate glass ceramic as temperature sensors. *Opt. Mater.* **2011**, *33*, 742–745.
13. Xu, X.; Wang, Z.; Lei, P.; Yu, Y.; Yao, S.; Song, S.; Liu, X.; Su, Y.; Dong, L. & Feng, J. α -NaYb(Mn)F₄:Er³⁺/Tm³⁺@NaYF₄ UCNPs as “Band-Shape” Luminescent Nanothermometers over a Wide Temperature Range. *ACS Appl. Mater. Interfaces* **2015**, *7*, 20813–20819.
14. Li, D.; Wang, Y.; Zhang, X.; Yang, K.; Liu, L. & Song, Y. Optical temperature sensor through infrared excited blue upconversion emission in Tm³⁺/Yb³⁺ codoped Y₂O₃. *Opt. Commun.* **2012**, *285*, 1925–1928.

15. Geitenbeek, R. G.; Prins, P. T.; Albrecht, W.; van Blaaderen, A.; Weckhuysen, B. M. & Meijerink, A. NaYF₄:Er³⁺,Yb³⁺/SiO₂ Core/Shell Upconverting Nanocrystals for Luminescence Thermometry up to 900 K. *J. Phys. Chem. C* **2017**, *121*, 3503–3510.
16. Mathews, M. D.; Ambekar, B. R.; Tyagi, A. K. & Köhler, J. High temperature X-ray diffraction studies on sodium yttrium fluoride. *J. Alloys Compd.* **2004**, *377*, 162–166.
17. Pompeo, F.; Nichio, N. N.; Souza, M. M. V. M.; Cesar, D. V.; Ferretti, O. A. & Schmal, M. Study of Ni and Pt catalysts supported on α -Al₂O₃ and ZrO₂ applied in methane reforming with CO₂. *Appl. Catal. A Gen.* **2007**, *316*, 175–183.
18. Yao, W.; Guo, Y.; Liu, X.; Guo, Y.; Wang, Y.; Wang, Y.; Zhang, Z. & Lu, G. Epoxidation of propylene by molecular oxygen over the Ag-Y₂O₃-K₂O/ α -Al₂O₃ catalyst. *Catal. Lett.* **2007**, *119*, 185–190.
19. Benninger, R. K. P.; Koç, Y.; Hofmann, O.; Requejo-Isidro, J.; Neil, M. A. A.; French, P. M. W. & deMello, A. J. Quantitative 3D mapping of fluidic temperatures within microchannel networks using fluorescence lifetime imaging. *Anal. Chem.* **2006**, *78*, 2272–2278.
20. Löw, P.; Kim, B.; Takama, N. & Bergaud, C. High-spatial-resolution surface-temperature mapping using fluorescent thermometry. *Small* **2008**, *4*, 08–914.
21. Bar-Cohen A. & Wang, P. On-chip Hot Spot Remediation with Miniaturized Thermoelectric Coolers. *Microgravity Sci. Technol.* **2009**, *21*, 351–359.
22. Aigouy, L.; Tessier, G.; Mortier, M. & Charlot, B. Scanning thermal imaging of microelectronic circuits with a fluorescent nanoprobe. *Appl. Phys. Lett.* **2005**, *87*, 1–3.
23. Jundt, D. H. Temperature-dependent Sellmeier equation for the index of refraction, n_o , in congruent lithium niobate. *Opt. Lett.* **1997**, *22*, 1553–1555.
24. Romero, J. J.; Arago, C.; Gonzalo, J. A.; Jaque, D. & Sole, J. G. Spectral and thermal properties of quasiphase-matching second-harmonic-generation in Nd³⁺:Sr_{0.6}Ba_{0.4}(NbO₃)₂ multiselection-frequency-converter nonlinear crystals. *J. Appl. Phys.* **2003**, *93*, 3111–3113.
25. Chen, X. Y.; Cook, R. E.; Skanthakumar, S.; Shi, D. & Liu, G. K. Crystallization, phase transition and optical properties of the rare-earth-doped nanophosphors synthesized by chemical deposition. *Nanotechnology* **2003**, *14*, 670–674.
26. Menyuk, N.; Dwight, K. & Pierce, J. W. NaYF₄:Yb,Er—An efficient upconversion phosphor. *Appl. Phys. Lett.* **1972**, *21*, 159–161.
27. Pandey, A. & Rai, V. K. Optical thermometry using FIR of two close lying levels of different ions in Y₂O₃:Ho³⁺-Tm³⁺-Yb³⁺ phosphor. *Appl. Phys. B Lasers Opt.* **2013**, *113*, 221–225.
28. Rakov, N.; Bispo, L. R. A. & Maciel, G. S. Temperature sensing performance of dysprosium doped aluminum oxide powders. *Opt. Commun.* **2012**, *285*, 1882–1884.
29. Rai, V. K. & Rai, A. Temperature sensing behavior of Eu³⁺ doped tellurite and calibo glasses. *Appl. Phys. B* **2007**, *86*, 333–335.
30. Li, C.; Dong, B.; Li, S. & Song, C. Er³⁺-Yb³⁺ co-doped silicate glass for optical temperature sensor. *Chem. Phys. Lett.* **2007**, *443*, 426–429.
31. Sohn, S.; Kwon, Y.; Kim, Y. & Kim, D. Synthesis and characterization of near-monodisperse yttria particles by homogeneous precipitation method. *Powder Technol.* **2004**, *142*, 136–153.

32. Fukushima, S.; Furukawa, T.; Niioka, H.; Ichimiya, M.; Sannomiya, T.; Miyake, J.; Ashida, M.; Araki, T. & Hashimoto, M. Synthesis of Y_2O_3 nanophosphors by homogeneous precipitation method using excessive urea for cathodoluminescence and upconversion luminescence bioimaging. *Opt. Mater. Express* **2016**, *6*, 831.



Chapter 9 – Summary, Conclusions and Perspectives



Robin Geitenbeek



Alfons van Blaaderen



Bert Weckhuysen



Andries Meijerink

Introduction

In the fields of chemistry and physics, temperature is one of the most important parameters as it can influence a large variety of phenomena, such as reaction kinetics. Due to the rapid development in the production of nanomaterials and nanoscale devices, application of classical thermometers such as thermocouples or resistance temperature sensors, face challenges due to intrinsic limitations. These intrinsic limitations include the downscaling of the thermometers and the non-invasiveness, which is required for many applications. To understand processes occurring at the nanoscale, it is crucial that new methods for monitoring of important parameters, such as temperature, on this length scale are developed.

In this thesis, we have investigated bandshape luminescence thermometry, a non-invasive method to monitor temperature. In combination with light microscopy, this method has the potential to monitor temperature at the (sub-)μm regime. Bandshape luminescence thermometry using lanthanide-doped nanocrystals has developed rapidly in the past five years with a focus on biological systems where temperatures between 300 and 350 K are monitored. Here, we extend the temperature range for bandshape luminescence thermometry to temperatures beyond 900 K and demonstrate successful temperature mapping in a variety of reaction conditions that are relevant in catalysis.

The first part of this thesis focuses on a more thorough understanding of the fundamentals of luminescence thermometry. Here, different lanthanide dopants, the origin of the physical processes responsible for the temperature-dependent luminescence, and several host materials have been evaluated to investigate the different temperature ranges and sensitivities in which these materials work. Furthermore, a more general description of the temperature-dependent emission in these lanthanide ions has been proposed on the basis of thorough investigations of the excited state dynamics.

The second part of this thesis focuses on the applications of luminescence thermometry. To showcase the potential of luminescence thermometry several chemical reactions have been investigated and the temperature has been mapped in reactors in which the spatial resolution of classical thermometers no longer suffices.

Fundamentals of luminescence thermometry

Analysis and calibration of the temperature dependence for bandshape luminescence thermometry is commonly based on Boltzmann equilibrium of the coupled levels. In **Chapter 2** we investigate the validity of this assumption by analyzing and modeling the emission by Eu^{3+} in NaYF_4 from ${}^5\text{D}_1$ in relation to the emission from ${}^5\text{D}_0$. The results show that for low Eu^{3+} concentrations temperature-dependent multiphonon relaxation accurately accounts for both the intensity ratio of the emissions and the dynamics of the emission decay. The analysis also reveals that Boltzmann equilibrium is not realized in the temperature regime investigated (300–900 K). Furthermore, upon increasing the Eu^{3+} concentration, cross-relaxation between neighboring Eu^{3+} ions enhances ${}^5\text{D}_1$ – ${}^5\text{D}_0$ relaxation

rates, thereby extending the temperature range in which emission intensity ratios are usable for reliable and accurate temperature sensing. The insights obtained are important to recognize, understand, and control deviations from Boltzmann behavior in luminescence (nano)thermometry, and are thus crucial for the development and understanding of reliable temperature sensors.

In **Chapter 3** we extend the temperature range for nanothermometry beyond 900 K using silica coated NaYF_4 nanoparticles doped with the lanthanide ions Yb^{3+} and Er^{3+} . Monodisperse ca. 20 nm $\text{NaYF}_4:\text{Er}^{3+},\text{Yb}^{3+}$ nanocrystals were coated with a ca. 10 nm silica shell. Upon excitation with infrared radiation bright green upconversion (UC) emission is observed. From the intensity ratio between ${}^2\text{H}_{11/2}$ and ${}^4\text{S}_{3/2}$ UC emission lines at 520 nm and 550 nm, respectively, the temperature can be determined up to at least 900 K with an accuracy of 1–5 K for silica coated NPs. For bare $\text{NaYF}_4:\text{Er}^{3+},\text{Yb}^{3+}$ NPs the particles degrade above 600 K. Repeated thermal cycling experiments demonstrate the high durability and reproducibility of the silica coated nanocrystals as temperature probes without any loss of performance.

In **Chapter 8** we report temperature-dependent luminescence of $\text{Yb}^{3+}/\text{Er}^{3+}$ -, Dy^{3+} - and Eu^{3+} -doped Y_2O_3 nanoparticles (NPs). The high chemical and thermal stability of Y_2O_3 makes these nanoprobables ideal for sensing in catalytic environments. A systematic study of the three types of luminescent NPs reveals that the temperature-dependent luminescence of $\text{Yb}^{3+}/\text{Er}^{3+}$, Dy^{3+} and Eu^{3+} serves different temperature ranges: lower T regime (300–800 K, accuracy <5 K) for $\text{Yb}^{3+}/\text{Er}^{3+}$, intermediate T for Dy^{3+} (400–900+ K, accuracy <15 K) and high T for Eu^{3+} (550–900+ K, accuracy <12 K). We have deposited these lanthanide-doped Y_2O_3 NPs on $\alpha\text{-Al}_2\text{O}_3$, a non-porous catalyst support material. The NPs are strongly adsorbed on the surface and no sintering was observed upon heating to 900 K for 12 h. The superior thermal and chemical stability of the $\text{Y}_2\text{O}_3/\alpha\text{-Al}_2\text{O}_3$ host (compared to for instance NaYF_4) in combination with different luminescent lanthanide dopants result in a robust system that can be tailored to monitor temperatures in different regimes with the highest possible sensitivity.

Applications of luminescence thermometry

In **Chapter 4** Bandshape luminescence thermometry during in situ temperature measurements has been reported by preparing three catalytically relevant systems, which show temperature-dependent luminescence. One of these systems was further investigated as a showcase for application. Microcrystalline NaYF_4 doped with Er^{3+} and Yb^{3+} was mixed with a commercial zeolite H-ZSM-5 to investigate the Methanol-to-Hydrocarbons (MTH) reaction, while monitoring the reaction products with on-line gas chromatography. Due to the exothermic nature of the MTH reaction, a front of increased temperature migrating down the fixed reactor bed was visualized, showing the potential for various applications of luminescence thermometry for in situ measurements in catalytic systems.

In **Chapter 5** an in-depth study on the temperature distribution within a sample holder with a heating coil was used as a showcase for high spatial resolution luminescence thermometry.

The sample holder for operando soft X-ray scanning transmission X-ray microscopy (STXM) measurements investigated in this work was custom-made by our group and fits in the limited space available during STXM measurements. Within the sample holder, a nanoreactor, originally made for in situ TEM measurements, is present with a heating spiral of ca. $300\ \mu\text{m} \times 300\ \mu\text{m}$. Combining luminescence thermometry with confocal microscopy allowed for temperature mapping with a spot size of ca. $7\ \mu\text{m}$. The results show a fairly homogeneous temperature distribution under vacuum conditions. However, upon introducing air, heat dissipation results in lower temperatures and a temperature gradient between the center and edges of the heater. At a setpoint of $600\ ^\circ\text{C}$, the temperature at the center of the heating spiral is $450\ ^\circ\text{C}$, which rapidly decreases to $250\ ^\circ\text{C}$ at the edge of the heating spiral. The results give new insights into temperatures during operando conditions. Furthermore, the experiments showcase the potential of luminescence thermometry in combination with (confocal) microscopy to monitor temperatures with spatial resolutions of at least $7\ \mu\text{m}$.

Another application of luminescence thermometry in which the spatial resolution is showcased is shown in **Chapter 6**. In this chapter, temperature measurements have been performed in multiple microfluidic reactors. Initial experiments are performed to compare luminescence thermometry with integrated resistance temperature detectors and show great agreement with only an average temperature difference of $0.34\ ^\circ\text{C}$ at the position of the resistance thermometer. Clear deviations were observed when moving away from this point. A second set of experiments showed that it is possible to monitor temperature differences induced by the exothermic reaction of hydrochloric acid and ammonia. Here, NaYF_4 NPs are coated with SiO_2 for chemical stability and dispersibility in polar media. Although the mixing of hydrochloric acid and ammonia was slow due to the laminar flow, temperature increases of ca. $15\ ^\circ\text{C}$ were observed upon mixing of the two liquids. A final showcase for the applicability of luminescence thermometry in microfluidics was performed in combination with confocal microscopy. Using integrated heaters and a heat sink, a temperature gradient from 60 to $40\ ^\circ\text{C}$ over ca. $500\ \mu\text{m}$ was obtained. The temperature distribution within this gradient was investigated and confirmed with a spatial resolution of ca. $9\ \mu\text{m}$. The different microfluidic devices used in this work, PDMS, glass and silicon, in combination with the different kind of experiments, show that luminescence thermometry is a versatile tool that is readily applicable for temperature mapping with high spatial resolution in microfluidics.

Monitoring temperature at the relevant length scale, while at the same time performing operando spectroscopy measurements is critical as shown from the above results. In **Chapter 7** we have combined $\text{NaYF}_4@\text{SiO}_2$ temperature probes with Rh catalyst NPs and $\text{Au}@\text{SiO}_2$ NPs in extrudates. While using Rh to catalyze the CO hydrogenation reaction, $\text{Au}@\text{SiO}_2$ NPs can be used to perform shell-isolated nanoparticles enhanced Raman spectroscopy (SHINERS) to investigate the adsorbed species while an on-line mass spectrometer can monitor the reaction products. Incorporation of the $\text{NaYF}_4:\text{Er}^{3+}, \text{Yb}^{3+}$ in the system ensured that the temperature read-out was performed at the catalyst level. Using

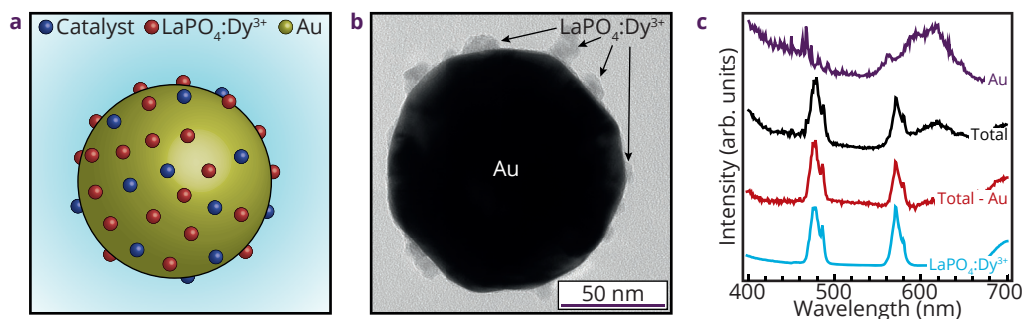


Figure 9.1 – LaPO_4/Au project for local SHINERS and temperature measurements. A schematic representation of catalyst (blue) and $\text{LaPO}_4:\text{Dy}^{3+}$ temperatures probes (red) deposited on gold NPs (a). A TEM image of LaPO_4 NPs deposited on a gold NP (b). Luminescence measurements (c) of bare Au NPs (purple), Au NPs with $\text{LaPO}_4:\text{Dy}^{3+}$ NPs deposited on the surface (black), the total luminescence with the gold luminescence subtracted (red) and a reference spectrum of pure $\text{LaPO}_4:\text{Dy}^{3+}$ NPs (cyan).

combined SHINERS, MS and luminescence thermometry, the reaction mechanism of the CO hydrogenation was investigated. The results suggest a mechanism pathway that involves the dissociation of CO and concurrent CO insertion to yield CH_4 and C_3H_8 after expulsion of H_2O . The experiments demonstrate the necessity for temperature measurements at the relevant length scales. Using a constant temperature setpoint of $350\text{ }^\circ\text{C}$ and constant gas flow of 20 mL min^{-1} , the composition of the synthesis gas was varied from pure CO to pure H_2 . While changing the gas composition from pure H_2 to pure CO, the temperature increased from 340 to $380\text{ }^\circ\text{C}$ due to the lower thermal conductivity of CO. These results show that in order to compare results between different studies, it is paramount to monitor temperature under relevant conditions and at the position where the reaction occurs.

Perspectives

In this PhD thesis the fundamentals of luminescence thermometry have been investigated extensively. In addition, the applicability of the technique has been showcased in multiple examples in which the temperature measurements were performed with mm– μm spatial resolutions and in a wide temperature range (up to 900 K).

Increasing of spatial and temporal resolution

To further develop the potential for luminescence thermometry, different research paths can be distinguished. To monitor smaller scale processes, the resolution should be increased further to the sub- μm regime. Although the initial results with the confocal microscopy show that temperature can be probed in areas of ca. $10\text{ }\mu\text{m}$, the spatial resolution of the confocal microscopes is much higher. However, to ensure proper temperature read-outs, the luminescence signal should be high enough. The interplay between amount of sample probed, the acquisition time and finally the brightness of the temperature probes will ultimately determine the limits for luminescence thermometry with respect to both spatial and temporal resolution. Optimizing the brightness of the temperature probes can enhance the potential of luminescence thermometry. This can be done by synthesizing

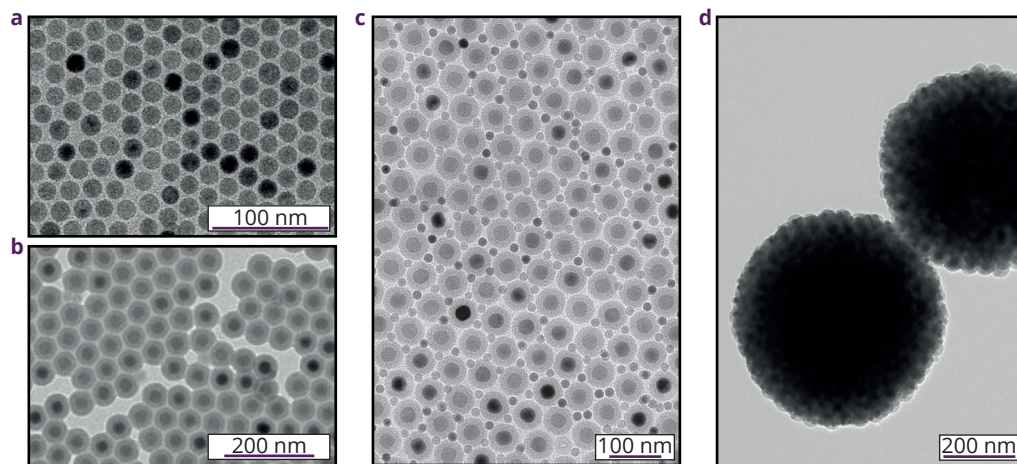


Figure 9.2 – Self-assembly experiments. TEM images of iron oxide catalyst NPs (a), NaYF₄@SiO₂ temperature probes (b), binary self-assembled monolayer of the catalyst and temperature probe (c), binary supraparticles of the catalyst and temperature probe (d).

luminescent NPs with a higher quantum yield or by for instance clustering the luminescent NPs within brighter supraparticles.

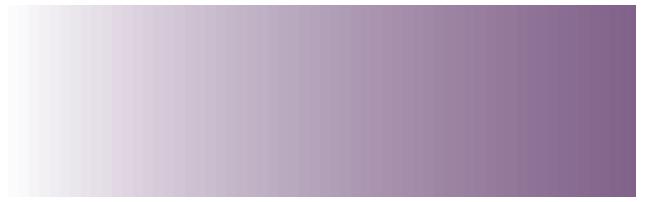
Develop new smart materials

Another example for additional research is to prepare smart materials in which both catalyst and temperature probe are incorporated. In **Chapter 7** we have already shown that the Au@SiO₂ and NaYF₄@SiO₂ NPs can be combined to perform both SHINERS and luminescence thermometry at the same time. However, if the NaYF₄@SiO₂ NPs of ca. 50 nm are replaced by LaPO₄ NPs of ca. 5 nm, the temperature probes could be deposited directly on the surface of the Au@SiO₂ as shown in Figure 9.1a and 9.1b. Pilot experiments show that the luminescence of Dy³⁺-doped LaPO₄ can be monitored on the Au@SiO₂ NPs as shown in Figure 9.1c. Since the LaPO₄ is only located on the surface of the Au@SiO₂, the luminescence measurements only probe a very specific area within 10–20 nm from the surface and the spatial resolution of the temperature measurements is increased to the nm-regime. By codeposition of catalyst NPs, catalysis can be performed, while monitoring the enhanced Raman signal due to the Au@SiO₂ NPs and the local temperature can be monitored using LaPO₄ NPs.

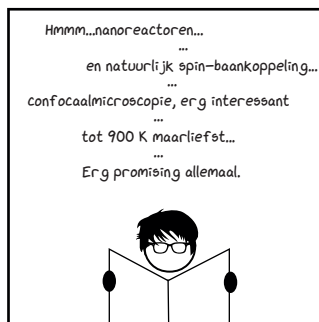
A second example for smart materials is to use the temperature probes as support material for catalyst NPs. The chemical and thermal stability of the silica-coated NaYF₄ NPs, as discussed in **Chapter 3**, can be used to prevent sintering of catalyst NPs at elevated temperatures. The separate NPs of iron oxide (Figure 9.2a) and NaYF₄@SiO₂ (Figure 9.2b) can be combined into a 2D (Figure 9.2c) or even 3D self-assemblies (9.2d). Here, the NaYF₄@SiO₂ can both determine the temperature at the catalyst level as well as prevent sintering of the catalyst NPs by keeping them spatially separated during chemical reactions.

Expand the applicability to different catalytic reactions

In this PhD thesis a few showcases demonstrate the applicability of luminescence thermometry to monitor temperatures during in situ or operando conditions. Furthermore, the necessity has been demonstrated in for instance **Chapter 5** and **Chapter 7** to monitor temperature locally in order to compare between different operando characterization studies. Since luminescence thermometry is an ideal candidate for the local probing of temperature, the technique should be preferably integrated into the toolkit of all research groups performing operando characterization studies.



Nederlandse Samenvatting



Robin Geitenbeek



Bert Weckhuysen



Alfons van Blaaderen



Andries Meijerink

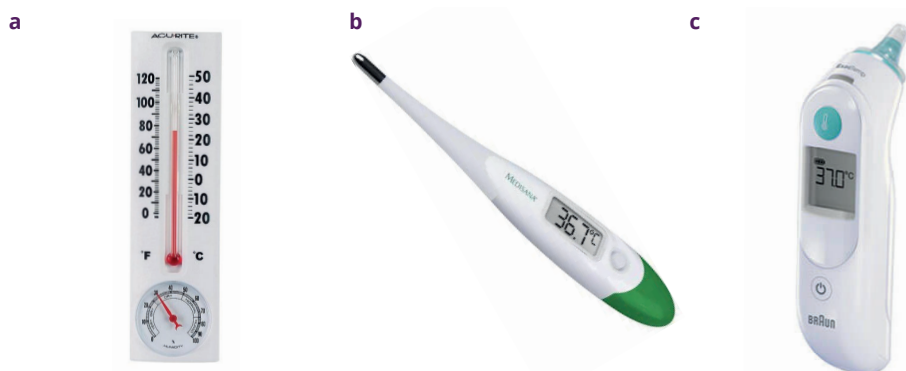
Dit hoofdstuk is geschreven voor iedereen die wel interesse heeft in het onderwerp van dit proefschrift, maar niet de wetenschappelijke achtergrond heeft om het werk ten volle te begrijpen of te waarderen. Het is opgedeeld in vier delen. Een inleiding waarin de beweegreden van dit onderzoek uitgelegd wordt, een stuk theorie om de resultaten en gebruikte methoden te begrijpen, de resultaten van dit onderzoek en ten slotte de conclusies die getrokken worden op basis van de resultaten.

Inleiding

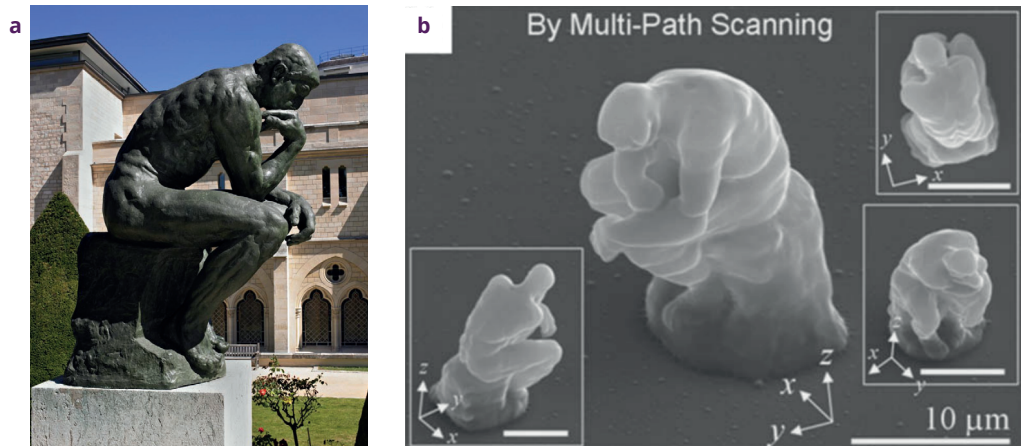
Een korte samenvatting van dit proefschrift is dat we onderzoek hebben gedaan naar lichtemissie (luminescentie) van specifieke lanthanide-ionen bij verschillende temperaturen om patronen in het luminescente gedrag te vinden. Die patronen hebben we vervolgens kunnen gebruiken om temperatuur te meten aan de hand van het uitgezonden licht. Hoe dat precies werkt, wordt besproken in de Theorie sectie.

Met andere woorden, in dit proefschrift wordt beschreven hoe een thermometer kan worden gemaakt die werkt door middel van licht en hoe deze vervolgens kan worden toegepast. Het meten van de temperatuur aan de hand van licht heeft namelijk voordelen ten opzichte van klassieke thermometers, welke weergegeven worden in Figuur 1.

Temperatuur is iets wat moeilijk direct te meten is, vandaar dat meestal een ander natuurkundig fenomeen bekeken wordt dat afhangt van de temperatuur. De thermometer van Figuur 1a gebruikt thermische expansie, het feit dat (vloei-)stoffen uitzetten zodra het warmer wordt. Door dit systeem goed te ijken kan een nauwkeurige temperatuurmeting gedaan worden. De thermometer in Figuur 1b maakt gebruik van het feit dat elektrische weerstand afhankelijk is van temperatuur. In het geval van platina, wat veel gebruikt wordt, kan hiermee van -200 tot en met 800 °C gemeten worden. Figuur 1c toont een thermometer die werkt op basis van infraroodstraling. Bij deze thermometer wordt gebruik gemaakt van het feit dat elk voorwerp straling uitzendt. In de meeste gevallen is dit infrarood straling en het menselijk oog kan dit niet waarnemen. Zodra voorwerpen zeer heet worden, kan dit ook zichtbaar licht zijn (bijvoorbeeld de gloeilamp). De 'kleur' van het licht is afhankelijk



Figuur 1 – De klassieke thermometers. De meest bekende thermometers die werken op het uitzetten van vloeistoffen (a), elektrische weerstand (b) en de emissie van een 'zwarte straler' (c).



Figuur 2 – Voorbeeld van 'nanotechnologie'. 'Le Penseur' oftewel 'De Denker' van kunstenaar Auguste Rodin. Het origineel (a) heeft de afmetingen van 180 bij 98 bij 145 cm, terwijl de creatie van enkele Zuid-Koreaanse wetenschappers slechts enkele micrometers groot is (b).

van de temperatuur van het voorwerp. Bijvoorbeeld een stuk metaal dat een smid wil bewerken zendt infrarood licht uit bij kamertemperatuur, begint rood te gloeien bij hogere temperaturen en kan zelfs wit gaan gloeien bij nog hogere temperaturen. De thermometers zoals afgebeeld in Figuur 1c meten de infrarood-straling en kunnen dit correleren aan temperatuur.

Er zijn dus al verschillende manieren om de temperatuur te meten, allemaal met specifieke voordelen en nadelen. Toch is het nuttig om onderzoek te doen naar nieuwe mogelijkheden. In dit geval omdat alle voorgaande thermometers hetzelfde gebrek hebben, de ruimtelijke resolutie van deze thermometer is vrij laag. Het is met een conventionele thermometer lastig om temperatuurverschillen te meten tussen twee locaties die bijvoorbeeld dichterbij elkaar liggen.

De wetenschap ontwikkelt zich gestaag en in de afgelopen decennia zijn er nieuwe synthesesmethoden ontwikkeld om kleinere deeltjes te maken met afmetingen op de nanometer (nm, 10^{-9} m) schaal. Nanotechnologie en nanomaterialen zijn in opkomst. De fabricage van materialen met telkens kleinere afmetingen wordt mooi geïllustreerd met het voorbeeld in Figuur 2. In Figuur 2a is 'Le Penseur' van kunstenaar Auguste Rodin te zien. De afmetingen van dit standbeeld zijn 180 bij 98 bij 145 cm. Een minuscule versie van dit beeld is nageemaakt door enkele Zuid-Koreaanse wetenschappers en is slechts enkele micrometers groot, zoals te zien in Figuur 2b. Dit standbeeld is dus nog op de micrometer schaal, maar tegenwoordig is het mogelijk om zelfs nog 1000 maal kleiner te gaan, naar de nanometerschaal.

Om op deze nanoschaal, oftewel een duizendste van een miljoenste meter, synthese te kunnen doen en controle te hebben over het proces, is het van cruciaal belang dat relevante parameters gemeten kunnen worden. Nu is temperatuur een hele belangrijke parameter

in de scheikunde en natuurkunde en het is dan dus ook belangrijk dat op de nanoschaal temperatuur gemeten kan worden. Een klassieke thermometer is veel te groot om op deze korte afstanden temperatuurverschillen te kunnen registreren.

De eerste voorbeelden van thermometers die op de millimeterschaal of kleiner werken zijn inmiddels gepubliceerd. De algemene tactiek bij deze voorbeelden is om de functionaliteit van de klassieke thermometers te verwerken in kleinere apparaten en op zo'n manier de temperatuur te kunnen meten op een kleinere schaal. Dit verloopt echter nog steeds moeilijk. Een deel van de nanothermometers is slechts voor eenmalig gebruik en bij andere nanothermometers kan niet gegarandeerd worden dat de thermometer geen invloed heeft op zijn omgeving. Daarnaast delen ze ook allemaal de eigenschap dat er dure en ingewikkelde technieken voor nodig zijn om ze te laten werken.

Een alternatief voor deze kleinschalige 'klassieke' nanothermometers is om te kijken naar temperatuurafhankelijke luminescentie van nanodeeltjes. Zodra het gedrag van temperatuurafhankelijke luminescentie goed onderzocht is ('ijken' van de thermometer), kan vervolgens het uitgezonden licht worden gebruikt om te berekenen wat de lokale temperatuur is van en rondom het nanodeeltje. In combinatie met lichtmicroscopie kan hiermee een resolutie worden bereikt van ongeveer 50 nm.

De eerste stappen in dit onderzoeksveld, zogenaamd luminescentie nanothermetrie, zijn inmiddels genomen, maar de meeste onderzoeksgroepen focussen op toepassing in de biomedische wetenschappen. Dit betekent dat zij geïnteresseerd zijn in het temperatuurgebied van 30–50 °C. In dit proefschrift is onderzoek gedaan naar de potentie van luminescentie thermometrie voor het meten van temperaturen in chemische reactoren. Hierbij kan de temperatuur veel verder oplopen en dat betekent dat de nanodeeltjes stabiel en luminescent moeten zijn tot bij voorkeur 600 °C.

In **hoofdstuk 3** en **hoofdstuk 8** van dit proefschrift hebben we gekeken naar verschillende materialen om in dit grote temperatuurbereik (25–600 °C) op basis van lichtemissie de temperatuur te meten. Uit onderzoek naar deze deeltjes is gebleken dat de relatie tussen temperatuur en luminescentie niet altijd correct beschreven wordt met de veelgebruikte wetenschappelijke modellen. Vandaar dat in **hoofdstuk 2** onderzoek is gedaan naar deze relatie wat geleid heeft tot nieuwe inzichten in de relatie tussen temperatuur en het licht dat deeltjes uitzenden.

Na de fundamentele kennis over de ontwikkeling van nieuwe materialen en de correlatie tussen temperatuur en luminescentie is er in dit proefschrift gekeken naar de toepasbaarheid. In **hoofdstuk 4** is een typische katalytische reactie onderzocht waarbij methanol wordt omgezet in simpele alkanen en andere koolwaterstoffen. Tijdens deze reactie komt veel warmte vrij, wat kan leiden tot lokale temperatuurverschillen. Door gebruik te maken van luminescentiethermetrie hebben wij deze temperatuurverschillen op de millimeterschaal kunnen meten in een werkende reactor en kunnen correleren aan het verloop van de chemische reactie.

hydrogen 1 H 1.0079																	helium 2 He 4.0026		
lithium 3 Li 6.941	beryllium 4 Be 9.0122																	neon 10 Ne 20.180	
sodium 11 Na 22.990	magnesium 12 Mg 24.305																	argon 18 Ar 39.948	
potassium 19 K 39.098	calcium 20 Ca 40.078	scandium 21 Sc 44.956	titanium 22 Ti 47.867	vanadium 23 V 50.942	chromium 24 Cr 51.996	manganese 25 Mn 54.938	ijzer 26 Fe 55.845	cobalt 27 Co 58.933	nikkel 28 Ni 58.693	koper 29 Cu 63.546	zink 30 Zn 65.39	gallium 31 Ga 69.723	germanium 32 Ge 72.61	arsenic 33 As 74.922	selenium 34 Se 78.96	bromine 35 Br 79.904	krypton 36 Kr 83.80		
rubidium 37 Rb 85.468	strontium 38 Sr 87.62	yttrium 39 Y 88.906	zirkon 40 Zr 91.224	niobium 41 Nb 92.906	molibdeen 42 Mo 95.94	technetium 43 Tc [98]	ruiterium 44 Ru 101.07	rhodium 45 Rh 102.91	paladium 46 Pd 106.42	zilver 47 Ag 107.87	cadmium 48 Cd 112.41	indium 49 In 114.82	tin 50 Sn 118.71	antimony 51 Sb 121.76	telluur 52 Te 127.60	ijodine 53 I 126.90	xenon 54 Xe 131.29		
caesium 55 Cs 132.91	barium 56 Ba 137.33	lanthanum 57-70 La 174.97	lutetium 71 Lu 174.97	hafnium 72 Hf 178.49	tantalum 73 Ta 180.95	wolfram 74 W 183.84	reinerium 75 Re 186.21	osmium 76 Os 190.23	iridium 77 Ir 192.22	platinaam 78 Pt 195.08	goud 79 Au 196.97	mercurium 80 Hg 200.59	thallium 81 Tl 204.38	lood 82 Pb 207.2	bilium 83 Bi 208.98	polonium 84 Po [209]	astatine 85 At [210]	radon 86 Rn [222]	
francium 87 Fr [223]	radium 88 Ra [226]	actinium 89-102 Ac [227]	thorium 90 Th 232.04	protactinium 91 Pa 231.04	uranium 92 U 238.03	neptunium 93 Np [237]	plutonium 94 Pu [244]	ameritium 95 Am [243]	curium 96 Cm [247]	berkelium 97 Bk [247]	californium 98 Cf [251]	esboorium 99 Es [252]	fermium 100 Fm [257]	mendelievium 101 Md [258]	nobelium 102 No [259]				
																			ununseptium 114 Uuq [289]
																			ununquadium 114 Uuq [289]

Figuur 3 - Het periodiek systeem der elementen. De lanthaniden staan onderin het periodiek systeem in het groen weergegeven.

Door de metingen te combineren met microscopie hebben we ook onderzoek gedaan naar twee andere systemen waarbij een hogere resolutie is bereikt. In **hoofdstuk 5** hebben we aangetoond dat er een temperatuurgradiënt ontstaat in een warmtespiraal van circa 300 micrometer breed en in **hoofdstuk 6** laten we temperatuurmetingen zien in een microkanaaltje van een microreactor over een afstand van 500 micrometer. Beide hoofdstukken zijn voorbeelden waarbij met een micrometerresolutie significante temperatuurverschillen waargenomen kunnen worden.

Om de functionaliteit van de temperatuursensoren te verhogen, hebben we de luminescente nanodeeltjes gecombineerd met andere nanodeeltjes. Zo kon aan de ene kant gekeken worden naar de temperatuur en aan de andere kant naar welke producten er gevormd worden tijdens een reactie aan de hand van de luminescentie van de verschillende onderdelen van het materiaal. Deze metingen van luminescentiethermometrie en zogenaamde Raman spectroscopie zijn beschreven in **hoofdstuk 7**.

In dit proefschrift is zowel aandacht voor de fundamentele theorie die ten grondslag ligt aan de temperatuursensoren alsook gekeken naar de toepasbaarheid in relevante chemische reacties.

Theorie

De luminescentie van deze nanodeeltjes komt voort uit lanthanide-ionen die verwerkt zitten in een anorganisch kristal met afmetingen van enkele tientallen nanometers tot enkele micrometers. De lanthaniden, vernoemd naar lanthaan, het eerste element uit deze

reeks, zijn in Figuur 3 weergegeven in het groen. In het periodiek systeem der elementen staan de lanthaniden tussen barium en lutetium, maar vanwege praktische redenen staan ze onderaan, samen met de actiniden.

De lanthanide ionen worden gekenmerkt door de gedeeltelijk gevulde 4f-orbitalen in hun driewaardig positieve toestand, Ln^{3+} . Deze 4f-orbitalen hebben 14 plekken waar per plek 1 elektron kan zitten. Van lanthaan tot ytterbium komt er per element een extra elektron in de 4f-orbitalen te zitten, waarbij lanthaan 0 elektronen in de 4f-orbitalen heeft zitten en ytterbium 13 elektronen. In het geval van erbium (Er^{3+}), zijn er 11 elektronen die verdeeld moeten worden over de 4f-orbitalen. Dit kan op 364 verschillende manieren en elke verschillende manier wordt een elektronenconfiguratie genoemd.

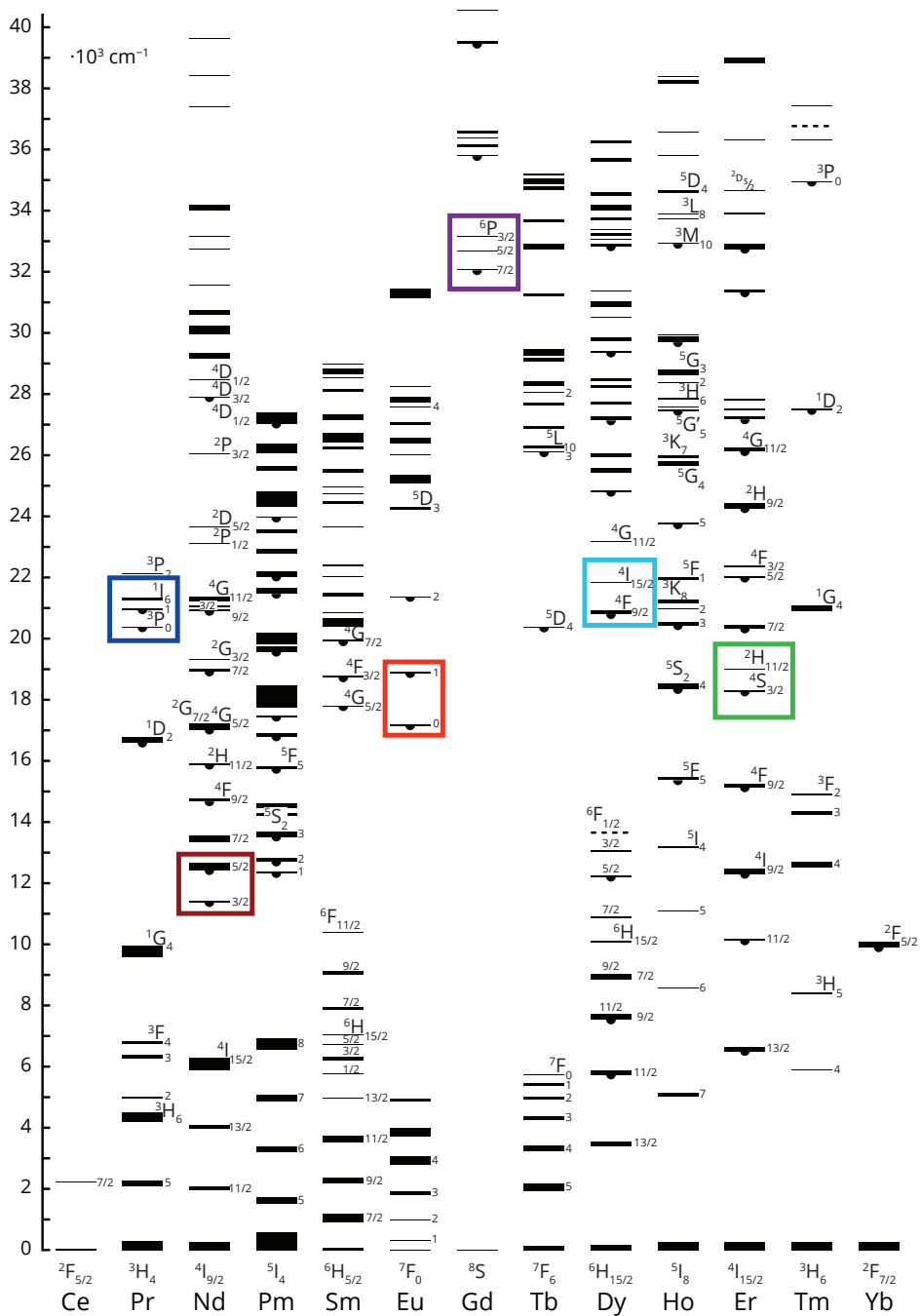
Elektronen hebben een negatieve lading en dus stoten elektronen elkaar onderling af. Dit feit, in combinatie met spin-baankoppeling zorgt ervoor dat niet elke elektronenconfiguratie dezelfde energie heeft. Dit is zowel te berekenen als te meten en dat heeft geleid tot het Diekediagram, weergegeven in Figuur 4, waarin alle energieniveaus van de lanthaniden tussen 0 en 40000 cm^{-1} zijn weergegeven.

In dit diagram zijn de verschillende elektronenconfiguraties, die nu met specifieke termen gelabeld worden, weergegeven. Hierbij is het onderste niveau, in het geval van erbium het $^4\text{I}_{15/2}$ -niveau, de grondtoestand. Dit is de toestand met de laagste energie en staat daarom bij een energie van 0. Alle andere configuraties liggen hoger in energie.

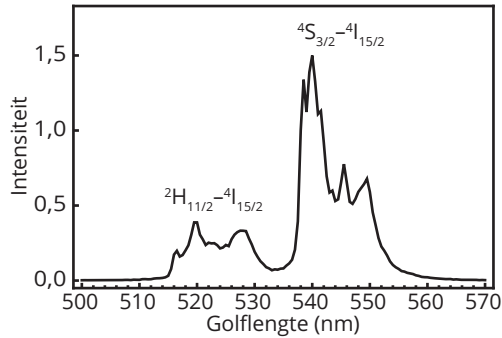
De natuur streeft altijd naar de laagst energetische toestand, de grondtoestand, maar een ion kan zich ook in een aangeslagen toestand bevinden zodra er energie (warmte, licht, elektriciteit) in het systeem wordt gestopt.

Eén van de manieren om een lanthanide-ion in een aangeslagen toestand te brengen, oftewel te exciteren, is door er licht met de juiste energie op te schijnen. In het geval van erbium is het energieverval tussen de grondtoestand ($^4\text{I}_{15/2}$) en de $^4\text{F}_{7/2}$ aangeslagen toestand (net boven het groene kader in Figuur 4) circa 488 nm. Door licht met een golflengte van 488 nm op erbiumionen te schijnen, kan een lichtdeeltje, ook wel een foton genoemd, geabsorbeerd worden. De energie van dit foton wordt dan geabsorbeerd en de energie wordt gebruikt om het ion in de $^4\text{F}_{7/2}$ aangeslagen toestand te brengen.

Het erbiumion in de $^4\text{F}_{7/2}$ aangeslagen toestand wil deze extra energie weer kwijtraken zodat het kan terugkeren naar de grondtoestand. Dit kan door middel van het uitzenden van een foton van 488 nm. In dit geval vindt precies het tegenovergestelde van absorptie plaats, emissie. Een tweede optie is om terug te vallen naar het $^2\text{H}_{11/2}$ niveau, wat net onder het $^4\text{F}_{7/2}$ niveau ligt, door middel van het afgeven van warmte aan de omgeving. Aangezien het energieverval tussen het $^4\text{F}_{7/2}$ en het $^2\text{H}_{11/2}$ niveau vrij klein is, kan dit proces gemakkelijk plaatsvinden. Vanuit het $^2\text{H}_{11/2}$ niveau heeft het ion wederom de optie om ofwel terug te vallen naar de grondtoestand door een foton uit te zenden (ditmaal een foton met een golflengte van 525 nm) of terug te vallen naar het $^4\text{S}_{3/2}$ niveau dat weer een kleine stukje lager ligt in energie. Dit kan zo meerdere keren doorgaan totdat er ofwel een foton wordt



Figuur 4 - Diekedigram. Het Diekedigram met daarin alle verschillende energieniveaus van de driewaardig positieve lanthaniden. De gekleurde kaders geven energieniveaus weer die onderzocht zijn voor luminescentie thermometrie.



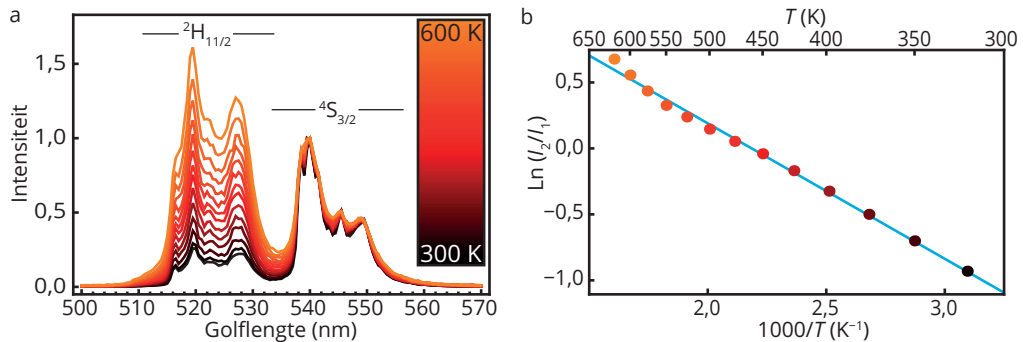
Figuur 5 – Emissiespectrum van erbium (Er^{3+}). Op de x-as staat de golflengte van het licht van 500–570 nm en op de y-as de intensiteit in arbitraire eenheden. In het figuur zijn twee emissiepieken te zien vanuit het $^2\text{H}_{11/2}$ -niveau naar de $^4\text{I}_{15/2}$ -grondtoestand en vanuit het $^4\text{S}_{3/2}$ -niveau naar de $^4\text{I}_{15/2}$ -grondtoestand.

uitgezonden ofwel alle energie afgegeven wordt in de vorm van warmte.

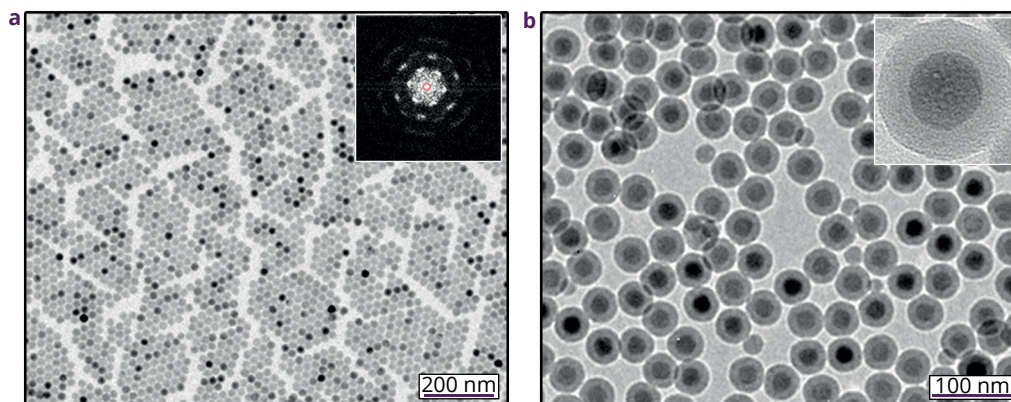
Het emissiespectrum van erbium voor excitatie bij 488 nm is weergegeven in Figuur 5. Hierin zijn de twee (gestructureerde) emissiepieken te zien die overeenkomen met de overgang van het $^2\text{H}_{11/2}$ en het $^4\text{S}_{3/2}$ niveau terug naar de grondtoestand.

In het geval van erbium, maar ook enkele andere lanthaniden, is het energieverval tussen enkele niveaus vrij klein (weergegeven met de gekleurde kaders in Figuur 4). Dit zorgt er voor dat het mogelijk is om vanaf de hoger aangeslagen toestand (in het geval van erbium het $^2\text{H}_{11/2}$ niveau) terug te vallen door warmte af te geven aan de omgeving. Maar omdat het energieverval dusdanig klein is, kan het omgekeerde proces, waarbij (thermische) energie van de omgeving wordt opgenomen om van het lagere aangeslagen niveau (in het geval van erbium het $^4\text{S}_{3/2}$ niveau) omhoog te gaan, ook plaatsvinden.

Dit fenomeen zorgt ervoor dat het onmogelijk is om bij kamertemperatuur (20–25 °C) emissie waar te nemen vanuit alleen het $^2\text{H}_{11/2}$ of het $^4\text{S}_{3/2}$ niveau. De ionen kunnen



Figuur 6 – Temperatuurafhankelijke emissie. Emissiespectra van erbium bij verschillende temperaturen van 25 °C (zwart) tot 300 °C (oranje) met stapjes van 25 °C. (a). De lineaire correlatie tussen de natuurlijke logaritme van de intensiteitsverhouding tussen twee emissiepieken en $1/T$ (b).



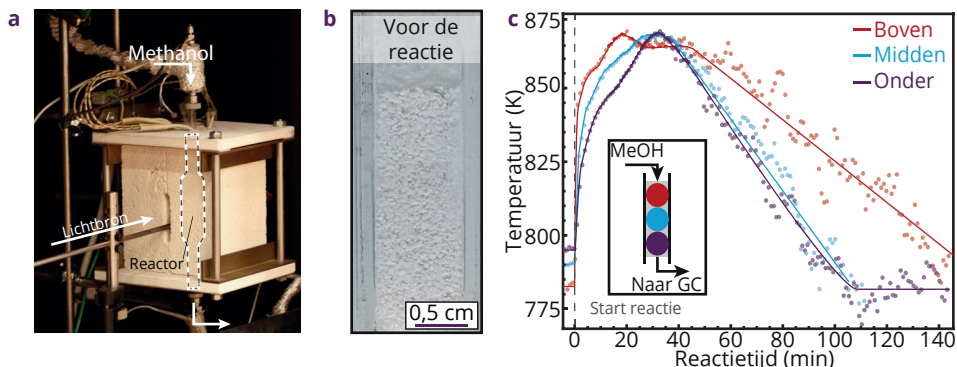
Figuur 7 – Nanodeeltjes gebruikt in dit proefschrift. Transmissie elektron microscopieplaatjes van NaYF_4 nanodeeltjes van circa 20 nm zonder (a) en met (b) laagje silica voor extra stabiliteit.

duddanig snel van het ene niveau naar het andere niveau (of vice versa) dat er altijd een distributie is over de twee verschillende niveau's. Deze distributie is de reden voor de temperatuurafhankelijkheid van de luminescentie. Hoe warmer de omgeving is, hoe meer thermische energie er is om vanaf het lagere ($^4\text{S}_{3/2}$) naar het hogere ($^2\text{H}_{11/2}$) aangeslagen niveau te gaan. Dit betekent dat er relatief meer emissie vanuit het $^2\text{H}_{11/2}$ is naarmate de temperatuur toeneemt. Dit fenomeen is gemeten en weergegeven in Figuur 6a. Hierbij is de emissie bij verschillende temperaturen van kamertemperatuur (300 K) tot en met 300 °C (ongeveer 600 K) gemeten en telkens genormaliseerd op de emissiepiek van het lagere $^4\text{S}_{3/2}$ niveau. Het is duidelijk te zien dat de intensiteit van de $^2\text{H}_{11/2}$ emissiepiek toeneemt in vergelijking met de $^4\text{S}_{3/2}$ emissiepiek als de temperatuur toeneemt van 300 K (zwart spectrum) naar 600 K (oranje spectrum).

De distributie over de twee verschillende niveau's volgt de zogenaamde Boltzmannstatistiek. Dit betekent dat de natuurlijke logaritme van de intensiteitsverhouding tussen de twee emissiepieken precies omgekeerd evenredig afhangt van de temperatuur. Dit is weergegeven in Figuur 6b waarbij de intensiteitsverhouding van de twee emissiepieken (datapunten) mooi op een lijn liggen (cyaan). Deze lijn kan vervolgens gebruikt worden om onbekende temperaturen te berekenen uit het spectrum.

Resultaten

Voordat de temperatuurmetingen uitgevoerd kunnen worden, moeten er nanodeeltjes worden gemaakt die stabiel zijn bij hogere temperaturen. Een veelbelovende kandidaat voor temperatuurmetingen zijn natriumyttriumfluoride (NaYF_4) nanodeeltjes waarin kleine hoeveelheden yttrium zijn vervangen voor erbium en ytterbium (Er en Yb). Deze nanodeeltjes vormen mooie kristallen die ook bij hogere temperaturen (circa 300 °C) stabiel zijn. Om de deeltjes bij nog hogere temperaturen stabiel te houden is er een laagje inert silica omheen gegroeid. Uit de resultaten is gebleken dat zelfs bij 600 °C deze deeltjes nog steeds stabiel zijn en niet aan elkaar smelten. Figuur 7 toont deze nanodeeltjes van NaYF_4



Figuur 8 – Reactormetingen. Foto van de reactoroven waarbij de optische fiber om de lichtmetingen te doen, de methanol introductie en de plaats van de reactor aangegeven zijn (a). Foto van de reactor met daarin een mengsel van de zeoliet ZSM-5 katalysator en de NaYF_4 (b). Temperatuur aan de bovenkant (rood), in het midden (blauw) en onderin (groen) de reactor uitgezet tegen de reactietijd (c).

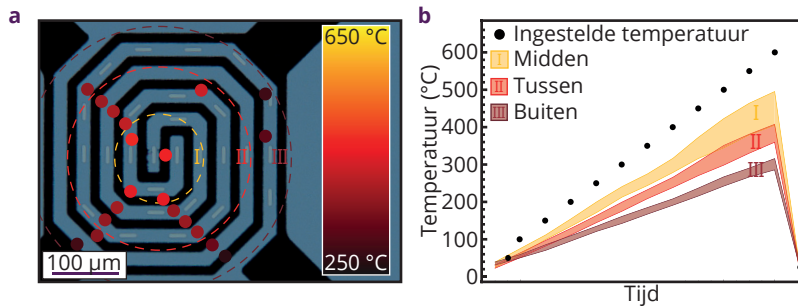
zonder (Figuur 7a) en met een silica schil (Figuur 7b).

De nanodeeltjes, die weergegeven zijn in Figuur 7, vertonen de karakteristieke luminescentie zoals te zien in Figuur 6. In het proefschrift zijn onder andere deze deeltjes gebruikt om de temperatuur te bepalen in verschillende chemische reactoren.

Het eerste systeem waarmee we de toepasbaarheid van de luminescentiethermometrie hebben aangetoond is een reactor gevuld met zeoliet H-ZSM-5, een katalysator materiaal voor de chemische reactie waarbij methanol wordt omgezet in simpele koolwaterstoffen, en microkristallijn NaYF_4 voor de temperatuurmetingen, zoals te zien is in Figuur 8a en 8b. In deze exotherme reactie, komt warmte vrij zodra de methanol wordt omgezet. Aangezien de methanol van boven in de reactor wordt geïntroduceerd, zal het dus ook initiëel bovenin opwarmen en pas daarna door het gehele reactorbed warmer worden. Dit is precies wat we waarnemen zodra we de temperatuur meten bovenin, in het midden en onderin het reactor bed, zoals weergegeven in Figuur 8c.

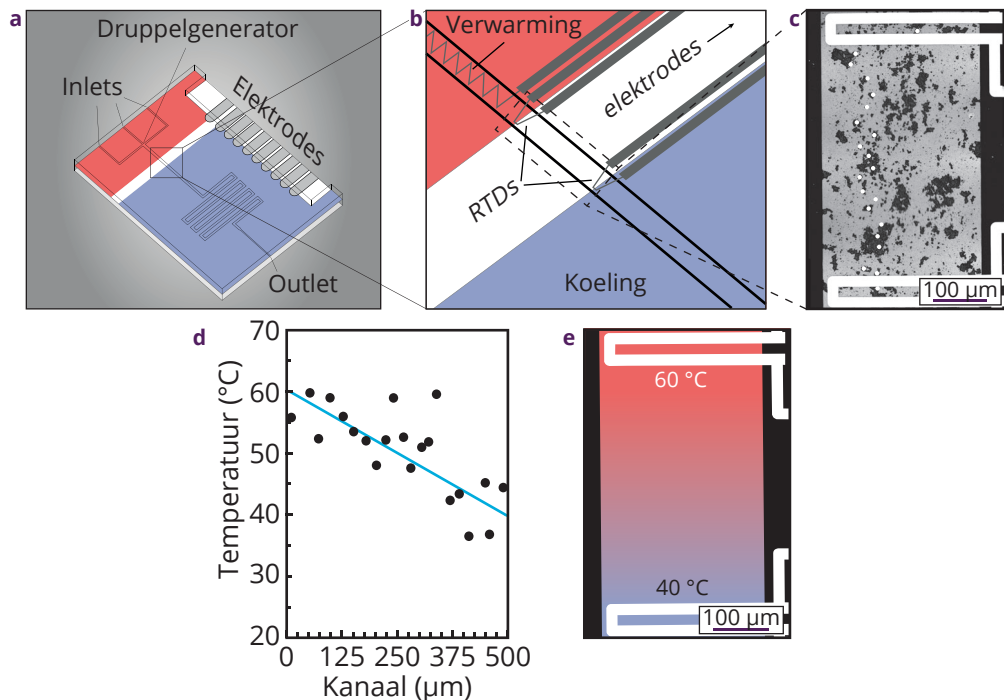
De metingen laten zien dat de luminescente deeltjes goed bestand zijn tegen de zware omstandigheden in een chemische reactor, maar de resolutie waarmee deze metingen zijn gedaan beperkt zich nog steeds tot het millimeterregime. Voor het realiseren van een hogere resolutie zijn er ook metingen gedaan in andere reactorsystemen waarbij de luminescentiemetingen zijn gecombineerd met een microscoop.

Om te kunnen meten wat het gedrag van enkele katalysatordeeltjes is bij verschillende temperaturen is een speciale cel ontworpen met een warme spiraal die een katalysatordeeltje opwarmt, terwijl er ondertussen metingen door middel van Röntgenstraling kunnen worden gedaan om te kijken hoe het katalysatordeeltje zich gedraagt. Hoewel de opstelling goed werkt, waren er toch discrepanties tussen deeltjes die in het midden van de warmtespiraal lagen en deeltjes die verder naar buiten lagen. Om te onderzoeken of dit komt door verschillen in temperatuur, is er gekeken naar de temperatuurverdeling over de spiraal. Aangezien de

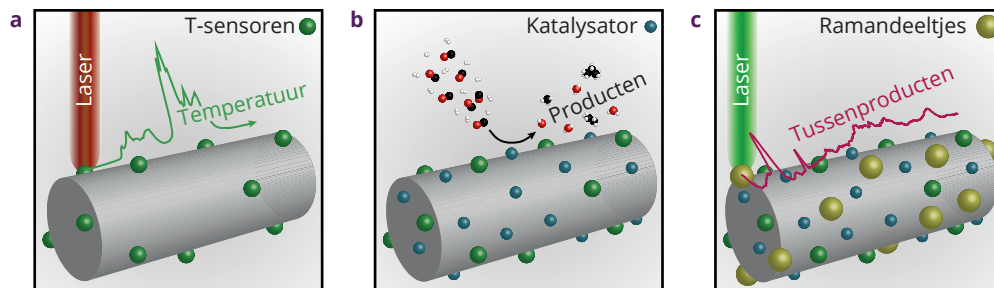


Figuur 9 – Mini-reactormetingen. Temperaturen gemeten in een warmtespiraal op verschillende plekken. Een overzicht van de spiraal met de bijbehorende meetlocaties (a). De temperaturen van de verschillende meetplekken (gekleurde rondjes) komen overeen met kleuren in de legenda. De ingestelde temperaturen van de spiraal zijn weergegeven met zwarte bolletjes en de temperaturen van de 3 verschillende regio's met geel, rood en donkerrood (b).

spiraal slechts 300 micrometer in doorsnee is, is er gebruik gemaakt van microscopie om op verschillende kleine plekken de temperatuur te meten en zo een temperatuurverdeling te maken. De spiraal is te zien in Figuur 9a en de gemeten temperaturen zijn weergegeven in Figuur 9b.



Figuur 10 – Minikanaalmetingen. Een microfluidische chip (a) met daarin een verwarmstuk en een koeling om te zorgen voor een temperatuurgradient (b). Een microscopieplaatje van het microkanaal met de temperatuursensoren (c) is gebruikt om de luminescentie te meten per plekje (witte spots) en vervolgens vertaald naar temperaturen (d). Deze temperaturen zijn gebruikt voor het visualiseren van de temperatuurgradient (e).

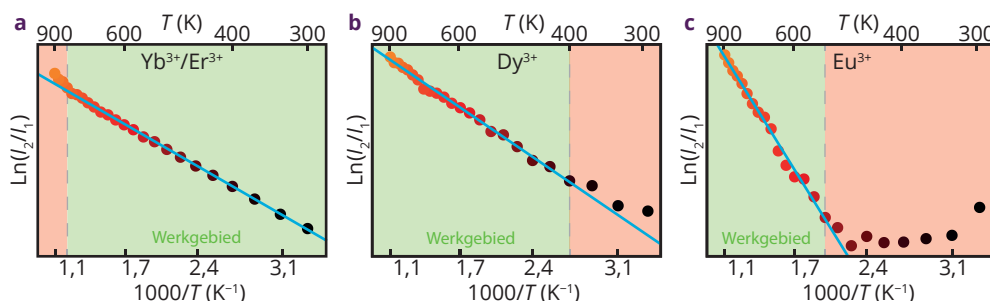


Figuur 11 - Operando Raman- en temperatuurmetingen. Een schematische weergave van de gesynthetiseerde deeltjes voor gecombineerde operando metingen. In eerste instantie is het dragermateriaal met de temperatuursensoren gemaakt (a), vervolgens zijn hier katalysatordeeltjes (b) en deeltjes voor Ramanspectroscopie aan toegevoegd (c). Nu kunnen deze deeltjes gebruikt worden voor metingen waarbij temperatuur, producten en tussenproducten gemeten kunnen worden.

Uit de metingen blijkt dat de temperatuurverdeling inderdaad niet mooi homogeen is. Binnen de gestippelde lijntjes van gebied I in Figuur 9a is de temperatuur het hoogst, maar de temperatuur in gebied II is maar liefst 100 °C lager en gebied III ligt zelfs nog lager. Dit experiment laat zien dat temperatuurfluctuaties op hele kleine schaal kunnen plaatsvinden, en dat het met de nieuwontwikkelde nanodeeltjes mogelijk is om dit soort verschillen te meten. De kleinste plekken die gemeten zijn in dit hoofdstuk zijn slechts 7 μm .

Een tweede voorbeeld van temperatuurmetingen met een hoge resolutie zijn weergegeven in Figuur 10. In dit werk zijn luminescentie thermometriemetingen gedaan op een microfluidisch systeem. Dit is een klein reactortje waarin kanaaltjes met micrometer afmetingen zijn gemaakt. Door deze kanaaltjes kan een vloeistof stromen, die snel kan opwarmen of afkoelen en waarin chemische reacties kunnen worden gedaan. In dit specifieke voorbeeld wordt een reactie gedaan bij 60 °C en dit moet vervolgens zo snel mogelijk afkoelen naar 40 °C. De afstand waarop de vloeistof moet afkoelen van 60 °C naar 40 °C is ongeveer 500 micrometer. Om te kunnen meten of dit ook daadwerkelijk zo snel gebeurt, hebben we luminescente nanodeeltjes in de kanaaltjes gebracht en daarmee op verschillende plekken in de chip de temperatuur gemeten. Ook hier is gebruik gemaakt van microscopie om zo de temperatuur te bepalen in gebieden van slechts 9 μm .

Om de functionaliteit van de temperatuurmetingen uit te breiden, is er in dit proefschrift ook geprobeerd luminescentiethermometrie te combineren met andere technieken die tijdens operandometingen kunnen worden gedaan. In dit werk hebben we gebruik gemaakt van NaYF_4 temperatuursensoren op een dragermateriaal (Figuur 11a), vervolgens zijn katalysatordeeltjes toegevoegd (Figuur 11b) en ten slotte zijn goudnanodeeltjes toegevoegd om Ramanspectroscopie mee te doen (Figuur 11c). Tijdens de reactie kan door middel van massaspectrometrie bekeken worden welke producten worden gevormd, met de NaYF_4 kan de temperatuur gemeten worden en ten slotte kan Ramanspectroscopie iets zeggen over welke tussenproducten aanwezig zijn tijdens de reactie op de katalysatordeeltjes. Met de gesynthetiseerde deeltjes is het mogelijk om een reactiemechanisme te vinden dat bepaalt welke producten worden gevormd bij specifieke katalysatoren en reactietemperaturen.



Figuur 12 – Temperatuurafhankelijke emissie van Er^{3+} , Dy^{3+} en Eu^{3+} in Y_2O_3 . Het logaritme van de luminescentieverhouding uitgezet tegen zowel temperatuur als de inverse temperatuur. In het geval van Er^{3+} (a) is dit analoog aan Figuur 6b. Voor Dy^{3+} (b) en Eu^{3+} (c) begint de lineaire trend pas bij hogere temperaturen. Het groene gebied is waarin de luminescentie lineair afhankelijk is van de inverse temperatuur.

Vrijwel al het werk in dit proefschrift is gedaan door middel nano- en microdeeltjes van NaYF_4 gedoteerd met ofwel Er^{3+} en Yb^{3+} ofwel Eu^{3+} . In de theorie is al verteld dat de luminescentie komt van de ionen waarmee het rooster is gedoteerd en dat er ionen zijn die temperatuurafhankelijke luminescentie vertonen. In dit proefschrift is echter ook onderzoek gedaan naar zowel een alternatief rooster alsook verschillende ionen waarmee dit rooster gedoteerd is. Het is namelijk zo dat hoe groter het energieverval tussen de twee aangeslagen toestanden (zie Figuur 4), hoe nauwkeuriger de temperatuurmetingen in theorie kunnen worden gedaan. Echter, als het verschil te groot wordt, dan is er niet langer sprake van Boltzmannstatistiek bij lagere temperaturen. Vandaar dat er in dit onderzoek is gekeken naar de temperatuurafhankelijke emissie van zowel Er^{3+} , Dy^{3+} als Eu^{3+} . Uit de resultaten volgt inderdaad dat alle ionen kunnen worden gebruikt voor thermometrie, maar dat dit pas bij hogere temperaturen begint voor Dy^{3+} en Eu^{3+} , zoals te zien in Figuur 12. Het rooster dat in dit werk gebruikt is, Y_2O_3 , is ook bewust gekozen om te onderzoeken of het een goed alternatief kan zijn voor NaYF_4 . NaYF_4 heeft het probleem dat het boven de $600\text{ }^\circ\text{C}$ van kristalstructuur verandert en dat het rooster ook geoxideerd kan worden, beide problemen die bij Y_2O_3 geen rol spelen. De Y_2O_3 deeltjes zijn succesvol gemaakt en getest en kunnen ook prima gebruikt worden voor de metingen, die gedaan zijn in dit proefschrift. Vanwege de hogere stabiliteit zijn Y_2O_3 nanodeeltjes veelbelovend voor (nano)thermometrie bij zeer hoge ($>1000\text{ }^\circ\text{C}$) temperatuur.

Conclusies

In dit proefschrift is luminescentie thermometrie onderzocht in de ruimste zin van het woord. Er is onderzoek gedaan naar de synthese van nanodeeltjes met karakteristieke luminescentie, er is in detail gekeken hoe de temperatuurafhankelijke luminescentie werkt, er is gekeken naar de mogelijke applicaties en daarnaast ook onderzocht hoe de functionaliteit uitgebreid kan worden door andere karakterisatietechnieken te combineren met luminescentie thermometrie.

De resultaten van **hoofdstuk 3** en **hoofdstuk 8** laten zien dat we nanodeeltjes kunnen maken met karakteristieke luminescentie die gebruikt kunnen worden voor

luminescentiethermometrie. Afhankelijk van het materiaal en de verschillende lanthanide-ionen kunnen verschillende temperatuurgebieden worden gemeten met maximale nauwkeurigheid. Daarnaast is er onderzocht of de gemaakte nanodeeltjes stabiel zijn zodat ze niet bij hoge temperaturen of onder zware, chemische omstandigheden aangetast worden en hun luminescentie verliezen.

Opmerkelijke resultaten in **hoofdstuk 2** laten zien dat de luminescentie niet altijd verandert met de temperatuur zoals de veelgebruikte modellen voorspellen. Dit is uitvoerig onderzocht door onder andere tijdafhankelijke luminescentiemetingen uit te voeren bij verschillende temperaturen tot 600 °C. Uit het onderzoek is gebleken dat de niet-stralende processen, die er voor moeten zorgen dat een evenwicht instelt tussen de twee thermisch gekoppelde energieniveaus, bij lagere temperatuur met ongeveer dezelfde snelheid verlopen als het uitzenden van licht. Omdat het systeem nog niet in zijn evenwicht is bij het uitzenden van licht, wordt het theoretisch voorspelde gedrag verstoord. Desondanks hebben we het gedrag kunnen modeleren en hebben we gevonden dat door middel van een hogere doteringconcentratie extra processen kunnen helpen om sneller in evenwicht te geraken. Dit zorgt ervoor dat de thermometers bruikbaar zijn vanaf lagere temperaturen.

Na de fundamentele van luminescentiethermometrie te hebben onderzocht, is er gekeken naar de toepasbaarheid. In **hoofdstuk 4** is dit gedaan door de methanol-naar-koolwaterstoffenreactie te bestuderen. Deze exotherme reactie wekt veel warmte op en de temperatuurprofielen en temperatuurstijgingen zoals gevonden door middel van luminescentiethermometrie komen goed overeen met de verwachtingen. De verkregen resultaten geven mooi weer wat de potentie van luminescentiethermometrie is; temperatuurbepalingen doen tijdens chemische reacties zonder de reactie zelf te verstoren.

De kracht van de luminescentiethermometrie is aangetoond in de eerste hoofdstukken van dit proefschrift, maar een groot voordeel van de techniek is hierbij niet gebruikt, de hoge ruimtelijke resolutie die bereikt kan worden. In **hoofdstuk 5** en **hoofdstuk 6** is hier verder onderzocht naar gedaan door te kijken naar temperatuurverschillen op kleinere schaal. In **hoofdstuk 5** is de temperatuurdistributie in een speciale minireactor voor Röntgenmetingen vastgesteld en hieruit valt te concluderen dat de temperaturen en temperatuurdistributies significant verschillen in lucht ten opzichte van vacuüm. In **hoofdstuk 6** is de temperatuur gemeten in een chip met microkanaaltjes voor chemische reacties op de microschaal. Hierbij is gevonden dat er een temperatuurgradiënt van 60 °C naar 40 °C ontstaat als 1 kant van de chip opgewarmd wordt. In zowel **hoofdstuk 5** als **hoofdstuk 6** is het totale gebied waarin gemeten wordt slechts honderden micrometers groot en is de meting van de temperatuurverschillen alleen mogelijk door de hoge ruimtelijke resolutie waarmee de temperatuur bepaald kon worden.

Om de toepasbaarheid verder uit te breiden is er in dit proefschrift gekeken om complexere functionele materialen te maken. In **hoofdstuk 7** zijn de temperatuursensoren gecombineerd met goud nanodeeltjes om zo naast thermometrie ook nog de verschillende soorten reactieproducten en mogelijke reactie-intermediären te bepalen door middel van

Ramanspectroscopie en massaspectrometrie.

Veel aspecten van luminescentiethermometrie zijn in dit proefschrift de revue gepasseerd. Na initiële onderzoeken naar de synthese van de nanothermometertjes en de precieze werking van de temperatuurafhankelijke luminescentie hebben we aangetoond dat de techniek gebruikt kan worden om temperatuurprofielen te meten op zowel grotere als kleinere schaal. Daarnaast is een begin gemaakt aan het integreren van de luminescentiethermometrie met andere technieken om zo nog functionelere materialen te maken die meerdere doelen tegelijk kunnen vervullen. De verwachting is dat de materialen en technieken die in dit proefschrift beschreven worden en ontwikkeld zijn in de toekomst sterk zullen bijdragen aan een beter begrip van en controle over chemische reacties in diverse typen reactoren en het ontwikkelen van betere katalysatoren voor efficiëntere productieprocessen in de chemische industrie.

Dankwoord/Acknowledgements

Ik heb enorm genoten van de afgelopen vier jaar en uiteraard ook veel geleerd. Dit had niet mogelijk geweest zonder een grote groep mensen. Het werk dat je nu leest had niet mogelijk geweest zonder deze mensen, vandaar dat ik nu deze mensen hier wil bedanken.

Als eerste wil ik graag **Andries Meijerink** bedanken. Je hebt eerst als begeleider van mijn Master's thesis, toen als contactpersoon bij mijn stageproject en nu als promotor mij een lange tijd begeleid. Ik waardeer alle kennis en aandacht die je mij gegeven hebt. Daarnaast heb ik ook heel hard met je kunnen lachen tijdens de vele conferenties en de beamtrip in Chicago. Het wordt uit jouw hele doen en laten duidelijk dat je een groot hart hebt voor de wetenschap. Ik mag van geluk spreken dat jij mijn promotor wilde zijn en dat je mij niet ontslagen hebt na het Kerstklaverjastoernooi of het bowlen.

Tijdens het schrijven van dit stuk weet ik nog niet of jouw naam ook daadwerkelijk op pagina 4 staat, **Alfons van Blaaderen**, maar hier hoor je er sowieso 100 % bij! Ik wil je graag bedanken voor alle tijd en ook je scherpe blik en visie op het werk in dit proefschrift (en het blijven hameren op het feit dat ik de 'past tense' meer moet gebruiken). Ook bij de MCEC-bijeenkomsten sprak ik je vaak over de mogelijkheden voor projecten en ik heb dankbaar gebruik gemaakt van je kennis en visie.

Ik wil ook graag **Bert Weckhuysen**, mijn derde promotor, bedanken. Bert, ik bewonder jouw vermogen om grote projecten te overzien en daarnaast ook aandacht te hebben voor individuen. Tijdens onze wetenschappelijke discussies waardeer ik je realisme maar ook je bewondering als je onder de indruk was. Dit zorgt ervoor dat ik goed kon peilen wat de impact van ons werk is, iets dat ik toch erg moeilijk vind. Ik heb daarnaast ook erg veel gehad aan onze gesprekken over mijn toekomstperspectief!

Ik had niet alleen bazen, ik mocht ook af en toe zelf de baas spelen over studenten! **Tim Prins**, jij begon op dezelfde dag als ik en dat heeft er voor gezorgd dat het project een vliegende start had! Ik waardeer je leergierigheid en je brede interesses, wat niet alleen geleid heeft tot grote hulp bij het opstellen van hoofdstuk 3 maar ook een meer fundamenteel artikel dankzij jouw harde werk met Marieke.

Bas Salzmann, ik ben blij dat je na de Bachelor's thesis terug bent gekomen naar CMI om te helpen met een prachtig stuk onderzoek. Ik heb genoten van het begeleiden en ook jij mag trots zijn op je werk wat beloond is met een mooie posterprijs bij CHAINS en nu ook een mooi gepubliceerd artikel.

Daan Groefsema, met jou heb ik uiteraard ook heel hard gelachen! Dat is ook niet zo gek aangezien we al vrienden en dispuutgenoten waren voordat je mijn student werd. Jij hebt ook bikkelhard gewerkt en samen met **Gerrit-Jan de Bruijn** een hele mooie basis gelegd voor vervolgonderzoek dat ik nog graag uitgewerkt zie worden!

Thimo Jacobs, ik ben blij dat ik samen met jou heb kunnen experimenteren op het gebied van operandometingen, maar ook met begeleidingsvormen! Je hebt Anne-Eva en mijzelf enorm geholpen met mooie metingen in slechts 10 weken tijd dankzij je toewijding en goede communicatie.

Ook al was je niet officieel mijn student, **Adriaan Frencken**, ik heb mij gelukkig wel lekker tegen jouw werk aan mogen bemoeien! Je had ongeluk met het project, maar dat was zeker niet vanwege jouw inzet! **Mark Mangnus**, jij was, in tegenstelling tot Adriaan, wel officieel mijn student, maar bij jou hoefde ik mij helemaal niet zo veel met het werk te bemoeien. Mathijs en ik hebben je lekker in het diepe gegooid, maar daar heb jij je prima weten te redden!

Ten slotte wil ik ook erg graag **Hannah Weijgertze** bedanken. Mede dankzij jouw werk heb ik hoofdstuk 6 van mijn proefschrift kunnen schrijven. Het waren lange dagen ik een donker hok, maar je hebt voorbeeldig werk geleverd en mag met trots terugkijken op jouw Bachelor's thesis.

Met drie promotoren, komen ook drie vakgroepen. Vanwege de inhoud van het promotieproject en het feit dat ik al bekend was bij de vakgroep Condensed Matter and Interfaces, was dit een logische onderzoeksgroep om als uitvalbasis te gebruiken. Ik heb het hier enorm naar mijn zin gehad en dat komt zonder meer door de collega's! **Tim Senden** en **Jacobine van Hest** (Joca), ik heb enorm genoten met jullie als kamergenoten! Als respectievelijk sportmaatje en GIF-goeroe hebben jullie een enorme stempel op mijn afgelopen vier jaar gezet en ik wil jullie daar graag voor bedanken. Omdat we nog maar lang de Untappdcompetitie vol mogen houden, voorzichtig mogen proeven van de Sjoemelradler en mogen roddelen over alles binnen en buiten WIDM!

Annelies van der Bok, wij gaan natuurlijk al way back naar het 26ste bestuursjaar van U.S.S. Proton, maar ook tijdens onze promotieprojecten bij CMI hebben we veel samen opgetrokken. Ik heb genoten van alle koppen thee die we op de PK zijn gaan drinken (hartelijk dank daarvoor 32ste!) en alle bordspelletjes die de afgelopen jaren de revue gepasseerd zijn. Ik ben blij je als vrienden te mogen benoemen en ik heb respect voor hoe hard jij werkt. Ik ben blij dat jij mijn paranimf wil zijn, dankjewel!

Professor Rabouw, tegenwoordig ook wel bekend als mede-atleet! Ik wil u graag bedanken voor het ehm... nou ja eigenlijk het goereren in het algemeen. Ik heb genoten van onze gesprekken op conferenties en tijdens het hardlopen. Ik ben blij dat ik iets voor u terug heb kunnen doen in de vorm van emotionele chantage en zo uw conditie heb weten te verbeteren.

I would also like to thank **Chun Che Lin** for all his kind words, nice talks and devotion to make the trip to Taiwan perfect. Both Joca and I were overwhelmed with all the hospitality that you, your students and your family have shown us. I enjoyed our dinner in the pannekoekenhuis recently and I hope to see you again soon!

Er zijn daarnaast nog veel meer collega's die geholpen hebben om dit promotieonderzoek tot een success te brengen. **Peter van den Beld**, dankjewel voor het zorgen dat alle apparatuur bleef werken ondanks dat ik en mijn medepromovendi ze af en toe wel aan het mishandelen waren! **Hans Ligthart**, jij hebt daarvoor deze taak prima vervuld en ook jou wil ik daar hartelijk voor bedanken. **Mathijs de Jong**, bedankt voor de lol in Chicago! **Elleke van Harten**, ik ben blij dat ik met jou het zeldzame fenomeen heb mogen meemaken dat Tim voor Ajax aan het juichen was! **Ward van der Stam** en **Joep Peters**, bedankt voor de gezelligheid tijdens het klaverjassen! **Maryam Alimoradi Jazi**, please don't ever change! And of course a big thanks for all the other colleagues at CMI: **Annalisa, Anne, Atul, Chenghui, Christa, Christiaan, Dechao, Federico, Jaco, Jantina, Jeppe, Joren, Jumpei, Kelly, Konyuan, Linda, Maaïke, Marlou, Nadine, Naud, Pedro** (Tank you), **Per-Anders, Peter, Pradip, Relinde, Saoirsé, Serena, Stephan, Shun, Thomas (2x), Ting, Vasya, Weiwei, Wenjin, Zijun, Harold, Onno, Daniël, Ingmar, Celso** and all other people that I did not mention here.

Ik heb ook veel mensen bij de Inorganic Chemistry and Catalysis and Soft Condensed Matter groepen mogen leren kennen. **Anne-Eva Nieuwelink**, dankjewel voor de geweldige samenwerking bij hoofdstuk 4! Samen hebben wij Bas en Thimo mogen begeleiden en ik denk dat dit onder andere gelukt is door jouw sociale vaardigheden en enthousiasme om iets te doen buiten je directe comfort zone! Daarnaast hebben we met **Joris Goetze** ook genoten om de setup als legoblokjes in elkaar te proppen. Anne-Eva, ik ben blij dat we elkaar nog vaak en in meerdere settings zien (ontsnappingsruimtes en het 53ste) en ik ben blij dat jij mijn paranimf wil zijn.

Een van de leukste projecten die ik heb mogen uitvoeren zijn de resultaten van hoofdstuk 7. Dat komt niet per se door de inhoud, maar vooral de collaborator, **Thomas Hartman**. Na 8 uur samen in een donker hok meten was het niveau van de humor drastisch gedaald, maar gelukkig bleef het wetenschappelijk gezien altijd nice! Dankjewel voor dit succesverhaal en ik hoop dat we elkaar nog lang muziek mogen blijven versturen.

Ilse van Ravenhorst, ik heb genoten van ons dubbelblind onderzoek. Toen we nog aan het starten waren met het onderzoek van hoofdstuk 5 verliep de communicatie nog niet zo supersoepel en dat heeft ervoor gezorgd dat ik data heb zitten uitwerken waarvan ik geen context had. Extra fijn dan dus dat het toch gewoon blijkt te kloppen! Ik denk dat we allebei heel erg trots mogen zijn op het eindresultaat. Hou vol het schrijven is ooit klaar ;).

My main accomplices at the Soft Condensed Matter group were **Ramakrishna Kotni** & **Chris Kennedy**. Chris, thanks to your perseverance, skills with the confocal microscope and

the help of **Jeroen Vollenbroek** and **Corentin Trégouët**, we have been able to perform some really nice measurements shown in Chapter 6. Rama, you are the supraparticle wizard! You were always able to make me smile when you showed me new images of the 2D self-assembled binary superstructures. Jeroen I am still laughing when I think of the picture of you on the kiddy tricycle.

Next to these people, there are many more colleagues from the ICC and SCM groups I would like to thank: **Beatriz, Carolien, Ernest, Giulia, Iris, Katarina, Katinka, Lennart, Lisette, Maarten, Max, Nynke, Pepijn, Petra, Ramon, Suzanne, Tom, Wiebke, Wouter** and all the people I am forgetting right now, thank you all.

I would also like to thank all my MCEC colleagues from outside of Utrecht for the fun times we had during the annual meetings, the MCEC schools, the excursions and mid-term evaluation: **Alvaro** (although I still don't trust you!), **Edwin, Freddy, Jan, José, Paolo, Peter, Renée** and **Robin**. Next to these people, I would like to thank the Community team of MCEC for allowing me to join them in organizing the fun activities during the schools, the interesting excursions and of course the Sinterklaas celebrations! Thank you, **Aditya Sengar, Anne-Eva, Ivan Devic, Lennart Weber** (you chemist), **Mathieu Odijk, Michel van Etten, Miguel Solsona, Stijn** and finally **Teresa de Martino**.

Er is meer in het leven dan werk, vandaar dat ik ook een grote groep mensen wil bedanken, die ik regelmatig tussen 5 en 9 zie, beginnend bij mijn bestuur. **Paul van Vliet, Gerda Korpershoek, Bart Saes, Stephan den Hartog** en **Annelies**. Ik zou hier graag wat anekdotes willen delen van onze avonturen de afgelopen jaren, maar ik denk dat het maar beter is dat die dingen niet zwart op wit staan! Ik zie uit naar ons volgende tripje (sowieso door Bart georganiseerd!) en hoop dat we nog lang in elkaars leven mogen blijven.

Daarnaast zijn er nog twee groepen mensen die ik wil bedanken. In een van die groepen help ik actief mee op monsters te slopen en kerkers te ontdekken. In de andere groep probeer ik juist door middel van die monsters het de spelers zo moeilijk mogelijk te maken! Hoe dan ook heeft iedereen altijd lol, deze avondjes waren soms zwaar na een lange dag werken, maar hebben wel geholpen met de broodnodige ontspanning de afgelopen jaren, dankjewel **Carlo van Overbeek, Paul, Cha Liang Chu, Jordy Groeneveld, Stijn, Joanna von Berg, Frans Dekker, Petra Keijzer, Annelies** en **Stephan!**

Jasper Immink mag op dit lijstje ook niet ontbreken. Sterker nog, vanwege hem is de Swessagroep in het leven geroepen. Naast Jasper, zorgen **Tim, Carlo, Paul** en **Stephan** ervoor dat ik altijd lol heb zodra deze groep mensen bij elkaar komt in Nederland, Zweden of België.

Ik heb daarnaast geluk dat ik tot het oudste en meest gerenommeerde dispuut binnen de Weekendcommissie der Utrechtse Scheikundige Studentenvereniging “Proton” behoor en doormiddel hiervan ook in een gezelschap terecht ben gekomen dat minstens net zo elitair (lees; tikkeltje verwaand) is, het WDDF. **Frans, Daan Verwijmeren** en **Daan Groefsema**, bedankt voor de vele avondjes ouwehoeren, slechte grappen maken, muziek luisteren en spelletjes spelen. Daan, ga eens een datumprikker versturen voor de volgende keer.

Naast deze fantastische mensen mag ik mij gelukkig prijzen dat ik ergens in mijn leven in contact ben gekomen met de volgende mensen die niet per se onder een specifieke groep vallen: **Leonie Koomen, Paul Peijzel, Josine Bulle** en **Ortwin Tange**.

During the writing of this PhD thesis I had some amazing help from **Max Lewis** and **Mirza Ramic** from **Arms and Sleepers**. They probably don't know it, but they helped me a lot to concentrate during the many hours of writing that were spend preparing this thesis. Let's just say your music helped me Find the Right Place, thank you for that!

Naast collega's en vrienden heb ik ook veel steun gehad aan mijn familie de afgelopen vier jaar. **Christel Voogt**, dankjewel voor de prachtige stripjes voor in mijn proefschrift. Ik heb heel veel lol gehad om deze samen te maken. **Pap, mam**, jullie ook enorm bedankt voor al het vertrouwen en steun tijdens de afgelopen vier jaar, en de studie daarvoor, en de tijd daarvoor, eigenlijk gewoon bedankt voor alles! **Femke, Arend, Gerben, Nikki, Stephan, Tanja, Marcin, Oliver, Aleksandra, Melvin, Piet, Marian, Joey, Sophie, Martijn**, lieve **Mila, Juul, Ewout, Oma, Jeanette, Thijs, Annelie, Mike, Eva** en **Sven** en alle andere familie, ook jullie enorm bedankt voor interesse de afgelopen vier jaar en de gezelligheid tijdens de vele verjaardagen.

Last but not least, **Marlique Huibregtse**. Het is voor mij nu een mooi moment om stil te staan bij wat jij voor mij hebt betekend in de afgelopen vier jaar, maar ook de negen jaar daarvoor en hopelijk nog vele jaren hierna. Ik wil jou enorm bedanken voor je toewijding en liefde en het feit dat jij van mij een beter mens maakt. Ik heb vier jaar lang nu onderzoek gedaan naar de constanten in de wereld, maar jij hebt de wereld veranderd, in ieder geval mijn wereld. Dankjewel.

List of publications

1. Geitenbeek, R. G.; Prins P. T.; Albrecht W.; van Blaaderen A.; Weckhuysen B. M. & Meijerink, A. NaYF₄:Er³⁺,Yb³⁺/SiO₂ Core/Shell Upconverting Nanocrystals for Luminescence Thermometry up to 900 K. *J. Phys. Chem. C* **2017**, *121*, 3503–3510.
2. Geitenbeek, R. G.; Nieuwelink, A.-E.; Jacobs, T. S.; Salzmann, B. B. V.; Goetze, J.; Meijerink A. & Weckhuysen, B. M. In Situ Luminescence Thermometry To Locally Measure Temperature Gradients during Catalytic Reactions. *ACS Catal.* **2018**, *8*, 2397–2401.
3. Geitenbeek, R. G.; Salzmann, B. B. V.; Nieuwelink, A.-E.; Meijerink, A. & Weckhuysen, B. M. Chemically and Thermally Stable Lanthanide-doped Y₂O₃ Nanoparticles for Remote Temperature Sensing in Catalytic Environments. *Chem. Eng. Sci.* **2018**, *In Press*
4. Geitenbeek, R. G.; de Wijn, H. W. & Meijerink, A. Investigation and Modeling on Non-Boltzmann Luminescence in NaYF₄:Eu³⁺: Implications for Luminescence Thermometry. *Phys. Rev. Appl.* **2018**, *In Press*
5. Geitenbeek, R. G.; van Ravenhorst, I. K.; van der Eerden, A. M. J.; Meirer, F.; Meijerink, A.; Weckhuysen, B. M. State-of-the-Art Holder for the Use of MEM Nano-Chips for STXM. *in preparation*
6. Geitenbeek, R. G.; Vollenbroek, J. C.; Weijgertze, H. M. H.; Trégouët, C. B. M.; Nieuwelink, A.-E.; Kennedy, C.; Weckhuysen, B. M.; van Blaaderen, A.; Odijk, M.; van den Berg, A. & Meijerink A. Luminescence Thermometry for In Situ Temperature Measurements in Microfluidic Devices. *Lab on a Chip*, *submitted*
7. Geitenbeek, R. G.; Hartman, T.; Whiting, G. & Weckhuysen B. M. Extrudate Sensors for Probing Metal-Support Interfacial Catalytic Reactions Using Operando SHINERS and Luminescence Thermometry. *Nat. Catal.* *submitted*

Other work

8. Geitenbeek, R. G.; Martin-Rodriguez, R. & Meijerink, A. Incorporation and Luminescence of Yb³⁺ in CdSe Nanocrystals. *J. Am. Chem. Soc.* **2013**, *135*, 13668–13671.
9. van der Stam, W.; Rabouw, F. T.; Geuchies, J. J.; Berends, A. C.; Hinterding, S. O. M.; Geitenbeek, R. G.; van der Lit, J.; Prévost, S.; Petukhov, A. V. & de Mello Donega, C. In Situ Probing of Stack-Templated Growth of Ultrathin Cu_{2-x}S Nanosheets. *Chem. Mater.* **2016**, *28*, 6381–6389.
10. Senden, T.; Geitenbeek, R. G. & Meijerink, A. Co-precipitation Synthesis and Optical Properties of Mn⁴⁺-doped Hexafluoroaluminate w-LED Phosphors. *Materials* **2017**, *10*, 1322.
11. Rabouw, F. T.; Prins, P. T.; Villanueva-Delgado, P.; Castelijns, M., Geitenbeek, R. G. & Meijerink, A. Quenching Pathways in NaYF₄:Er³⁺,Yb³⁺ Upconversion Nanocrystals. *ACS Nano* **2018**, *12*, 4812–4823.

Conference contributions

Luminescence Nanothermometry

at the MCEC labtour 2015 in Utrecht, The Netherlands (oral)

Synthesis, luminescence and silica coating of Eu^{3+} -doped LaVO_4 nanoparticles

at the 27th International Krutyn Summer School in Krutyn, Poland (poster)

The effect of silica overgrowth on the temperature-dependent luminescence of $\text{NaYF}_4:\text{Yb}^{3+}/\text{Er}^{3+}$

at the 4th International conference on the Physics of Optical Materials and Devices in Budva, Montenegro (poster)
and at CHAINS 2015 in Veldhoven, The Netherlands (poster)

Temperature probes for catalytic applications

at the MCEC annual meeting 2016 at Veldhoven, The Netherlands (poster, 1st prize)

Luminescence thermometry

at the Hong Kong International Symposium on Luminescence, Spectroscopy and Applications in Hong Kong, Hong Kong (oral)

Towards luminescent temperature sensing in catalytic environments using $\text{Y}_2\text{O}_3:\text{Ln}^{3+}/\alpha\text{-Al}_2\text{O}_3$ complexes

at CHAINS 2016 in Veldhoven, The Netherlands (poster, 1st prize)

Fundamentals and application of luminescence thermometry

at the MCEC midterm evaluation in Amsterdam, The Netherlands (oral)

Outside the comfort zone: Measuring temperature outside the Boltzmann regime

at the MCEC annual meeting 2017 in Enschede, The Netherlands (poster)

$\text{NaYF}_4:\text{Er}^{3+},\text{Yb}^{3+}/\text{SiO}_2$ core/shell upconverting nanoparticles for luminescence thermometry up to 900 K

at the European Materials Research Society Spring Meeting 2017 in Strasbourg, France (oral)

Investigation of unusual temperature-dependent luminescence $\text{NaYF}_4:\text{Eu}^{3+}$

at the 18th International Conference on Luminescence 2017 in João Pessoa, Brazil (oral)

Life as a PhD

at the MCEC annual meeting 2018 in Enschede, The Netherlands (poster)



About the author

Robin Geitenbeek was born in Gouda, The Netherlands, on the 3rd of August 1988. He graduated from the Zeldenrust Steeland College in 2007 and subsequently started his Chemistry studies at Utrecht University, The Netherlands. After finishing his Chemistry bachelor in 2011, he was the full-time secretary in the Board of U.S.S. Proton, the study association, for a year. Afterwards, he continued his studies by joining the honours track of the master's programme 'Nanomaterials: Chemistry and Physics' at the same academic institution. During this master, he worked on the incorporation of Yb^{3+} in CdSe nanocrystals in the Condensed Matter and Interfaces group under the supervision of Andries Meijerink. He finished his studies with an internship at Philips in Eindhoven for six months where he investigated the photoluminescence stability of quantum dots for LED lighting purposes under the supervision of Marcel Böhmer and Andries Meijerink.

He started as a PhD researcher on a joint project between Andries Meijerink (Condensed Matter and Interfaces), Alfons van Blaaderen (Soft Condensed Matter) and Bert Weckhuysen (Inorganic Chemistry and Catalysis) and was part of the Netherlands Center for Multiscale Catalytic Energy Conversion, a Gravitation programme funded by the Netherlands Organization of Scientific Research (NWO). The results of the project are described in this thesis, published in peer-reviewed scientific journals and presented at (inter)national conferences. In the course of his PhD, Robin has supervised 7 bachelor and master students, was a teaching assistant during the first year spectroscopy course and was a lab assistant at multiple chemistry labcourses.